

Modification of Gelatin-Methacrylate, Hyaluronic-  
Methacrylate and Poly(ethylene) glycol Diacrylate  
hydrogel bioinks towards the additive  
manufacturing of articular cartilage

A Dissertation submitted in fulfilment of the requirements for the  
degree

of

MASTER OF SCIENCE

of

RHODES UNIVERSITY

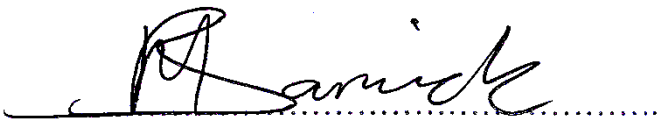
by

Matthew William Barwick

March 2021

## **Declaration**

I declare that this thesis is of my own, unassisted work. This thesis has not been submitted before for any degree or examination at any other universities and is being submitted for the degree of Master of Science of Rhodes University.

A handwritten signature in black ink, appearing to read 'M. Barwick', is written over a horizontal dotted line.

**Mr Matthew William Barwick**

## Abstract

Cartilage degradation is most commonly associated with Rheumatoid arthritis and Osteoarthritis, affecting millions of people worldwide. Joint transplants commonly use titanium alloys, which have a shelf life of between 10-15 years. Although the titanium transplant restores partial mobility, side effects such as inflammation, swelling, faulty implants, and metal poisoning in some cases resulting from the transplant. The use of additive manufacturing of articular cartilage sheds new, innovative prospects for joint replacements. This study sets out to formulate and characterize five different hydrogel types towards the additive manufacturing of articular cartilage. Chondrogenic and Adipogenic differentiation was carried out on two separate adipose-mesenchymal stem cell lines A270620-01A, and A311019-02T and validation and efficiency of the differentiation and chondrogenic gene expression was carried out using Alcian Blue stain, Oil Red O stain and Quantitative Reverse Transcription PCR (RT-qPCR). Hydrogel formulation and characterisation of 10 % Gelatin-methacryloyl (GelMA), 10 % Poly (ethylene) glycol diacrylate (PEGDA), 5 % GelMA/5 % PEGDA, 10 % GelMA/0.5 % Hyaluronic Acid Methacrylate (HAMA) and 10 % PEGDA/0.5 % HAMA was carried out through swelling and degradation ratios, surface area and porosity characterisation using Scanning Electron Microscopy (SEM). Hydrogel component and spectroscopic analysis were carried using Real-Time Quantitative Cell Analysis (RTCA) and Fourier-transform Infrared Spectroscopy (FTIR) analysis for each formulated hydrogel's chemical characterisation. Three-dimensional printing (3D) of 10 % PEGDA/0.5 % HAMA and 5 % GelMA/5 % PEGDA was performed using the Zortrax INKSPIRE Resin Ultra-Violet (UV) LCD Desktop 3D Printer. Hydrogel sterility and cell viability were carried out for each hydrogel type using fluorescence microscopy. Both A270620-01A and A311019-02T cell lines showed adipogenic and chondrogenic differentiation ability, with A311019-02T cell line showing greater chondrogenic differentiation of Alcian blue staining. The A270620-01A cell line resulted in a greater collagen gene expression based on the RT-qPCR results. The hydrogel 10 % GelMA showed the greatest swelling ratio of 1260 % in DPBS and 1192 % in DMEM. A significant difference between hydrogel swelling and swelling with Dulbecco's Phosphate Buffered Saline (DPBS) and Dulbecco's Modified Eagle Medium (DMEM) was observed. The 10 % PEGDA hydrogel had the greatest degradation ratio of 59 % mass remaining, where the 10 % GelMA/0.5 % HAMA showed the least amount of degradation with a mass remaining at 91 %. The 10 % GelMA showed the greatest porosity will the largest pore size of 14  $\mu$ m in diameter. Hydrogel component and spectroscopic analysis showed no cytotoxic effects for the visible light photoinitiator used to polymerize the hydrogel and no cytotoxic effects for the concentrations used in chondrogenic differentiation. The FTIR analysis showed partial gelatin and hyaluronic acid modification with methacrylic anhydride; however, the distinction between the hybrid hydrogels and single polymer hydrogels could not be made effectively. UV and ethanol washing showed to completely sterilise the hydrogel disks from any contaminants, making them suitable for tissue culture. The cell viability analysis showed the 10 % GelMA/HAMA having the

highest cell viability of 77.3 % using 5000 cells/disk and 89.64 % viability using 50 000 cells/disk over a 7-day incubation period. Overall, the combination of two polymers, GelMA and HAMA, has good potential as a 3D hydrogel scaffold towards additive manufacturing of articular cartilage.

## **Acknowledgements**

I would like to thank my supervisor, Prof Earl Prinsloo, for all the assistance and insight he has provided me over the years. I would like to thank my parents, André and Laura, for all the love, support and financial help they provided for my tertiary education. I would then like to thank my aunt and uncle, Sue and Graham Park, for providing the contacts to acquire the stem cells that played an influential role in completing my research. I want to thank Prof Michael S Pepper and Candice Murdoch and the Institute for Cellular and Molecular Medicine for providing the stem cells used in my research. I acknowledge and thank my lab colleges for their help, guidance and friendship. Lastly, I would like to thank the National Research Foundation and the South African Medical Research Council for their financial support for 2020 for this research.

## **Outputs**

Fanucci, S., Barwick, M. W. and Prinsloo, E. (2019) 'Bioprinting: Prospects, considerations and challenges for application in South African clinical environments', *South African Medical Journal*, 109(8), pp. 34–39. doi: 10.7196/SAMJ.2019.v109i8b.13838.

### **Author contributions:**

Editing of text in manuscript

# Table of Contents

<b>Declaration</b> .....	I
<b>Abstract</b> .....	II
<b>Acknowledgements</b> .....	IV
<b>Outputs</b> .....	V
<b>List of Figures</b> .....	X
<b>List of Tables</b> .....	XIII
<b>List of Equations</b> .....	XIV
<b>List of abbreviations</b> .....	XV
<b>List of symbols and Units</b> .....	XVII
<b>Chapter 1: Literature review</b> .....	1
<b>1.1 Introduction</b> .....	1
<b>1.2 Articular Cartilage</b> .....	2
<b>1.2.1 Damage &amp; Disease of Articular Cartilage</b> .....	3
<b>1.3 Bioinks, Biomaterials and Hydrogels</b> .....	4
<b>1.3.1 Gelatin-Methacryloyl (GelMA)</b> .....	6
<b>1.3.2 Hyaluronic Acid</b> .....	8
<b>1.3.3 Poly(ethylene) glycol diacrylate</b> .....	10
<b>1.4 Three-dimensional printing and bioprinting technologies</b> .....	12
<b>1.4.1 Extrusion Bioprinting</b> .....	14
<b>1.4.2 Inkjet Bioprinting</b> .....	14
<b>1.4.3 Stereolithographic Bioprinting</b> .....	15
<b>1.4.3.1 Photoinitiators</b> .....	15
<b>1.4.3.2 Irgacure</b> .....	16
<b>1.4.3.3 Lithium phenyl-2,4,6-trimethylbenzoylphosphinate</b> .....	17
<b>1.4.3.4 Visible light photoinitiator (Eosin Y, TEA, NVP)</b> .....	17
<b>Problem Statement</b> .....	19
<b>Research questions</b> .....	19
<b>Aims and Objectives</b> .....	20

<b>Chapter 2: Establishment of Mesenchymal Stromal/Stem Cell Differentiation &amp; Validation Protocols</b> .....	22
<b>2.1 Introduction</b> .....	22
<b>2.1 Methods and Materials</b> .....	24
2.1.1 Adipose-derived mesenchymal stem cell source .....	24
2.1.2 Adipose-derived mesenchymal stem cell (ad-HMSC) culture.....	24
2.1.3 Chondrogenic Differentiation .....	24
2.1.4 Adipogenic Differentiation .....	25
2.1.5 Alcian Blue staining .....	26
2.1.6 Oil Red O staining.....	26
2.1.7 PCR optimization of gene primers, Col10a1, Col2a1 and GAPDH.....	26
2.1.8 RT-qPCR for gene expression of chondrocytes differentiated for 14 days.....	27
<b>2.2 Results and Discussion</b> .....	29
2.2.1 Chondrogenic and Adipogenic Differentiation staining .....	29
2.2.2 RT-qPCR gene expression of collagen gene markers for Chondrogenic Differentiation .....	37
<b>Chapter 3: Hydrogel formulation and characterisation</b> .....	42
<b>3.1 Introduction</b> .....	42
<b>3.2 Methods and Materials</b> .....	44
3.2.1 Materials .....	44
3.2.2 Gelatin Methacrylate (GelMA) hydrogel.....	44
3.2.3 Hyaluronic Acid-Methacrylate (HAMA) hydrogel.....	44
3.2.4 PEGDA hydrogel.....	44
3.2.5 GelMA preparation.....	45
3.2.6 GelMA/PEGDA and HAMA/PEGDA preparation .....	45
3.2.7 Swelling analysis.....	45
3.2.8 Degradation analysis.....	45
3.2.9 Scanning Electron Microscopy (SEM) of formulated hydrogels.....	46
3.2.10 Numerical Data & Statistical Analysis .....	46
<b>3.3 Results and Discussion</b> .....	47



<b>Chapter 4: Hydrogel and Chondrogenic differentiation Component Characterisation and Spectroscopic Analysis</b> .....	63
<b>4.1 Introduction</b> .....	63
<b>4.2 Methods and Materials</b> .....	67
<b>4.2.1 Materials</b> .....	67
<b>4.2.2 HeLa Cell Culture &amp; Maintenance</b> .....	67
<b>4.2.3 Real-Time Quantitative Cell analysis (RTCA) cytotoxicity assay</b> .....	67
<b>4.2.5 Three-dimensional printing of formulated hydrogels GelMA + PEGDA and PEGDA + HAMA</b> .....	68
<b>4.3 Results and discussion</b> .....	71
<b>4.3.1 Cytotoxicity assay of visible light photoinitiator components and chondrogenic differentiation supplements</b> .....	71
<b>4.3.2 Attenuated total reflectance – Fourier transform Infrared spectroscopy</b> .....	78
<b>4.3.3 Three-Dimensional printing of formulated hydrogel bioinks</b> .....	85
.....	86
<b>Chapter 5: Cell adherence and viability on hydrogel scaffolds</b> .....	89
<b>5.1 Introduction</b> .....	89
<b>5.2 Methods and Materials</b> .....	92
<b>5.2.1 Materials</b> .....	92
<b>5.2.2 Hydrogel preparation</b> .....	92
<b>5.2.3 Hydrogel preparation for cell viability assay.</b> .....	92
<b>5.2.4 Sterility testing of formulated hydrogels</b> .....	92
<b>5.2.5 HeLa cell culturing and seeding onto hydrogels</b> .....	93
<b>5.2.6 Live/dead cell staining in GelMA, PEGDA, GelMA/PEGDA, GelMA/HAMA and PEGDA/HAMA hydrogels</b> .....	93
<b>5.2.7 Numerical Data &amp; Statistical Analysis</b> .....	94
<b>5.3 Results and Discussion</b> .....	95
<b>5.3.1 Sterility testing of formulated hydrogels</b> .....	95
.....	95
<b>5.3.2 Cell viability analysis of hydrogel scaffolds</b> .....	98

<b>Chapter 6: Conclusions and Future Work</b> .....	116
<b>6.1 Conclusion</b> .....	116
<b>6.2 Future Work</b> .....	118
<b>Chapter 7: References</b> .....	120
<b>Appendix</b> .....	139

## List of Figures

Figure 1: Organization levels of articular cartilage.....	3
Figure 2: Schematic illustration showing the complex requirements for the constraints needed to consider an idealistic scaffold design for cell culture.....	5
Figure 3: Schematic illustration of the synthesis of GelMA.....	7
Figure 4: Molecular structure of Hyaluronic Acid obtained from wikimedia commons.....	8
Figure 5: Molecular structure of poly (ethylene) glycol diacrylate. ....	11
Figure 6: Chondrogenic differentiation media changes and Alcian Blue staining day diagram. 25	
Figure 7: Alcian blue staining of chondrogenic differentiation 7 days after induction.....	29
Figure 8: Alcian blue staining of chondrogenic differentiation 14 days after induction.....	30
Figure 9: Alcian blue staining of chondrogenic differentiation 21 days after induction.....	31
Figure 10: Oil Red O staining for Adipogenic differentiation after 7 days of induction.....	32
Figure 11: Oil Red O staining for Adipogenic differentiation after 14 days of induction.....	33
Figure 12: Oil Red O staining for Adipogenic differentiation after 21 days of induction.....	34
Figure 13: Primer optimization of gene markers GAPDH (A) and Col10a1 (B).. ....	38
Figure 14: Gene Expression Levels of chondrogenic differentiation marker genes for collagen (A) Col10a1 and (B) Col2a1. ....	39
Figure 15: Swelling ratio (%) calculated for the crosslinked hydrogels after 24-hour exposure in DPBS and DMEM.....	47
Figure 16: Images of GelMA, PEGDA, GelMA/PEGDA, GelMA/HAMA and PEGDA/HAMA hydrogels before swelling (i), after swelling in DPBS (ii), in media (iii) and freeze-dried (iv).....	48
Figure 17: Degradation rate of cross-linked 10 % GelMA 5 % GelMA and 5 % PEGDA and 10 % GelMA and 0.5 % HAMA hydrogels exposed to ranging concentrations of Tri-sodium citrate solution (M, pH 7.5). ....	51
Figure 18: Degradation rate of crosslinked 10 % PEGDA and 10 % PEGDA and 0.5 % HAMA (E) exposed to ranging concentrations of Tri-sodium citrate solution (M, pH 7.5). ....	52
Figure 19: Scanning Electron Microscopy images of 10 % GelMA hydrogel disk at 1.30 kx (A), 755 x (B) and 17 x (C) magnification.....	55
Figure 20: SEM images of 10 % GelMA and 0.5 % HAMA hydrogel disk at 1.34 kx (A), 760 x (B) and 16 x (C) magnification. ....	56
Figure 21: SEM images 5 % GelMA and 5 % PEGDA hydrogel disk at 1.29 kx (A), 751 x (B) and 16 x (C) magnification. ....	57
Figure 22: SEM images of 10 % PEGDA hydrogel disk at 130 kx (A), 763 x (B) and 17 x (C) magnification.....	58
Figure 23: SEM images of 10 % PEGDA and 0.5 % HAMA hydrogel disk at 1.29 kx (A), 709 x (B) and 17 x (C) magnification.....	59

<b>Figure 24: Z-Suite printer settings for 3D print of hydrogel bioinks for Zortrax resin UV printer.</b>	70
<b>Figure 25: IC50 graphs of the photoinitiator components Eosin Y (A), TEA (B) and NVP (C).</b>	72
<b>Figure 26: IC50 graphs of the chondrogenic differentiation supplements, Ascorbic Acid (A), Dexamethasone (B), TGF-<math>\beta</math>3 (C) and L-Proline (D).</b>	73
<b>Figure 27: FTIR spectra of GelMA, PEGDA, GelMA/PEGDA, GelMA/HAMA, PEGDA/HAMA hydrogels.</b>	79
<b>Figure 28: FTIR spectra of GelMA, PEGDA, GelMA/PEGDA, GelMA/HAMA, PEGDA/HAMA hydrogels.</b>	80
<b>Figure 29: Magnified FTIR spectra views of formulated hydrogels (A)GelMA, PEGDA, GelMA/PEGDA, (B) GelMA/HAMA and PEGDA/HAMA.</b>	81
<b>Figure 30: Zortrax INKSPIRE Resin UV LCD Desktop 3D Printer.</b>	85
<b>Figure 31: PEGDA/HAMA 3D prints using the Zortrax resin printer.</b>	86
<b>Figure 32: GelMA/PEGDA 3D prints using Zortrax resin printer.</b>	86
<b>Figure 33: Vegitone agar plates 48-hours after plating pre-polymerized (I), unsterilized (II) and sterilized (III) hydrogel disks.</b>	95
<b>Figure 34: Cell viability images from formulated hydrogels after 24-hours cell seeding at a cell density of 5000 cells/hydrogel disk</b>	99
<b>Figure 35: Cell viability images from formulated hydrogels after 36-hours cell seeding at a cell density of 5000 cells/hydrogel disk.</b>	100
<b>Figure 36: Cell viability images from formulated hydrogels after seven days cell seeding at a cell density of 5000 cells/hydrogel disk.</b>	101
<b>Figure 37: Cell viability (%) of formulated hydrogels after 1,3 and 7 days with an initial 5000 cell seeding density using HeLa cells.</b>	104
<b>Figure 38: Cell viability images from formulated hydrogels after 24-hours cell seeding at a cell density of 50 000 cells/hydrogel disk.</b>	106
<b>Figure 39: Cell viability images from formulated hydrogels after 36-hours cell seeding at a cell density of 50 000 cells/hydrogel disk.</b>	107
<b>Figure 40: Cell viability images from formulated hydrogels after seven days cell seeding at a cell density of 50 000 cells/hydrogel disk.</b>	108
<b>Figure 41: Cell viability (%) of formulated hydrogels after 1,3 and 7 days with an initial 50 000 cell seeding density using HeLa cells.</b>	110

<b>Figure S 1: Primer optimization of gene markers Col2a1 (2-4), Runx2 (Lane 5-7) and Aggrecan (Lane 8-10) (A) and Col10a1 (Lanes 2-4) and Beta-Catenin (Lanes 5-7) (B).</b>	139
<b>Figure S 2: Melt Curve plots of the Gene Expression Levels of chondrogenic differentiation marker genes for collagen (A) Col10a1, (B) Col2a1 and the housekeeping gene GAPDH (C).</b>	140
<b>Figure S 3: Amplification plots of the Gene Expression Levels of chondrogenic differentiation marker genes for collagen (A) Col10a1, (B) Col2a1 and the housekeeping gene GAPDH (C).</b>	141
<b>Figure S 4: RTCA cell index graphs of Ascorbic Acid(A), Dexamethasone (B), TGF-<math>\beta</math>3 (C), L-Proline (D).</b>	143
<b>Figure S 5: RTCA well plate layout of the chondrogenic differentiation components and ranging concentrations.</b>	144
<b>Figure S 6: RTCA cell index graphs of Eosin Y (A), TEA (B) and NVP (C).</b>	145
<b>Figure S 7: RTCA well plate layout of the visible light photoinitiator components and ranging concentrations.</b>	145
<b>Figure S 8: Cell viability images of negative controls from formulated hydrogels after 24-hours cell seeding at a cell density of 5000 cells/hydrogel disk.</b>	146
<b>Figure S 9: Cell viability images of negative controls from formulated hydrogels after 36-hours cell seeding at a cell density of 5000 cells/hydrogel disk.</b>	147
<b>Figure S 10: Cell viability images of negative controls from formulated hydrogels after 7 days cell seeding at a cell density of 5000 cells/hydrogel disk.</b>	148
<b>Figure S 11: Cell viability images of negative controls from formulated hydrogels after 24-hours cell seeding at a cell density of 50 000 cells/hydrogel disk.</b>	149
<b>Figure S 12: Cell viability images of negative controls from formulated hydrogels after 36-hours cell seeding at a cell density of 50 000 cells/hydrogel disk.</b>	150
<b>Figure S 13: Cell viability images of negative controls from formulated hydrogels after 7 days cell seeding at a cell density of 50 000 cells/hydrogel disk.</b>	151

## List of Tables

<b>Table 1: Overview of self-assembly strategies, biomimicry and microtissue methods for bioprinting.</b> .....	13
<b>Table 2: Optimized PCR reaction setup.</b> .....	27
<b>Table 3: Optimized Thermocycling conditions.</b> .....	27
<b>Table 4: RT-qPCR reaction parameters for QuantStudio™ 3 thermocycler.</b> .....	28
<b>Table 5: Chondrogenic differentiation primer sequences, product length and annealing temperatures for RT-qPCR gene expression assay and PCR optimization.</b> .....	28
<b>Table 6: Zortrax Inkspire 3D resin printer settings.</b> .....	69
<b>Table 7: IC50 values of reagents used in RTCA analysis on HeLa cells.</b> .....	74
<b>Table 8: Biomaterial mechanical property influence on cell and signalling pathways.</b> .....	89
<b>Table 9: Contamination count from pre-polymerized, unsterilized and sterilized hydrogels plated on vegitone agar plates for 48-hours.</b> .....	95
<b>Table 10: Statistical analysis of the cell viability of the formulated hydrogels between 5000 cells/disk and 50 000 cells/disk after 1, 3 and 7 days of incubation.</b> .....	111

## List of Equations

Equation 1: Gene expression fold equation format where Ct=cycle threshold.....	28
Equation 2: Swelling ratio (%) formula. ....	45
Equation 3: Cell viability (%) formula modified from (Kartolo et al., 2018).....	93

## List of abbreviations

2D	Two Dimensional
3D	Three Dimensional
Ad-HMSC	Adipose-Human Mesenchymal Stem Cells
Ad-MSC	Adipose-Mesenchymal Stem Cells
AIM	Adipogenic Induction Media
AM	Additive Manufacturing
AMM	Adipogenic Maintenance Media
BMSCs	Bone Marrow Stromal Cells
Cat. No.	Catalogue Number
Col10a1	Collagen, type X, alpha 1
Col2a1	Collagen, type II, alpha 1
CT	Computed Tomography
Ct	Cycle Threshold
DAPI	4',6-Diamidino-2-Phenylindole
dd	Double Distilled
DMEM	Dulbecco's Modified Eagle Medium
DNA	Deoxyribonucleic Acid
dNTPs	Deoxyribonucleotide Triphosphate
DoF	Degree of Functionalization
DPBS	Dulbecco's Phosphate Buffered Saline
DS	Degree of Substitution
ESCs	Embryonic Stem Cells
FBS	Fetal Bovine Serum
FFR	Free Form Fabrication
FTIR	Fourier-Transform Infrared Spectroscopy
GAGs	Glycosaminoglycans
GAPDH	Glyceraldehyde 3-Phosphate Dehydrogenase
GelMA	Gelatin Methacrylate
GFP	Green Fluorescent Protein
HA	Hyaluronic Acid
HAMA	Hyaluronic Acid Methacrylate
IBMX	3-isobutyl-1-methylxanthin
IC2959	2-Hydroxy-1-[4-(2hydroxyethoxy)phenyl]-2-methyl-1-
ICMM	Institute for Cellular and Molecular Medicine
IDT	Integrated DNA Technologies
IEP	Isoelectric Point



iPSCs	Induced Pluripotent Stem Cells
LAP	Lithium Phenyl-2,4,6-trimethylbenzoylphosphinate
MEM- $\alpha$	Minimum Essential Medium-alpha
MSC	Mesenchymal Stem Cells
NVP	1-vinyl-2 pyrrolidinone
PCR	Polymerase Chain Reaction
PBS	Phosphate Buffered Saline
PEG	Poly (ethylene) Glycol
PEGDA	Poly (ethylene) Glycol Diacrylate
Pen/Strep	Penicillin/Streptomycin
PGA	Poly (glycolic acid)
PLA	Poly (lactic acid)
POE	Polyethylene Oxide
PRG	Protein Proteoglycans Propane
RGD	Arginine-Glycine-Aspartic Acid
RNA	Ribonucleic Acid
ROS	Reactive Oxygen Species
RP	Rapid Prototyping
Rpm	Revolutions per Minute
RTCA	Real-Time Quantitative Cell Analysis
RT-qPCR	Quantitative Reverse Transcription PCR
SEM	Scanning Electron Microscopy
SLA	Stereolithography
TEA	Triethanolamine
TGF $\beta$ -3	Transforming Growth Factor beta-3
US	United States
USA	United States of America
USD	United States Dollar
v	Volume
w	Weight

## List of symbols and Units

$\beta$	Beta
cm	Centimetre
Da	Dalton
$^{\circ}\text{C}$	Degrees Celsius
$\emptyset$	Diameter
kDa	KiloDaltons
L	Litre
MDa	MegaDaltons
m	Meter
$\mu\text{L}$	Microlitre
$\mu\text{M}$	Micromolar
$\mu\text{s}$	Microsecond
mL	Millilitre
M	Molar
ng	Nanograms
nm	Nanometer
N	Normality
%	Percentage

# Chapter 1: Literature review

## 1.1 Introduction

According to the Western Cape government publication on organ donation in South African approximately 4300 people await for organ and cornea transplants with only 0.2% of the population being registered as donors (Western Cape Government , 2019). The shortage of organs for transplants and tissue replacements has become a significant public health challenge within South African with only a small percentage receiving the vital organs and tissues that mostly have a limited lifespan and require the need for drugs to help prevent failure and increase the longevity of the organs and tissues (Dzobo *et al.*, 2018). The shortage of organs and tissue is not solely due to a lack of organs and tissue availability but also due to the organ and tissue rejection of the immune system's recipient. Tissue engineering is a field, which has become prominent in drug discovery and regenerative tissue therapies (O'Brien, 2011; Rimann and Graf-Hausner, 2012; Ravi *et al.*, 2015) employing engineering and biological properties for the creation of new tissues and organs, as well as promoting the regeneration of diseased or damaged tissue (Dzobo *et al.*, 2018). Tissues and organs such as skin, cartilage, heart, liver and kidney are some of the main focus points in regenerative medicine (Dzobo *et al.*, 2018). Three-dimensional bioprinting has become the primary focus in regenerative medicine and tissue engineering studies addressing tissue and organ transplant suitability, sustainability and availability (Atala and Murphy, 2014). Three-dimensional (3D) bioprinting has broadened the horizons for regenerative medicine having a decisive impact on the success and expansion of knowledge in drug discovery, *in vivo* and *in vitro* systems. Three-dimensional bioprinting aims to provide an artificial extracellular matrix (ECM) with better cellular interaction and structural complexes that are more representative of *in vivo* environments than 2D tissue cultures (Edmondson *et al.*, 2014). Bioprinting thus allows the formulation of complex constructs and materials in which cells can survive and interact, providing an environment as close to the cellular *in vivo* environment as possible (Mandrycky *et al.*, 2016), increasing the potential in regenerative medicine, tissue engineering and drug discovery.

Cartilage degradation and defects are the most common form of the disease in joints, causing swelling, pain, and joint function loss resulting in physical disability and significant economic burden (Wang *et al.*, 2017; Dong *et al.*, 2018; Pahoff *et al.*, 2019). It is a disease that affects millions of people worldwide, with millions of dollars being invested in treating cartilage degradation. Cartilage healing in regenerative medicine is a significant challenge due to the cells' slow growth and proliferation. This is also since cartilage tissue does not contain lymph or nerves and blood vessels (Li *et al.*, 2019). Current research aims to find more effective ways to enhance cartilage regeneration and replacement, less invasive and more cost-effective methods to treat the disease. The use of 3D bioprinting is the most promising way forward to achieve these goals through a simple combination of different biomaterials,

manipulation of the printing of bioscaffolds, and specific cells such as Mesenchymal Stem cells. The following literature review sets out to describe tissue engineering as the emerging medical regenerative tissue therapy centralizing around 3D scaffold formation of bioinks towards specific tissue types with the focus on articular cartilage tissue engineering for degenerative diseases such as osteoarthritis, rheumatoid arthritis and wear and deterioration on articular cartilage within the joints of the body.

## 1.2 Articular Cartilage

Articular cartilage can be defined as the connective tissue covering the epiphyseal surface of articulating bones, forming the base layer in joints and consists of up to 80% water (Sophia Fox, Bedi and Rodeo, 2009). It consists of three major types of cartilage, hyaline, fibrous and elastic. All three types have a low chondrocyte density, which synthesizes and secretes the major components of cartilage into the extracellular matrix (ECM) (Krishnan and Grodzinsky, 2018). Articular cartilage consists of only one cell type, chondrocytes and lacks blood vessels, nerves and lymphatics however the heterogeneous composition, complex organization levels and specific biochemical properties make it a highly specialized, complex and challenging tissue to engineering and regenerate (Armiento *et al.*, 2018). In addition to this, the ECM of cartilage is only sustained by chondrocytes, accounting for 1% to 5% of the total volume of cartilage. The lack of blood vessels and the density of chondrocytes in cartilage result in the low regeneration capacity of cartilage tissue (Abbadessa *et al.*, 2016; Li *et al.*, 2019). Due to the strength and elasticity of articular cartilage, it acts as a dynamic stress-bearing tissue, distributing and withstanding the stress between the contiguous bones while still providing movement to the synovial joint with low coefficient friction (Mabuchi *et al.*, 1999; Pan *et al.*, 2009; Armiento *et al.*, 2018).

The ECM of articular cartilage consists of two phases, a solid and liquid phase. The solid phase comprises collagen II, responsible for the overall shape of the tissue, glycosaminoglycans (GAGs), proteoglycans and glycoproteins. The liquid phase consists of water and electrolytes ( $\text{Ca}^{2+}$ ,  $\text{K}^+$ ,  $\text{Na}^+$  and  $\text{Cl}^-$ ). The challenge in recreating articular cartilage is mainly the complexity of articular cartilage, which can be seen in Figure 1. Figure 1 shows the five different regions or zones found within articular cartilage, the superficial, middle, deep, calcified and subchondral bone zones (Sophia Fox, Bedi and Rodeo, 2009; Armiento *et al.*, 2018). The superficial zone has a high density of flat chondrocytes with collagen type II fibres aligned parallel to the joint surface and protein proteoglycans (PRG). The middle zone consists of spherical chondrocytes within thick collagen fibres. The deep zone consists of mainly large chondrocytes surrounded by collagen VI fibre pericellular matrix (Sophia Fox, Bedi and Rodeo, 2009; Armiento *et al.*, 2018). The complexity and arrangement of each zone consisting of chondrocytes, collagens and proteoglycans as seen in figure one adds additional dimensional in recreating articular cartilage to try and represent the synthetic as close to the natural as possible.

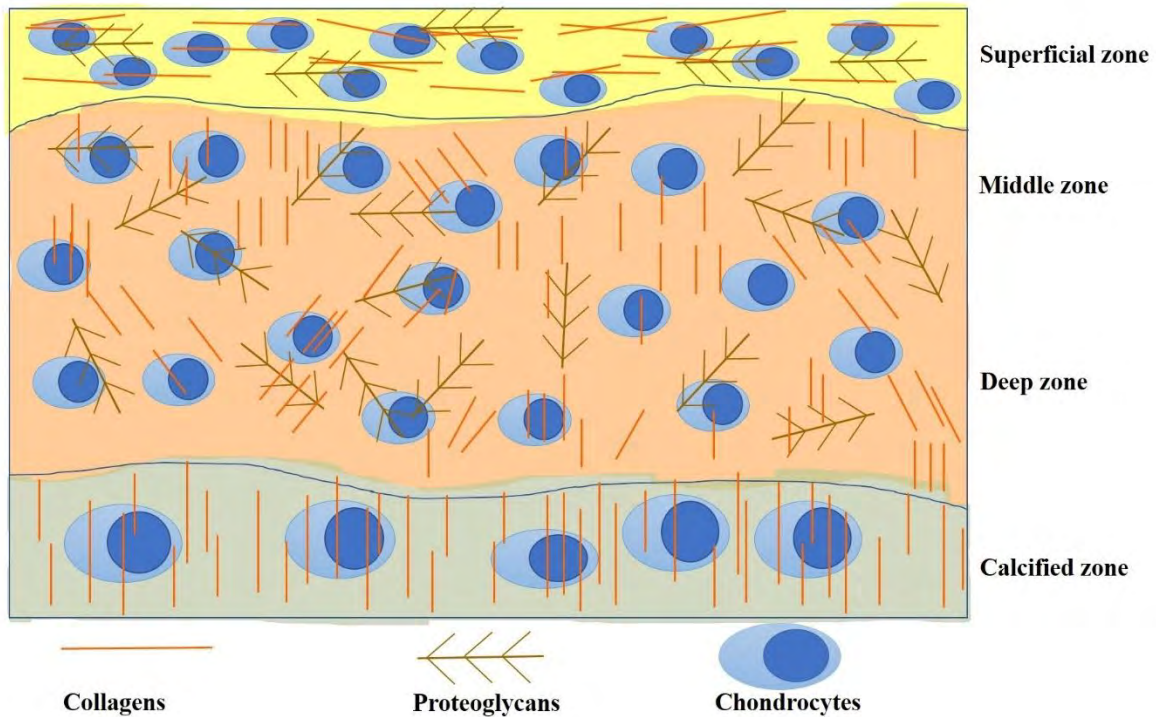


**Figure 1: Organization levels of articular cartilage.** Diagram showing the various layers and complex organization levels of articular cartilage adapted from Liu *et al.*, 2017.

Hyaline cartilage appears glassy and is the most common form of cartilage found in the body. It occurs in the articulating surfaces of bones in the synovial joints, nose, ribs, bronchi, trachea, larynx and growth plates. Joint movement is enabled by articular hyaline cartilage providing a lubricating surface and significantly low coefficient of friction. Several different types of collagen molecules are expressed in articular cartilage with the backbone of the fibrillar network of cartilage being type II collagen. Other important collagen molecules found in articular cartilage include type III, type X, type XI, type XII, and type XIV.

It is suggested that the presence of osteocytes plays an integral role in articular cartilage's structural integrity. The structural differences that occur in articular cartilage, especially close to the subchondral bone are believed to result from the chemical interactions occurring between the cartilage and subchondral bone cells. This, therefore, emphasizes the importance of an osteogenic niche to support the structural integrity of articular cartilage (Findlay and Atkins, 2014).

### 1.2.1 Damage & Disease of Articular Cartilage

Cartilage degeneration is a common effect mostly seen in diseases such as rheumatoid arthritis (RA) and osteoarthritis (Robin Poole *et al.*, 2004; Jones, 2009) of which approximately 90 million adults in the US and over hundreds of millions of people worldwide are affected by the disease. Within South Africa, it affects 55.1 % of people in urban areas and 29.5-82.7 % of people over the age of 65 in rural

areas (Rangiah, Govender and Badat, 2020). Osteoarthritis primary affects the articular hyaline cartilage such as the hip, knee and shoulder (load bearing joints) and is commonly seen in the hands and feet. Advances of the disease cause serve degeneration of the cartilage, reducing subchondral bone thickening, narrowing of the joint space the then causes inflammation in the joint, the formation of osteophytes or bone spurs accompanied by pain and swelling (Krishnan and Grodzinsky, 2018). Although current procedures for cartilage repair such as autografts, microfracture (marrow stimulation), and autologous chondrocyte implantation have been successful in certain aspects, limitations of these methods, which include unmatched property of the repaired region, lack of integration and donor-site morbidity influence the success of the cartilage repair. These limitations provide a scope and a field of interest for future tissue engineering applications and 3D bioprinting for articular cartilage repair (Liu, Zhou and Cao, 2017).

### **1.3 Bioinks, Biomaterials and Hydrogels**

Bioinks and biomaterials play a vital role and are necessarily the foundation for 3D bioprinting. In a review done by Groll *et al.*, 2019, they discuss the terms of bioinks and their role in 3D bioprinting and come to an appropriate definition of a bioink of what it is and the functionality of it. A bioink can be defined as "a formulation of cells suitable for processing by an automated biofabrication technology that may also contain biologically active components and biomaterials (Groll *et al.*, 2019).

Bioinks and biomaterials differ due to the target tissue requiring specific types of cells used in the biofabrication process. The type of bioprinter also dictates the type of bioinks and materials used. For example, extrusion type bioprinting requires a semi-viscous bioink that is extruded through a very narrow nozzle whereas to avoid blockage, with resin printing, no nozzle is present, but the bioink requires a photocurable property to polymerize and construct the 3D structure (Gungor-Ozkerim *et al.*, 2018; Groll *et al.*, 2019). Although each bioink is specialized for the type of cells and bioprinter used, bioinks have desirable physicochemical properties including good rheological, mechanical, chemical and biological characteristics. These properties need to favour (1) the generation of tissue constructs while still retaining the tissue-matching mechanics with sufficient robustness and mechanical stress; (2) biocompatibility and biodegradability, mimicking the natural microenvironment of the tissues; (3) have the ability for chemical modifications meeting tissue-specific needs; (4) adjustability for gelation and stabilization to aid the bioprinting of structures; and (5) the potential for the bioink to be produced on a large scale platform with minimum batch-to-batch variations (Gungor-Ozkerim *et al.*, 2018). Bioinks can come in two forms, natural or synthetic, each with their advantages and disadvantages in 3D bioprinting. Natural bioinks have the advantages of biomimicry of the ECM composition, have self-assembly abilities, biocompatibility and biodegradability properties. Synthetic bioinks have advantages such as controllability of mechanical stability, photo-crosslinking ability, temperature responsiveness,

pH responsiveness, all of which natural bioinks lack (Gopinathan and Noh, 2018). Both types of bioinks have been used and shown success, however, each has advantages that the other lacks. Insight of this, combining parts of natural and synthetic bioinks together has shown great success in bioprinting and has opened new windows of variability for bioink formulations. Interpenetrating polymer networks (IPNs) are referred to as semisynthetic hydrogels/bioinks as they form a system containing two or more polymer components. The use of IPNs is by combining favourable properties of each polymer to create a new system with new properties that will then differ from the two original single polymers. INPs are classified into two groups – mechanical blends and graft polymers. Mechanical blends have no chemical bonds being formed between the two or more polymers. Graft polymers have primary bonds between the polymer components and can therefore be further classified in subsections based on the presence or absence of cross-linking between the components (Zoratto and Matricardi, 2018).

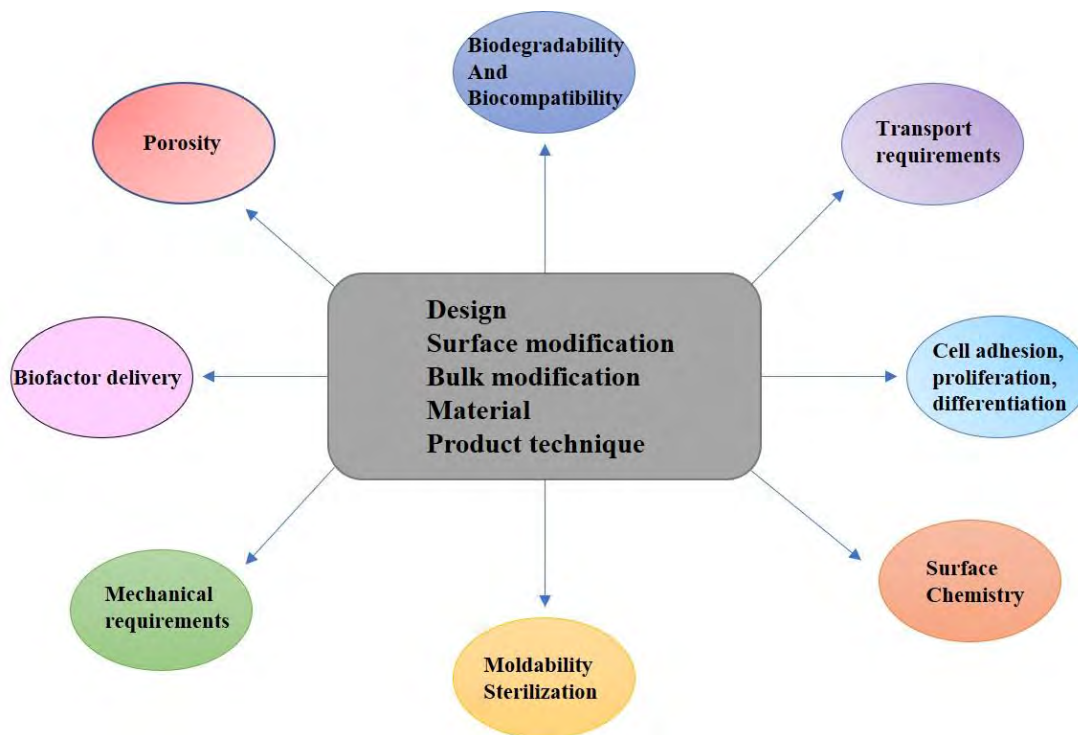


**Figure 2: Schematic illustration showing the complex requirements for the constraints needed to consider an idealistic scaffold design for cell culture.** The diagram has been adapted from (Billiet *et al.*, 2012).

Bioinks and biomaterials form an essential part of hydrogels, which interact and influence biological systems and processes to evaluate, augment, treat or replace tissue, organs or function within the body (O’Brien, 2011). Figure 2 shows the various factors that need to take into consideration when designing or formulating a hydrogel scaffold. The scaffold should try to include most of the factors shown in Figure 2 to have optimal effect as a cellular scaffold. Cell adhesion and surface chemistry, proliferation and differentiation if using stem cell, biofactor delivery porosity and transport requirements,

biodegradability and biocompatibility are all essential factors, which should be addressed for the scaffold design, bulk modification and product technique of the tissue scaffold. Factors such as mechanical properties, scaffold architecture and manufacturing technology are some of the main factors with scaffold design and bioink/biomaterial formulations for 3D bioprinting, which also need consideration when designing the scaffold for macroscale production of 3D bioprinting (O'Brien, 2011; An *et al.*, 2015). Hydrogels themselves are a formulation of bioinks and materials added together to form a three-dimensional hydrophilic polymer network containing the same water content as soft tissue and highly resemble that of the natural extracellular matrix. Hydrogels can swell in water, becoming much more significant than their initial mass without disintegration and offering mimetic conditions for cell culture (Sun *et al.*, 2018; Li *et al.*, 2019). The high-water content of hydrogels supports cell survival and allows for the homogenous encapsulation of cells, biological and chemical cues. Hydrogels thus provide initial structural support while promoting new tissue formation (Abbadessa *et al.*, 2016). The materials that makeup hydrogels are split between natural and synthetic materials. Examples of natural polymers include gelatin, alginate, fibrin, hyaluronic acid and chitosan. Synthetic polymers include polyethylene oxide (PEO), polyacrylic acid, polyvinyl alcohol and poly(ethylene) glycol (PEG). While natural polymers possess unique biological activities such as osteoconductivity – property allowing host cells to grow in a 3D graft structure promoting the growth of bone cells within the 3D structure and on the surface (Klenke and Siebenrock, 2016), they lack in mechanical strength. Synthetic polymers have high mechanical strength but have poor biocompatibility. The use of both natural and synthetic is often done, improving the hydrogel's overall functionality for regenerative medicine (Li *et al.*, 2019) through optimizing properties shown in Figure 2 such as porosity, biodegradability and biocompatibility, cell adhesion, proliferation and differentiation and biofactor delivery.

### **1.3.1 Gelatin-Methacryloyl (GelMA)**

Gelatin-methacryloyl (GelMA) shows promise as a suitable scaffold for cartilage replacement and regeneration. GelMA is semi-synthetic hydrogel derivatized of gelatin with methacrylic anhydride (Pepelanova *et al.*, 2018). This modification of gelatin with methacrylate allows it to be cross-linked using UV light exposure and allows for variation of the degree of functionalization (DoF), a desirable trait for 3D cell culture and bioprinting (Shirahama *et al.*, 2016; Pepelanova *et al.*, 2018). The modification of gelatin with methacrylic groups with UV cross-linking prevents the rapid disassembly of polymer networks, a trait required for tissue scaffolds shown in Figure 2 as mechanical requirements and biodegradability (Abbadessa *et al.*, 2016). Gelatin is one of the most abundant proteins in articular cartilage and the body, it is acquired from collagen's partial hydrolysis. It is biodegradable and biocompatible, contains RGD (Arginine-Glycine-Aspartate) motifs providing suitable attachment for cells, has reduced presence of aromatic groups making it less immunogenic than collagen and has an integral role in cellular function, proliferation and differentiation making it a suitable choice as a biomaterial in tissue engineering for cartilage replacement (Shirahama *et al.*, 2016; Zhu *et al.*, 2019).



GelMA also displays enzymatic cleavage (degradation in response to matrix metalloproteinases) an essential feature in tissue replacement (Klotz *et al.*, 2016).

In comparison to other natural materials with respect to biomaterials, gelatin is easily accessible and low in cost. However, gelatin on its own has limited capability with regard to functionality as a bioink and more importantly 3D printing. Raw, unmodified gelatin is only able to form a physical hydrogel at specific temperatures and concentrations with low forms of mechanical strength and stiffness. The addition of cross-linking chemicals and photo-crosslinking chemicals (e.g., glutaraldehyde and methacrylic anhydride) are ways to improve the mechanical strength and stiffness of gelatin, providing more variation and manipulation of gelatin. Photo-crosslinking allows for fast, uniform *in situ* curing. Numerous different chemicals can be used with gelatin however methacrylic anhydride (MAA) is the most widely used. Bioapplications such as micropatterning, 3D scaffolds, fluidic systems and bioprinting with different cell types including stem cells, fibroblasts, hepatocytes and chondrocytes have all been integrated with the use of GelMA (Shirahama *et al.*, 2016). Preparation of GelMA is through the synthesis of gelatin with MAA where the monomers react with the lysine and hydroxy lysine groups of gelatin, which can be seen below in Figure 3.

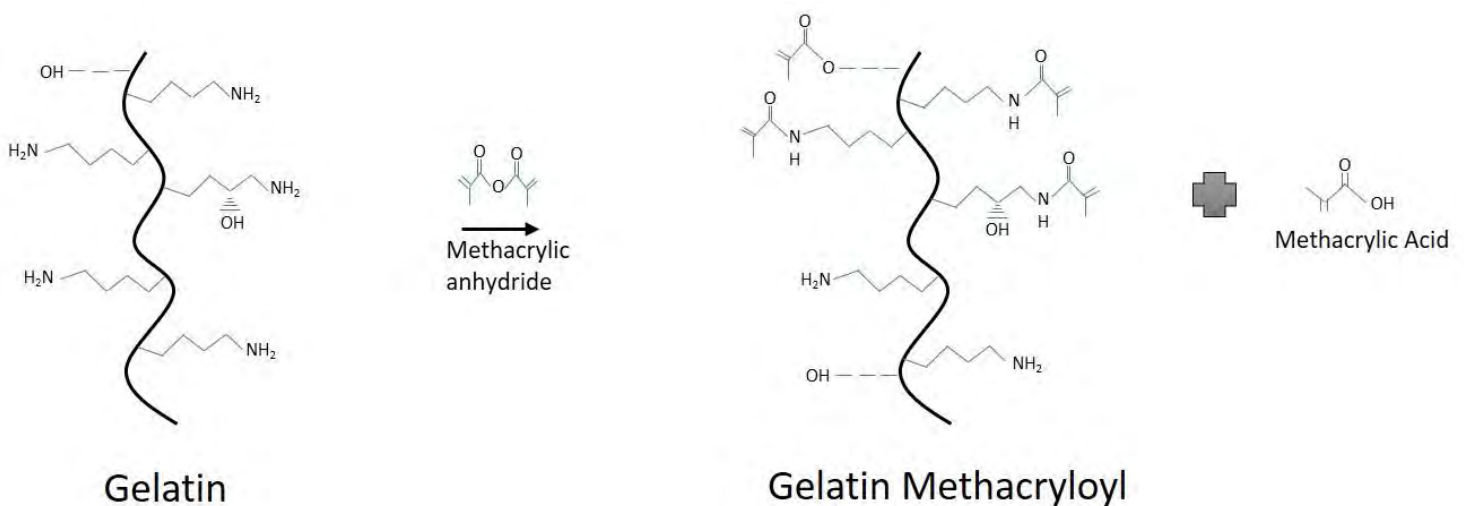


**Figure 3: Schematic illustration of the synthesis of GelMA.** Diagram modified from (Shirahama *et al.*, 2016; Zhu *et al.*, 2019).

The feed ratio gelatin to MAA can be adjusted and affects the degree of substitution (DS), which in turn affects the DoF (Shirahama *et al.*, 2016; Zhu *et al.*, 2019). If the feed ratio affects the degree of substitution, subsequently, the photocurability and biophysiochemical properties of GelMA will be affected. Although the feed ratio is the most prominent factor to affect DoF, it is not the only factor. Monitoring and controlling the pH can influence the DS and DoF of GelMA. Alteration of the pH influences the free amino groups of lysine, which react with MAA. GelMA can be produced using a calcium carbonate buffer via two ways. The first is a sequential method where the pH is continuously adjusted during the addition of MAA. The second is a one-pot method where the pH is initially adjusted

to a high pH, followed by the addition of MAA. Both types of methods aim to maintain the pH above the isoelectric point (IEP) above that of gelatin, causing the free amino groups of lysine to remain neutral, allowing them to react with MAA (Shirahama *et al.*, 2016; Zhu *et al.*, 2019). GelMA has shown to be an effective hydrogel for the 3D cell culture towards chondrogenic tissue culture (Pepelanova *et al.*, 2018; Pahoff *et al.*, 2019) however the addition of more viscous components such as hyaluronic acid (HA) and poly(ethylene glycol) diacrylate can significantly enhance the GelMA hydrogel for cartilage tissue engineering (Schuurman *et al.*, 2013; Pahoff *et al.*, 2019).

### 1.3.2 Hyaluronic Acid

Hyaluronic Acid (HA) is a linear polysaccharide consisting of alternating units of a repeating disaccharide,  $\beta$ -1,4-D-glucuronic acid- $\beta$ -1,3-N-acetyl-D-glucosamine. Hyaluronic Acid is a non-sulphated glycosaminoglycan and forms part of proteoglycans, which play a vital role within cartilage tissue and thus shows the importance of HA in tissue regeneration (Burdick and Prestwich, 2011; Walimbe and Panitch, 2020). Proteoglycans form one the of the main components of the ECM having diverse functions in cartilage. They provide the basis for absorbing high compressive loads, bind water, cytokines, morphogens, chemokines and growth factors. By doing this it acts as a depot of regulating factors when matrix degradation occurs, as well as protecting the above-mentioned factors against proteolysis (Bertrand and Held, 2017). Proteoglycans thus serve as important molecules in regulating cell functioning within cartilage. The polymer is a highly hydrophilic polyanionic macromolecule with molecular weights ranging from 100 000 Da to 800 000 Da (Burdick and Prestwich, 2011; Mero and Campisi, 2014).

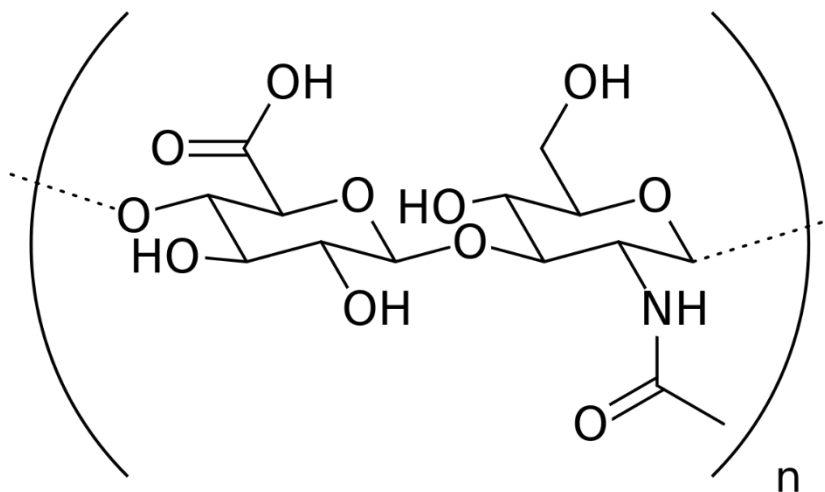


**Figure 4: Molecular structure of Hyaluronic Acid obtained from Wikimedia Commons.** Hyaluronic acid.svg. (2020, October 26), Ed (Edgar181), Public domain, via Wikimedia Commons.

Hyaluronic Acid can have a high molecular mass up to 10 MDa due to the interlinking networks shown above in Figure 4, accounting for physiology and forming an ECM. Such physiological roles include

maintenance of viscoelasticity of liquid in connective tissue, organization of proteoglycans in the ECM, control of tissue hydration and water transport, cellular signalling, matrix organization, morphogenesis and wound repair (Burdick and Prestwich, 2011; Mero and Campisi, 2014; Li *et al.*, 2019). It is ubiquitous in the human body, vital for many cellular and tissue functions and has immunoneutral properties. It has been used clinically for over 30 years; however, it has recently been an essential building block in biomaterial creation for tissue engineering and regenerative medicine (Burdick and Prestwich, 2011). Based on reviews assessing the interaction HA has on chondrogenic metabolism, the use of HA shows the increase in the synthetic amount of chondroitin-6-sulphate, collagen II, hydroxyproline, GAGs and DNA, all components present and required with cartilage tissue. When using MSCs with HA-based hydrogels, the HA showed increased morphological differentiation of the stem cells and rebuilding the cartilage tissue. Hyaluronic Acid also has beneficial effects for the recovering viscosity and elasticity of the synovia by providing lubrication and buffering effects (Li *et al.*, 2019). Hyaluronic Acid has shown great interest in the field of drug delivery due to its advantages such as 1) biocompatibility; 2) ease of modification; 3) biodegradability; 4) high potential drug loading and 5) intrinsic targeting and selective interactions properties with receptors like hyaluronan receptors for endocytosis (HARE) and CD44 (Mero and Campisi, 2014).

Although HA has many advantages as a biomaterial for tissue engineering and regeneration, disadvantages such as a hydrophilic natural and poor mechanical integrity influence its use as a 3D scaffold for tissue engineering and regeneration and therefore requires chemical modifications to be made to overcome the disadvantages to be used as an effective 3D tissue scaffold. The most common type of modification to HA is to the hydroxy and carboxylic acid groups. Modification can be done by an ester bond to the hydroxy group. The carboxylic group is modified by hydrazide and cross-linked with an ester bond. The physicochemical properties of HA can be improved by the addition of other functional groups during the modification. Another type of modification is through the partial decetalization of HA through the treatment with acidic or alkaline substances, which degrade HA into free amino groups that can be cross-linked by amides imino or secondary amine bonds. In addition to this, HA, in the presence of methacrylic acid ester can undergo automatic and photo-cross-linking. Methacrylates are also the most common reactive groups used in radical polymerization due to reacting rapidly with radicals (Burdick and Prestwich, 2011; Li *et al.*, 2019). With the advantages of HA in addition to the advantages of modified HA, with specific reference to methacrylic acid, it enhances the usage of HA as a hydrogel scaffold. Besides methacrylic acid increasing the scaffold's mechanical strength, it also adds enhanced cellular affinity (Burdick and Prestwich, 2011). Magelheas *et al.*, 2014 found that chondrocytes showed a spherical morphology and increased adherence to the HAMA scaffold. These results show chondrocytes' ability to proliferate and synthesize a hyaline matrix containing rich collagen II and GAGs amounts (Burdick and Prestwich, 2011; Magalhães *et al.*, 2014). The addition hyaluronic acid to PEGDA hydrogels is a promising modification towards the construction

of 3D scaffolds composing mammalian cells for drug testing as well for chondrocytes towards the regeneration of cartilage tissue. Hyaluronic Acid by itself has disadvantages such as rapid degradation, participation in hydrolytic reactions and difficult to handle in cell culture however the combination HA with PEGDA could improve these qualities, increasing proteoglycan retention in the gel promoting more cellular growth and hence large amounts of cartilage regeneration through the use of stem cells (Ansari *et al.*, 2017).

### **1.3.3 Poly(ethylene) glycol diacrylate**

Poly(ethylene) glycol diacrylate (PEGDA) is a popular synthetic scaffold used for tissue engineering, focusing on cartilage repair and the right combination of hydrogel bioinks, even cartilage replacement. PEG hydrogels create and provide a 3D environment, resembling the native cartilaginous tissue environment (Nguyen *et al.*, 2012). In addition to this, the compression made from fully hydrated PEGDA hydrogel is close to the value of the modulus for bovine articular cartilage, which has been measured at 950 KPa making the PEGDA a suitable choice as a scaffold for cartilage regeneration as the compression modulus is a vital requirement for cartilage tissue (Sánchez-Télez, Télez-Jurado and Rodríguez-Lorenzo, 2017). The mechanical properties of PEGDA hydrogel, a factor of consideration for hydrogel scaffolds, is largely dependent on the molecular weight and concentration of the PEGDA precursors. This results in PEG hydrogels with higher concentrations having a higher compression and tensile modulus. PEG concentration at the same percentage but lower molecular weight leads to the hydrogel being more brittle due to a lower tensile modulus (Nguyen *et al.*, 2012). PEGDA is a photocurable hydrogel bioink either requiring UV light or visible light, depending on the photoinitiator added to initiate the hydrogel's polymerization and crosslinking. After UV or visible light exposure, the hydrogel becomes a fluid-filled, crosslink three-dimensional scaffold suitable for cell use (Nguyen *et al.*, 2012). Unique properties such as solubility in organic solvents and water, non-toxicity and non-immunogenicity make it a popular hydrogel for cell culture and tissue engineering. Although low protein adhesion is one unique property of PEGDA and can be advantageous for drug testing and other relative assays, the low protein adhesion can lead to low cell adhesion since adhesion of cells is mostly due to cell membrane proteins (Riley *et al.*, 2001; Nguyen *et al.*, 2012; Christensen *et al.*, 2020).

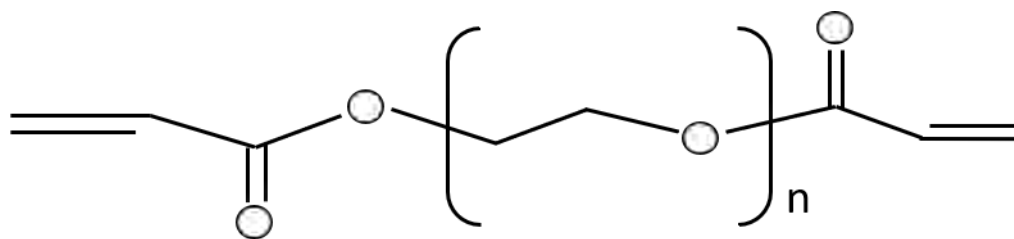


**Figure 5: Molecular structure of poly (ethylene) glycol diacrylate.** Diagram adapted from (Zhu and Marchant, 2011).

The PEG hydrogel consists of covalently bonded PEG chains, formed from multifunctional PEG precursor. The fabrication using photopolymerization in the presence of photoinitiators with acrylate or methacrylate moieties lead to the polymerization and crosslinking of the PEG hydrogel. Free radicals are created from the fragmented photoinitiators when exposed to UV light. Carbon-carbon double bonds present in the acrylate groups are attacked by the radicals initiating polymerization. In the presence of aqueous solvents, the crosslinked network's swelling occurs until the swelling forces the network and retractive (elastic) forces of the polymer chain to be balanced (Bahney *et al.*, 2011; Nguyen *et al.*, 2012).

The PEGDA hydrogel has become a popular scaffold due to the chemical and physical manipulation that it can undergo, which can be added to the biological functionality (Bahney *et al.*, 2011). A hydrophilic environment is created when crosslinked aiding to the popularity of the hydrogel for tissue engineering. In addition to this, PEGDA has a high resolution for stereolithographic 3D printing (Bahney *et al.*, 2011; Christensen *et al.*, 2020). The addition of acrylate groups allows for the photopolymerization of the hydrogel and allows for cellular encapsulation under physiological conditions (Bahney *et al.*, 2011). Although synthetic hydrogels lack some advantage that natural or semi-synthetic hydrogels have, it enables more precise control and tuning over degradation rates and cross-linking densities or mechanical properties, where the natural hydrogels lack these properties. PEG hydrogels have been shown in studies to be impermeable to large proteins (22-45 kDa) and therefore most likely to be impermeable to immunological cells such as white blood cells and macrophages. PEG applications also extend to drug testing where the PEG monomers are tethered to drugs, extending the drugs circulatory lifetime (Riley *et al.*, 2001).

One major downfall to PEGDA is that it is a nonbiodegradable synthetic polymer. Biodegradability is a vital consideration for scaffolds in tissue engineering. Biodegradation rate coinciding with new tissue regeneration is a highly desirable trait for hydrogel scaffolds to have in tissue engineering. This is one main advantage natural polymers like gelatin, or hyaluronic acid have over synthetic hydrogels. It is therefore essential to tether PEGDA to other biodegradable polymers such as poly(lactic acid) (PLA) or poly(glycolic acid) (PGA), GelMA or HAMA for example, to help the biodegradability of the synthetic polymer (Zhu and Marchant, 2011). In terms of the combination of HAMA hydrogel with PEGDA as a cellular scaffold for tissue engineering, HA plays an integral role in retaining

proteoglycans and water, which are important factors for the regeneration of cartilage. HA provides a more natural like matrix for chondrogenic cells in the PEG hydrogel (Mahapatra, Jin and Kim, 2016). Hyaluronic acid also provides and regulates cellular processes by anchoring the cell surface receptors like CD44 and RHAMM increasing cell adhesion, cellular communication and nutrient uptake (Mahapatra, Jin and Kim, 2016; Ansari *et al.*, 2017). The addition and combination of natural polymers such as GelMA and HAMA will not only help the biodegradability of PEGDA, but also significantly increase the biocompatibility, cellular attachment, survival and proliferation of mammalian cells in terms of cartilage tissue regeneration or even replacement, cellular differentiation with the use of MSC and providing an environment more closely mimicking that of cartilage tissue.

### **1.4 Three-dimensional printing and bioprinting technologies**

Three-dimensional printing also referred to as additive manufacturing (AM), rapid prototyping (RP) or free form fabrication (FFR) is a technology, which has become significantly popular in recent years (Yuxuan Wang *et al.*, 2020). The idea of 3D printing was conceived by Charles Hull where he based the concept of 3D printing, creating 3D objects by adding successive layers of a base material on top of each other to create or 'print' objects (Bishop *et al.*, 2017). The interest in 3D printing/AM has become a multi-disciplinary technology with significant impacts in engineering, medicine, and education where it is used as architectural models for construction to surgical equipment and prostheses as educational tools and prototypes in hospitals. In the US, the use of AM in hospitals was at 3 % in 2010, in 2016 it increased to 99 %, showing the demand and value of AM technologies (Bishop *et al.*, 2017; Fanucci, Barwick and Prinsloo, 2019). The use of AM technologies towards tissue engineering has shown great promise for regenerative medicine. Additive manufacturing uses data computer-aided-design (CAD) software or 3D scanners to transform digitally created or scanned objects into 3D ones. AM can be defined as the process of joining materials, layer upon layer, making parts and objects from 3D data (Fanucci, Barwick and Prinsloo, 2019; Paolini, Kollmannsberger and Rank, 2019). The main interest and promising aspect of AM technology in hospitals are for 3D printing organ models from scans for surgical guides and education to custom prosthetics. With the interest of AM technology in tissue engineering, 3D bioprinting has become the main focus in tissue engineering and regenerative medicine. Three-dimensional bioprinting can be described as the precise layering of cells, biological factors and scaffolds with the aim of replicating or regenerating a biological tissue. The 3D bioprinting technology allows for greater precision regarding the spatial relationship between individual elements of the desired tissue (Bishop *et al.*, 2017). There are three general approaches to bioprinting, and although they are not exclusive to bioprinting, these approaches are applied to the larger scope of regenerative medicine and should be considered for the optimal approach to bioprinting objectives. These central approaches are self-assembly, biomimicry and microtissue-based methods (Jakab *et al.*, 2010; Bishop *et al.*, 2017). Table 1 below shows an overview of these general approaches towards bioprinting strategies.

**Table 1: Overview of self-assembly strategies, biomimicry and microtissue methods for bioprinting.** Table adapted from (Bishop *et al.*, 2017).

Strategy	Self-assembly	Biomimicry	Microtissues
<b>Description</b>	Allows for autoregulation and self-production of raw elements by replication of embryonic environment.	Duplication of environment and growth stimulants for the target tissue.	Formation of smallest possible structural and functional units, which can then be combined to form mature tissue
<b>Advantages</b>	Automation is scalable. Allows for high cellular densities. Fast and efficient	Each step of tissue development can be controlled. Precision of cellular positioning is high.	Automation is scalable. Fast and efficient. Reduces limitations in the engineering of vascular tissue.
<b>Disadvantages</b>	Outcome during self-assembly is difficult to change	All factors must be reproduced increasing complexity.	Difficulty in creating microtissues.
<b>Scaffold requirement</b>	No	Yes	No

The bioprinting process has three distinct phases, the pre-processing phase, processing phase and post-processing phase. The pre-processing phase includes all planning details preceding production of bioprinted tissue. This mainly includes analyzing atomic structures or design scaffold to transform imaging data into cross-sectional layers of appropriate scale using specialized software programs (CAD) to print the constructs layer by layer. The processing phase involves all steps in the construction and manufacturing of the bioprinting tissue. Requirements such as specific printing methods and the formulation of materials such as scaffolds, bioinks and other additives need to be chosen. Each parameter has the ability to change the interaction with the individual components, thus affecting the final tissue product as a result. Post-processing phase includes all steps that need to be completed before the bioprinted tissue is fully mature and ready for *in vivo* use. Most 3D bioprinting applications occur within a bioreactor, aiding in providing and recreating a similar environment to the *in vivo* one (Mironov, Kasyanov and Markwald, 2011; Campbell *et al.*, 2012; Bishop *et al.*, 2017; Zhang *et al.*, 2017).

AM technology still has a way to go from being used clinically today; however, there has been rapid growth in hardware and software advancement, bioink and biomaterial development, and preclinical testing for everyday clinical use. There are several different types of 3D printing technologies that can be integrated into 3D bioprinting, each having its own advantages and limitations. These 3D printing technologies include inkjet bioprinting, extrusion-based bioprinting, laser-assisted bioprinting and Stereolithography bioprinting (Seol *et al.*, 2014; Bishop *et al.*, 2017; Fanucci, Barwick and Prinsloo, 2019).

### 1.4.1 Extrusion Bioprinting

Extrusion based bioprinting systems with the aid of CAD software connected to the printer, dispense continuous filaments of bioinks or hydrogels with cells and other additives through a nozzle or micronozzle to fabricate either 2D or 3D constructs. It is among the most widely used 3D bioprinting technology used due to its ability to print using high viscosity bioinks such as spheroids, polymers and clay-based substrates. It also allows for a more diverse selection of biomaterials to be printed, flexible geometric shapes, easily updated software and hardware, the benefit of using multiple types of biomaterials and cell types, as well as the ability to print very high cell densities for tissue formation wherewith the inkjet bioprinting these are some of the limitations (Seol *et al.*, 2014; Bishop *et al.*, 2017; Fanucci, Barwick and Prinsloo, 2019). A significant disadvantage of the extrusion-based bioprinting technology is the distortion of cellular structures and consequence cell viability due to the pressure that results from the bioink being extruded. Although printing at cell densities is its significant advantage, the effect on cell viability can get as low as 40 %. Extrusion-based bioprinting costs are average compared to inkjet and stereolithographic, which are neither low nor high as thus does not pose as an advantage or disadvantage for the bioprinting technology (Seol *et al.*, 2014; Bishop *et al.*, 2017).

### 1.4.2 Inkjet Bioprinting

The inkjet bioprinting system is a non-contact technique that prints biological ink and bio-ink droplets to create the 2D or 3D constructs. The inkjet bioprinter uses several different types of mechanisms to form the bio-ink droplet and subsequent 2D or 3D constructs. The different mechanisms include electromagnetic forces to expel successive drops of bioink onto a substrate, thermal expulsion and the piezoelectric actuator method force and laser-induced forward transfer method, replicating the CAD design with the printed tissue (Seol *et al.*, 2014; Bishop *et al.*, 2017). The thermal method involves using a heat generator at the printer's nozzle, increasing the bio-ink in the chamber. The heating creates a bubble causing the bio-ink to eject from the nozzle creating a small droplet. The droplets are then layered to create the 2D or 3D construct. Although the thermal mechanism method can be seen as a disadvantage due to the temperature of the nozzle reaching and cells being exposed to 300 °C, the time of exposure is  $\sim 2\mu\text{s}$ . Bishop *et al.*, 2017 makes reference to studies that show the thermal methods have shown no significant impact of the heat with mammalian cells' cell viability. The piezoelectric actuator uses a piezo-crystal pulse actuator mediated by electrical input, which then creates a pulse, resulting in a small droplet's ejection. The laser-induced forward transfer method generates vaporization by a laser system producing a small droplet. Both the thermal and piezoelectric actuator method is the most commonly used methods for the inkjet bioprinting. The inkjet bioprinting system's advantages include high printing speed, low costs, high fabrication resolution, and availability. Disadvantages include the requirement of low viscosity bioinks, limiting several effective bioinks for tissue engineering, lack of precision with regard to droplet size and placement compared to other bioprinting technologies, nozzle clogging, and cellular distortion (Seol *et al.*, 2014; Bishop *et al.*, 2017).



### 1.4.3 Stereolithographic Bioprinting

Stereolithography (SLA) bioprinting method uses photopolymerization to construct bioinks in 2D or 3D structures. The polymerization process uses UV light or laser directed in a pattern over a photopolymerizable liquid polymer path, cross-linking the liquid polymers into a solid layer (Guvendiren *et al.*, 2016; Bishop *et al.*, 2017). The SLA bioprinters consist of a build stage, which lowers into the bioink. The resin or bioink then flows over the build stage and printed surface where the next layer is polymerized on top of the previous layer resulting in the construction of the 2D or 3D structure. Like other bioprinting technologies, SLA uses CAD software directing the pattern the UV light follows, as well as the different height increments the build stage must follow to allow the layers to be formed on top of each other (Guvendiren *et al.*, 2016; Bishop *et al.*, 2017). The use of resin and curable acrylics results in a high degree of fabrication accuracy compared to other bioprinting technologies. Low printing times compared to other technologies also offer an additional advantage of the SLA bioprinting system over printing technologies and the costs of SLA bioprinting compared to other bioprinting technologies. Disadvantages of the SLA include the use of high-intensity UV light, extended post-processing and lack of compatible materials as it requires additives present to ensure effective polymerization, inadequate mechanical properties and lack of biocompatible and biodegradable components in the resin or bioink (Guvendiren *et al.*, 2016; Bishop *et al.*, 2017). Although exposure to UV light can negatively affect cell viability, studies have reported cell viability of > 90 % using the SLA bioprinting technology (Gauvin *et al.*, 2012; Derakhshanfar *et al.*, 2018). In some cases SLA has been used to create computed tomography (CT)-based molds for generating artificial heart valves and several educational molds and tools used for medical learning and preparation for surgeries and in dental practices (Bishop *et al.*, 2017).

#### 1.4.3.1 Photoinitiators

Photoinitiators are molecules that when exposed to radiation, produce reactive species such as free radicals, cations or anions which then react with monomer and oligomer units (Schwalm, 2001; Zhang and Xiao, 2018). Photoinitiators are essentially used in processes where thermal curing cannot be used (Schwalm, 2001). The use of photoinitiators has become a promising technology in varying fields like dentistry, food industry, drug delivery, surgery and biomaterials for tissue engineering. The use has allowed for more versatility in curing liquids to solids with economic, environmental, and production benefits (Zhang and Xiao, 2018). Properties of photoinitiators include 1) high reactivity of the radical towards the monomer, 2) high quantum yield of formation of initiating species and 3) high molar extinction coefficient and high absorption at the exposure wavelength. Reactivity is increased through amine co-initiators, which can cause two effects. The first effect relies on a C-H group adjacent to a nitrogen atom provides a suitable hydrogen atom donor allowing a radical to be formed, initiating polymerization.

The second effect occurs when a radical scavenges oxygen atoms, which results in polymerization inhibition (Schwalm, 2001). Efficient photoinitiation relies on the absorption bands of the photoinitiator overlapping with the source's emission spectrum with minimal competing absorption of different species in the formulation at the corresponding photoinitiator wavelength (Photoinitiators, 2001). There are two types of photoinitiators, type I categorized as photocleavable photoinitiators (e.g. acetophenone derivatives, benzoin derivatives, acylphosphine oxides, hydroxyalkylphenones and benzyl ketal). Type II photoinitiators are categorized as bimolecular photoinitiators (e.g. camphorquinone, benzophenone and thioxanthone). Type I photoinitiators absorb incident photons and perish into two primary radicals, causing cross-linking and polymerization initiation. Type II cause the separation of the hydrogen from a co-initiator producing secondary radicals for cross-linking (Pereira and Bártolo, 2015). Due to their superior initiation efficiency, type I photoinitiators are usually the first choice and go to photoinitiators due to rapid polymerization, but the majority require the use of UV light and thus cause toxic effects on encapsulated cells.

Type II photoinitiators have had a recent increase of interest as most can use visible light for polymerization. The primary concerns with light-mediated polymerization, particularly UV light for cell encapsulation, are the cytotoxic effects of free radicals generated by the photoinitiators. During the photopolymerization process, free radicals can react with cellular components such as proteins, DNA and cell membranes through either the formation of reactive oxygen species or direct contact, thus increasing the chances of the viability of the cells to be compromised and lead to DNA damage. The cytotoxic effects are largely dependent on photoinitiator type, concentration, light intensity, and exposure time. The use of type II photoinitiators using visible light holds excellent significance due to the fact that it negates the use of UV light thereby reducing the major cytotoxic effects of the type I photoinitiator (Pereira and Bártolo, 2015). There are various types of photoinitiators on the market for the various types of applications they are used for. Hydrogel scaffolding for 3D printing requires photoinitiators to be highly water-soluble, high photoabsorption below 400 nm and little to no cytotoxic effects. Various types of photoinitiators are present on the market for 3D printing, hydrogel scaffold design for cell culture. Irgacure is one trendy one that is used for cellular hydrogel scaffold design.

#### **1.4.3.2 Irgacure**

There are various types of different photoinitiators on the market for commercial and research use, each used depending on the material wanting to be polymerized. For cell culture, 2-Hydroxy-1-[4-(2hydroxyethoxy)phenyl]-2-methyl-1-propanone (Irgacure – IC2959) is a well-known and commonly used photoinitiator due to its cytocompatibility. The other forms of Irgacure are also available however, the chemical structure and specific functional groups differ, allowing the molecule to absorb at different wavelengths (Zhang and Xiao, 2018). IC2959 exhibits minimal toxicity and is water soluble and has a wide use in the fabrication of biomaterials; however, the light absorption needed for the photoinitiator to polymerize the biomaterials influences living cells negatively way promoting either cell death or

mutagenic effects. The exposure of UV (365 nm) to irradiation to IC2959 creates a benzoyl group and acetyl free radical from the alpha cleavage. The generated free radicals polymerize the GelMA via chain-growth, thus creating the hydrogel stabilized network (Pahoff *et al.*, 2019). In addition to this, it is very light sensitive and is adversely affected if dissolved oxygen is present in the biomaterial. The downsides of IC2959, therefore limits the amount of success achieved when polymerizing biomaterials. Lithium phenyl-2,4,6-trimethylbenzoylphosphinate and visible light photoinitiators consisting of Eosin-Y, TEA and NVP are other photoinitiators that eliminate the downsides of IC2959, making them more viable options for biological applications.

#### **1.4.3.3 Lithium phenyl-2,4,6-trimethylbenzoylphosphinate**

Lithium phenyl-2,4,6-trimethylbenzoylphosphinate (LAP) has shown to be a promising photoinitiator due to its properties to support high cell viability, GAG production *in vitro*, high water solubility, non-oxygen inhibition and cross-linking via visible light mitigating mutagenic effects that can be caused by IC2959 (Pahoff *et al.*, 2019). LAP is a free radical photoinitiator, which upon exposure to light, initiates free radical chain polymerization at wavelengths of 405 nm (visible light) and 365 nm UV light (Pereira and Bártolo, 2015; Nguyen *et al.*, 2020). One benefit of LAP is that it is type I photoinitiator, thus not requiring a co-initiator to initiate and accelerate polymerization (Fairbanks *et al.*, 2009). Although LAP can cause polymerization when exposed to UV light, the use of UV light is a significant limitation due to the detrimental effects to DNA damage, impairing of cellular function and exposure to free radicals. LAP's ability to use visible light over UV light is what makes it such a suitable photoinitiator over IC2959. The use of visible light expects to cause less cellular damage, as well as to have more efficiency transmitting through tissues, giving a greater curing depth (Monteiro *et al.*, 2018). Although the use of LAP shows to a better photoinitiator than IC2959 since it can initiate polymerization near 405 nm, the 405 nm strong blue light is still toxic to mammalian cells and disrupts their cellular processes (Z. Wang *et al.*, 2018).

#### **1.4.3.4 Visible light photoinitiator (Eosin Y, TEA, NVP)**

Eosin Y is a type II photoinitiator requiring a co-initiator and accelerant species to initiate sufficient polymerization. Eosin Y is highly water-soluble and initiates polymerization when exposed to green light, visible light or even UV light (405 nm, 500 nm and 600 nm). Since eosin-Y absorption range is relatively wide allowing for UV-light absorption dual benefits of sterilization and polymerisation can occur. It has widely been employed for radical polymerization in aqueous biological environments using low-intensity visible light irradiation (Shih and Lin, 2013; Lilly *et al.*, 2018; Z. Wang *et al.*, 2018). Eosin Y is a xanthene dye photosensitizer and initiates polymerization when paired with the co-initiator triethanol amine (TEA). When exposed to visible light, the eosin molecule excites to the triplet state, abstracting hydrogen from TEA, yielding a protonated eosin radical and a protonated TEA radical. Polymerization is initiated via the TEA radical while the regeneration of the eosin radical occurs through disproportionation with an inhibiting radical species. The formation of the polymer in systems where

inhibiting species are 1000-fold more concentrated than eosin is enabled from eosin's cyclic regeneration. The eosin Y visible light system has been used for the initiation of bulk gelation of tissue engineering cell-laden scaffolds with reports of high cell viability (Matsumura *et al.*, 2008; Lilly *et al.*, 2018). Although eosin Y and TEA are able to polymerize hydrogel scaffolds, the addition of N-vinylpyrrolidone (NVP) aids to counteract the inhibitory effect of oxygen, which can occur during the polymerization of hydrogel scaffolds (Aguirre-Soto *et al.*, 2019). NVP acts as a comonomer for the eosin-mediated synthesis of hydrogels. In addition to the comonomer aiding in the reduction of oxygen inhibition, NVP also contributes to enhancing the rate of radical polymerization and final conversion (Kizilel, Pérez-Luna and Teymour, 2004; Aguirre-Soto *et al.*, 2019). In a study performed by Lilly *et al.*, 2018 they stated in addition to eosin Y acting as a photoinitiator, their research group used eosin Y for film coatings on living cell membrane substrates towards rare cell sorting and immunoisolation of transplantable cells. The strategy is based on using eosin for hydrogel polymerization at the cell membrane by labelling cell-surface proteins. Eosin is coupled with antibodies to form labels, localizing eosin to the cell membrane of antigen-positive cells. When irradiation occurs with the eosin-labelled cells in a monomer and TEA solution, polymerization occurs only at eosin-primed cell surfaces, thus resulting in a high cell viability of ~90%. This does, however, require preparation of custom eosin-biomolecule conjugates localizing the initiator at the cell membrane (Lilly *et al.*, 2018). Eosin Y solution as a photoinitiator provides several advantages over other type I photoinitiators, e.g. IC2959 and LAP in terms of increased biocompatibility and lower cellular toxicity due to the use of visible light however there are limitations. These include the use of a co-initiator and comonomer for efficient polymerization to occur. Eosin still follows the principle of other photoinitiators in which the concentration of photoinitiator directly influences the cell viability. The higher the photoinitiator concentration, more adverse effects can be seen on cell viability (Z. Wang *et al.*, 2018). This, therefore, limits the amount of eosin used, which in turn affects the rate of polymerization. However, despite these drawbacks, using the right concentration where the photoinitiator does not affect the cell viability while still providing sufficient polymerization still show great results for the hydrogel scaffold polymerization and cell encapsulation offering good biocompatibility when compared to other photoinitiators for the use of hydrogel scaffold polymerization and cell encapsulation.

## Problem Statement

Tissue engineering has dramatically improved with the use of 3D printing, providing models for drug discovery, toxicology and transplantation of several tissues. Creating an *ex vivo* environment that mimics the *in vivo* environment remains a challenge in tissue engineering. One of these challenges is the production of articular cartilage via 3D bioprinting using mesenchymal stem cells (MSCs) to construct an articular cartilage scaffold for the regeneration of degenerated cartilage. This is aimed at cartilage specific disease, osteoarthritis, as well as for knee and hip transplants from incidents of injuries in athletes and mainly age. An estimation of over 3.5 million athletes receive medical treatment due to sports injuries each year with the global cartilage repair/regeneration market expected to reach USD 6.7 billion by 2025 according to a report by Grand View Research Inc., May 2017 (Regeneration *et al.*, 2021). According to the University of North Carolina, ±1 million people in the US receive knee and hip transplants every year resulting in an economic burden of 136.8 billion USD annually. The high organization level, heterogeneous composition and specific biomechanical characteristics make articular cartilage a complex tissue structure and difficult to generate in a similar format to the *in vivo* environment, as well as using optimal biomaterials within the hydrogel scaffold to promote MSC differentiation into chondrocytes and sustaining growth and proliferation within the scaffold. Research on cellular scaffolds and differentiation of cells in chondrocytes and osteocytes will improve the understanding of *in vivo* systems and give greater understanding to cellular toxicity and potential drugs that can be used to improve tissue engineering systems.

## Research questions

1. Will modification and combination of gelatin-methacrylate, hyaluronic acid methacrylate and poly(ethylene) glycol diacrylate hydrogels enhance the proliferation and cell survival of mammalian cells?
2. Will the formulated hydrogel types be suitable for stereolithographic 3D printing?
3. How will different adipose-mesenchymal stem cell lines differ in terms of their ability to perform differential and gene expressions towards chondrogenic differentiation, with the use of specific transforming forming growth factors for the eventual use with the 3D formulated scaffolds to give uniform layering as found within *in vivo* articular cartilage?

## **Aims and Objectives**

### **Aim 1:**

- Determine chondrogenic and Adipogenic differential potential of two separate adipose-mesenchymal stem cell line through 2D monoculture using Alcian Blue and Oil Red O staining and RT-qPCR.

### **Objectives of aim 1:**

1. Establish both ad-MSc lines and grow cultures until a confluency of 70 % is reached to enable the start of cellular differentiation.
2. Optimize and validate the Adipogenic and chondrogenic differentiation protocols through 2D monolayer cell culturing.
3. Determine and compare the efficiency of adipogenic and chondrogenic differentiation of both ad-MSc lines using differentiation staining techniques and microscopy.
4. Optimize RT-qPCR protocols for collagen gene expression markers Col10a1, Col2a1 and housekeeping gene, GAPDH.
5. Quantify and compare gene expression markers of both ad-MSc lines.

### **Aim 2:**

- To design and formulate five different hydrogels, GelMA, PEG, GelMA/PEG, GelMA/HAMA and PEG/HAMA for the optimization of mammalian cell culture.

### **Objectives of aim 2:**

1. Make up hydrogel polymer mixtures and freeze-dry mixtures and store at -20 °C for long term use.
2. Reconstitute freeze-dried mixtures in DPBS and test the different hydrogels' polymerization efficiency and relative combinations using a visible light photoinitiator.
3. Characterize and analyze each hydrogel formation and their relative properties through swelling, degradation, SEM and FTIR analysis.

**Aim 3:**

- Determine the optimal hydrogel composition for mammalian cell viability and proliferation.

**Objectives of aim 3:**

1. Determine the IC50 values of the photoinitiators components and chondrogenic differentiation components.
2. Perform sterility testing to determine if hydrogel scaffolds are suitable for cell culture.
3. Determine cell viability of mammalian cells in hydrogel scaffolds using ReadyProbes™ Cell Viability Imaging Kit (Blue/Green).
4. Optimize resin 3D printer to print formulated hydrogel bioinks.

**Section 1: Establishment of differentiation and validation protocols for Adipose derived mesenchymal stem/stromal cells for further tissue engineering.**

Section 1 (Chapter 2) sets out to test the efficiency of differentiation between two ad-MSK lines isolated from different parts of the body via liposuction. The cell lines were grown and induction of chondrogenic differentiation was carried out over 7, 14 and 21 days. This firstly tests the validation of the differentiation protocols used, secondly it shows the variability and consistency on initial through to terminal differentiation of both cell lines. Testing the efficiency of both cell lines gives insight to firstly the chondrogenic differential ability in a 2D monolayer layout so be used a comparison of 3D differentiation and secondly, which cell line shows the most promise to be used in the developed hydrogel scaffolds towards additive manufacturing of articular cartilage.

**Section 2: Development of Hydrogels and characterization of the mechanical and chemical properties and evaluation of the develop scaffolds as suitable extracellular environments for cell culture.**

Section 2 (Chapter 3-5) sets out to developed five types of hydrogels, GelMA, GelMA/HAMA, GelMA/PEGDA, PEGDA and PEGDA/HAMA from which characterization and comparison of the mechanical properties of each hydrogel was done, as well as the chemical makeup of the developed gels. Section 2 also sets out to determine the cytotoxic effects of reagents used in the polymerization of the hydrogel scaffolds and differentiation components. Following from this the cell viability and adherence comparison between each hydrogel type was determined showing the optimal development hydrogel type for ad-MSK use and additive manufacturing of articular cartilage.

## Chapter 2: Establishment of Mesenchymal Stromal/Stem Cell Differentiation & Validation Protocols

### 2.1 Introduction

Stem cells are specialized cells capable of self-renewal and can differentiate into multi-lineage cells. Stem cells are categorized into three groups; embryonic stem cells (ESCs), induced pluripotent stem cells (iPSCs) and adult stem cells. The use of adult stem cells is one of the most used types of stem cells for research and regenerative medicine as isolation is relatively easy and harmless and has fewer ethical concerns when compared to pluripotent stem cells. Mesenchymal Stem Cells (MSCs) are adult stem cells isolated from human and animal sources, with the primary sources from humans originating from the bone marrow and adipose tissue stromal vascular fraction (Pittenger *et al.*, 2019). MSCs are multipotent stem cells that can differentiate into the mesodermal lineage, including adipocytes, osteocytes, neurocytes, hepatocytes, and chondrocytes (Ullah, Subbarao and Rho, 2015; Pittenger *et al.*, 2019).

Cell therapy was performed only for bone marrow and epidermis transplantation for haematological diseases and excessive skin burns. However in recent years it has opened up to the various stem cell types for tissue repair and regeneration. The ability of MSCs to differentiate into osteogenic, adipogenic and chondrogenic lineages and the cells' immunological properties as immune tolerant agents with immunosuppressive capacities, anti-inflammatory and immunoregulatory abilities has shown great promise towards tissue engineering, repair and regenerative medicine (Hosseini *et al.*, 2018; Han *et al.*, 2019). The use of ad-MSC for regenerative medicine, in particular, regenerative medicine towards the additive manufacturing of articular cartilage, has gained much interest towards regeneration and even replacement of cartilage within joints where the cartilage has worn out due to old age, injury or sports injuries and diseases such as arthritis and rheumatoid arthritis.

Two routine methods to determine cellular differentiation of mesenchymal stem cells into subsequent cell lines include staining through the use of dyes and gene expression markers using RT-qPCR. Differentiation into chondrocytes is commonly determined through the use of Alcian Blue stain. Alcian Blue stain forms part of the basic polyvalent dyes. This stains acidic polysaccharides such as glycosaminoglycans (GAGs) and proteoglycans, mainly aggrecans, which are rich within the extracellular matrix of cartilage, resulting in a dark blue stain using the copper-containing dye, Alcian Blue (PromoCell GmbH, 2015). Differentiation into adipocytes commonly uses Oil Red O dye as it is cheap, easy to use, can be performed within a few hours and is non-hazardous. It is used to assess the degree of differentiation by strongly staining neutral lipids produced as a result of the differentiation from MSCs to adipocytes (Kraus *et al.*, 2016; Eom *et al.*, 2018).



It is known from literature that the different types of stem cell groups have different plasticities where some are better suited for a particular cell lineage. In some cases, ad-MSc isolation from certain parts of the body via liposuction have shown to promote better cellular differentiation, i.e. chondrogenic differentiation, than other parts of the body (Francis *et al.*, 2018; Voga *et al.*, 2019). Research on the effect of cellular differentiation with ad-MSc of different cell lines isolated from different sections of the body are limited, and although all ad-MSc can differentiate into chondrocytes and adipocytes, cell lineage effect on the cellular differentiation requires more insight to achieve better results towards tissue engineering via the use of 3D cellular scaffolds.

**Aim:**

- Determine and compare cellular differentiation of two separate ad-MSc lines isolated from the abdominal and thigh areas through 2D cell culture using Alcian Blue and Oil Red O staining and RT-qPCR.

**Objectives:**

1. Establish both ad-MSc lines and grow cultures until a confluency of 70 % is reached to enable the start of cellular differentiation.
2. Optimize and validate the adipogenic and chondrogenic differentiation protocols through 2D monolayer cell culturing.
3. Determine and compare the efficiency of adipogenic and chondrogenic differentiation of both ad-MSc lines using differentiation staining techniques and microscopy.
4. Optimize RT-qPCR protocols for collagen gene expression markers Col10a1, Col2a1 and housekeeping gene, GAPDH.
5. Quantify and compare gene expression markers of both ad-MSc lines.

## **2.1 Methods and Materials**

### **2.1.1 Adipose-derived mesenchymal stem cell source**

The adipose-mesenchymal stem cells were acquired from the Institute for Cellular and Molecular Medicine (ICMM), Department of Immunology, University of Pretoria. Cell line A270620-01A was isolated from the abdominal area via liposuction on the 26 June 2020. Cell line A311019-02T was isolated via liposuction from the thighs on the 31 October 2019.

### **2.1.2 Adipose-derived mesenchymal stem cell (ad-HMSC) culture**

Ad-HMSC culturing was carried out by incubating the cells at 37°C, 5% CO<sub>2</sub>. Two separate ad-HMSC cell lines (A270620-01A) and (A311019-02T) were grown and used as a comparison to test their differentiation ability to one another. Both cell lines were grown until 70 % confluency for subculturing into new flasks or plates for differentiation assays. Both cell lines were cultured in MEM-alpha - Gibco (sourced from Thermo Fisher Cat. No. 12561072), supplemented with 10 % FBS, 1 % Pen/Strep until induction of differentiation.

### **2.1.3 Chondrogenic Differentiation**

Chondrogenic differentiation was based on (Zuliani *et al.*, 2018). Ad-MSCs were seeded into a 96-well plate at a cell density of 10 000 cells per well. The plate was then left in an incubator at 37 °C with 5 % CO<sub>2</sub> until cells had become confluent. Once confluent, the spent media was removed. Differentiation media was added consisting of DMEM (high glucose Thermo Fisher Cat. No. 10566016) supplemented with 1 % (v/v) Pen/Strep, 10 % (v/v) FBS, 10 ng/ml TGF-β<sub>3</sub> (Sigma Cat. No. SRP3171), 100 nM dexamethasone (dissolved in 100 % methanol), 50 µg/ml ascorbic acid (Sigma Cat. No. A4544), 40 µg/ml L-proline (Sigma Cat. No. P0380) and 1x Insulin-transferrin-sodium selenite (Sigma Cat. No. I3146). Differentiation media was changed every three days with Alcian Blue staining performed 7, 14 and 21 days after chondrogenic induction as shown in Figure 6 below. Controls included ad-MSCs incubated in MEM-alpha, 10 % FBS, 1 % Pen/Strep where media was changed when differentiation media was changed. Three replicate wells for the controls and ad-MSCs differentiation were performed in the 96-well plate. The differentiation assay was performed in triplicate.

## 2.1.4 Adipogenic Differentiation

Adipogenic differentiation was based on Chen *et al* (2007) and Kramer *et al* (2014) with modifications. Ad-MSC were seeded into a 96-well plate at a cell density of 10 000 cells per well and cells were grown to confluence. Once the cells had become confluent, the spent media was removed and cells fed with adipogenic induction media (AIM) consisting of DMEM (high glucose) supplemented with 10 % FBS, 1 % Pen/Strep, 0.5 mM 3-isobutyl-1-methylxanthin (IBMX) (Sigma Cat. No. I5879), 10 µg/ml human insulin (Sigma Cat. No. I3536), 1 µM dexamethasone (dissolved in methanol). The IBMX was dissolved in ethanol, and human insulin was dissolved in sterile ddH<sub>2</sub>O. Cells were fed with AIM for three days, after which adipogenic maintenance media (AMM) consisting of DMEM (high glucose) 10 % FBS, 1 % Pen/Strep, 10 µl/ml human insulin and was used for another three days. The AIM/AMM media change occurred in 3-day cycles. Cycles were repeated after every six days. Controls were fed using Alpha-MEM supplemented with 10 % FBS, 1 % Pen/Strep. Media was changed when differentiation media was changed. Three replicate wells for the controls and ad-MSC differentiation were performed in the 96-well plate. The differentiation assay was performed in triplicate.

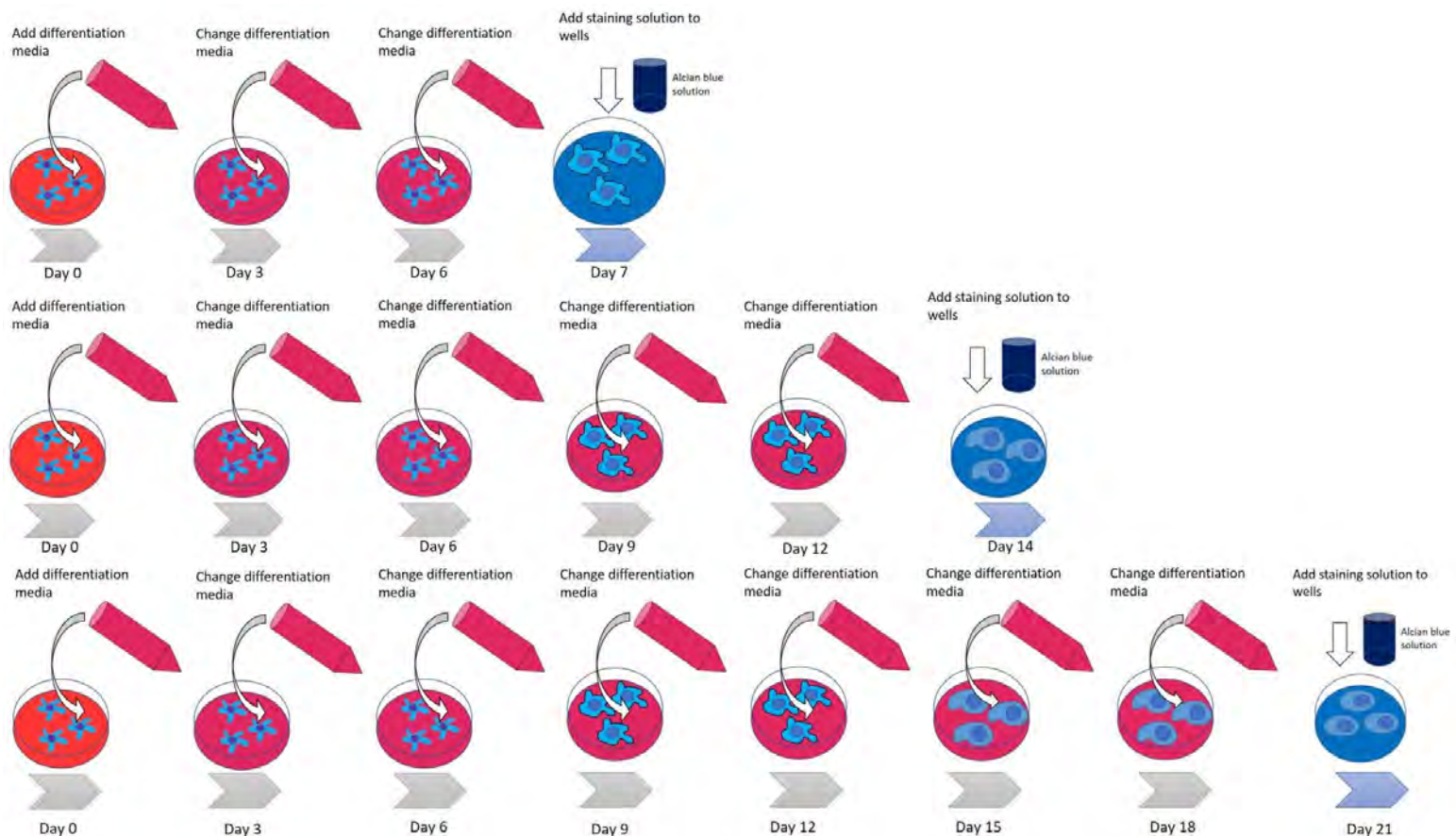


Figure 6: Chondrogenic differentiation media changes and Alcian Blue staining day diagram.

### **2.1.5 Alcian Blue staining**

Staining for chondrocyte differentiation was adapted from (Biological Industries, 2015) Staining was done on day 7, 14 and 21 days after chondrogenic induction. All media was removed from differentiated wells of both cell lines, as well as control wells. Wells were washed twice with warmed  $\text{Ca}^{2+}/\text{Mg}^{2+}$  - DPBS (pH 7.4), after which the cells were then incubated in 10 % (v/v) Formalin (4 % (w/v) paraformaldehyde) for 1 hour. The 10 % (v/v) formalin was removed, and wells washed once with ddH<sub>2</sub>O. The ddH<sub>2</sub>O was removed, and 200  $\mu\text{l}$  1 % (w/v) Alcian Blue 8Gx solution (Sigma Cat. No. 8438) was added to each well and left to incubate at room temperature overnight protected from light. After overnight incubation of the stain, the stain was removed and washed four times with 0.1N HCl and three times with ddH<sub>2</sub>O. After the last wash, ddH<sub>2</sub>O was added to the wells for visualization using the EVOS FL Auto 2 microscope at 10 x magnification.

### **2.1.6 Oil Red O staining**

Staining for adipogenic differentiation was detected using Oil Red O (Sigma Cat. No. O0625). Staining of adipocytes was done on days 7, 14 and 21 after differentiation induction. An Oil Red O stock solution 3.5 % (w/v) was prepared by dissolving Oil Red O in 100 % isopropanol, followed by filtering (0.2  $\mu\text{m}$ ). A working solution was then prepared, consisting of 60 % (v/v) Oil Red O stock solution and 40 % (v/v) sterile ddH<sub>2</sub>O. It was left at room temperature for 30 minutes, after which it was filtered (0.2  $\mu\text{m}$ ). All media from the wells was removed and washed once with warmed  $\text{Ca}^{2+}/\text{Mg}^{2+}$  free DPBS (pH 7.4). The DPBS was removed, and cells were incubated at room temperature in 10% Formalin (4 % formaldehyde) for 1 hour. The 10 % formalin (4 % formaldehyde) was removed and washed with 60 % isopropanol. The wells were allowed to dry completely before adding 200  $\mu\text{l}$  of the Oil Red O working solution for 10 minutes. The Oil Red O staining solution was removed after 10 minutes, and wells washed four times with ddH<sub>2</sub>O. For visualization, 200  $\mu\text{l}$  of ddH<sub>2</sub>O was added to each well. Visualization was done using the EVOS FL Auto 2 microscope at 20x magnification.

### **2.1.7 PCR optimization of gene primers, Col10a1, Col2a1 and GAPDH**

DNA isolation was performed using the Quick-DNA™ Miniprep Plus Kit (D4068) from Zymo Research. DNA isolation was carried out according to the kit manual instructions. All gene primers were ordered from Integrated DNA Technologies (IDT) and were validated using Primer-BLAST from NCBI-NIH (Ye *et al.*, 2012). All primers were received at a stock concentration of 100  $\mu\text{M}$  in IDTE buffer pH 8.0 with standard Desalting. Working concentrations of the primers from the stock concentrations were made by diluting the primers in nuclease-free water to a concentration of 10  $\mu\text{M}$ . One *Taq* Hot Start DNA Polymerase (M0481) and dNTPs (N0447) from New England Biolabs were used to run the primer PCR optimization. A 100 bp DNA ladder (N32315) from New England Biolabs was used to quantify the product sizes obtained in the agarose gel run. Optimization of the PCR gene primers was done using the standard concentrations and thermocycling conditions for a routine PCR found in the instruction manual for a 25  $\mu\text{l}$  reaction of the One *Taq* Hot Start DNA Polymerase

kit. Optimized PCR concentrations and thermocycling conditions are shown below in Table 2 & 3. Results of the PCR optimization for Col10a1 and GAPDH are shown in Figure S1 in the appendix section.

**Table 2: Optimized PCR reaction setup.**

Component	25 $\mu$ l reaction volume	50 $\mu$ l reaction volume	Final concentration
5x One <i>Taq</i> Standard Reaction Buffer	10 $\mu$ l	20 $\mu$ l	2x
10 mM dNTPs	1.25 $\mu$ l	2.5 $\mu$ l	500 $\mu$ M
10 $\mu$ M Forward Primer	1.25 $\mu$ l	2.5 $\mu$ l	0.5 $\mu$ M
10 $\mu$ M Reverse Primer	1.25 $\mu$ l	2.5 $\mu$ l	0.5 $\mu$ M
One <i>Taq</i> Hot Start DNA Polymerase	0.5 $\mu$ l	1 $\mu$ l	2.5 Units
Template DNA (50 ng/ $\mu$ l)	2 $\mu$ l	4 $\mu$ l	100 ng
Nuclease-free water	8.75 $\mu$ l	17.5 $\mu$ l	

**Table 3: Optimized Thermocycling conditions.**

Step	Temperature ( $^{\circ}$ C)	Time
Initial Denaturation	94	30 seconds
30 cycles	94	25 seconds
	55-60	40 seconds
	68	30 seconds
Final Extension	68	10 minutes
Hold	4	

### 2.1.8 RT-qPCR for gene expression of chondrocytes differentiated for 14 days.

Ad-MSC cell lines A270620-01A and A31101Q-02T were used as a biological comparison to test the chondrogenic gene expression. Cells were seeded in a 6-well plate at a cell density of 47 500 cells per well and were grown until confluent before starting differentiation. Chondrogenic differentiation was performed in the 96-well plate. Control cells were fed with alpha-MEM, 10 % FBS, 1 % Pen/Strep. Cells were differentiated for 14-days as done in section 2.2.3, after which the RNA was extracted and isolated using the Quick-RNA<sup>TM</sup> Miniprep Plus Kit (Zymo Cat. No. R1057). The Luna Universal One-Step RT-qPCR kit (E3005S) was used to perform the RT-qPCR with the QuantStudio<sup>TM</sup> 3 96-well 0.2 ml Block. The expression level of mRNA was normalized to GAPDH as the endogenous control and was calculated using the  $2^{-\Delta\Delta C_t}$  method (BioRad, 2006; Rao *et al.*, 2013) shown in equation 1. The RT-qPCR reactions and gene primers used, annealing temperatures and product sizes are shown in the tables below.

$$\Delta CT = Ct(\text{gene of interest}) - Ct(\text{housekeeping gene})$$

$$\Delta\Delta CT = \Delta Ct(\text{treated sample}) - \Delta Ct(\text{untreated sample})$$

$$\text{Gene expression fold} = 2^{-(\Delta\Delta Ct)}$$

**Equation 1: Gene expression fold equation format where Ct=cycle threshold.** Formula acquired from (BioRad, 2006; Rao *et al.*, 2013).

**Table 4: RT-qPCR reaction parameters for QuantStudio™ 3 thermocycler.**

Stage	Cycle Step	Temperature (°C)	Time	Cycles
Hold	Reverse Transcription	55	10 minutes	1
	Initial Denaturation	95	1 minute	1
PCR	Denaturation	95	10 seconds	40
	Extension	60	60 seconds	
Melt curve/dissociation	Denaturation	95	10 seconds	1
	Annealing	60*	1 minute	1
	High Resolution Melting	95	15 seconds	1
	Annealing	60	15 seconds	1

\*Subject to change based on Ta of primers used.

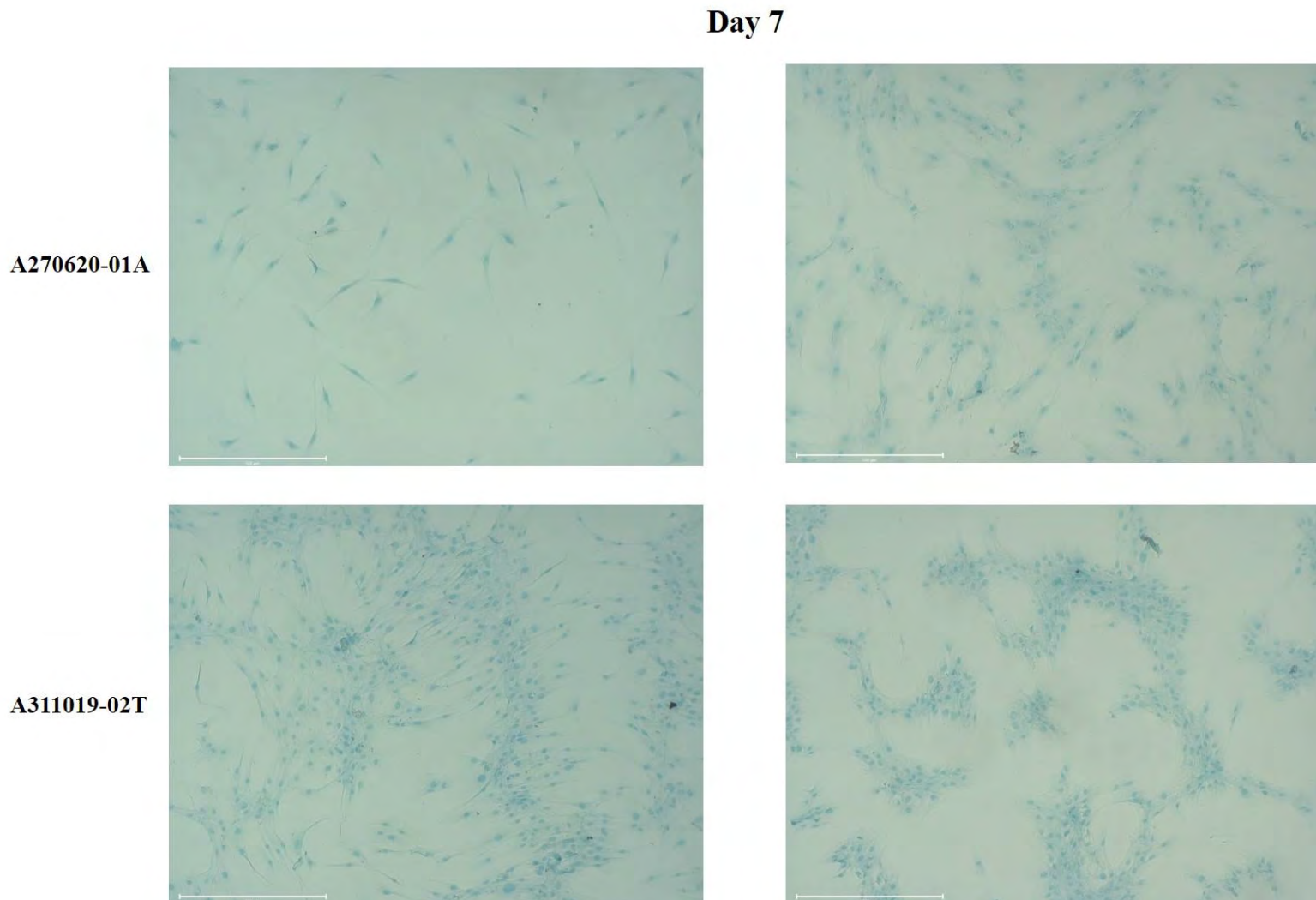
**Table 5: Chondrogenic differentiation primer sequences, product length and annealing temperatures for RT-qPCR gene expression assay and PCR optimization.**

Gene	Forward primer – Sequence	Reverse primer – Sequence	Annealing Temperature (°C)	Product length (bp)	Reference
Col2a1	GAGACAGCATGACGCCGAG	GCGGATGCTCTCAATCTGGT	55	67	Tanthisong <i>et al.</i> , 2017
Col10a1	CCCTCTTGTTAGTGCCAACC	AGATTCCAGTCCTTGGGTCA	58	155	Mueller <i>et al.</i> , 2013
GAPDH	GGACTCATGACCACAGTCCATGCC	TCAGGGATGACCTTGCCACAG	60	152	Peran <i>et al.</i> , 2013

## 2.2 Results and Discussion

### 2.2.1 Chondrogenic and Adipogenic Differentiation staining

Chondrogenic and adipogenic differentiation was carried out using adipose-mesenchymal stem cells from two separate cell lines A270620-01A and A31101Q-02T, for 21 days to firstly determine the differentiation ability of each cell line and secondly the differentiation comparison between each cell line. Chondrogenic and adipogenic differentiation images are shown below in Figures 7-12.



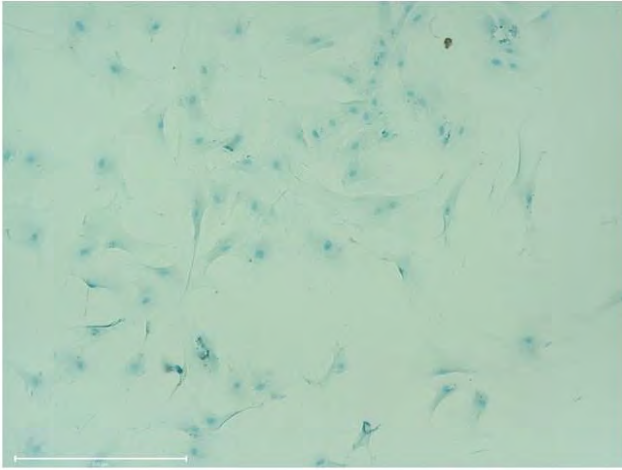
**Figure 7: Alcian Blue staining of chondrogenic differentiation 7 days after induction.** Images on the left show the negative controls, and images on the right show ad-MSCs 7 days after chondrogenic induction. Scale bar = 500  $\mu$ m and each image represents N = 6 and each batch experiment had n = 3.

Figure 7 shows the Alcian Blue staining images of adipose-mesenchymal stem cells 7 days after chondrogenic differentiation induction. Both cell lines showed little Alcian Blue staining within the ECM of the cells showing early stages of chondrogenic differentiation. The A311019-02T cell line showed more cellular growth and more retention of the Alcian Blue stain in the ECM than the A270620-01A cell line after 7 days of chondrogenic differentiation induction.



## Day 14

A270620-01A



A311019-02T

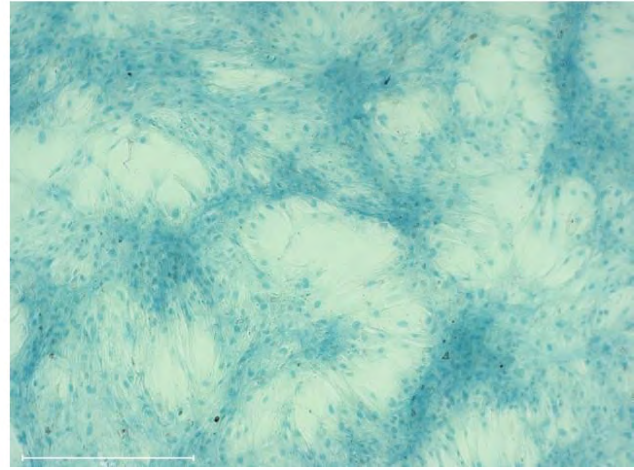
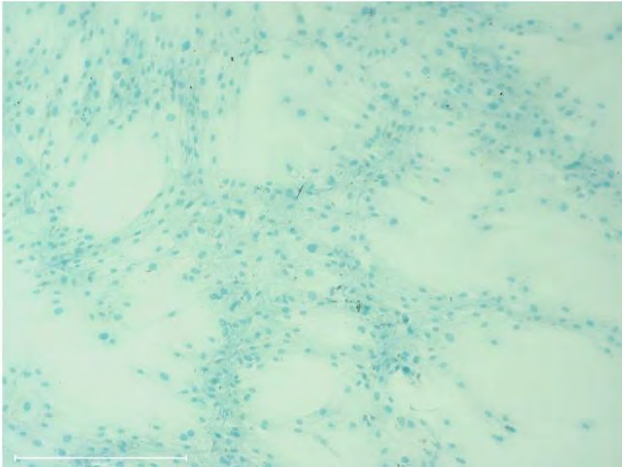


**Figure 8: Alcian Blue staining of chondrogenic differentiation 14 days after induction.** Images on the left show the negative controls, and images on the right show ad-MSCs 14 days after chondrogenic induction. Scale bar = 500  $\mu$ m and each image represents N = 6 and each batch experiment had n = 3.

Figure 8 shows the Alcian Blue staining of the chondrogenic differentiation induced adipose-mesenchymal stem cells 14 days after induction. Both cell lines showed an increase in the retention of the Alcian Blue stain in the ECM compared to 7 days after induction and controls and more cellular growth. Cell line A311019-02T showed higher retention of Alcian Blue stain in the ECM than cell line A270620-01A indicating chondrogenic differentiation is occurring. A change in cellular morphology can be seen on the images on the right than controls, indicating that chondrogenic differentiation occurred.



Day 21

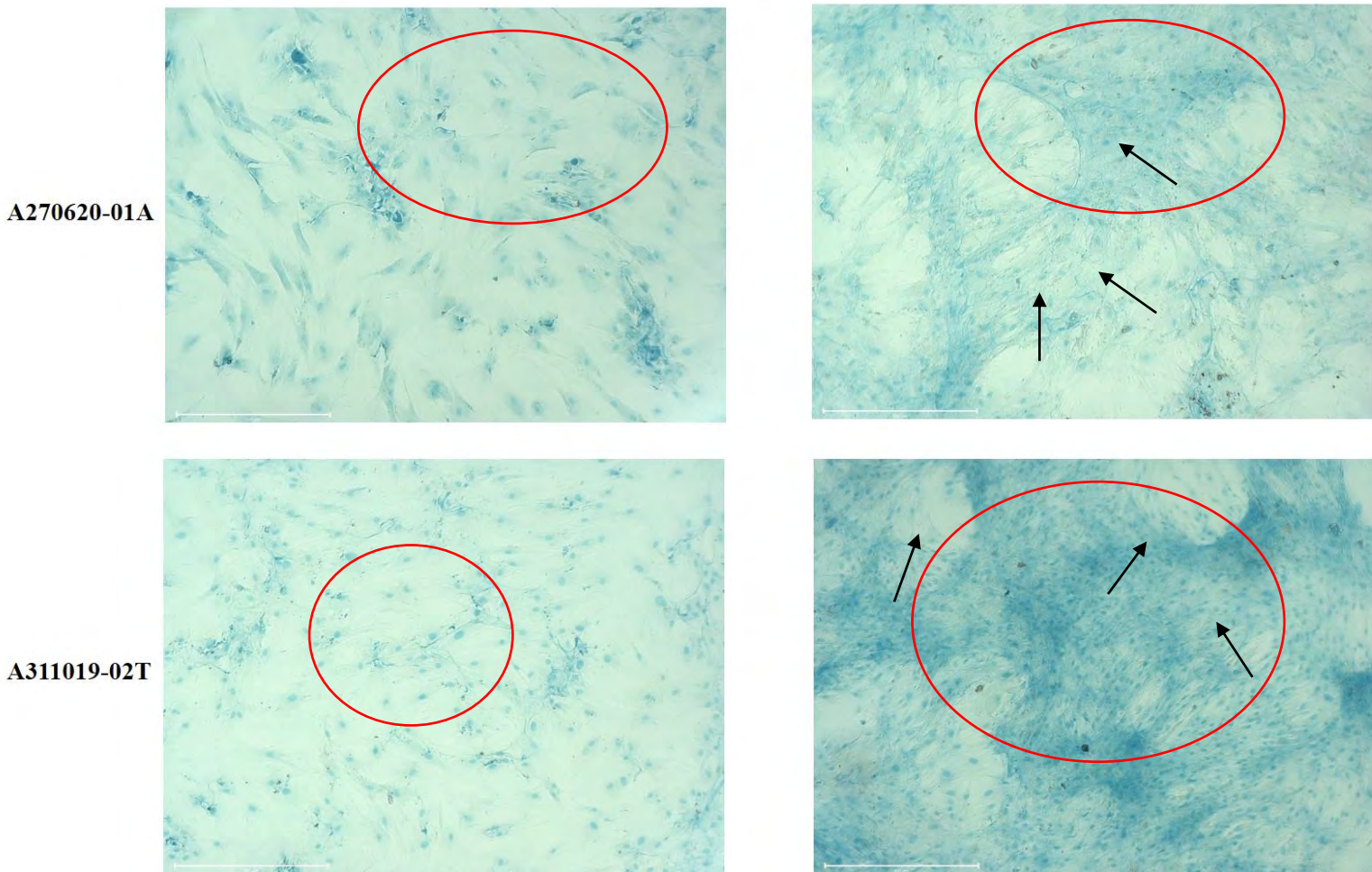
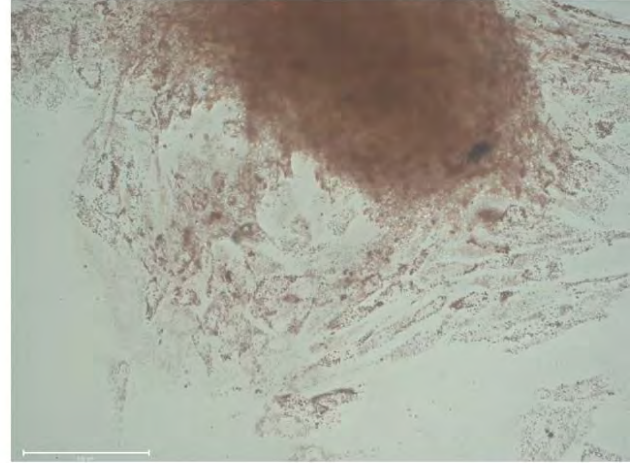
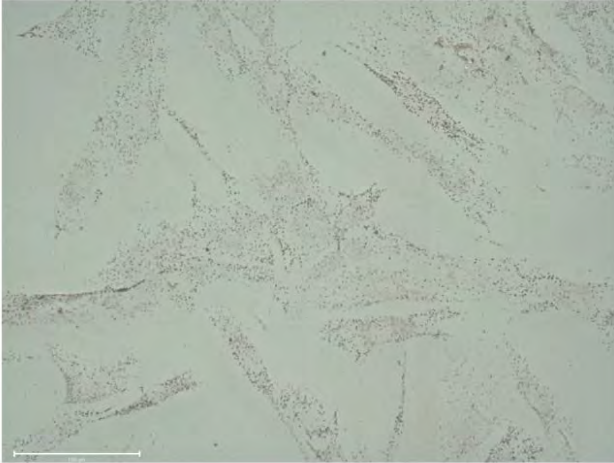


**Figure 9: Alcian Blue staining of chondrogenic differentiation 21 days after induction.** Images on the left show the negative controls, and images on the right show ad-MSCs 21 days after chondrogenic induction. Scale bar = 500  $\mu$ m and each image represents N = 6 and each batch experiment had n = 3.

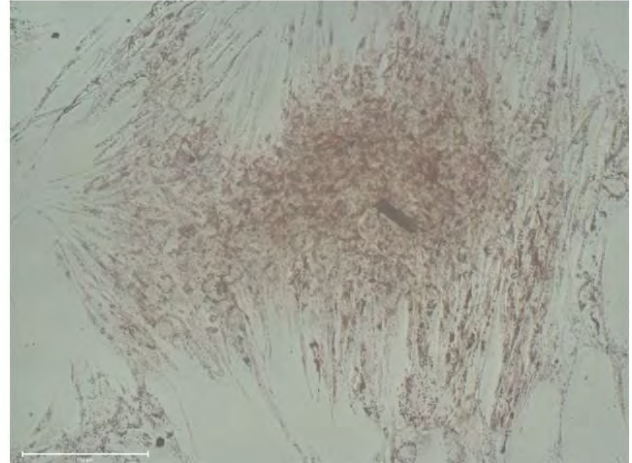
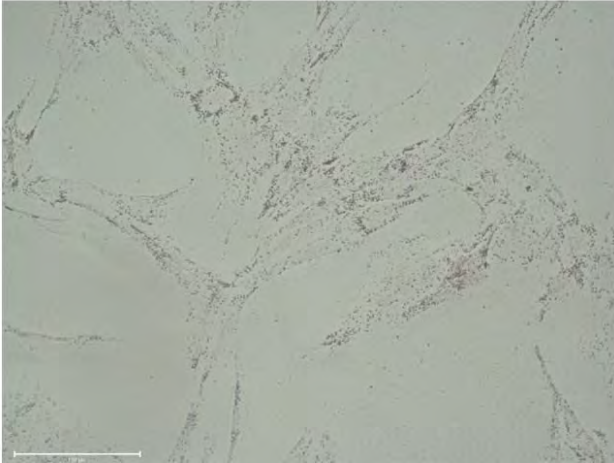
Figure 9 shows the Alcian Blue staining for chondrogenic differentiation 21 days after induction. Both cell lines displayed an increase in stain retention, indicating that chondrogenic differentiation has occurred. In addition to this, cell morphology changes between the control on the left and differentiated cells on the right where the differentiated cells show significantly more clumping and aggregation than the dispersed control cells on the left indicate differentiation had occurred and, more specifically, chondrogenic differentiation. The difference in cell morphology is highlighted by the red circles in Figure 9. Cell line A311019-02T produced a more intense Alcian Blue stain than the A270620-01A showing a greater degree of differentiation based on the increased secretion of GAGs present in the ECM, an identifiable characteristic of chondrogenesis, as well as a feature found in the ECM of cartilage. Cell line A270620-01A, however, showed a greater spread of the ECM than the A311019-02T but less GAG production as a result of less Alcian Blue stain present and is shown by the black arrows in Figure 9.

**Day 7**

**A270620-01A**



**A311019-02T**



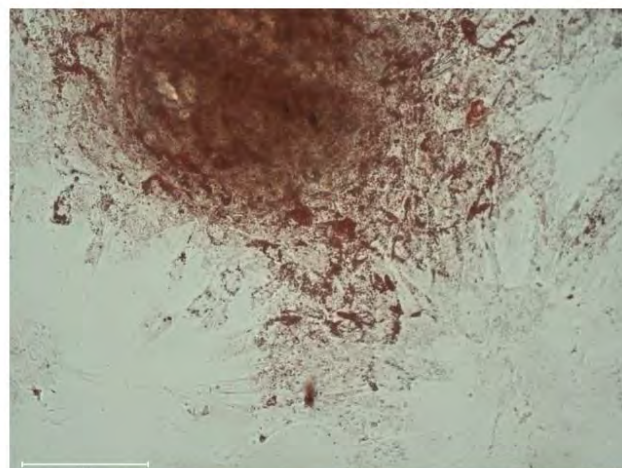
**Figure 10: Oil Red O staining for adipogenic differentiation after 7 days of induction.** Images on the left show the negative controls, and images on the right show ad-MSCs 7 days after adipogenic induction. Scale bar = 150  $\mu$ m and each image represents N = 6 and each batch experiment had n = 3.

Figure 10 shows the Oil Red O staining for adipogenic differentiation 7 days after induction. Small lipid droplets were stained due to the Oil Red O stain indicating that the adipose-mesenchymal stem cells had begun to differentiate into adipocytes. In the control group small smear droplets in the cytoplasm, which are smaller than the differentiate cell group can be observed and is characteristic of cells to accumulate lipids. Cell line A311019-02T showed more dispersion of lipid droplets than cell line A270620-01A. A greater intensity of Oil Red O stain is shown in the differentiated A270620-01A cell line, which could contribute to mass cell clumping.



## Day 14

A270620-01A



A311019-02T

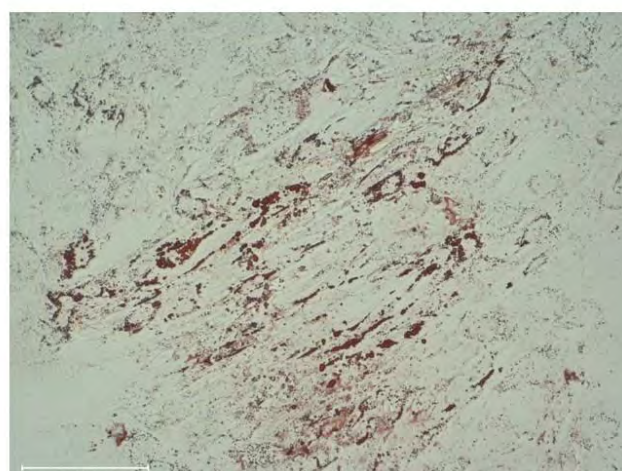
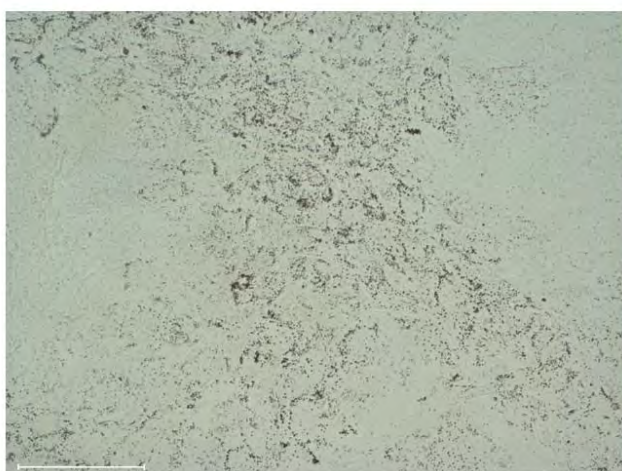
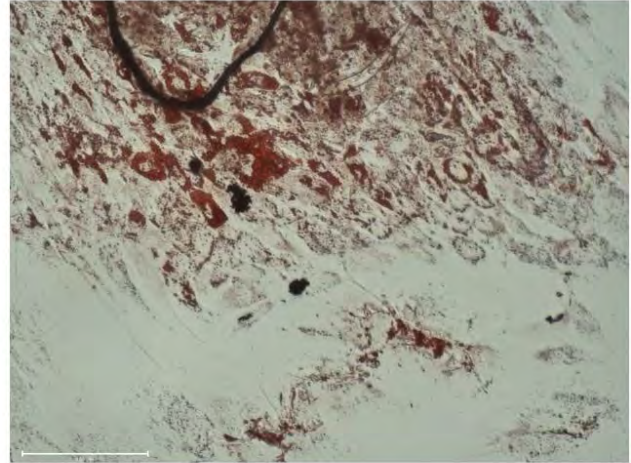
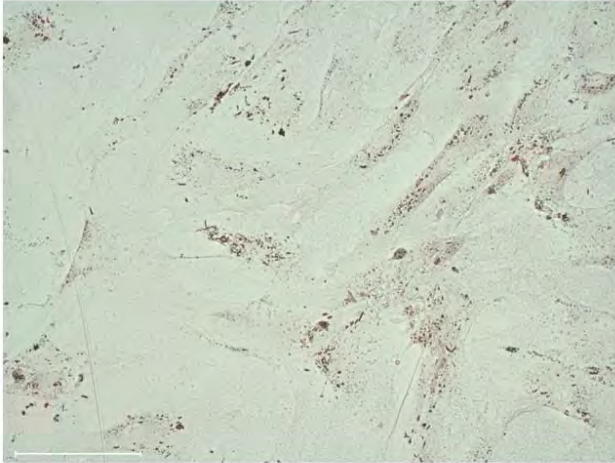


**Figure 11: Oil Red O staining for adipogenic differentiation after 14 days of induction.** Images on the left show the negative controls, and images on the right show ad-MSCs 14 days after adipogenic induction. Scale bar = 150  $\mu\text{m}$  and each image represents N = 6 and each batch experiment had n = 3.

Figure 11 shows the Oil Red O staining for the adipogenic differentiation 14 days after induction. An increase in lipid droplet production had increased from day 7 for both cell lines. The size of the lipid droplets had also increased. Cell line A311019-02T displayed a more significant lipid droplet production than cell line A270620-01A. Similarly, day 7, cell line A270620-01A production a more intense Oil Red O stain than cell line A311019-02T, which can be contributed to the mass cell clumping.

## Day 21

A270620-01A



A311019-02T

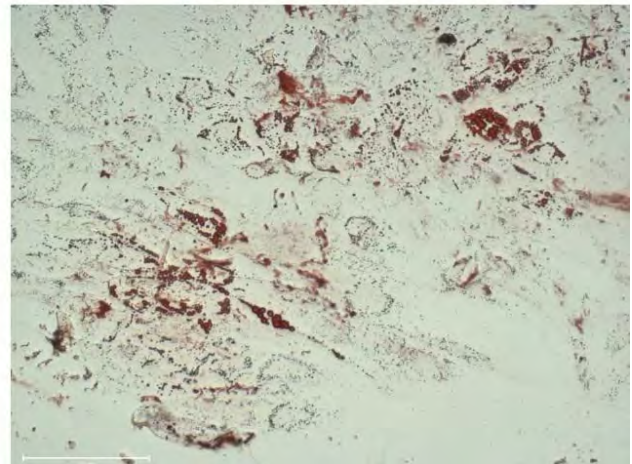
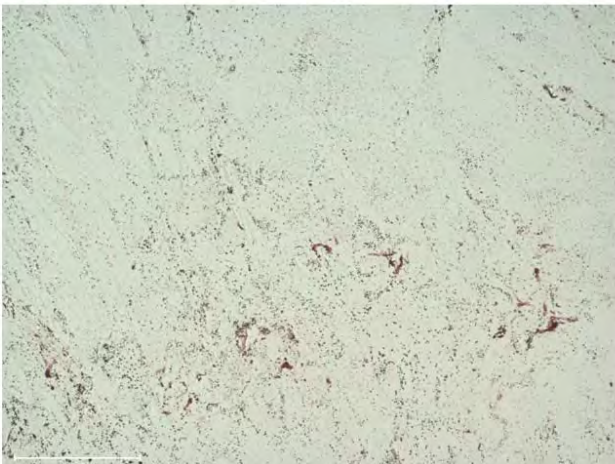


**Figure 12: Oil Red O staining for adipogenic differentiation after 21 days of induction.** Images on the left show the negative controls, and images on the right show ad-MSCs 21 days after adipogenic induction. Scale bar = 150  $\mu$ m and each image represents N = 6 and each batch experiment had n = 3.

Figure 12 shows the adipogenic differentiation 21 days after induction. A significant increase in lipid droplet production is observed for both cell lines than the controls and days 7 and 14. A greater dispersion of lipid droplets can be seen for cell line A311019-02T than the A270620-01A cell line. Lipid droplet size also increased though observation of the images in both cell lines when compared to days 7 and 14. Slightly more intense retention of Oil Red O stain can be observed in the A270620-01A cell line. Small amounts of Oil Red O stain are seen in the controls for both cell lines, suggesting lipid droplets.

Figures 7-12 shows the progression of differential staining of chondrocytes and adipocytes from ad-MSC after 7, 14, and 21 days of induction. Both cell lines displayed cellular differentiation for chondrogenic and adipogenic differentiation. Adipogenic differentiation was used to compare the chondrogenic differentiation to confirm that cellular differentiation was able to occur within the two ad-MSC cell lines. Relatively little amounts of Alcian Blue stain could be visualized in Figure 7. Both cell lines after 7 days of chondrogenic induction displayed only small amounts of Alcian Blue stain present within the extracellular matrix indicating trace amounts GAGs and aggrecans present within the



extracellular matrix. This indicates primary chondrogenic differentiation had occurred. Similarly, with the adipogenic differentiation after 7 days of induction in Figure 10, only small amounts of Oil Red O stain can be visualized, indicating only small amounts of lipid production. Yao *et al.*, 2013 showed similar results where lipid production of adipocytes from endothelial cells was minimal after 5 days however after 17 days mass lipid production was observed. Within both Figures 7 and 10, cell line A311019-02T showed slightly more staining than with cell line A270620-01A suggesting cell line A311019-02T has a slightly better ability to differentiate into both adipocytes and chondrocytes.

After 14 days after chondrogenic induction, greater amounts of Alcian Blue stain was present in the A311019-02T compared to the A270620-01A cell line, however is still more than 7 days after chondrogenic induction. The increase in Alcian Blue stain indicates increased amounts of GAGs and proteoglycans, namely aggrecans present within the cells' extracellular matrix. The increase in GAGs and aggrecans in the ECM confirms that chondrogenic differentiation occurred in the mid-differentiation phase. Peran *et al.*, 2013, Zubillaga *et al.*, 2020 and Tanthaisong *et al.*, 2017 show Alcian Blue staining of chondrogenic differentiation of BMSCs after 14 days. Both cellular morphologies observed in Figure 8 between the control and differentiated cells and the staining differences between the control and differentiate cells and comparisons of differentiation effect from 7 days (initial differentiation) correspond to the results found with literature. Tanthaisong *et al.*, 2017 also shows the slight staining of the control group's nuclei compared to the differentiated cells, which is also observed with the control group in Figure 8. Due to the characteristics of ad-MSCs, some lipid production can occur (Hu, Zhao and Li, 2019) and thus can explain why slight retention of the Oil Red O stain has occurred in the control group and in the study done by Tanthaisong *et al.*, 2017.

A large amount of Oil Red O stain was observed in Figure 11 for both cell lines. The increase in Oil Red O stain shows increased lipid production confirming adipogenic differentiation had occurred. Bunnell *et al.*, 2008 demonstrates similar lipid production results after 14 days of adipogenic differentiation of adipose mesenchymal stem cells. Similarly, with Figure 11 where the A311019-02T showed higher differentiation ability, the A311019-02T cell line for adipogenic differentiation showed a higher differentiation ability than cell line A270620-01A as there was a more dispersed amount of lipids produced. The A270620-01A cell line produced a more intense Oil Red O stain; however, this was due to mass cell clumping and aggregation observed in most of the images taken and observed in all replicates, which could result in retention of a stain rather than staining of the lipids present done with the A311019-02T cell line. The cell clumping appeared prior to the start of differentiation, after seeding of the ad-MSC into the 96-well plate. As the ad-MSCs for the adipogenic differentiation used the last remains of the cell suspension, the clumping observed could be the result of insufficient resuspension of the pellet of the A270620-01A as they were more confluent and formed a larger pellet than the A311019-02T cell line. Harsher and more resuspension may allow for the breakup of the cell clumping resulting in even dispersion as seen for the rest of the differentiation images. Literature on

different adipose-mesenchymal stem cells with respect to comparisons been made on their differential ability is limited. Lee *et al.*, 2015, Aldridge *et al.*, 2013 and Bunnell *et al.*, 2008, however demonstrate the use of different cell lines and their differential effects observing only slight differences in lipid size and production throughout the 7-21 days of differentiation.

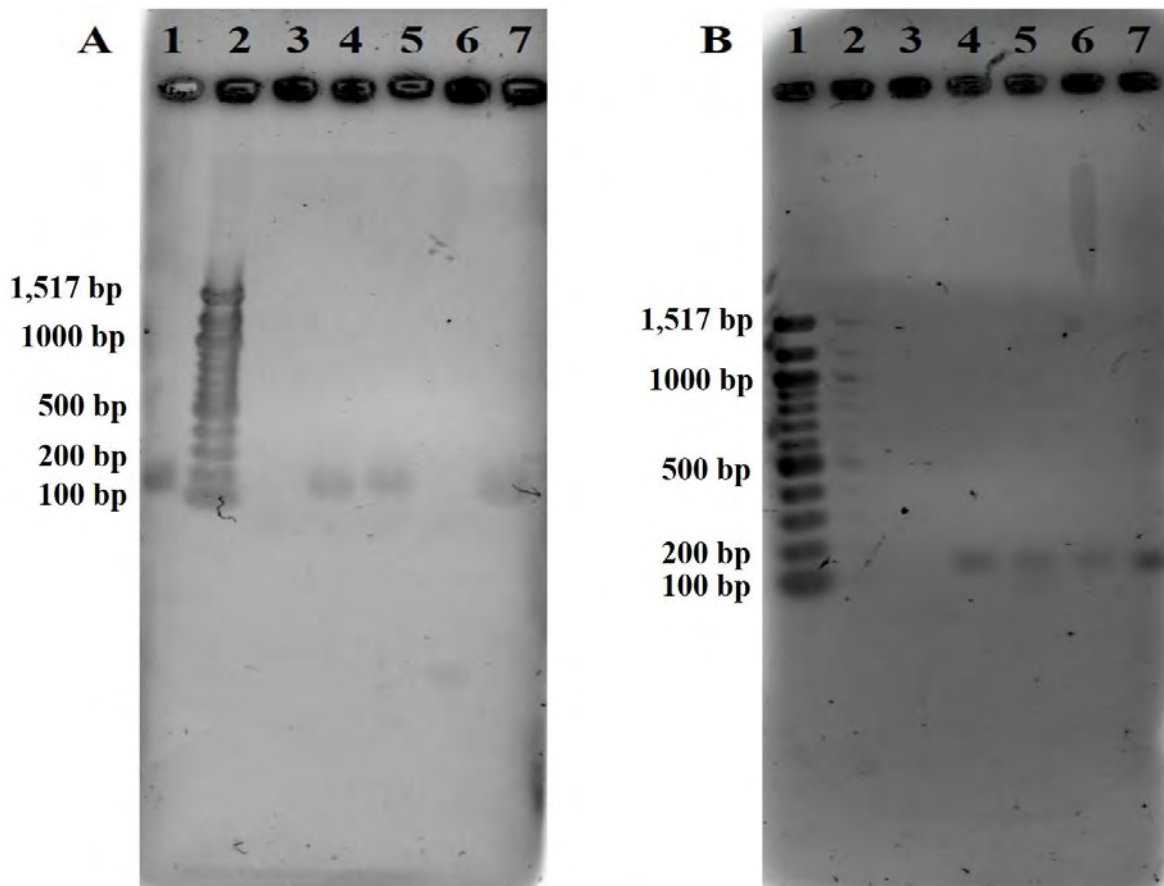
Terminal differentiation for chondrogenic differentiation and adipogenic differentiation is set after 21 days and shown in Figures 9 and 12 for chondrogenic and adipogenic differentiation. After 21 days of chondrogenic differentiation induction, high amounts of Alcian Blue stain were present in cell line A311019-02T, indicating excessive amounts of aggrecans and GAGs present within the ECM, confirming chondrogenic differentiation had taken place. The A270620-01A cell line showed less retention of the Alcian Blue, indicating fewer aggrecans and GAGs in the ECM. However, Alcian Blue stain is still present within the ECM control. More Alcian Blue stain was present after 21 days of differentiation compared to after 14 days of differentiation, which indicated progression of chondrogenic differentiation. Cho *et al.*, 2015 and Zubillaga *et al.*, 2020 show similar results of chondrogenic differentiation staining with Alcian Blue stain after 21 days after induction where stain retention is high and progression of Alcian Blue stain increases over the differentiation period from 7-21 days. Both cell lines also displayed mass changes in morphology with cellular grouping and expansion of the ECM occurring compared to the controls characteristic of chondrogenic differentiation, further confirming chondrogenic differentiation. Cho *et al.*, 2015 displays similar morphological changes after 21 days between the control group and the differentiated cells corresponding to the morphology changes observed throughout the differentiation period of 7-21 days.

Figure 12 shows terminal adipogenic differentiation after 21 days which numerous Oil Red O stain being retained, indicating lipid droplets present. Compared to 14 days of adipogenic differentiation, a significant increase in lipid production and size is observed after 21 days of adipogenic differentiation. The effects of increased lipid production and lipid size after 21 days are shown in our laboratory by Honiball, 2017 and independently by Aldridge *et al.*, 2013, which corresponds to the results obtained in Figure 12. Aldridge *et al.*, 2013, produced larger lipids, but this could result from using bone marrow stem cells wherein this study adipose stem cell was used and thus can demonstrate the differentiation effect adipogenic differentiation of different cell lines. Despite the use of different cell line, it still demonstrates the progress of adipogenic differentiation over 21 days. Cell line A270620-01A displayed more Oil Red O stain than cell line A311019-02T indicating after 21 days of adipogenic differentiation that it has a higher ability to differentiate into adipocytes as the lipid size and dispersion was more significant than seen with cell line A311019-02T. For conclusive evidence for stain retention and lipid accumulation, quantitative measurements using a plate reader could be used, extraction the Oil Red O stain with isopropanol. The controls do show small amounts of Oil Red O stain, indicating some presence of lipid production. Gojanovich *et al.*, 2018 obtained similar results using mesenchymal stromal stem cells where the undifferentiation control retained Oil Red O stain indicating lipid droplets'

presence. According to Nava, Raimondi and Pietrabissa, 2012 and Badimon, Oñate and Vilahur, 2015, the niche formation of Ad-MSK and even stem cells themselves can produce small amounts of lipids and even in some cases, undergo partial differentiation of a specific cell lineage due to the microenvironment and cytokines, which interact within the cellular niche. The minimal production of lipid droplets by the ad-MSK is the most likely explanation of why the control group showed lipid accumulation.

### **2.2.2 RT-qPCR gene expression of collagen gene markers for Chondrogenic Differentiation**

Gene expression of chondrogenic differentiation was performed on both cell lines A270620-01A and A311019-02T. A 6-well plate was used for the RT-qPCR assay which should generate  $0.5-1 \times 10^6$  cells when confluent. Gene expression markers Col10a1 and Col2a1 were used to test the expression of collagen formation levels, an essential part of chondrogenic differentiation. Optimization of the annealing temperatures for each gene marker was performed using PCR with only the Col10a1 and GAPDH gene markers producing consistent product bands at annealing temperatures of 58 and 60 °C respectively and can be seen in Figure 13. During one PCR run Col2a1 did produce a band at 55 °C however when repeats were performed no bands appeared. The annealing temperatures for Col10a1, Col2a1 and GAPDH did match with the theoretical annealing temperatures on primer-BLAST (NCBI). PCR band production for the other gene markers Aggrecan, Beta-catenin and Runx2 showed the same results as seen for the Col2a1 gene marker with most of them showing higher annealing temperatures than the theoretical annealing temperature found on primer-BLAST (NCBI). Due to low RNA yields that were acquired through RNA isolation of the chondrogenic differentiation 6-well plate gene markers Aggrecan, Beta-catenin and Runx2 could not be used in the gene expression profile of chondrogenic differentiation and the only collagen expression markers were used. Melt curves and amplification plots of the Col10a1 and Col2a1 expression markers can be found in the appendix. Lack of optimization and replicates of the RNA isolation and gene expression profile for chondrogenic differentiation was due to mass contamination in the laboratory incubator that infected all replicate 6-well chondrogenic differentiation plates used for RT-qPCR. Comparison of the collagen expression markers, Col10a1 and Col2a1 between cell lines A270620-01A and A311019-02T are shown below in Figure 14 and melt curves and amplifications plots in Figures S2 and S3 in the appendix section.



**Figure 13: Primer optimization of gene markers GAPDH (A) and Col10a1 (B).** Each lane shows the various annealing temperatures ( $T_a$ ) used during optimization of the GAPDH and Col10a1 gene expression markers. For gel A: Lane 1 –  $T_a = 60^\circ\text{C}$ ; Lane 2 – 100bp DNA ladder; Lane 3 –  $T_a = 50^\circ\text{C}$ , Lane 4 –  $T_a = 55^\circ\text{C}$ ; Lane 5 –  $T_a = 60^\circ\text{C}$ ; Lane 6 –  $T_a = 50^\circ\text{C}$ ; Lane 7 –  $55^\circ\text{C}$ . For gel B: Lane 1 – 100 bp DNA ladder; Lane 2 –  $T_a = 53^\circ\text{C}$ ; Lane 3 –  $T_a = 58^\circ\text{C}$ ; Lane 4 –  $T_a = 62^\circ\text{C}$ ; Lane 5 –  $T_a = 53^\circ\text{C}$ ; Lane 6 –  $T_a = 58^\circ\text{C}$ ; Lane 7 –  $T_a = 62^\circ\text{C}$ . A 1.5 % (w/v) TAE agarose gel was used to run PCR products at 60 V, 30 mA for 1 hour. Gels were stained with 0.5  $\mu\text{g/ml}$  ethidium bromide post run. Each gel image is representative of  $n = 2$ .

Figure 13 shows the results of the optimized PCR run on a stained ethidium bromide, 1.5 % (w/v) TAE agarose gel. For gel A in Figure 13, the GAPDH housekeeping gene produced the most intense bands at  $\pm 150$  bp based off the 100 bp DNA ladder at an annealing temperature of  $60^\circ\text{C}$ . For gel B in Figure 13, the Col10a1 collagen gene expression marker produced the most intense bands at  $\pm 150$  bp based off the 100 bp DNA ladder at an annealing temperature of  $58^\circ\text{C}$ . The require product length for GAPDH and Col10a1 is 152 bp and 155 bp respectively and therefore can conclude the bands acquired for GAPDG and Col10a1 in Figure 13 are the correct bands and that the annealing temperatures for GAPDH and Col10a1 are  $60^\circ\text{C}$  and  $58^\circ\text{C}$  respectively.



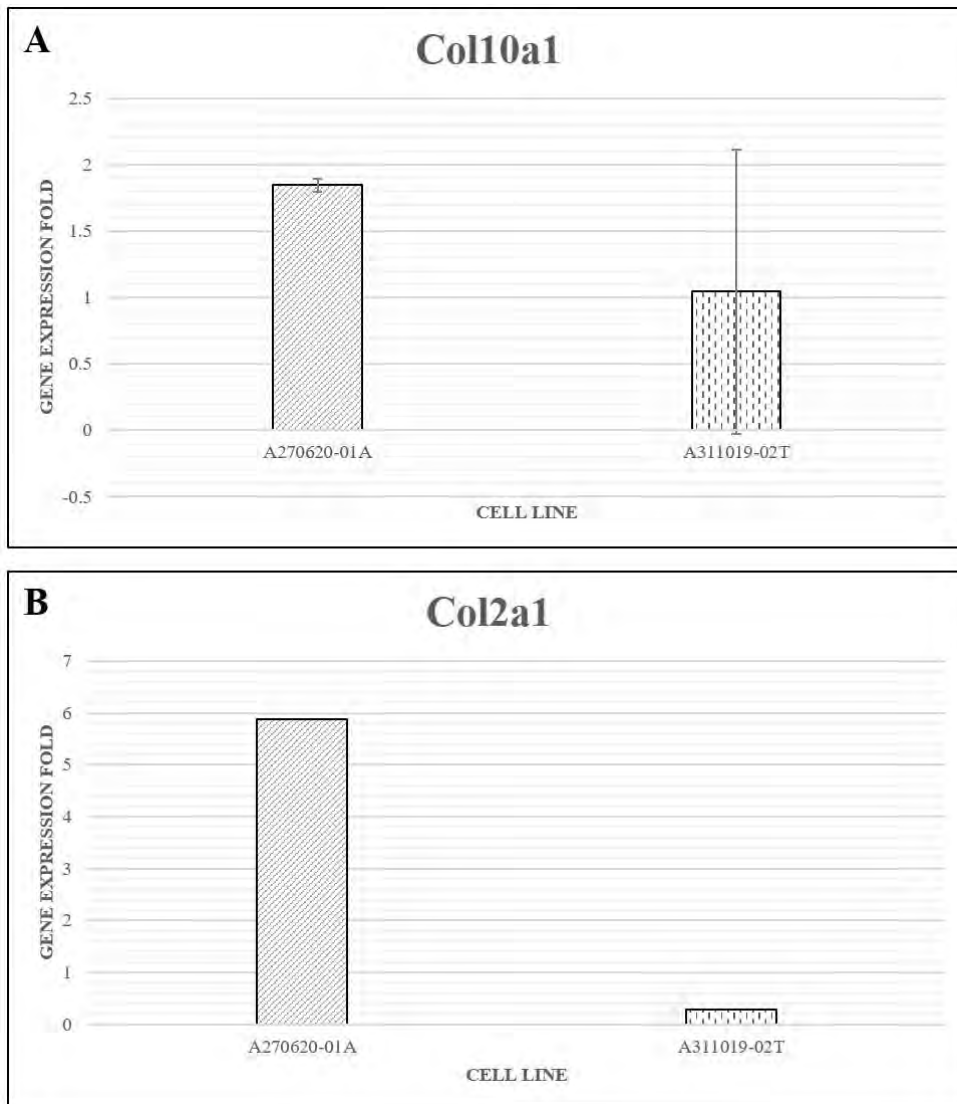


**Figure 14: Gene Expression Levels of chondrogenic differentiation marker genes for collagen (A) Col10a1 and (B) Col2a1 14 days after induction.** Gene expression was normalized to corresponding GAPDH and calculated by the relative expression compared to the control cells. Graphs were constructed using Microsoft Excel 365. Normalizing and calculation of the gene expression was done using the cycle threshold (CT) values obtained from the QnatStudio™ RT-qPCR machine from which the  $\Delta Ct$  and  $\Delta\Delta Ct$  values were calculated. Gene expression fold ( $2^{-(\Delta\Delta Ct)}$ ) was then calculated and graphed. The data are expressed as mean $\pm$ SD. The data in the figure is representative of N=2 where (A) and (B) are representative of n=2 and n=1 respectively.

Col10a1 encodes for the alpha chain of type X collagen, representing a short-chain within hyaline cartilage and plays a vital role in the chondrogenesis and enchorial ossification process (Gu *et al.*, 2014; Kong *et al.*, 2019). Col2a1 is a human gene responsible for the production of the pro-alpha1(II) chain of type II collagen, which acts as a cartilage-specific marker gene for collagen type II and is responsible for adding strength and structure to the connective tissues supporting muscles, organs, skin and joints (Bishop, 2010; MedlinePlus, 2020).

Figure 14 shows the collagen gene expression markers Col10a1 and Col2a1 14 days after chondrogenic differentiation induction. A single RT-qPCR run for the Col2a1 gene expression marker was done due to insufficient RNA yield acquired from the RNA extraction post chondrogenic differentiation induction. This was mainly due to low cell numbers acquired after trypsinizing as the cells struggle to lift, as well as possible disruption of the pellet when removing the supernatant causing less than optimal cell numbers for mRNA isolation. Both cell lines showed collagen expression via the collagen gene markers Col10a1 and Col2a1. The A311019-02T cell line showed less collagen expression than cell line A270620-01A for both gene markers Col10a1 and Col2a1. Cell line A270620-01A showed a significantly higher gene expression fold value for Col2a1 than for Col10a1 for both cell lines. Both cell lines for the gene marker Col10a1 produced a higher gene expression fold than for the cell line A311019-02T for gene marker Col2a1. Tanthaisong *et al.*, 2017 performed a chondrogenic gene expression profile derived from MSCs, which resulted in Col2a1 and Col10a1 having a relative gene expression of 5 and 1.3 respectively, after four weeks after chondrogenic induction. Mueller *et al.*, 2013 obtained similar results for Col10a1 having a relative expression level of 0.9 after 21 days of chondrogenic differentiation using BMSCs. Eslaminejad, Karimi and Shahhoseini, 2013 performed gene expression levels for chondrogenic differentiation with BMSCs resulting in Col2a1 have a relative gene expression for TGF- $\beta$ 3 of 4 after 14 days after chondrogenic induction.

All values for Col10a1 were similar to the acquired gene expression values obtained for cell lines A270620-01A and A311019-02T. Col2a1 gene expression level for cell line A270620-01A was higher than found in literature, where the Col10a1 corresponded to the literature results. This could be the result of using different cell lines compared to the cell lines used in literature. Although the Col2a1 gene expression is high for cell line A270620-01A and low for A311019-02T, these results are only based on a single RT-qPCR, and additional repeats need to be performed to validate these results. The RT-qPCR comparison to the monolayer staining results shows conflict between the chondrogenic differentiation between the two cell lines, where the stain in cell line A311019-02T shows more chondrogenic differentiation cell line A270620-01A shows a higher gene expression level for both Col10a1 and Col2a1. This could be since the Alcian Blue stain targets Aggrecans within the ECM where the RT-qPCR was testing collagen expression.

To improve comparisons between the two cell lines, collagen staining can be done and perform gene expression levels of aggrecan to determine which cell line has better chondrogenic differentiation ability. High confluency of both cell lines needs to be achieved before initiating differentiation as it will increase differentiation efficiency. It will also ensure sufficient mRNA present to perform multiple replicates and use other essential gene markers to determine chondrogenic differentiation, such as B-catenin and aggrecan, of which both play vital roles in chondrogenic differentiation. Alternatively, the use of bigger flasks will allow more cells to be present and ensure sufficient mRNA to be extracted. Additional observations were made with the melt curves of the Col10a1, Col2a1 and GAPDH gene

markers shown in Figure S2 where the  $T_a$  resulted in temperatures of  $\pm 20\text{ }^\circ\text{C}$  and  $\pm 25\text{ }^\circ\text{C}$  higher than the theoretical and optimized  $T_a$  for Col10a1, Col2a1 and GAPDH respectively from the PCR optimization. Eslaminejad, Karimi and Shahhoseini, 2013 and Tanthaisong *et al.*, 2017 both reported having annealing temperatures for all the chondrogenic expression markers at  $60\text{ }^\circ\text{C}$  and  $62\text{ }^\circ\text{C}$  for Col2a1, as well as for Col10a1. All other chondrogenic gene expression markers such as Aggrecan, Beta-Catenin and Runx2 were also reported having annealing temperatures higher than  $60\text{ }^\circ\text{C}$ , which is contrasting to the theoretical annealing temperatures, which range between  $52\text{-}58^\circ\text{C}$ . The result of higher annealing temperatures for the gene markers in the RT-qPCR may have influenced the gene expression profile. As a result further optimization with the annealing temperatures to assess whether having higher annealing temperatures would positively affect the gene expression profile of the gene markers.

In conclusion, both cell lines A270620-01A and A31101Q-02T were able to undergo chondrogenic and adipogenic differentiation. The A31101Q-02T cell line showed a greater differentiation ability towards chondrogenic and adipogenic differentiation using Alcian Blue and Oil Red O staining. Cell line A270620-01A showed greater collagen expression than A31101Q-02T for marker genes Col10a1 and Col2a1 after 14 days of induction where similar results were observed in literature however replicates for both cell lines need to be performed for validation of the results. In addition to this, collagen II staining and aggrecan gene expression levels need to be performed to compare the two cell lines better and validate, which cell line has a better differentiation ability. Ad-MSCs should be grown for longer to acquire a higher confluence before inducing differentiation to achieve a higher RNA yield and complete the chondrogenic gene expression comparison between the two cell lines that could not be completed with low RNA yields of the A270620-01A cell line.

## Chapter 3: Hydrogel formulation and characterisation

### 3.1 Introduction

The swelling ratio (%) and degradation rate are essential characteristics of hydrogels for tissue engineering. The swelling ratio (%) can be defined as the fractional increase of the hydrogel's mass due to water absorption (Park *et al.*, 2009). Swelling ratios allow for the increase in spatial heterogeneity of a polymer. Although hydrogel composition, polymerisation, and temperature affect the hydrogel's structural and mechanical characteristics after gelation, changes in the properties can occur over time as a result of hydrogel swelling (Subramani *et al.*, 2020). It is essential to determine the swelling values as they will be considered as the equilibrium swelling ratio. The equilibrium swelling ratio is the point at which the hydrogel cannot take any more water and reaches complete equilibrium while remaining in its crosslinked state (Bennour and Louzri, 2014).

The idea of hydrogel degradation is that the hydrogel scaffold can degrade at the same rate as tissue formation, resulting in a completely degraded hydrogel scaffold and a fully formed functional tissue (Zustiak and Leach, 2010). Most natural hydrogels like gelatin, collagen and hyaluronic acid are biodegradable over time and via hydrolytic or enzymatic degradation. Synthetic polymers such as PEG and PEO are non-biodegradable hydrogels (Zustiak and Leach, 2010; Camci-Unal *et al.*, 2013). Since synthetic hydrogels cannot degrade, natural polymers are often integrated with synthetic to aid in the degradation of the hydrogel scaffolds. The degradation defines the degradability of the hydrogel and gives a general representation of what to expect to occur in the *in vivo* environment (Zustiak and Leach, 2010; Wu *et al.*, 2016).

Morphological analysis of hydrogels gives definitive characteristics of hydrogel surfaces tailored to cellular attachment, surface pore sizes for cellular infiltration, nutrient diffusion and oxygen transfer. The porosity of the hydrogels also influences cellular growth, expansion and interconnectivity with the polymer and adjacent cells creating a cellular niche. Although the swelling ratio influences these factors, as mentioned above, the porosity is the factor influencing them. Determining hydrogel's porosity can be done using a high-powered microscope such as a scanning electron microscope (SEM). SEM works by focussing electron beams in a static or sweep way across the surface of the sample using secondary backscatter electrons and photons of various energies to produce the 2D image (Goldstein *et al.*, 1992). This allows for high definition and the ability to analyse each formulated hydrogel and hybrid hydrogels' porosity, allowing for a more in-depth characterisation of each hydrogel type and determining the effect on cellular infiltrations and nutrient diffusion etc. Comparing the morphological analysis of each hydrogel type allows for an excellent comparison towards which formulated hydrogel type should be

better suited for tissue engineering as a cellular scaffold (Kaberova *et al.*, 2020; Spicer, 2020). The use of SEM requires the biological sample to be under vacuum. In addition to this, the state of hydrogels having a high-water content requires that the hydrogels undergo dehydration to prevent any form of evaporation and moisture building to occur while exposed to the vacuum, which can cause potential damage to the microscope. Dehydration of the hydrogels also prevents morphological changes due to the high presence of water and a high vacuum environment (Kaberova *et al.*, 2020). SEM has advantages over light microscopes such as the superior resolution it provides. Other microscope technologies such as transmission electron microscopy (TEM) and atomic force microscopy (AFM) require the samples to be thinly cut for viewing. TEM and SEM performs good analysis for viewing biological samples with pronounced topography and multiple surfaces, making SEM a convenient and versatile tool (Goldstein *et al.*, 1992).

This chapter describes the design and formulation of five different hydrogels: GelMA, PEG, GelMA/PEG, GelMA/HAMA and PEG/HAMA, as engineered scaffolds for 3D mammalian cell culture. The aims and objectives of this chapter included:

**Aim:**

- To design and formulate five different hydrogels, GelMA, PEG, GelMA/PEG, GelMA/HAMA and PEG/HAMA for the optimization of mammalian cell culture.

**Objectives of aim:**

1. Make up hydrogel polymer mixtures and freeze-dry mixtures and store at -20 °C for long term use.
2. Reconstitute freeze-dried mixtures in DPBS and test the different hydrogels' polymerization efficiency and relative combinations using a visible light photoinitiator.
3. Characterize and analyze each hydrogel formation and their relative properties through swelling, degradation, SEM and FTIR analysis.

## 3.2 Methods and Materials

### 3.2.1 Materials

Materials and solvents were acquired from Sigma Aldrich and Thermo Fisher Scientific unless stated otherwise. Poly (ethylene) glycol diacrylate  $\pm$ Mn 700 kDa (Cat. No. 455008), Bovine gelatin (type B) (Cat. No. G9391), hyaluronic acid sodium salt from *Streptococcus equi* (Cat. No. 53747 – 1G), methacrylic anhydride (Cat. No. 276685-500 ml) visible light photoinitiator consisting of 0.01 mM Eosin Y (Cat No. E4009), 0.50% TEA (Cat. No. T0886) and 37 nM NVP (Cat. No. V3409) were all sourced from Sigma-Aldrich. Pierce Snake-Skin™ Dialysis tubing 10K MWCO, 22 mm (Cat. No. 68100) was purchased from Thermo Fisher Scientific.

### 3.2.2 Gelatin Methacrylate (GelMA) hydrogel

The protocol for GelMA was derived from Kolesky *et al.*, 2014. A 10% (v/v) gelatin type B (bovine skin) solution was prepared by dissolving gelatin in DPBS at 60 °C with vigorous stirring (60 rpm) for 2 hours after which it was cooled down to 40 °C, and 0.14 mL of methacrylic anhydride was added dropwise for each gram of gelatin in solution while stirring at 60 rpm. The solution was left at 50 °C for 4 hours while stirring at 40 rpm. Subsequently it was quenched to make a 4.5 % solution by adding DPBS warmed to 40 °C. The solution was then dialysed using Pierce Snake-Skin™ Dialysis tubing (10K MWCO) against 18.2 M $\Omega$  double distilled water at a hydrogel/water ratio of 10 ml/1L for six days with water changes twice a day. Thereafter, it was freeze-dried for 4 days, after which it was stored at -20 °C for further use.

### 3.2.3 Hyaluronic Acid-Methacrylate (HAMA) hydrogel

The protocol used for HAMA was derived from Costantini *et al.*, 2016. A 2 % (w/v) HAMA hydrogel was made up by dissolving HA in ddH<sub>2</sub>O at 60 °C with vigorous stirring until completely dissolved. A 20 X molar excess of methacrylic anhydride (20-fold molar excess to repeating disaccharide units of HA) was added dropwise and the pH adjusted to 8.0 using 5 M NaOH. The reaction was then left on a shaker at 4 °C for 24-hours. The solution was dialysed using Pierce Snake-Skin™ Dialysis tubing (10K MWCO) against 18.2 M $\Omega$  double distilled water at a hydrogel/water ratio of 10 ml/1L for 5 days changing the water twice a day after which it was then freeze-dried for 4 days and stored at -20 °C until further use.

### 3.2.4 PEGDA hydrogel

The poly (ethylene) glycol diacrylate was ordered from Sigma-Aldrich and kept at 4 °C. At 4 °C PEGDA is in a solid state. Before use is placed in an incubator at 60 °C until it was in liquid form. A 10 % (v/v) PEGDA solution was made up by mixing the PEG in DPBS at 40 °C for 5 minutes. Polymerisation of the PEGDA was carried out by adding 0.05 mM Eosin Y, 0.75 % TEA and 37 nM

NVP allowing it to mix on a magnetic stirrer for 10 minutes, 40 °C. It was then exposed to UV light (405 nm) for 7 minutes to cause crosslinking and complete polymerisation.

### 3.2.5 GelMA preparation

The freeze-dried GelMA hydrogel was mixed and dissolved in DPBS at 50 °C with vigorous stirring until completely dissolved to make a 10 % (w/v) solution. A visible light photoinitiator consisting of 0.05 mM Eosin Y, 0.75 % TEA and 37 nM NVP was added to the solution and allowed to mix for 30 minutes. The GelMA solution was then crosslinked by exposure to UV light (405 nm) for 22 minutes.

### 3.2.6 GelMA/PEGDA and HAMA/PEGDA preparation

The freeze-dried GelMA, HAMA hydrogels were mixed and dissolved in DPBS at 40 °C with vigorous stirring until completely dissolved to make a 5 % (w/v) solution. PEGDA was then prepared and added to the 5 % hydrogel solution at a concentration of 5 % (v/v). The visible light photoinitiator; 0.05 mM Eosin Y, 0.75 % TEA and 37 nM NVP was then added to the solution and allowed to mix for 10 minutes at 40 °C. The GelMA/PEGDA and HAMA/PEGDA solution were crosslinked using UV (405 nm) for 7 minutes and 5 minutes respectively.

### 3.2.7 Swelling analysis

The swelling analysis was carried out for all hydrogels made. All hydrogels were crosslinked as previously described. Hydrogel disks of diameter 8 mm and 2 mm in height were punched using a sterile metal punch ( $\varnothing = 8$  mm) from the UV crosslinked gels. The mass of the disks were recorded prior to swelling. The gel disks were submerged in excess DPBS and DMEM (10 % FBS, 1 % Pen/Strep) for 24-hours after which the masses were recorded. An additional three disks from each gel were cut out and freeze-dried for 24-hours with the masses measured before and after 24-hours. Images of the disks before and after swelling in DPBS or DMEM and after freeze-drying were taken using an iPhone XS max showing the surface displacement of swelling. The average of the disks was calculated and recorded to calculate the average mass swelling ratio; i.e the ratio of the swollen mass to the dry mass of the polymer using equation 1 where all masses were recorded in grams. The analysis was carried out in triplicate.

$$\text{Swelling Ratio} = \frac{(\text{swollen mass} - \text{dry mass})}{\text{dry mass}} \times 100$$

**Equation 2: Swelling ratio (%) formula.** Formula obtained from (Bennour and Louzri, 2014).

### 3.2.8 Degradation analysis

The rate of degradation was determined for all hydrogel types. Hydrogel disks ( $\varnothing = 8$ mm, height = 2 mm) were prepared as performed in the swelling analysis. The hydrogel disks were immersed in 0.5, 0.1, 0.025 and 0.010 M Tri-sodium citrate (pH 7.5), (Fanucci, 2017) for 24-hours with the mass being

recorded hourly for 10 hours followed by the final recording at 24-hours after immersion. A negative control was included, which comprised of ddH<sub>2</sub>O. Experiments were carried out in triplicate for every Tri-Sodium Citrate concentration and every hydrogel type. Mass (grams) loss over time was recorded, and the remaining percentage mass plotted over time.

### **3.2.9 Scanning Electron Microscopy (SEM) of formulated hydrogels.**

Hydrogels were prepared and crosslinked as performed in 3.2.4, 3.2.5 and 3.2.6. Once crosslinked the hydrogel disks were cut out and prepared for dehydration for the super critical point dryer. The hydrogel disks were dehydrated by submerging in increasing ethanol concentrations (v/v) of 50 %, 60 %, 70 %, 80 %, 90 % and 100 % for 1 hour at each concentration. After 1 hour of dehydration in 100 % ethanol the hydrogel disks were dried using the super critical point dryer overnight. After drying the samples were mounted on SEM sample stands and coated with gold under vacuum using a Quorum Q150R S gold sputter. The coated samples were then viewed and images taken using the SEM (Tescan, Vega).  
3.

### **3.2.10 Numerical Data & Statistical Analysis**

All experiments were carried out in triplicate and data represented as mean  $\pm$  standard deviation. The swelling ratio and degradation analysis graphs were done using Microsoft Excel 365. All error bars are representative of standard deviation. Statistical analysis was done by TIBCO Statistica (version 13.5.0.17) using a one-way ANOVA for single comparisons, Factorial ANOVA was performed for determination of the statistical significance between DPBS and DMEM in the swelling ratio analysis and a Tukey HSD post hoc test was performed for all comparisons.



### 3.3 Results and Discussion

A swelling analysis was performed on the punched crosslinked hydrogel disks: GelMA, PEGDA, GelMA/PEGDA, GelMA/HAMA and PEGDA/HAMA in excess volumes of either DPBS or DMEM for 24-hours to determine the swelling ratio of each fabricated hydrogel type. DPBS and DMEM was used for a comparison to determine the differences of swelling ratios (%) when exposed to DPBS and DMEM for 24-hours. The swelling ratio (%) was calculated to determine the swelling characteristics of each hydrogel type is displayed in the graph below (Figure 15). Images of the crosslinked hydrogel disks before and after swelling (Figure 16) were taken, as well as the disks freeze-dried to visually show the expansion that occurs with the hydrogel disks after 24-hour exposure.

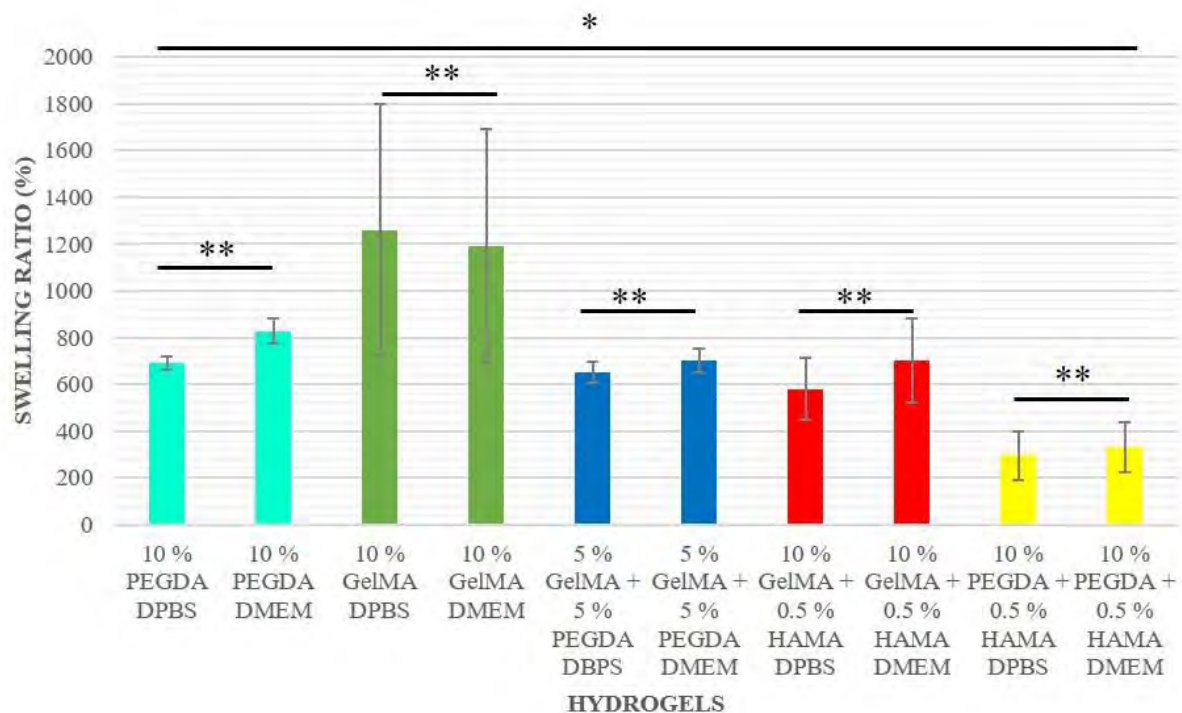


**Figure 15: Swelling ratio (%) calculated for the crosslinked hydrogels after 24-hour exposure in DPBS and DMEM.** Error bars are representative of standard deviation (SD). Bar graphs are representative of the swelling ratio calculated from the formula in 3.2.7. Each bar represents N = 9 and each batch experiment had n = 3. The statistical significance gave  $p < 0.05$  for hydrogels in DPBS and DMEM. The comparison between the swelling ratios of DPBS and DMEM gave a statistical significance of  $p > 0.05$ . \* $p < 0.05$ ; \*\* $p > 0.05$ .

Based on Figure 15, the 10 % GelMA hydrogel gave the greatest swelling ratio for both mediums, DPBS and DMEM of 1260 % and 1192 % respectively. The lowest swelling ratio experienced was for the 10 % PEGDA/0.5 % HAMA hydrogel for both mediums, DPBS and DMEM, having swelling ratios of 296 % and 331 % respectively. The one-way ANOVA test determined that  $p < 0.05$  for all hydrogels in DPBS and DMEM with the current effect of  $F(4,40)=21.342$  and  $F(4,40)=16.907$  respectively. A OL|+Tukey HSD post hoc test was performed showing that there is a statistical difference with the swelling ratios between 10 % PEGDA, 10 % GelMA and 10 % PEGDA + 0.5 % HAMA for both

medium types. No statistical difference was observed for DPBS and DMEM, as well as between 10 % PEG, 5 % GelMA + 5 % PEGDA and 10 % GelMA + 0.5 % HAMA. A Factorial ANOVA test was done to test the statistical difference in swelling ratios between DPBS and DMEM and showed no statistical difference between the two types of medium giving  $p > 0.05$  with a current effect of  $F(4,80)=0.50776$ . A Tukey HSD post hoc test was done and which confirmed no statistical differences were observed between the two mediums.

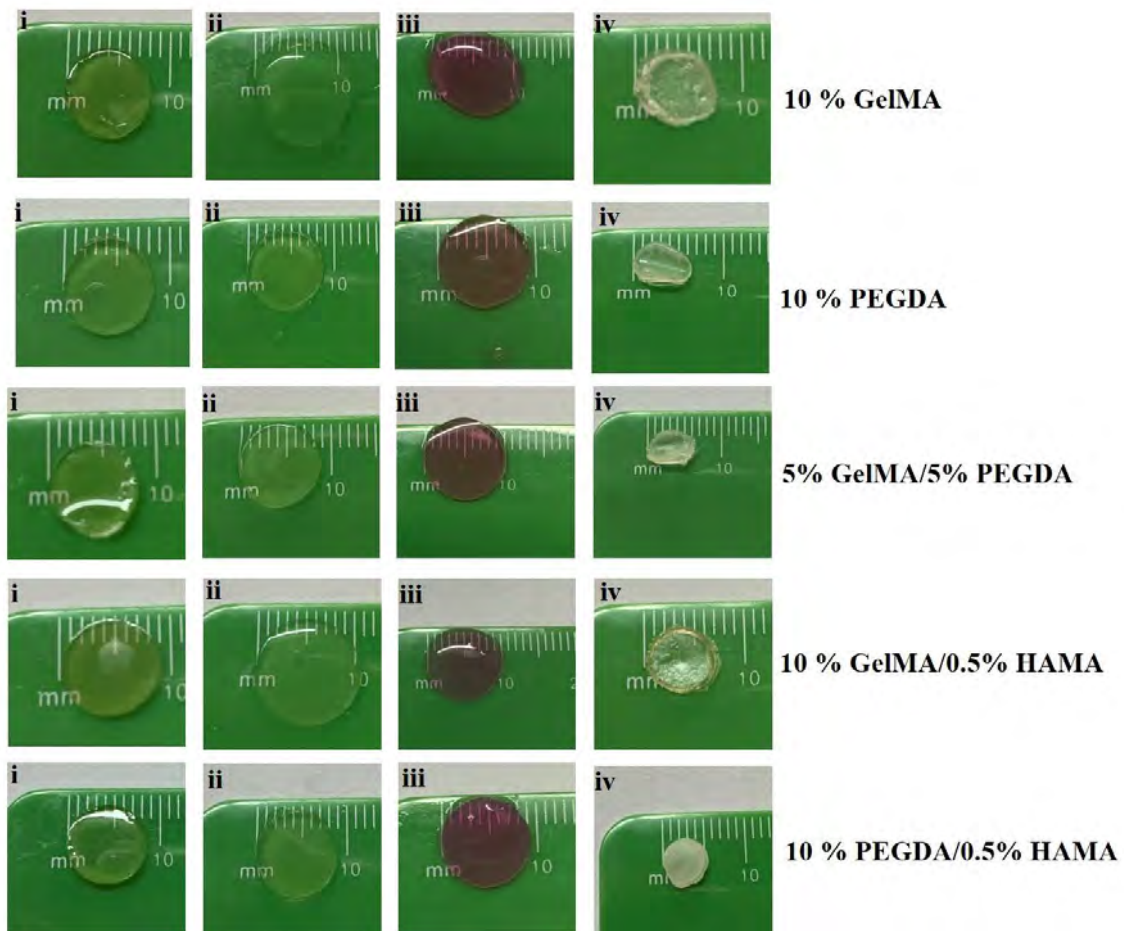


**Figure 16: Images of GelMA, PEGDA, GelMA/PEGDA, GelMA/HAMA and PEGDA/HAMA hydrogels before swelling (i), after swelling in DPBS (ii), in DMEM (iii) and freeze-dried (iv). Images are representative of  $n = 3$ . All images were taken using an iPhone XS Max.**

From the images taken in Figure 16 displaying the surface area displacement resulting from the swelling of 24-hours, all hydrogel types except the 10 % PEGDA hydrogel disk increased in surface area as a result of swelling in DPBS. The 10 % PEGDA disk surface area did however increase when exposed to DMEM for 24-hours. All other hydrogels disks resulted in having a greater surface area when exposed to DMEM when compared to DPBS. These findings correlate with the swelling ratio (%) in Figure 15 where disks submerged in excess DMEM obtained a greater swelling ratio (%) than those exposed to DPBS. The freeze-dried hydrogel disks resulted in a decrease in surface area, which was to be expected.

Having high swelling ratios (%) is a desirable trait for a hydrogel polymer. The swelling ratio allows for increase water absorption, creating more highly porous networks due to polymer expansion as a result of increased water absorption. It is therefore assumed that the increased water absorption expanded the pores within the polymer network resulting in a highly porous polymer however analysis using SEM or AFM before and after swelling followed by natural dehydration allowing the hydrogel disk to retain its shape should be performed to test proof of the assumption. This increase in porosity allows for more effective nutrient diffusion, biomolecules, oxygen and allowing the exchange of toxins and metabolites away from the cells. Porosity of hydrogels also affects cell infiltration, cell growth, cellular expansion and interconnectivity. The challenge faced with swelling is to ensure the major changes occur with the network stretching of the polymer i.e. the increase in porosity of the hydrogel with no additional triggers, which can affect the mechanical strength of the hydrogel (Spicer, 2020; Wu, Pang and Liu, 2020).

Figure 15 shows that the 10 % GelMA had the highest swelling ratio (1260 %) of all hydrogel types, however with also had the greatest standard deviation. The swelling ratio of 10 % GelMA is different to a study done by Fanucci, 2017 however in that study a 4 % GelMA hydrogel was tested. In another study done by Y. Wang *et al.*, 2018, a high swelling ratio resulted in a 10 % GelMA hydrogel and in comparison to other GelMA compositions tested, the 10 % GelMA hydrogel had the highest swelling ratio. Zhao *et al.*, 2016 found 5-20 % GelMA hydrogels to have swelling ratios between 500-1500 %, similarly corresponding to the results found in this study and could therefore be contributed to gelatin's hydrophilic characteristic. The large standard deviation experienced with the 10 % GelMA in this study does present a problem as it lacks in consistency and therefore making consistent swelling ratio unreliable. This constant change in swelling ratio will result in different degrees of hydrogel porosity within the 10 % GelMA hydrogel thereby resulting in a constant change in nutrient diffusion, cellular infiltration, growth and interconnectivity between assays. The PEGDA and PEGDA integrated hydrogels showed the most consistency of standard deviation of swelling ratios, as well as the lowest standard deviations of all hydrogel types, indicating that the use of PEGDA or addition of PEGDA in a hydrogel is able to stabilise and reproduce the same swelling effect time again. Similar swelling ratio trends of PEGDA hydrogel were found in a study done by Zustiak and Leach, 2010. Although the swelling ratio is not as significant than the 10 % GelMA hydrogel, a moderate amount of swelling did occur, thereby increasing the porosity of the hydrogels allowing for nutrient diffusion, cell infiltration, growth and interconnectivity to occur. The addition of PEGDA to GelMA decreased the swelling ratio thereby decreasing the porosity of the hydrogels however the SD was significantly lower than the GelMA hydrogel. This could also be the result that 5 % of GelMA was used instead of 10 %. The addition of PEGDA to GelMA also allows for more mechanical strength and uniformity, which can be seen with the images in Figure 16. The surface area difference before and after swelling between the PEGDA, GelMA and GelMA/PEGDA hydrogels are different where it shows that the addition of

PEGDA in a hydrogel aids in creating uniformity and stability in the change of the hydrogel. Uniformity and stable swelling can be seen as beneficial for tissue engineering. Using the hydrogel scaffold within the body only gives limited space and can be disadvantageous if the surface area of the hydrogel increases significantly which can lead to adverse effects when placed in the body. The addition of HAMA to the hydrogels significantly reduced the swelling ratio compared to the GelMA and PEGDA hydrogels. Similar results were observed by Camci-Unal *et al.*, 2013 where the addition of 1 % HAMA to GelMA caused a significant decrease to the swelling ratio. They state that the results were expected as increase in polymer concentrations allows for higher crosslinking densities, creating smaller pores and allowing less water in thus causing reduction in swelling ratios. This decrease in swelling ratio shows the addition of HAMA in a hydrogel acts in a similar way to the PEGDA creating a denser polymer and thus retains the structural integrity and strength of the hydrogel while still allowing swelling to occur allowing nutrient diffusion and cell infiltration. The use of two separate polymers to create an IPN or semi-IPN allows for increased mechanical strength and structure while still allowing for the intake of water and nutrient diffusion, all of which are desirable traits for tissue engineering and thus shows the advantages of using IPN or semi-IPNs as 3D cellular scaffolds. The increase mechanical strength and structure of the IPN or semi-IPN gives a further favourable trait towards aim of a 3D scaffold for articular cartilage. One factor of the articular cartilage is the requirement for high mechanical strength and support to be able to withstand load bearing pressure exerted by the joint movement.

A degradation rate analysis was performed to test the degradation rate ability of the five formulated hydrogel types. Hydrogel disks were submerged in ranging concentrations (M) of Tri-sodium citrate and rate of degradation by loss of mass of the hydrogel disks measured hourly with a final recording after 24-hours. The results of hydrogel degradation are presented in Figures 17 and 18.

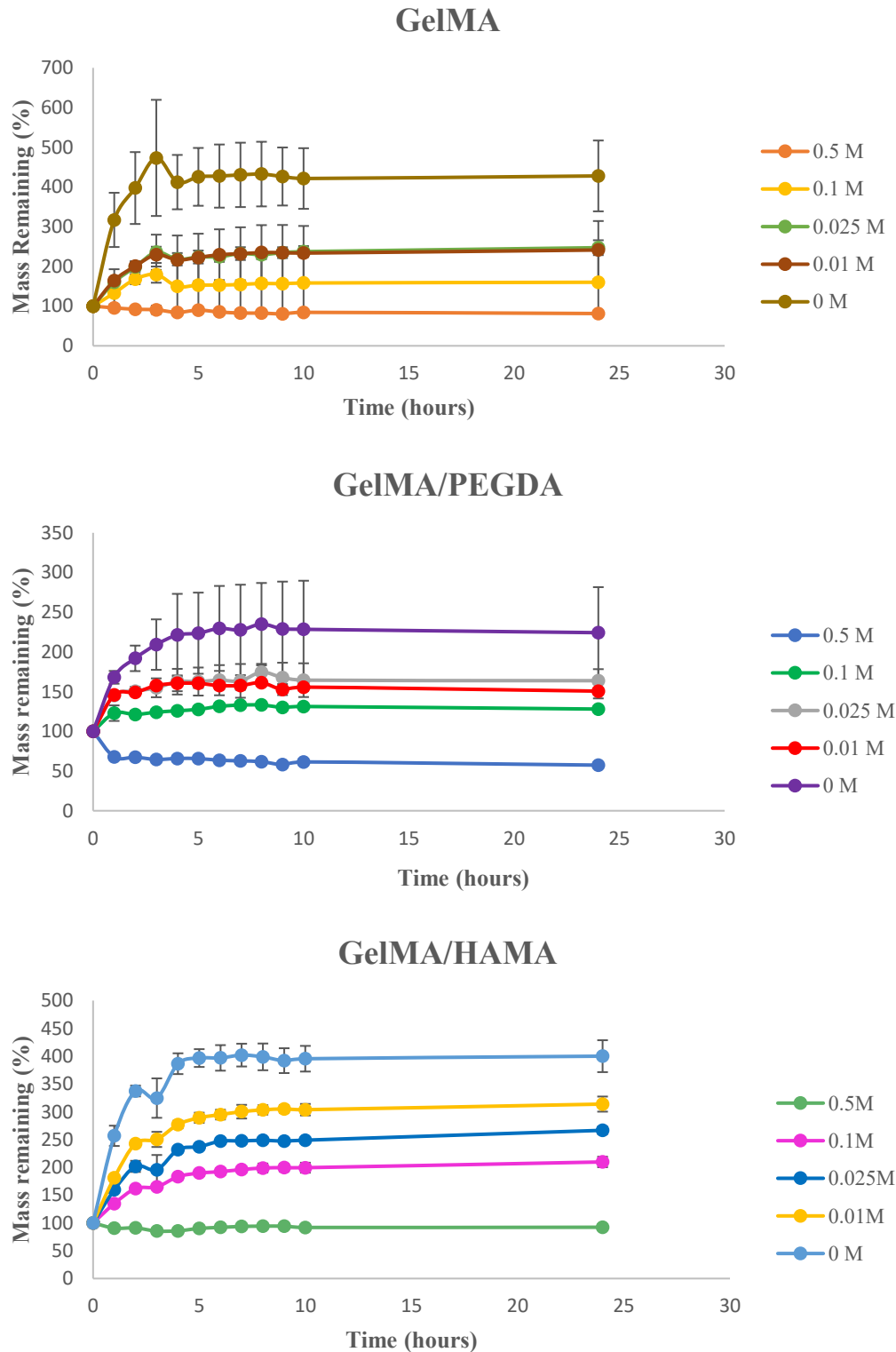


**Figure 17: Degradation rate of cross-linked 10 % GelMA 5 % GelMA and 5 % PEGDA and 10 % GelMA and 0.5 % HAMA hydrogels exposed to ranging concentrations of Tri-sodium citrate solution (M, pH 7.5).** Hydrogel disks were exposed to varying concentrations of Tri-sodium citrate for a period of 24-hours. The legend on the right of the graphs shows the concentrations tested; the 0 M solution consisted of ddH<sub>2</sub>O which was used in place of Tri-sodium citrate and therefore acts as the negative control. Error bars represent standard deviation where each bar represents N = 9 and each batch experiment had n = 3.

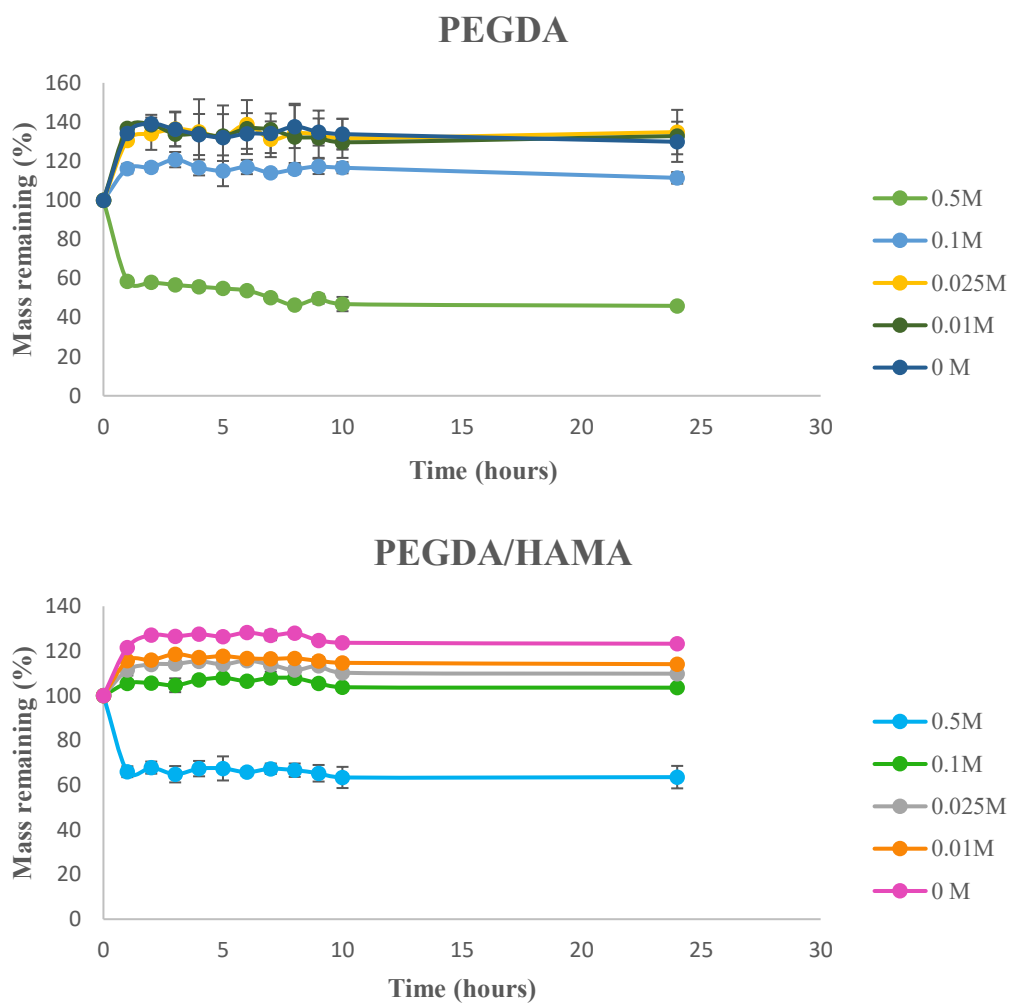


**Figure 18: Degradation rate of crosslinked 10 % PEGDA and 10 % PEGDA and 0.5 % HAMA (E) exposed to ranging concentrations of Tri-sodium citrate solution (M, pH 7.5).** Hydrogel disks were exposed to varying concentrations of Tri-sodium citrate for a period of 24-hours. The legend on the right of the graphs shows the concentrations tested; the 0 M solution consisted of ddH<sub>2</sub>O, which was used in place of Tri-sodium citrate and therefore acts as the negative control. Error bars represent standard deviation where each bar represents N = 9 and each batch experiment had n = 3.

The degradation profiles showed a similar trend across all five hydrogel types. When exposed to excess 0.5 M Tri-Sodium Citrate, all hydrogels had an initial decrease in mass in the first hour. The 10 % PEGDA and 10 % PEGDA + 0.5 % HAMA hydrogel disks showed the greatest decrease in mass from 100 to 59 % and 100 to 66 % mass (%) remaining respectively. The 10 % GelMA and 10 % GelMA + 0.5 % HAMA showed the least amount of degradation in the first hour of 100 to 96 % and 100 to 91 % mass remaining. From 1-hour onwards to 24-hours, no significant degradation occurred between hydrogel types as the curve began to plateau. After 24-hours, the 10 % PEGDA hydrogel disk showed the greatest degradation with a mass remaining of 46 % following by 5 % GelMA + 5 % PEGDA with a remaining mass of 58 % and 10 % GelMA of 81 % mass remaining. The 10 % PEGDA + 0.5 % HAMA hydrogel decreased slightly with a mass remaining of 64 %. The 10 % GelMA + 0.5 % HAMA was the only hydrogel that increased in mass from 91 to 92 %. In addition, the mass loss was measured by scale for each of the polymerised hydrogel disks. During the 1<sup>st</sup> hour of the degradation assay, discolouration of the hydrogel disks and small bits of the gel disk began to break off when exposed to the 0.5 M Tri-Sodium Citrate solution, whereas with the polymerised hydrogel disks exposed to 0.1 M Tri-Sodium citrate solution, the hydrogel disks mostly remained intact.

The general trend for Tri-Sodium Citrate concentrations 0 – 0.1 M showed an increase in hydrogel mass as the Tri-Sodium Citrate concentration became less. These degradation results show that all hydrogel types are to degrade with the use a strong chelator such as Tri-Sodium Citrate, which is able to chelate metal ions from the hydrogel scaffold (Wu *et al.*, 2016) at a concentration of 0.5 M or higher. Synthetic hydrogels such as PEGDA lack the relative functional groups, hydrolytic and enzymatic degradation sites to degrade, using different molecular weights or end-functionalised PEG derivatives with acylate have allowed the degradable crosslinkers in the final PEG hydrogel network allowing PEGDA to degrade with the right physiological relevant environments (Hill, Sell and Zustiak, 2017). The PEGDA used in this assay is paired with diacrylate and has a molecular mass of 700 kDa enabling it to degrade over time with under the right physiological conditions. This corresponds to the results obtained for the PEGDA hydrogel and PEGDA incorporated hydrogel. In study done by Chen *et al.*, 2018, a decrease in PEGDA hydrogel mass had decrease 48 % within the first 24-hours and after 48-hours it had decrease 56 %. This decrease in masses also shown with the PEGDA hydrogel in this study. In study done by Camci-unal *et al.*, 2013, a hybrid hydrogel of GelMA and HAMA was formulated, the degradation analysis showed a decrease of 40 % with a 10 % GelMA hydrogel however when integrated with 1-2 % HAMA to 78 and 82 % respectively. The main difference in GelMA degradation is due to the collagenase enzyme used by Camci-unal *et al.*, 2013, which actively degrades collagen, a main constituent of GelMA, where in this study, Tri-Sodium citrate was used. The use of collagenase, hyaluronidase or ester hydrolysis (targeting the ester backbones of PEGDA) will give a more representative result of the degradation of GelMA and the effective of degradation when coupled with other polymers such as PEG or HAMA. As it is specifically targeted to collagen, hyaluronic acid and

PEGDA the degradation of the resultant mass loss will be due to the degraded gelatin, hyaluronic acid or PEGDA and not potential water loss from the hypertonic solution.

The use of hybrid hydrogels, using HAMA and PEGDA, HAMA and GelMA and PEGDA and GelMA to create IPN and semi-IPNs is still a very novel idea with little research on the characterisation and advantages these IPNs and semi-IPNs could have towards cellular scaffolds for tissue engineering. No studies on the degradation rate of 10 % PEGDA + 0.5 % HAMA could be found to be used as a comparison for the degradation assay. Studies performed by Camci-unal *et al.*, 2013 and Chen *et al.*, 2018, however show the degradation of GelMA. Based on these studies, significant reduction in mass loss when integrated with HAMA was observed. With the mass loss observed with the PEGDA and GelMA hydrogels in studies done by Chen *et al.*, 2018 and Camci-unal *et al.*, 2013, it can be concluded that by integrating HAMA in hydrogel mixtures it considerably reduces the mass loss (%) over time for all hydrogels and thereby formulating hydrogel mixtures with HAMA has a positive effect on the longevity of the hydrogel, a desirable trait for a hydrogel in tissue engineering. In other studies done by Wu *et al.*, 2016 and Moeinzadeh and Jabbari, 2015 present degradation assays of hydrogels over weeks to months period to acquire a better representation on the expected degradation rate of the hydrogels *in vivo*. This long continuation period of degradation should be carried out in these hybrid hydrogels to give a better representation of *in vivo* degradation in the future. As Tri-Sodium citrate is a strong chelating agent of calcium ions, the use of it was not appropriate as used by Wu *et al.*, 2016 where the probable target of degradation would be the alginate included in GelMA. The breakoff of hydrogel disks and discolouration to a milky white colour is most likely due to the strong hypertonic trisodium citrate solution (0.1 M and 0.5 M), which was the main cause of mass loss as no mass loss was experienced for the lower concentrations.

The use of more specific enzymes and reagents such as hyaluronidase and collagenase as performed by Eslami *et al.*, 2014 would give a better representation of the degradation effects of each hydrogel as the enzymes are tailored to the type of hydrogels and hybrid hydrogels. Hydrolytic degradation or oxidative degradation as carried out by Browning *et al.*, 2014 targets the ester backbones of the PEGDA monomer increasing the degradation process of PEGDA and giving a more representative result of the degradation effect of PEGDA *in vivo*. The hyaluronidase and collagenase enzymes target the degradation of hyaluronic acid and collagen, the main constituents present the GelMA and HAMA hydrogels and would therefore provide a more intuitive representation on the degradation effects on the formulated hydrogels.

Hydrogel morphology analysis was performed using SEM analysis. The hydrogels were crosslinked and disks cut out. The hydrogels disks were dehydrated and dried for SEM analysis. Images were taken using the SEM (Tescan, Vega) each image representing  $n = 3$ . Pore sizes of the hydrogels were measured and calculated the actual size of pores based on the scale bar of each image.



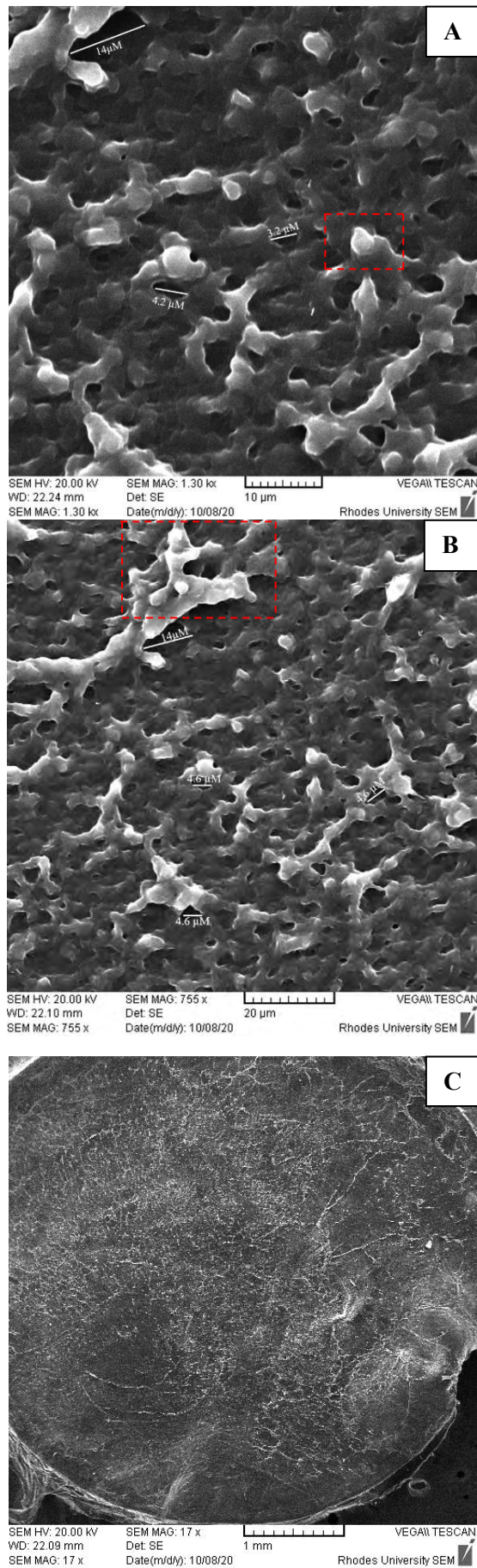


**Figure 19: Scanning Electron Microscopy images of 10 % GelMA hydrogel disk at 1.30 kx (A), 755 x (B) and 17 x (C) magnification.**

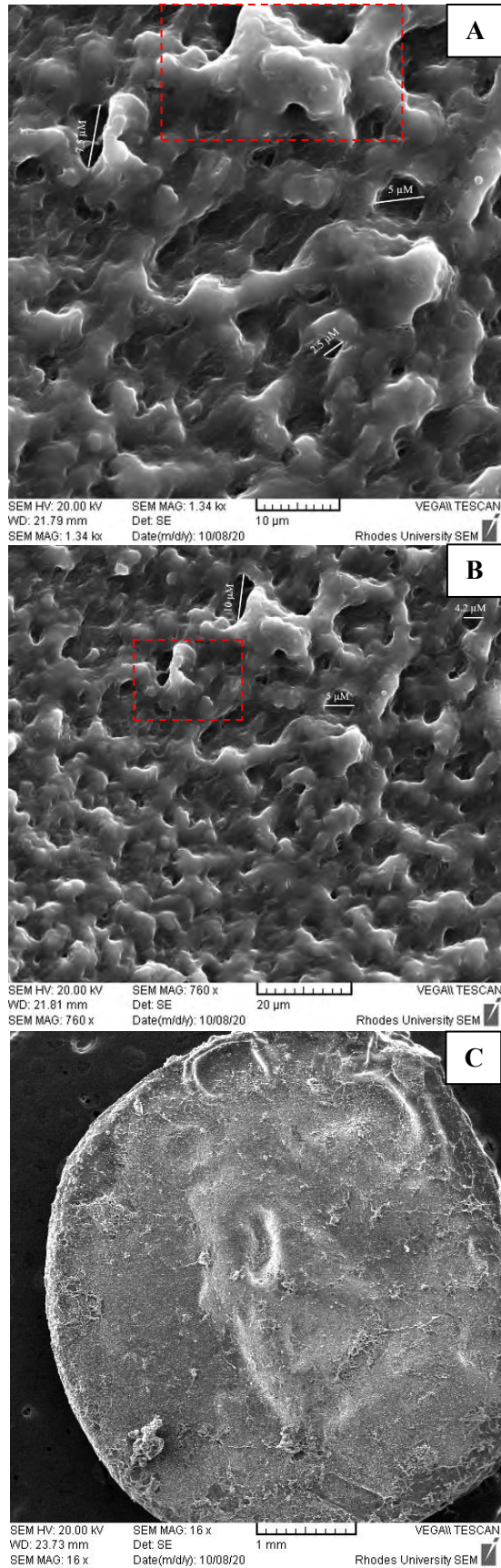


**Figure 20: SEM images of 10 % GelMA and 0.5 % HAMA hydrogel disk at 1.34 kx (A), 760 x (B) and 16 x (C) magnification.**

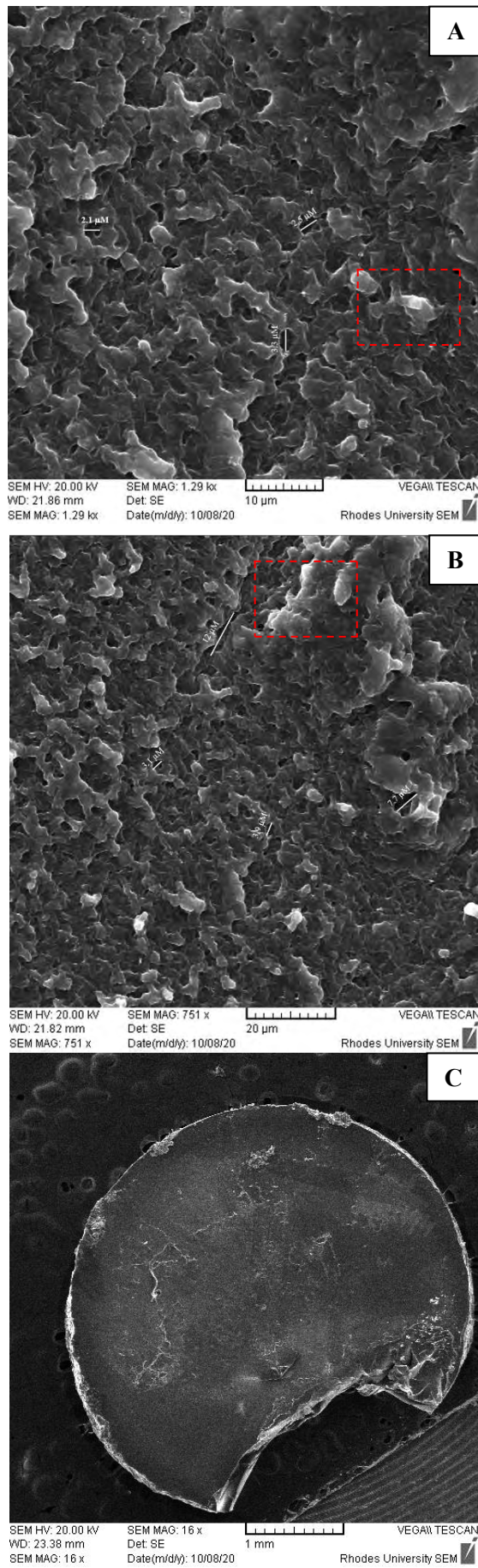


**Figure 21: SEM images 5 % GelMA and 5 % PEGDA hydrogel disk at 1.29 kx (A), 751 x (B) and 16 x (C) magnification.**



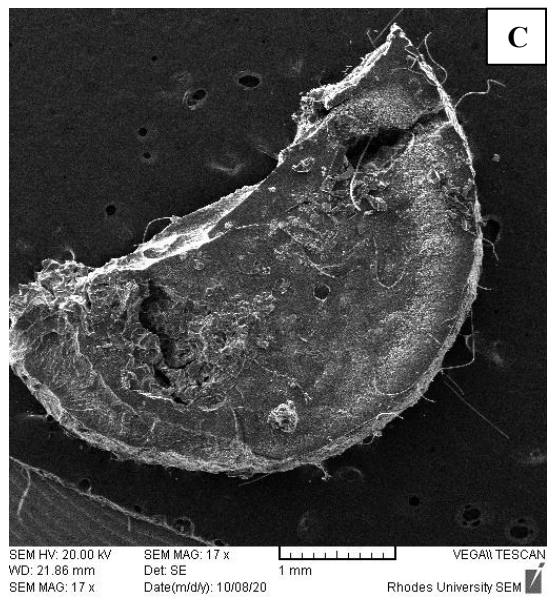
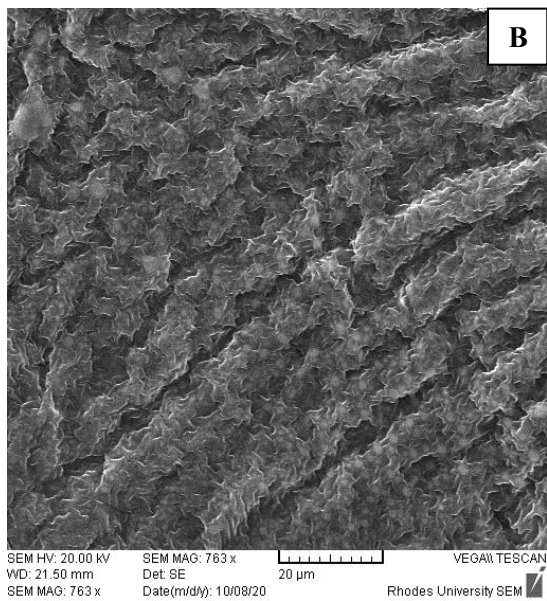
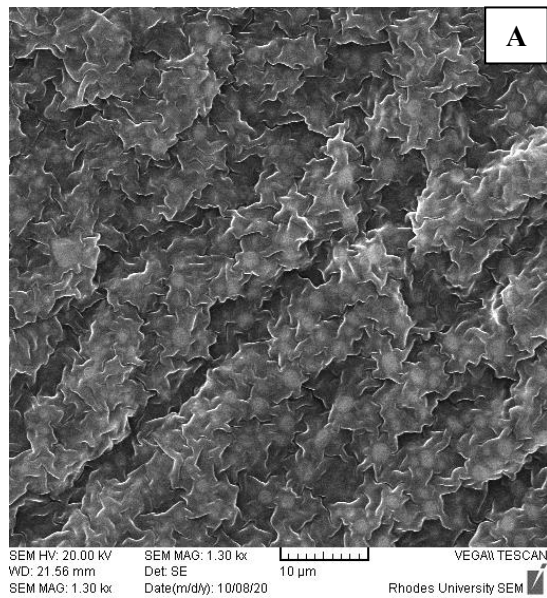


**Figure 22: SEM images of 10 % PEGDA hydrogel disk at 130 kx (A), 763 x (B) and 17 x (C) magnification.**

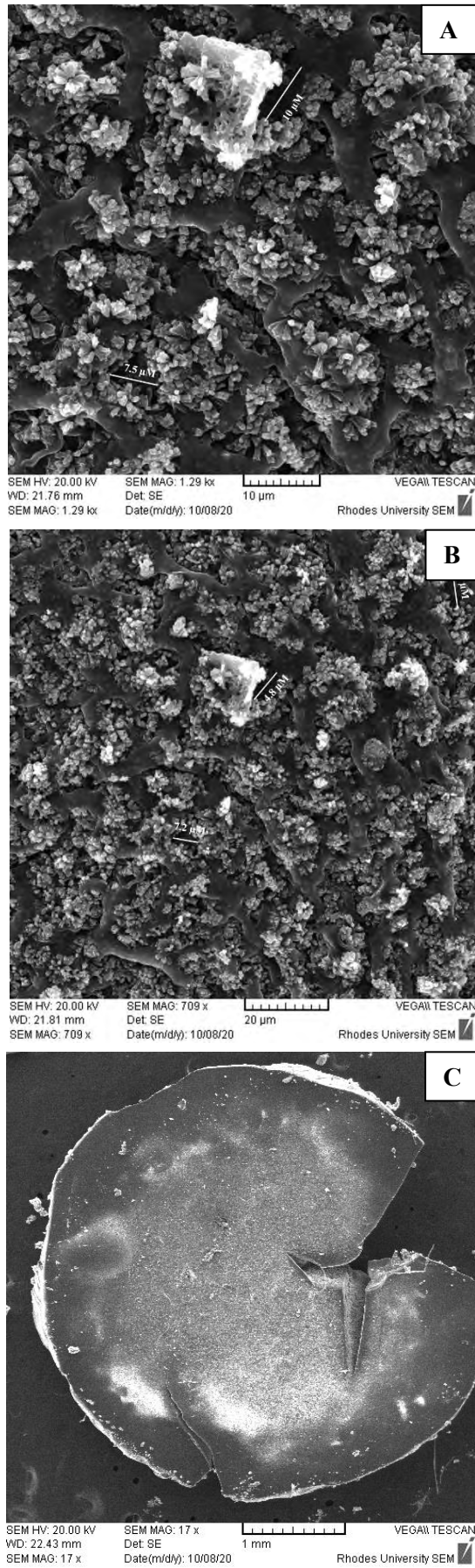


**Figure 23: SEM images of 10 % PEGDA and 0.5 % HAMA hydrogel disk at 1.29 kx (A), 709 x (B) and 17 x (C) magnification.**

Figures 19-23 show the SEM images of the formulated hydrogels, labelled with the pore sizes present within the hydrogel. Figure 19 shows the top surface and pores present in 10 % GelMA with the greatest pore size 14  $\mu\text{m}$  and the smallest of 3.2  $\mu\text{m}$ . In figure 20, hydrogel hybrid 10 % GelMA + 0.5 % HAMA showed the greatest pore size of 10  $\mu\text{m}$  and smallest of 2.5  $\mu\text{m}$ . Figure 21, hydrogel hybrid 5 % GelMA + 5 % PEGDA showed the greatest pore size of 12  $\mu\text{m}$  and the smallest of 2.1  $\mu\text{m}$ . Figure 22, hydrogel 10 % PEGDA showed no pores present on the surface of the hydrogel disk. Figure 23, hydrogel 10 % PEGDA + 0.5 % HAMA showed the biggest pore size of 10  $\mu\text{m}$  and smallest of 4.8  $\mu\text{m}$ . In general, for all hydrogel types, there were on average 4-5 pores present as seen in the images on the surface of each hydrogel type with exception to 10 % PEGDA. The measurement of the pore size is a notable characteristic to determine if cells would be able to infiltrate into the hydrogel. The size of mammalian cells average between 10 and 100  $\mu\text{m}$  depending on the cell type (Guertin and Sabatini, 2006). The cell size of interest for this study were HeLa and ad-MSCs, which have average sizes of 15 – 45  $\mu\text{m}$  (Romeo *et al.*, 2004) and 15 – 30  $\mu\text{m}$  depending on their culturing conditions (Krueger *et al.*, 2018). Based on the average cell sizes of HeLa and ad-MSCs and the pore sizes obtained from the formulated hydrogels, the pores in the hydrogels are too small to allow for cell infiltration and will most likely result in the cells remaining on the surface of the hydrogel. In studies done using GelMA, GelMA + PEGDA, HAMA and PEGDA/HAMA, SEM analysis was performed on the morphology of the porosity in the hydrogels. Y. Wang *et al.*, 2018 and Wang *et al.*, 2020 both obtained porosity sizes with an average pore size 34 – 42  $\mu\text{m}$  in both studies. Chen *et al.*, 2021 reported having pore sizes in their HAMA hydrogel of up to 200  $\mu\text{m}$ , Kim and Cha, 2018 observed significant pore sizes ranging from 78 – 111  $\mu\text{m}$  with 10 % PEGDA/5 % HAMA hydrogel while Seale *et al.*, 2018 showed low porosity in the 10 % PEGDA/2 % PEGMA hydrogel with pore sizes ranging from 4 – 44  $\mu\text{m}$ . Although the diameter of the pores is considerably lower than the hydrogels observed in Chen *et al.*, 2021 and Kim and Cha, 2018 the largest pores are still large enough to allow for potential cell infiltration. The evidence from these papers suggests the incorporation of additional polymers such HAMA increases the porosity of the PEGDA polymer, a trend observed in the SEM images where the PEGDA hydrogel showed no pores however when incorporated with additional polymers can result in the increase in porosity as seen with the PEGDA/HAMA and GelMA/HAMA hydrogels.

Influences of the porosity of hydrogels are mainly the polymerisation time and percentage of polymer used to make up the hydrogel. Types of photoinitiator used to polymerise the hydrogels may play a role as they affect the rate of polymerisation but no evidence in studies suggests the type of photoinitiator to have a considerable effect on the porosity of hydrogel scaffolds. Differences in porosity between these hydrogel scaffolds and the ones mentioned, differ in the percentage of polymer used and polymerisation times. However Kim and Cha, 2018, Y. Wang *et al.*, 2018 and Wang *et al.*, 2020 did use the same polymer percentage for GelMA and PEGDA as the hydrogels tested in this study. Chen *et al.*, 2021 however used a higher percentage of 3 % HAMA and resulted in the highest porosity

percentage compared to all other studies. Kim and Cha, 2018 did use a 5 % HAMA however it was incorporated into a 10 % PEGDA based gel. The addition of PEGDA therefore seems to reduce the porosity of HAMA hydrogels within an optimal range for cell infiltration. A possible reason for the low porosity of these hydrogels could be due to the dehydration via ethanol, which they were exposed to. During the dehydration process, once the hydrogels were exposed to 80 % and higher, protein precipitation started to occur out of the hydrogels and become smeared on the surface of the hydrogels thus covering pores located on the surface of the hydrogel. This extrusion of protein can be seen in the SEM as the bright white bumps occurring on the surface of the hydrogels seen in the red dotted outlines in Figures 19-21 A & B. Ethanol of 80 – 100 % is known to cause mass precipitation of proteins and thus is most likely the result of this. In order to determine the true porosity of the formulated hydrogels, a cross-section of the disk could be done, exposing the internal and unaffected porosity of the hydrogel disks however damage to the pores could occur. Using an X-ray microtomography gives cross-sections of physical objects using x-rays, avoiding any physical damage done to the pores (Rennie *et al.*, 2014; Guntoro *et al.*, 2019). Different dehydration methods could be done to avoid using ethanol causing the precipitation of protein. Freeze-drying is a possible solution to dehydrate the hydrogel disk as Y. Wang *et al.*, 2018 and Wang *et al.*, 2020 performed freeze-drying and obtained excellent morphology of the porosity of their hydrogels, alternatively the hydrogels disks could be left uncovered for 24-hours allowing for natural dehydration of the hydrogel disk to take place within the petri dishes.

The results presented for the characterisation of the formulated hydrogels as 3D scaffolds for tissue engineering show that all hydrogel types have the ability to swell thus allowing an increase in porosity, nutrient diffusion, metabolite exchange and cellular growth and interconnectivity. The addition of PEGDA and HAMA to the GelMA positively impacted the integrity of the hydrogel disk once swollen. Hydrogels GelMA + PEGDA and GelMA + HAMA and PEGDA showed the best swelling ratio (%) while still retaining their structural integrity. The degradation rate of the formulated hydrogels showed that the hydrogels are able to degrade when exposed to 0.5 M of Tri-sodium citrate however use of more tailored enzymes such as hyaluronidase and collagenase would provide a better representation of the degradation rates for the formulated hydrogels. In addition to this, the length of degradation should be extended over several weeks rather than hourly to 24-hours to give a more accurate representation of degradation of the formulated hydrogels when exposed to enzymes targeted to polymers present within the hydrogel. SEM analysis showed the presence of pores on the surface of all hydrogel types except for PEGDA. The pore sizes of the hydrogels are too small to allow for any cellular infiltration of HeLa or ad-MSC cells. Protein precipitation due to dehydration via ethanol may have caused a decrease in visual porosity as the precipitated protein covered the surface of the hydrogel disks and thus covering pores present on the surface of the hydrogel disks. Polymerisation times could be shortened to increase the porosity of the gels. The surface of the hydrogel disks however did show a potential for good cell adhesion. Based on the SEM images GelMA + PEGDA, GelMA + HAMA and PEGDA and

HAMA showed the greatest potential for cellular infiltration and adhesion, as well as for nutrient diffusion and metabolite exchange. Given that a visible light photoinitiator was used, crosslinking using visible light to encapsulate the cells could be done in an aseptic environment however crosslinking times would increase due to the lower energy output of the visible light wavelengths compared to the high energy output of UV light. The use of visible light and subsequent cell encapsulation would eliminate the need for cell adhesion and cell infiltration due to the use of visible lights as appose to UV light, which is has a cytotoxic effect.



## Chapter 4: Hydrogel and Chondrogenic differentiation

### Component Characterisation and Spectroscopic Analysis

#### 4.1 Introduction

The aim of developing a 3D scaffold for tissue engineering is to replicate the *in vivo* microenvironment of the target tissue. Tissues and organs are dynamic structures consisting of an extracellular matrix and a range of signalling molecules playing a crucial role of the cellular microenvironment. The ECM acts, as a link between the microenvironment and the cells, transmitting mechanical and biochemical signals which affect cell behaviour (Tamay *et al.*, 2019). Three-dimensional printing is a type of additive manufacturing technology, which layers and overlaps materials onto each other to create the final 3D structure with desired properties and well-controlled architecture and spatial chemistry (Tamay *et al.*, 2019; Sinha, 2020). Additive manufacturing of tissue scaffold engineering has various 3D bioprinting methods such as extrusion based bioprinting, Laser-assisted bioprinting, inkjet bioprinting and stereolithography (SLA) bioprinting each of which have different methods to print the structure (Tamay *et al.*, 2019; Sinha, 2020).

Stereolithography bioprinting has shown much interest for bioprinting of 3D scaffolds due to the significant decrease in printing times compared to other printing technologies. It also allows for high resolution accuracy of up to 20  $\mu\text{m}$  of the external geometry and internal architecture of the scaffold, which can be controlled using the light source of the printer (Tamay *et al.*, 2019). In order for the light source to polymerize the bioink and create the necessary layers for the construct, photoinitiators need to be added to the bioink to initiate the polymerization. Several different types of photoinitiators such as IC2959 or Eosin-Y can be used either using UV light or visible light. With the damaging effects of UV light on cells, visible light photoinitiators show more promise for cell encapsulation in the scaffold. The aim of the scaffold as mentioned above is to create an ECM microenvironment for tissue generation. This required the components of the cell scaffold not to have any cytotoxic effect on the cells seeded on or encapsulated within the scaffold. The choice of bioink is chosen to promote cellular adhesion, proliferation and differentiation of the cell types however the photoinitiators are additives of the scaffold and therefore one should determine if they have any negatives effects of cell viability of growth and if so at what concentrations would they start to affect the cells. The visible light photoinitiator Eosin Y is a type II photoinitiator requiring a co-initiator (triethanol amine) and accelerant species (N-vinylpyrrolidone) to initiate sufficient polymerization. All three need to be added to the bioink for polymerization and printing of the scaffold to occur. The cytotoxic effects of the individual components of the visible light photoinitiator therefore need to be determined.

Eosin Y is a xanthene dye photosensitizer and initiates polymerization when paired with the co-initiator triethanol amine (TEA). When exposed to visible light, the eosin molecule excites to the triplet state, abstracting hydrogen from TEA, yielding a protonated eosin radical and a protonated TEA radical. The eosin Y visible light system has been used for the initiation of bulk gelation of tissue engineering cell-laden scaffolds with reports of high cell viability (Matsumura *et al.*, 2008; Lilly *et al.*, 2018). Although eosin Y and TEA are able to polymerize hydrogel scaffolds, the addition of N-vinylpyrrolidone (NVP) aids to counteract the inhibitory effect of oxygen, which can occur during the polymerization of hydrogel scaffolds (Aguirre-Soto *et al.*, 2019). NVP acts as a comonomer for the eosin-mediated synthesis of hydrogels. In addition to the comonomer aiding in the reduction of oxygen inhibition, NVP also contributes to enhancing the rate of radical polymerization and final conversion (Kizilel, Pérez-Luna and Teymour, 2004; Aguirre-Soto *et al.*, 2019). Although studies mentioned by Z. Wang *et al.*, 2018 have revealed that the visible light photoinitiator system of Eosin-Y, NVP and TEA have less cytotoxic effects on cell viability the principle of other photoinitiators in which the concentration of photoinitiator directly influences the cell viability however does still apply to the visible light photoinitiator system. (Z. Wang *et al.*, 2018).

Part of the 3D scaffold design to engineering specific tissues types is choosing the bioinks to support the generation of the target tissue. The combination of stem cell and 3D scaffolds allows various combinations of tissue to be creating. Adipose-mesenchymal stem cells are multipotent cells that have the ability to differentiate in various tissue types such as fat, bone and cartilage tissues. However, in order to direct and initiate the differentiation, specific supplements are required. Since focus of this study is on the generation of articular cartilage within a 3D scaffold, chondrogenic differentiation supplements are required to initiate and maintain chondrogenic differentiation of the ad-MSC. To direct chondrogenic differentiation the supplements required include ascorbic acid, dexamethasone, TGF- $\beta$ 3 and L-Proline. Although these supplements are needed to chondrogenic differentiation and proliferation using excessive concentrations could have adverse effects on the cell viability and proliferation. It is therefore important to determine the inhibitory effect on cell viability of each supplement to determine the concentration threshold of each supplement. Knowing the cytotoxic effect of each supplement gives valuable knowledge when performing cellular differential within the scaffold as if the cell viability decreases and differentiation does not occur, the results show that the supplements do not have an effect on the decreased cell viability and therefore evidence suggests that the fault lies with the biomaterial scaffold.

Ascorbic acid is characterized as an antioxidant, neutralizing free-radicals, reducing oxidative stress and acts as an essential cofactor in many enzymatic and metabolic reactions (Mamede *et al.*, 2012; Roberts *et al.*, 2015). It is directly related to cellular proliferation and differentiation and a molecule aiding in the suppression of aging (Fujisawa *et al.*, 2018). However at high concentrations and specifically targeted towards cancer cells such as HeLa cells, it causes the induction of apoptosis

through generating reactive oxygen species (ROS) hydrogen peroxide (Roberts *et al.*, 2015). In other cell types as ad-MSC, higher ascorbic acid concentrations can be used. However at higher concentrations, ROS increases leading to an increase of hydrogen peroxide production, which can inhibit glyceraldehydes-phosphate dehydrogenase (GAPDH). Ultimately to a decrease of cell viability therefore care must be taken to the concentration of ascorbic acid used (Markmee, Aungsuchawan and Pothacharoen, 2019).

Dexamethasone is a synthetic steroid belonging to the glucocorticoid class of steroid drugs functioning as an anti-inflammatory and immunosuppressant (Wang *et al.*, 2012). It is widely used for adipogenic, chondrogenic and osteogenic differentiation, aiding in the enhancing and regulation of differentiation and proliferation of stem cells (Dentistry and Hospital, 1986; Wang *et al.*, 2012). It is also routinely used in chemotherapy at various doses to reduce toxicity and protect normal tissue of patients against long-term effects of genotoxic drugs. It is additionally used towards inflammatory disorders such as asthma, dermatitis, rheumatoid arthritis and other autoimmune diseases (Mattern *et al.*, 2007; Buxant *et al.*, 2015). Although dexamethasone has beneficiary effects against cancerous and stem cell lines, high concentrations have shown to suppress proliferation of HMSC without affecting differentiation, cause differentiation shifts from osteogenic to adipogenic cells lines and have negative effects on cell viability (Xiao *et al.*, 2010; Nuzzi *et al.*, 2012).

Transforming growth factor 3 (TGF- $\beta$ 3) forms part of the TGF- $\beta$  family consisting of TGF- $\beta$ 1 and 2 of the bone morphology proteins (BMPs), inhibins and actins. They play key roles in tissue morphology and development, as well as principal roles in normal tissue remodelling and adaptation in adults (Popovic and Wilson, 2010). Aside from being a versatile cytokine having multiple effects on cell behaviour such as proliferation, invasion, immune responsiveness, migration and angiogenesis (Seystahl *et al.*, 2017), both TGF- $\beta$ 1 and 3 have shown to play vital roles in endochondral ossification regulation and promoting chondrogenic differentiation of mesenchymal stem cells and embryonic chondrocytes (Pfeifer *et al.*, 2019). Both TGF- $\beta$ 1 and 3 are routinely used for chondrogenic differentiation with TGF- $\beta$ 3 becoming more routinely used due to its ability to enhance chondrogenesis, specifically enhancing GAG content, type II collagen (70 % of total collagen) and possess a physiologic Youngs Modulus (Ng *et al.*, 2008) in MSC and articular chondrocytes (ACs), as well as been abundant in the collagen matrix of cartilage (Dahlin *et al.*, 2014; Huang, Schor and Hinck, 2014; Wang, Rigueur and Lyons, 2014).

L-Proline/Proline is a nonessential, multifunctional amino acid having essential roles primary metabolism and physiological functions such as bioenergies, apoptosis and cellular redox control (Cappelletti *et al.*, 2018). Proline plays a key role in cellular differentiation and is found in high concentrations in collagen, consisting of one-third of amino acids of collagen proteins (Wu *et al.*, 2011). Numerous studies show no indication that L-Proline is cytotoxic, as well as many other amino acids

(AA) towards mammalian cells, the studies in fact, like TGF- $\beta$  target the inhibition of these as potential treatments to various cancers (Liu *et al.*, 2019; D’Aniello *et al.*, 2020).

Three-dimensional scaffolds are made up of polymers of which the chemical structure is known. However, with natural polymers such as gelatin, the major disadvantage is that it only gels/solidifies at low temperature temperatures at which cells would not be able to survive. At temperatures of 37 °C or higher gelatin enters a liquid state and is unable to retain its structural integrity. Modification of the polymer needs to be done to allow it to polymerize and retain its structural integrity at the required temperatures and different uses. To help determine the extent of modification chemical analysis of the bioink can be performed using Attenuated Total Reflectance-Fourier Transform Infrared Spectroscopy.

Attenuated Total Reflectance-Fourier Transform Infrared Spectroscopy (ATR-FTIR) is a useful tool for the quantification and qualification of organic substances in liquid, solid or gas state. The use of ATR-FTIR of solids and liquids allows for minimal preparation to measure samples and allowing for easy sample recovery after use (Kazarian and Chan, 2006; Melucci *et al.*, 2019). IR spectroscopy uses the infrared part of the electromagnetic spectrum measuring the absorbance of the IR frequencies given out by the sample in the path of the IR beam. It is a well-used method for the characterization of the chemical structures of samples and molecules (Kazarian and Chan, 2006; Sun, 2010). The main drawbacks of ATR-FTIR is the spectral overlapping that occurs of the signals of the analytes and possible contaminants in the sample (Javidnia *et al.*, 2013). A factor to consider is that the thickness of the sample has an impact on the penetration depth of the IR light in the sample and thus can be considered as a drawback for biological samples (Kazarian and Chan, 2006). Proton Nuclear Magnetic Resonance ( $^1\text{H}$  NMR) is another type of spectroscopy technique commonly used besides ATR-FTIR for the characterization of the chemical structures of molecules and samples (Osmani *et al.*, 2008).

**Aim:**

- To determine the cytotoxicity of the photoinitiator and chondrogenic differentiation components, chemical composition of hydrogel mixtures and printability of hydrogel bioink.

**The objectives include:**

1. Determine the IC50 values of the photoinitiators components and chondrogenic differentiation components using RTCA system.
2. Obtain the chemical composition of hydrogel mixtures using ATR-FTIR analysis.
3. Determine the 3D printing capability of the GelMA/PEGDA and PEGDA/HAMA hydrogel bioinks using a UV resin printer.

## **4.2 Methods and Materials**

### **4.2.1 Materials**

All solvents, media and reagents were purchased through Thermo Fisher Scientific and Sigma Aldrich unless otherwise stated. DMEM – high glucose (Thermo Fisher Cat. No. 10566016), Ca<sup>2+</sup>/Mg<sup>2+</sup> free Dulbecco's phosphate buffered saline (pH 7.4) (Thermo Fisher Cat. No. 10010001), Trypsin/EDTA 0.25 %, phenol red (Thermo Fisher Cat. No. 15050057). Eosin Y (Sigma Cat. No. E4009), TEA (Sigma Cat. No. T0886) and NVP (Sigma Cat. No. V3409), TGF-β3 (Sigma Cat. No. SRP3171), ascorbic acid (Sigma Cat. No. A4544), L-proline (Sigma Cat. No. P0380). All HeLa cells obtained and used were gifted from Dr Garth Abrahams, department of Microbiology, Rhodes University.

### **4.2.2 HeLa Cell Culture & Maintenance**

HeLa cell culturing was carried out by incubating the cells at 37 °C, 5 % CO<sub>2</sub> in a humidified atmosphere. All cell visualization was done using the Zeiss AxioVert.A1 FL-LED fluorescence microscope at 10 X magnification with phase 2 contrasting. Cells were initially cultured in 25cm<sup>3</sup> flask in DMEM – high glucose, 10 % FBS, 1 % Penicillin/Streptomycin until approximately 70 % confluent. Cells were split into two 75cm<sup>3</sup> flask once they had reached 70 % confluency in the 25cm<sup>3</sup> flask. The cells were split according to normal adherent cell culture protocols. Cell viability was determined when splitting the cells using a haemocytometer and counting the viable and non-viable cells where the non-viable cells stained blue as a result of the trypan blue. Cells were seeded at a cell density of 5000/cm<sup>2</sup> and once 70 % confluent, the cells were used for the cytotoxicity assay. Cell health was determined before each cell seeding. All cells used for the cytotoxicity assay were used between passage 143-145.

### **4.2.3 Real-Time Quantitative Cell analysis (RTCA) cytotoxicity assay**

HeLa cells were used to perform the cytotoxicity analysis of the visible light photoinitiator components Eosin Y, TEA and NVP and chondrogenic differentiation components TGF-β3, dexamethasone (dissolved in 100 % methanol), ascorbic acid, L-proline. DMEM was added to each and the 96-well E-Plate inserted into the RTCA machine to perform a background read. The background read consisted of 1 sweep at a 1 minute interval. Cells were then seeded into the wells at a density of 6000 cells/well. After seeding the plate was incubated at 37 °C, 5 % CO<sub>2</sub> for 24-hours to obtain a cell growth curve before induction of the photoinitiator components. The setup of the growth phase consisted of 49 sweeps at 30-minute intervals. After 24-hours, cell media in the wells was removed and the cells were induced with DMEM (high glucose), 10 % FBS, 1 % Penicillin/Streptomycin and the photoinitiator components at ranging concentrations, Eosin-Y (0.001 – 0.1 mM), TEA (0.01 – 1 %) and NVP (3.7 – 370 nM). After induction, the assay was run for additional 48-hours. The setup for the induction phase consisted of 49 sweeps at 30-minute intervals. The IC<sub>50</sub> graph was generated using the RTCA 1.2.1 software at time points 20-hours after induction. Each assay was repeated three times with each containing three

replicates for each visible light and chondrogenic differentiation component to give N = 6 and each batch experiment had n =2 for the visible light and N = 4 and each batch experiment had n =2 for the chondrogenic cytotoxicity assay. Cell index graphs of the visible light photoinitiator and chondrogenic differentiation components can be found in Figures S4-S7 in the appendix section.

#### **4.2.4 Attenuated total reflectance-Fourier transform infrared (ATR-FTIR) spectroscopy**

ATR-FTIR spectroscopy was performed on all formulated hydrogel mixtures in the absence of the photoinitiators Eosin Y, TEA and NVP and before cross-linking with UV light was done. The Perkin & Elmer 100 FTIR spectrometer was used to obtain the individual FTIR spectral readings, which were performed three times for each sample with the spectra width ranging from 4000 to 650  $\text{cm}^{-1}$ . SpectraGryph 1.2.14 software was used to analyse the spectra readings obtained with a prominence of 2 and threshold of 5.0 % for the unstacked and stacked ranging from 4000 – 650  $\text{cm}^{-1}$  and for the stacked ranging from 4000 – 900  $\text{cm}^{-1}$  a prominence of 3 and threshold of 5.0 % was used.

#### **4.2.5 Three-dimensional printing of formulated hydrogels GelMA + PEGDA and PEGDA + HAMA**

Three-dimensional printing of hydrogels was performed using the Zortrax INKSPIRE Resin UV LCD Desktop 3D Printer (Figure 30). Hydrogel mixtures 5 % GelMA + 5 % PEGDA and 10 % PEGDA + 0.5 % HAMA were mixed for 3-hours after which photoinitiator 0.1 mM Eosin-Y, 0.75 % TEA and 37 nM NVP were added to the hydrogel mixture and left on a magnetic stirrer to mix overnight. The hydrogel bioink mixture was then added to the resin tank and the resin printer set up to print disk constructs ( $\phi = 8$  mm and height = 2 mm). Disk constructs were designed using Trimble SketchUp 17.2.2555 64-bit software after which were exported as an stl. file. The resin printer settings (Table 6) and stl. file was modified using the CAD software Z-Suite 2.16.1 software Prints were performed with and without the use of supports for the constructs. Printer settings are shown in the table below and CAD software of print layout (Figure 24) below for both hydrogel bioink mixtures and inclusion and exclusion of supports for the constructs. Images of the 3D resin printer and printed constructs were taken using an iPhone XS max.

**Table 6: Zortrax Inkspire 3D resin printer settings.**

<b>Print settings</b>	<b>Specifications</b>
Material/Resin	External
Layer Height	0.025 mm
Raft	No
Model Lift Height	1 mm
Cross Support	Yes
Layer Exposure Time	180 s
Exposure off Time	30 s
Bottom Layer Exposure Time	240 s
Bottom Layer	5 pcs
Additional Support Exposure Time	60 s
Model Smoothing	No
X Overgrowth correction	0 pcs
Y Overgrowth correction	0 pcs
Hollow	No
Z Lift Distance	5 mm
Platform Lower Speed	50 mm/m
Platform Lift Speed	50 mm/m

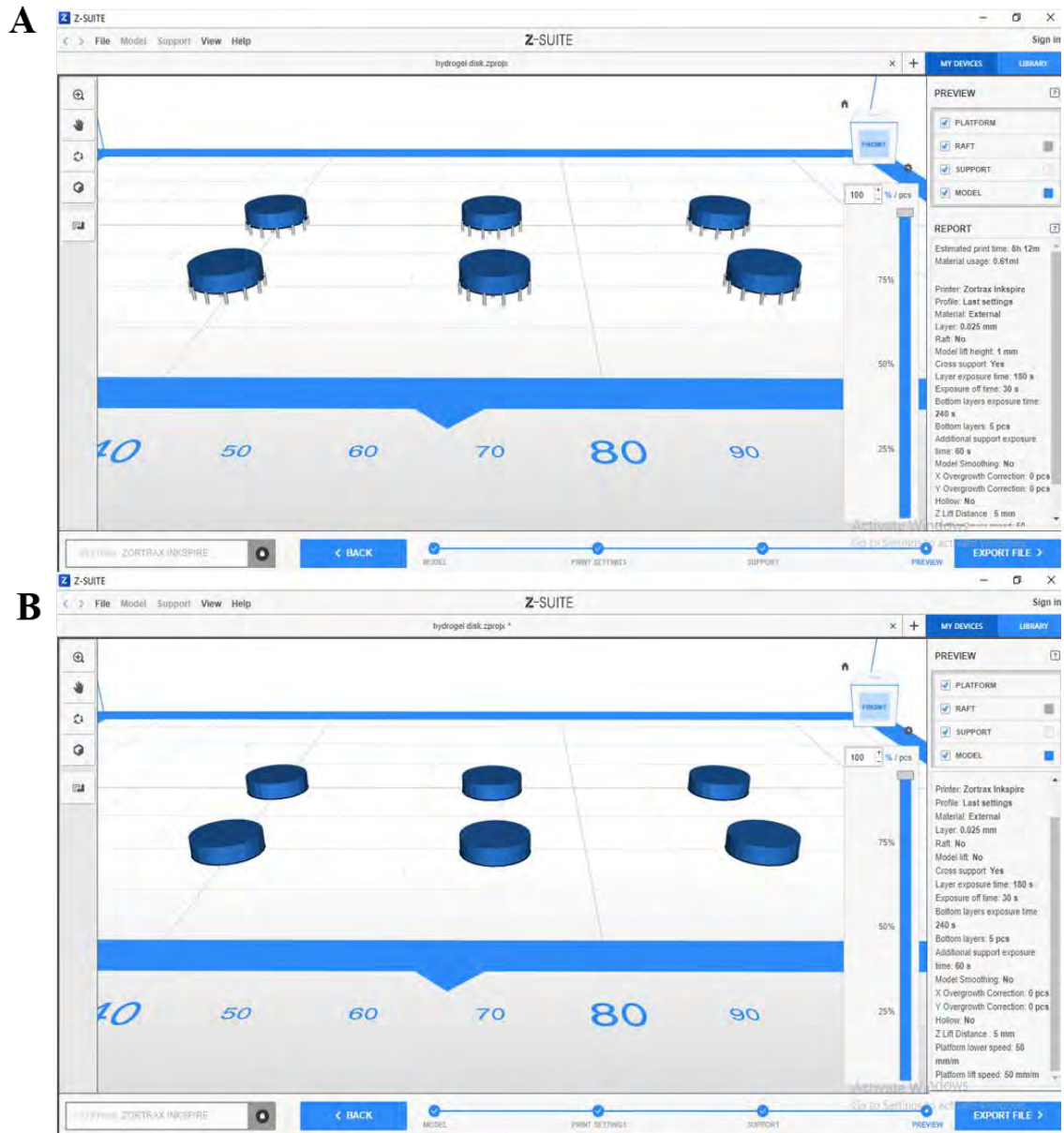


**Figure 24: Z-Suite printer settings for 3D print of hydrogel bioprints for Zortrax resin UV printer.**



## **4.3 Results and discussion**

### **4.3.1 Cytotoxicity assay of visible light photoinitiator components and chondrogenic differentiation supplements**

Real-Time Quantitative Cell Analysis was performed using HeLa cells to test the cytotoxic effects of visible light photoinitiator eosin-Y, TEA and NVP, as well as the cytotoxicity of chondrogenic differentiation supplements. HeLa cells are rapidly dividing cells that are easily cultured. They allow for suitable standardized and entry level testing for cytotoxicity assays as if the relative compounds are detrimental to cell survival, non-cancerous would survive. Cells had an initial 24-hour growth period after which induction of the different visible light photoinitiator and differentiation components were added. The assays were run for additional 48 and 103-hours respectively. All cell index graphs from the RTCA can be found in the appendix section. IC<sub>50</sub> time points were taken 20-24 hours after induction. Figures 25 and 26 show the IC<sub>50</sub> graphs and Table 7 shows the IC<sub>50</sub> values of the graphs for the visible light photoinitiator and chondrogenic differentiation supplements respectively.

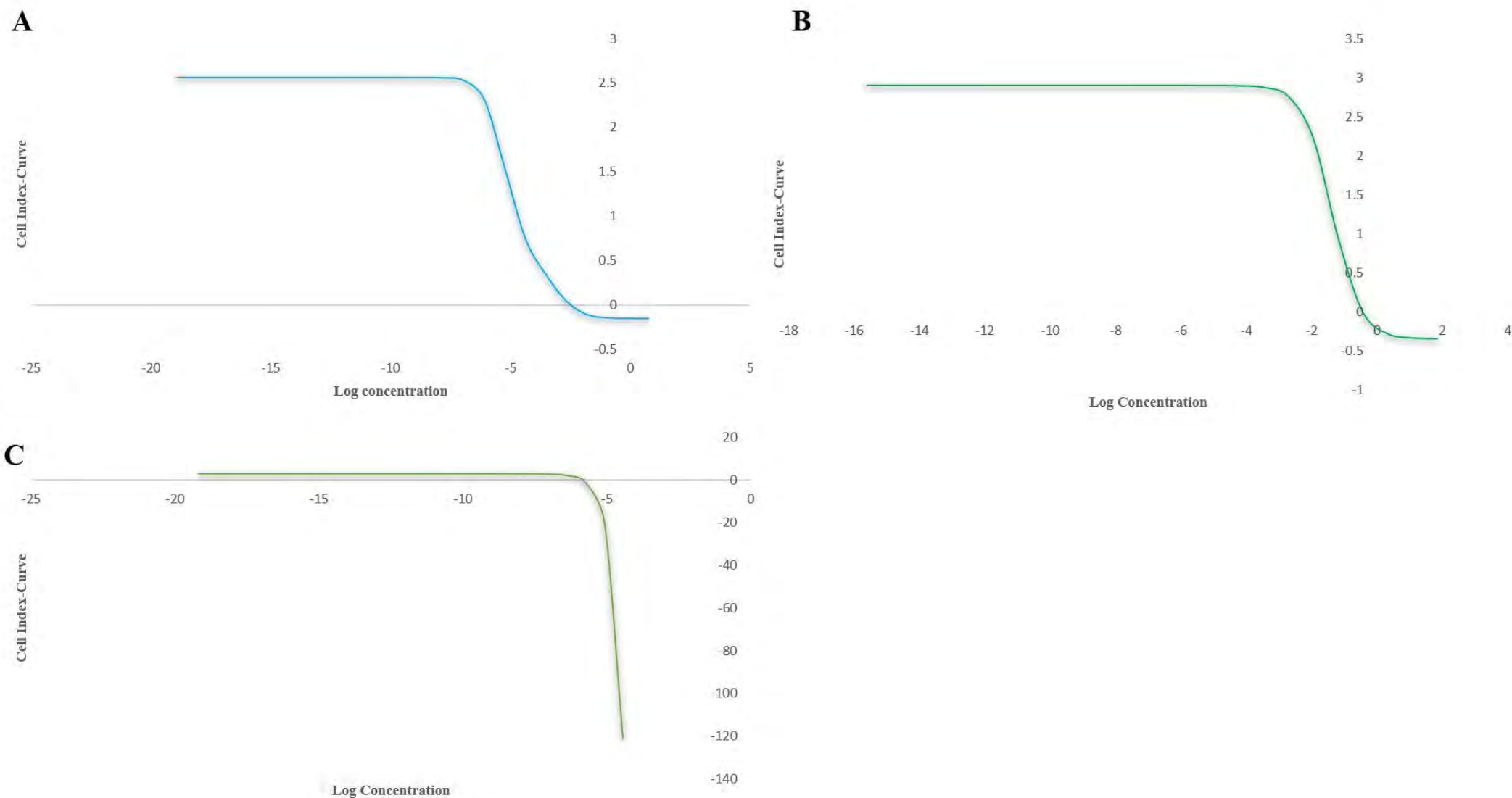


**Figure 25: IC<sub>50</sub> graphs of the photoinitiator components Eosin Y (A), TEA (B) and NVP (C).** IC<sub>50</sub> time points were taken at 44:15:49 hours after start of cytotoxicity assay of photoinitiators. Graphs were constructed using Microsoft Excel 365 and each graph represents N = 9 and each batch experiment had n = 3.

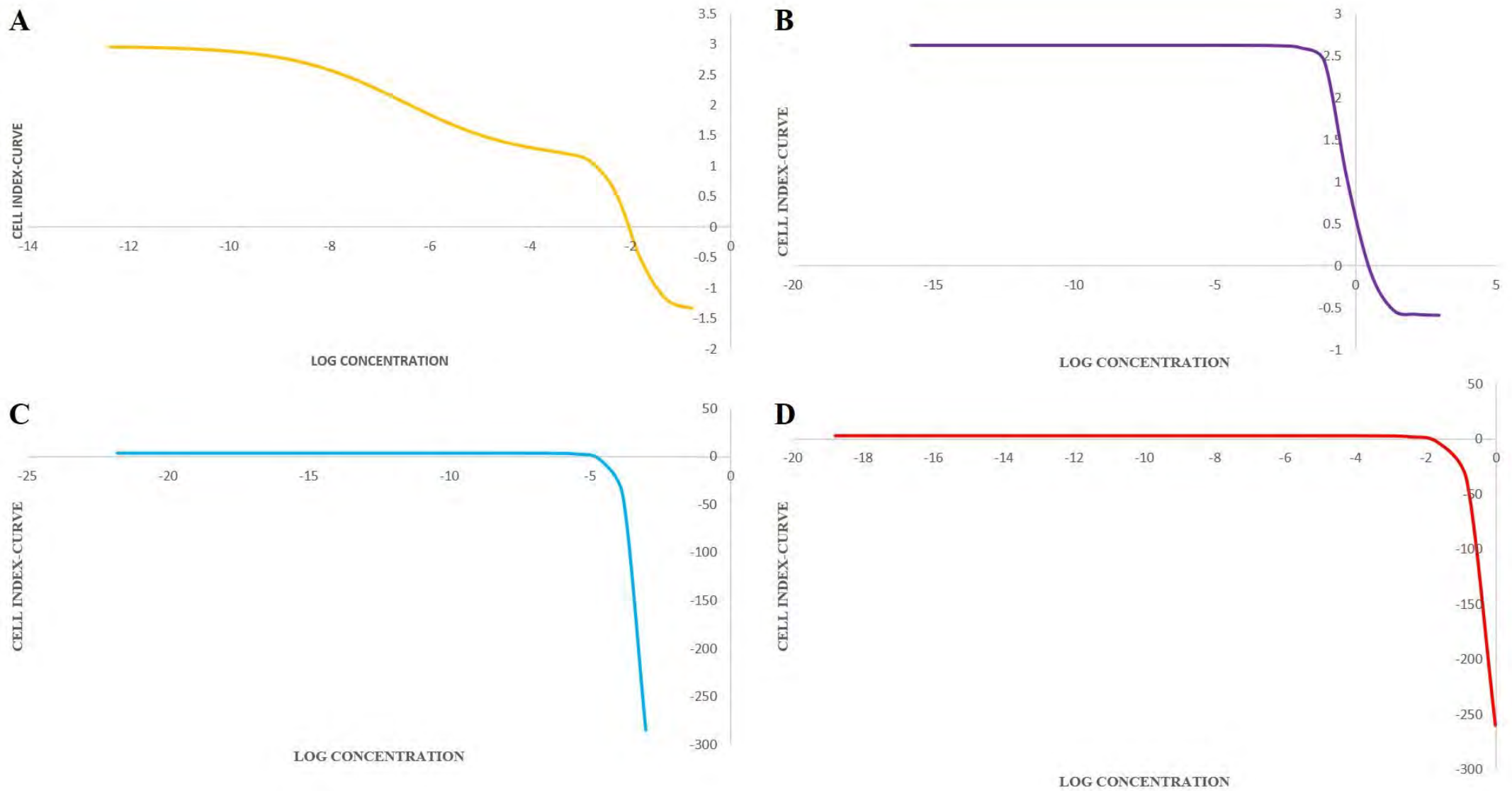


**Figure 26: IC<sub>50</sub> graphs of the chondrogenic differentiation supplements, Ascorbic Acid (A), Dexamethasone (B), TGF- $\beta$ 3 (C) and L-Proline (D).** IC<sub>50</sub> time points were taken at 47:48:47 hours after start of cytotoxicity assay of chondrogenic differentiation supplements. Graphs were constructed using Microsoft Excel 365 and each graph represents N=4 and each batch experiment had n = 2.

**Table 7: IC<sub>50</sub> values of reagents used in RTCA analysis on HeLa cells.**

Reagent	IC <sub>50</sub> value
<b>Eosin-Y</b>	30 ± 2.71 μM
<b>TEA</b>	48.1 ± 14.1 M
<b>NVP</b>	41.47 ± 5.68 mM
<b>Ascorbic Acid</b>	30.64 ± 41.79 μM
<b>Dexamethasone</b>	474 ± 169.71 mM
<b>L-Proline</b>	175.02 ± 69.40 M
<b>TGF-β3</b>	144 ± 16.97 μM

Figure 25 shows the IC<sub>50</sub> graphs for the visible light photoinitiator components produced from the RTCA analysis of the effects of the ranging concentrations of the visible light photoinitiator. The IC<sub>50</sub> values were calculated from the RTCA system and gave the following results - eosin-Y with 30.5 ± 2.71 μM, TEA with 41.47 ± 5.68 mM and NVP with 48.4 ± 14.1 M. Both eosin-Y and TEA show that there is a limit of concentration until it becomes cytotoxic, NVP showed to be non-cytotoxic even at the highest concentration tested. Eosin-Y and TEA shown by Figure 25 A & B both follow a standard dose response curve with the calculated IC<sub>50</sub> value within the range of the concentrations used in the assay. NVP shown by Figure 25 C does not follow the standard dose response curve with the IC<sub>50</sub> value well out of the concentration range used. The shape of the curve and IC<sub>50</sub> value of NVP can be explained by the XCELLigence curves, which show consistent cell proliferation instead of cell death, which can be observed for both the Eosin-Y and TEA XCELLigence curves at the high concentrations used.

Figure 26 shows the IC<sub>50</sub> graphs produced from the RTCA analysis of the effect of ranging concentrations of chondrogenic differentiation supplements have on HeLa cells. The IC<sub>50</sub> values were calculated using the RTCA system and gave values of 30.64 ± 41.79 μM for ascorbic acid, 474 ± 169.71 mM for dexamethasone, 175.02 ± 69.40 M for L-Proline and 144 ± 16.97 μM for TGF-β3. The shape of the IC<sub>50</sub> graph for ascorbic acid in Figure 26 A shows to be slightly skewed when compared to the other IC<sub>50</sub> graphs in Figures 25 and 26. This is due to the wide variance of the data obtained and is shown by the standard deviation in Table 7. The wide variance in data could be due to errors in the electrodes of the RTCA machine or pipetting errors during the induction period the ascorbic acid supplement when performing the replicates. Although the graph is skewed it still follows the standard dose response curve with the calculated IC<sub>50</sub> value fitting within the range of concentrations used. Dexamethasone shown in Figure 26 B follows the standard dose response curve with the IC<sub>50</sub> value within the range of concentrations used. Both L-Proline and TGF-β3 in Figure 26 C & D do not follow the standard dose response curve with the IC<sub>50</sub> values sitting well without the range on concentrations used. Similarly, to the NVP curve explanation, shape of the curve can be explained by the XCELLigence curves, which show great and consistent proliferation rather than cell death, which was experienced for

the dexamethasone XCELLigence curves, which thus results in the shape and IC<sub>50</sub> values obtained for the L-Proline and TGF-β3 supplements.

Based on the IC<sub>50</sub> values calculated from Figure 25 and displayed in Table 7, eosin-Y and TEA's IC<sub>50</sub> values are higher than the required minimum concentrations to polymerize the hydrogels. Required minimum concentrations of eosin-Y, TEA and NVP are 0.01 mM, 0.1 % and 37 nM respectively. This therefore allows the use of concentrations up to 0.03 mM, 0.55 % and 37 nM for eosin-Y, TEA and NVP to be used respectively before the reagent's eosin-Y and TEA would start to have a negative impact on cell viability. NVP IC<sub>50</sub> value was calculated to be 48.4 M indicating that it requires a significantly high concentration to have any effect on cell viability. These IC<sub>50</sub> values do fall within the range of concentrations used in most papers however some studies such as performed by Bikram *et al.*, 2007 and Bahney *et al.*, 2011 used higher concentrations of 10 mM eosin-Y, 1.5 % TEA, 37 mM NVP, 0.1 mM eosin-Y, 0.75 % TEA and 37 nM NVP respectively. The effects on cell viability using high concentrations were also shown and resulted in a decreased cell viability. Bikram *et al.*, 2007 obtained cell viabilities of 60-69 %. Bahney *et al.*, 2011 then conducted similar studies using photoinitiator concentrations of 0.1 mM, 0.75 %, 37 nM of eosin-Y, TEA and NVP respectively and lower concentrations of 0.01 mM, 0.1 %, 37 nM of eosin-Y, TEA and NVP respectively. They conducted cell viability assay, which showed that the higher use of the visible light photoinitiator concentrations did cause a decrease in cell viability of 68.8 % when compared to lower concentrations of the photoinitiator, which resulted in a cell viability of 88.4 %. Another study conducted by Wang *et al.*, 2015 used low concentrations of the visible light photoinitiator of 0.01 mM eosin-Y, 0.1 % TEA and 37 nM NVP and resulted in cell viabilities of up to 80 %. These studies correlate with the IC<sub>50</sub> values calculated in Figure 25 and Table 7 and can therefore conclude eosin-Y and TEA do have cytotoxic effects at high concentrations however using them at low concentrations has no adverse effects on cell viability while still enabling polymerization of hydrogels.

The IC<sub>50</sub> graphs and values calculated in Figure 26 and Table 7 show the cytotoxic effects of the chondrogenic differentiation supplements have on HeLa cells. Based on the values in Table 7, which were produced from Figure 26, ascorbic acid, dexamethasone, TGF-β3 and L-proline at concentrations of  $30.64 \pm 47.79 \mu\text{M}$ , 474 mM,  $144 \pm 16.97 \mu\text{M}$  and  $175.02 \pm 69.40 \text{ M}$  will have negative effects on cell viability.

When comparing the IC<sub>50</sub> values calculated to the concentrations of the supplements used for chondrogenic differentiation in this study, as well as other studies towards chondrogenic differentiation, the concentrations are well below the calculated IC<sub>50</sub> values calculated from the RTCA assay. This indicates that they should not have any negative effects on cell viability. Studies on the cytotoxicity of ascorbic acid on HeLa cells show much lower IC<sub>50</sub> values and concentrations used to induce cytotoxic effects on HeLa cells. Roberts *et al.*, 2015 reported using a concentration of 5 mM and higher to induced

apoptosis of HeLa cells, Zhang *et al.*, 2011 and Uetaki *et al.*, 2015 reported similar ascorbic concentrations used to induce apoptosis of HeLa cells. Mamede *et al.*, 2012 showed IC<sub>50</sub> values 25.10 mM 48-hours after induction on adenocarcinoma cell line (WiDr) cells. These concentrations and IC<sub>50</sub> values are lower than the IC<sub>50</sub> calculated however when taking into account the standard deviation of the IC<sub>50</sub> value of ascorbic acid, the IC<sub>50</sub> value does fall closer to the range obtained in the studies mentioned. The standard deviation is significant indicating possible errors occurring in the preparation of the assay and during the assay, which then resulted in a higher IC<sub>50</sub> value being generated compared to other studies. The variance in the cell index data, generated IC<sub>50</sub> values and subsequent generated graphs of the individual ascorbic acid assay show the large variance that produced the significant standard deviation. Errors such as incorrect pipetting of ascorbic acid supplements or well reading errors of the RTCA machine could have led to the significant standard deviation error. When comparing the IC<sub>50</sub> value of ascorbic acid to the concentrations used for chondrogenic differentiation, the IC<sub>50</sub> value is higher than concentrations used for differentiation of ad-MSC. Markmee, Aungsuchawan and Pothacharoen, 2019 showed the cytotoxic effects of ascorbic acid on human amniotic fluid mesenchymal stem cells with an induction of apoptosis only occurring with 100 – 200 µg/ml after 48-hours. This correlates with the IC<sub>50</sub> value calculated in this study, as well as correlates with the general concentration used for ascorbic acid for chondrogenic differentiation. There is a difference in concentrations used for HeLa cell cytotoxicity and stem cell cytotoxic. This is due to the effect ascorbic acid has on cancerous cells. Ascorbic acid is directly related to cellular proliferation and differentiation for stem cells (Fujisawa *et al.*, 2018). However with the use of cancerous cell line such as HeLa cells and at high concentrations of ascorbic acid, it can cause the induction of apoptosis through increased generation of reactive oxygen species (ROS) hydrogen peroxide (Roberts *et al.*, 2015). Cancer cells differ from normal cells as they produce high levels and unregulated levels of ROS leading to oxidative damage resulting in cancer initiation and progression (Kumari *et al.*, 2018). L-ascorbic acid is considered to be an antioxidant and essential cofactor in many metabolic and enzymatic reactions at physiological levels of ± 6 µM. At high levels, greater than 1 mM it is considered to be a pro-oxidant. Roberts *et al.*, 2015 mentions that using excessively high concentrations of ascorbic acid it further induces ROS, increasing the already high ROS levels in the cancer cell line and as a result causes the intrinsic pathway of apoptosis (Roberts *et al.*, 2015), thus giving the possible reasons to why the concentrations of ascorbic acid and subsequent effects on cell viability are vastly different.

Dexamethasone is routinely used for cellular differentiation and has beneficiary effects against cancerous cells lines. High concentrations of dexamethasone have shown to suppress cellular proliferation and affect cell viability (Walsh *et al.*, 2001; Wang *et al.*, 2016). Figure 26B shows the IC<sub>50</sub> curve of dexamethasone, which resulted in an IC<sub>50</sub> value of 474 ± 169.71 mM. The IC<sub>50</sub> value is higher than the concentration used for adipogenic and chondrogenic differentiation. Wang *et al.*, 2012 and Buxant *et al.*, 2015 studied the effects of ranging concentrations of dexamethasone of mesenchymal

stem cells and MCF-7 cell lines both showing that a concentration of  $10^{-7}$  M or higher caused a significant inhibition in cell proliferation and viability. Nuzzi *et al.*, 2012 found that a concentration of 2.55  $\mu$ M or higher showed a decrease in viability conditions (%) on mesenchymal stem cells. All findings are lower than the  $IC_{50}$  calculated from Figure 26B. The difference in values could be due to the use of HeLa cells, which are affected less than MCF-7 and mesenchymal stem cells or a high cell density was used in this study compared to the studies mentioned however these reasons are unlikely for the significant difference in concentration values. The XCELLigence graphs plots obtained show only decreases in cell viability for the high concentrations 600 nM – 1 M of dexamethasone where the remainder continue to increase in proliferation and show no decreases in cell viability. More likely reasons could be errors in dexamethasone preparation, pipetting errors during induction or faulty pins of the RTCA machine, which are more likely due to the high standard deviation calculated for the  $IC_{50}$  value calculated. Despite this, from the studies performed by Nuzzi *et al.*, 2012, Wang *et al.*, 2012 and Buxant *et al.*, 2015 all showed  $IC_{50}$  values for dexamethasone to be higher than the concentrations used for adipogenic and chondrogenic differentiation proving that the concentrations used for dexamethasone in this study for differentiation have no cytotoxic effects in cellular proliferation and viability.

Figure 26C shows the  $IC_{50}$  graph of TGF- $\beta$ 3 and from the graph the  $IC_{50}$  value was calculated to be  $144 \pm 16.97$   $\mu$ M. When compared literature using TGF- $\beta$ 3 for chondrogenic differentiation, concentration value is generally 50 ng/ml (Zhang *et al.*, 2010; Zuliani *et al.*, 2018). The  $IC_{50}$  value is considerably higher than the standard concentration used indicating that TGF- $\beta$ 3 had no cytotoxic effects on the HeLa cell line. The standard deviation is also very small indicating a small distribution of the  $IC_{50}$  values calculated and there by strengthening the accuracy of the  $IC_{50}$  value and effect TGF- $\beta$ 3 has on mammalian cells. In comparison to literature, cytotoxicity of TGF- $\beta$ 3 on cancer cells or stem cells is absent with no studies indicating any results of TGF- $\beta$ 3 having cytotoxic effects on either cancerous cell lines or stem cells *in vitro* (Potten, Booth and Haley, 1997, Wahdan-Alaswad *et al.*, 2016 and Bhola *et al.*, 2013). This confirms the  $IC_{50}$  graph and values in Table 7 and Figure 26C that TGF- $\beta$ 3 shows to have no cytotoxic effects even at the highest concentration tested at 500 ng/ml (0.02 nM). More interestingly studies by Potten, Booth and Haley, 1997, Wahdan-Alaswad *et al.*, 2016 and Bhola *et al.*, 2013 looked at the effect of TGF inhibition as possible treatments of various cancerous cells lines thereby further confirming that TGFs have no cytotoxic effects on mammalian cell lines, which corresponds to the XCELLigence graph data obtained, which shows even at the highest concentration of 100 ng/ml showed an increase in cell proliferation and subsequent cell viability of the HeLa cells.

L-Proline cytotoxicity on HeLa cells is shown by the  $IC_{50}$  graph in Figure 26D and  $IC_{50}$  value in Table 7. The  $IC_{50}$  was calculated from the Figure 26D and resulted in an  $IC_{50}$  value of  $175.02 \pm 69.40$  M. The standard concentration value of L-Proline for chondrogenic differentiation is 40  $\mu$ g/ml (0.35  $\mu$ M) making the  $IC_{50}$  value significantly higher than the normal L-Proline concentration used therefore

showing that L-Proline has no cytotoxic effect on mammalian cells. The  $IC_{50}$  value is considerable higher than expected, in addition to this the standard deviation of the  $IC_{50}$  value is also high resulting in great variance of the  $IC_{50}$  value and thus the accuracy of the cytotoxic range of L-Proline. This is mainly due to the fact that in one replicate assay an  $IC_{50}$  value of 125.95 M was calculated and in the other the  $IC_{50}$  was calculated to be 224.1 M. This  $IC_{50}$  value was the expectation range for L-Proline simply based on the standard concentrations used for L-Proline in chondrogenic differentiation, which are routinely used at 40  $\mu\text{g/ml}$  (Tanthaisong *et al.*, 2017; Zuliani *et al.*, 2018). The great discrepancy in the  $IC_{50}$  values between assays resulting in a great standard deviation could be due to improper supplement preparation, pipetting errors or electrode issues with the RTCA system. This can be in the XCELLigence graph plots were in the replicate a higher increase in cell index within the first 24-hours than in the original assay where the cell index curve started off slightly lower than the replicate. Despite this, Liu *et al.*, 2019 and D'Aniello *et al.*, 2020 mention no cytotoxic effects of L-Proline on normal and cancerous stem cell lines, as well as cancerous cell lines. Both Liu *et al.*, 2019 and D'Aniello *et al.*, 2020 focus on Proline inhibition towards the treatment of various cancer cell lines. Although the  $IC_{50}$  value is significantly higher than expected, based on literature, L-Proline has no cytotoxic on mammalian cell lines and the standard concentration of L-Proline used in chondrogenic differentiation will have negative effects on cell viability.

#### **4.3.2 Attenuated total reflectance – Fourier transform Infrared spectroscopy**

An assessment of the chemical composition of the five formulated hydrogel mixtures, GelMA, PEGDA, GelMA/PEGDA, GelMA/HAMA and PEGDA/HAMA was performed using FTIR spectroscopy. Infrared absorption spectra are presented in Figures 27 and 28-29 showing the unstacked and stacked spectral readings of the components characterizing the five formulated hydrogels.



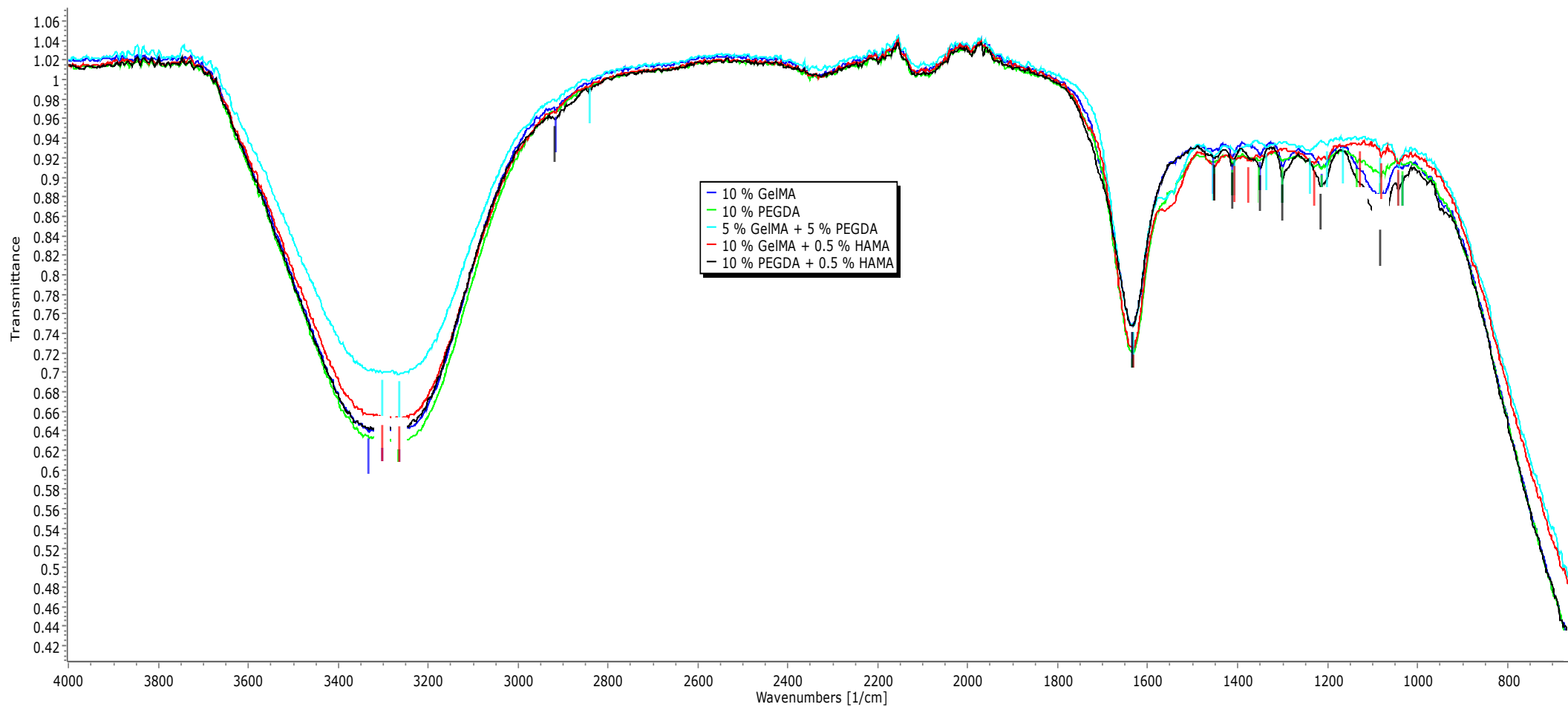


**Figure 27: FTIR spectra of GelMA, PEGDA, GelMA/PEGDA, GelMA/HAMA, PEGDA/HAMA hydrogels.** Unstacked spectral view interval ranging from 650 to 4000  $\text{cm}^{-1}$ . All spectral are represented as transmittance vs wavenumbers ( $\text{cm}^{-1}$ ).

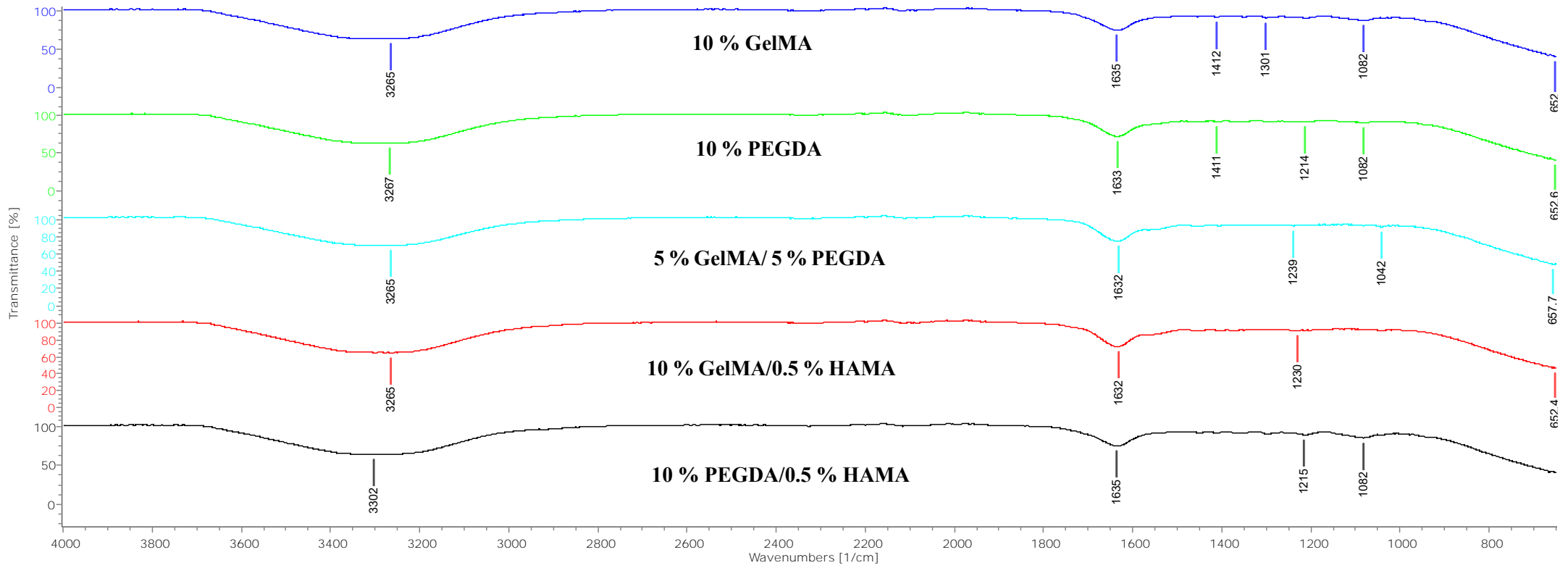


**Figure 28: FTIR spectra of GelMA, PEGDA, GelMA/PEGDA, GelMA/HAMA, PEGDA/HAMA hydrogels.** Multi-stacked spectral view interval ranging from 650 to 4000  $\text{cm}^{-1}$ . All spectral are represented as transmittance vs wavenumbers ( $\text{cm}^{-1}$ ).

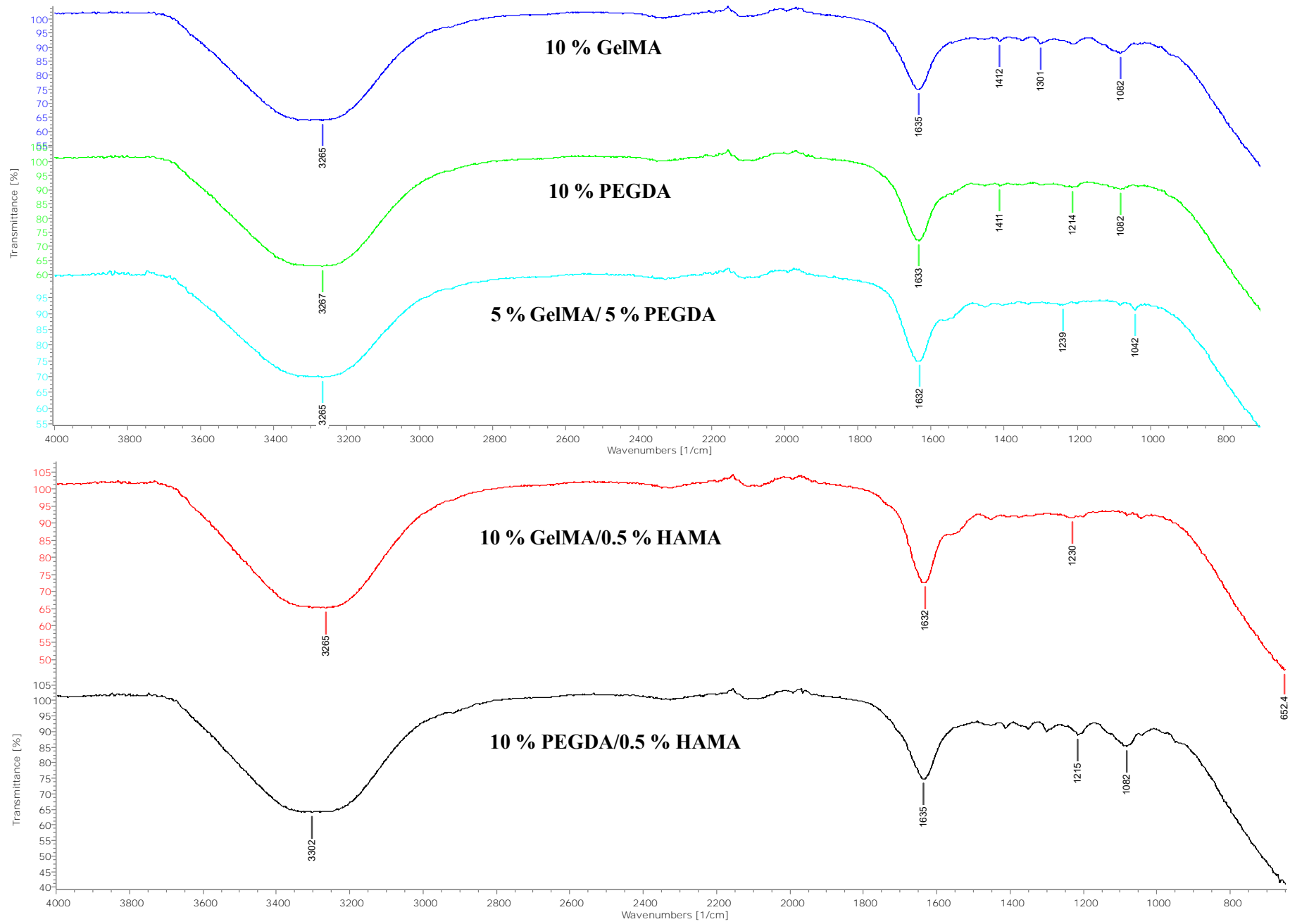


**Figure 29: Magnified FTIR spectra views of formulated hydrogels (A)GelMA, PEGDA, GelMA/PEGDA, (B) GelMA/HAMA and PEGDA/HAMA.**

Figure 28 and 29 shows the stacked FTIR spectra of 10 % GelMA, 10 % PEGDA, 5 % GelMA/5 % PEGDA, 10 % GelMA/0.5 % HAMA and 10 % PEGDA/0.5 % HAMA. The peaks for 10 % GelMA represent at  $3265\text{ cm}^{-1}$  O-H stretching (carboxylic acid group),  $1635\text{ cm}^{-1}$  C=C stretching (alkene group, monosubstituted),  $1411\text{ cm}^{-1}$  O-H bending (alcohol group),  $1301\text{ cm}^{-1}$  C-O stretching (aromatic ester),  $1082\text{ cm}^{-1}$  represents C-N stretching (amine group) and  $652.6\text{ cm}^{-1}$  represents C-Br stretching (halo compound). Absorption bands at  $3420\text{ cm}^{-1}$ ,  $2928\text{ cm}^{-1}$ ,  $1645\text{ cm}^{-1}$ ,  $1540\text{ cm}^{-1}$  and  $1240\text{ cm}^{-1}$  are attributed to O-H and N-H stretching of amide A, C-H stretching of  $\text{CH}_2$  groups, C=O stretching amide I peptide groups, N-H bending coupled to C-H stretching amine II groups and C-N stretching and N-H bending of amine III groups indicate the structural backbone of gelatin (Li, Mu and Lin, 2016). Modification to gelatin does not alter the spectra of the gelatin backbone however with modification of methacrylate C=C stretching occurs between  $1680\text{--}1620\text{ cm}^{-1}$  showing an increase in the amide I band. In addition to this bands at spectra wavelengths of  $860$  and  $950\text{ cm}^{-1}$  are characteristic of C-H stretching of C=C bonds which arise in gelatin modified with methacrylic acid and shows increased peak intensity and subsequent increased degree of substitution (Li, Mu and Lin, 2016). Based on Figure 28 and 29 and the peaks observed the backbone of gelatin is observed. The peak present at  $1635\text{ cm}^{-1}$  is indicative of methacrylic modification however peaks at  $860$  and  $950\text{ cm}^{-1}$  should also be displayed indicating the presence of methacrylic acid. Based on the level of intensity of the peak observed at  $1635\text{ cm}^{-1}$ , the degree of modification is not as high as seen in other studies done by Zhou *et al.*, 2016, Li, Mu and Lin, 2016 and Aldana *et al.*, 2019. As the degree of substitution is low it could explain why no peaks are observed at  $860$  and  $950\text{ cm}^{-1}$  however there should still be a small peak been observed. This low degree of substitution could also explain the reason for long polymerization times when compared to literature. Increased addition of methacrylic anhydride, shorter dialysis times and longer reaction times between gelatin and methacrylic anhydride could improve the methacrylic content in the GelMA and thereby increasing the degree of substitution.

Peaks for 10 % PEGDA represent at  $3267\text{ cm}^{-1}$  O-H stretching (alcohol group, intermolecular bonded),  $1633\text{ cm}^{-1}$  C=C (alkene, disubstituted),  $1411\text{ cm}^{-1}$  (O-H bending, alcohol or carboxylic acid group),  $1214\text{ cm}^{-1}$  C-O stretching (alkyl aryl ether group),  $1082\text{ cm}^{-1}$  C-O stretching (primary alcohol group), and  $652.6\text{ cm}^{-1}$  C-Br stretching (halo compound). The peak band at  $3267\text{ cm}^{-1}$  is characteristic of the O-H bond alcohol group which is associated with poly(ethylene glycol). In PEG samples, a peak between  $3500\text{--}3400\text{ cm}^{-1}$  is highly defined however with the addition of acrylate, the PEGDA sample has greatly diminished peak (Askari *et al.*, 2019) which is observed in Figure 28 and 29. The peak present at  $1633\text{ cm}^{-1}$  indicates a C=C aliphatic bond in PEGDA samples and is present as a strong peak as seen by Askari *et al.*, 2019. The PEGDA sample in Figure 28 and 29 does show the presence of this peak however is not as strong as present by Askari *et al.*, 2019. Either the spectra needed to be zoomed in more to observe the strength of the peak or there may have been an issue the FTIR spectrophotometer where the absorption emittance and capture may have been impeded by dirty crystals in the machine.

In another study by Hamid and Lim, 2016 however similar peaks at  $1633\text{ cm}^{-1}$  were observed where the peak was weak and could therefore just indicate the zooming in on the peaks could reveal the strength that Askari *et al.*, 2019 observed. The PEGDA overall spectra present in Hamid and Lim, 2016 is very similar to the spectra observed for PEGDA in Figure 28 and 29.

Peaks for 5 % GelMA/ 5 % PEGDA represent at  $3265\text{ cm}^{-1}$  O-H stretching (alcohol, intermolecular bond),  $1632\text{ cm}^{-1}$  C=C (alkene, disubstituted),  $1239\text{ cm}^{-1}$  C-N stretching,  $1042\text{ cm}^{-1}$  C-N stretching (amine group). The peaks observed in Figure 28 and 29 align both with peaks observed in GelMA and PEGDA samples found in literature Li, Mu and Lin, 2016 and Askari *et al.*, 2019. The lack of distinction between the peaks could be due to overlapping peak bands. However as seen in the spectra bands of GelMA/PEGDA observed in the supplementary information by Shrimali *et al.*, 2018 two separate peaks are observed between  $3500 - 300\text{ cm}^{-1}$  where in Figure 28 and 29 there is a single peak. A strong, instance peak is also observed in Shrimali *et al.*, 2018 at  $1200 - 1100\text{ cm}^{-1}$ , which isn't observed in the GelMA/PEGDA sample. This could be the result of insufficient mixing of the two hydrogels leading to the majority of the one hydrogel been measured, as well as the lack on band intensities seen in the GelMA and PEGDA samples in Figures 28 and 29 when compared to literature. Although the lack of mixing may have been the case with the FTIR analysis, when polymerizing the GelMA/PEGDA hydrogel, quick and efficient polymerization of the hydrogel occurred. The reason for lack of mixing could be due to the fact that when the photoinitiator is added to the hydrogel mixture, longer mixing times occur whereas with the FTIR analysis no photoinitiator was added resulting in shorter mixing times of the hydrogels and subsequent insufficient mixing. The combination of two different polymers can be classified as hybrid polymers or interpenetrating polymer networks (IPN). Before cross-linking of the IPN, polymer blends can be classified into two groups: mechanical blends and graft copolymers. Mechanical blends are the combination of two or polymers with no chemical bonds formed between the polymers. Graft copolymers allow for primary bonds between the polymers to occur to occur (Zoratto and Matricardi, 2018). It is possible that the polymers used in this study created a mechanical blend with no chemical bonding taking place. As a result of this integration of the polymers would not be great causing the presence of the main polymer to mainly be observed through the FTIR.

Peaks for 10 % GelMA/0.5 % HAMA represent  $3265\text{ cm}^{-1}$  O-H stretching (alcohol group, intermolecular bonded),  $1632\text{ cm}^{-1}$  C=C stretching (alkene disubstituted),  $1230\text{ cm}^{-1}$  C-N stretching,  $652.4\text{ cm}^{-1}$  C-Br stretching (halo compound). The use of hybrid hydrogels involving GelMA and HAMA is still a novel idea with limited literature showing the use of this hybrid combination and characterization of it using FTIR. Expected peaks for the hybrid should show peaks of the gelatin backbone at  $3420, 2928, 1645^1, 1540$  and  $1240\text{ cm}^{-1}$ . Peaks at  $1680-1620\text{ cm}^{-1}, 860$  and  $950\text{ cm}^{-1}$  should also be present showing the addition of the methacrylic groups. Based on literature Alves *et al.*, 2017 and Yousefi, Kandel and Pleshko, 2018 performed FTIR spectra on hyaluronic acid and hyaluronic acid methacrylate anhydride, producing spectrums at  $3447\text{ cm}^{-1}$  attributed to O-H and N-H stretching,  $1638$

$\text{cm}^{-1}$  corresponding to amide carbonyl,  $1420 \text{ cm}^{-1}$  attributed to  $\text{COO}^-$  stretching, which is the result of the acid group of the HA molecule (Alves *et al.*, 2017). Peaks at  $1708\text{-}1712 \text{ cm}^{-1}$  show the influence of methacrylation on the HA. The  $\text{C}=\text{O}$  ester bond arises from the addition of the methacrylate group added to the HA backbone at peaks  $1708\text{-}1712 \text{ cm}^{-1}$  (Yousefi, Kandel and Pleshko, 2018). In a study performed by Carneiro *et al.*, 2016 they acquired major peak bands for HA at  $3443$ ,  $1648$  and  $1034 \text{ cm}^{-1}$ , which corresponds to the results obtained by Alves *et al.*, 2017. Figure 28 and 29 for the GelMA/HAMA spectra does not show major peaks at  $3443$ ,  $1648$  and  $1043 \text{ cm}^{-1}$ , they show rather similar peaks to the 10 % GelMA spectrum. This could be due to similar faults as discussed for the 5 % GelMA/5 % PEGDA FTIR spectrum where insufficient mixing of the hybrid hydrogel could have been the result of lack of correct peaks displayed in the spectra. In addition to this the percentage of HAMA in the GelMA hybrid hydrogel is significantly lower than the 10 % GelMA present, which could be the reason for insignificant peaks been produced without having to zoom into the individual peaks to visualize the presence of the HAMA group in the hybrid hydrogel. Increase the content of HAMA by 10-fold could also influence the strengths of the peaks. However, although the peaks are not visible showing the presence of HAMA, during the polymerization and morphology of the hydrogel disks, the polymerization was quick and efficient when compared to the 10 % GelMA hydrogel, the colour of the GelMA/HAMA disk was a murky white colour compared to the GelMA hydrogel disk, a characteristic of HA and thereby confirming that HAMA is present in the hybrid hydrogel despite the fact that no significant peaks were observed in the FTIR spectra.

Peaks for 10 % PEGDA/0.5 % HAMA represent at  $3302 \text{ cm}^{-1}$  O-H stretching (alcohol, intermolecular bond),  $1635 \text{ cm}^{-1}$   $\text{C}=\text{C}$  (alkene, disubstituted),  $1215 \text{ cm}^{-1}$  C-N stretching (amine group),  $1082 \text{ cm}^{-1}$  C-N stretching (amine group). As with the GelMA/HAMA hybrid hydrogel, the use of PEGDA/HAMA hydrogel is a relatively novel idea with results on FTIR spectrums been absent. However based on literature Askari *et al.*, 2019 shows peak bands at  $3267 \text{ cm}^{-1}$ , characteristic of the O-H bond alcohol group, which is associated with poly(ethylene glycol). Small peaks between  $3500 - 3400 \text{ cm}^{-1}$  should also be observed showing the addition of acrylate (Askari *et al.*, 2019), which is observed in Figure 28 and 29. The peak present at  $1633 \text{ cm}^{-1}$  indicates a  $\text{C}=\text{C}$  aliphatic bond in PEGDA samples and is present as a strong peak as seen by Askari *et al.*, 2019. With respect to the HAMA addition, peaks at  $3447$ ,  $1638$ ,  $1420 \text{ cm}^{-1}$  show the addition of HA in the hydrogel mixture (Alves *et al.*, 2017). Peaks at  $1708\text{-}1712 \text{ cm}^{-1}$  show the influence of methacrylation on the HA with  $\text{C}=\text{O}$  ester bond arises from the addition of the methacrylate group added to the HA backbone at peaks  $1708\text{-}1712 \text{ cm}^{-1}$  (Yousefi, Kandel and Pleshko, 2018). Similarly, to the spectra observed with GelMA/HAMA, these peaks for the HAMA are absent whereas the peaks for the PEGDA are present. This could be the same effective as seen with the GelMA/HAMA spectra, due to low percentage of HAMA (0.5 %) being present in the PEGDA (10 %) insufficient peaks are observed. By increasing the percentage of HAMA could result in more significant peaks being produced. Mixing of hydrogel mixtures could also be a result as mentioned in the

GelMA/PEGDA and GelMA/HAMA spectra discussion. Similarly, to the GelMA/HAMA hybrid hydrogel, polymerization of the PEGDA/HAMA hydrogel was quick and efficient, as well as the hydrogel disk presenting a murky white colour characteristic of HA and therefore suggests that HAMA is present in the hybrid hydrogels.

### 4.3.3 Three-Dimensional printing of formulated hydrogel bioinks

Hydrogel hybrid bioinks PEGDA/HAMA and GelMA/PEGDA were made up with the addition of visible light photoinitiator components. The printability of the bioinks was tested using the Zortrax UV resin printer using an integrated UV LCD screen at 405 nm shown in Figure 30. Only two hydrogel bioinks, the PEGDA/HAMA and GelMA/HAMA were tested due to minimal GelMA and HAMA reagents available. The choice of hybrid hydrogel bioinks were chosen based on the polymerization times observed from the swelling, degradation and cell viability assays. Results of the 3D prints for the hybrid hydrogel bioinks are shown in Figure 31 and 32.

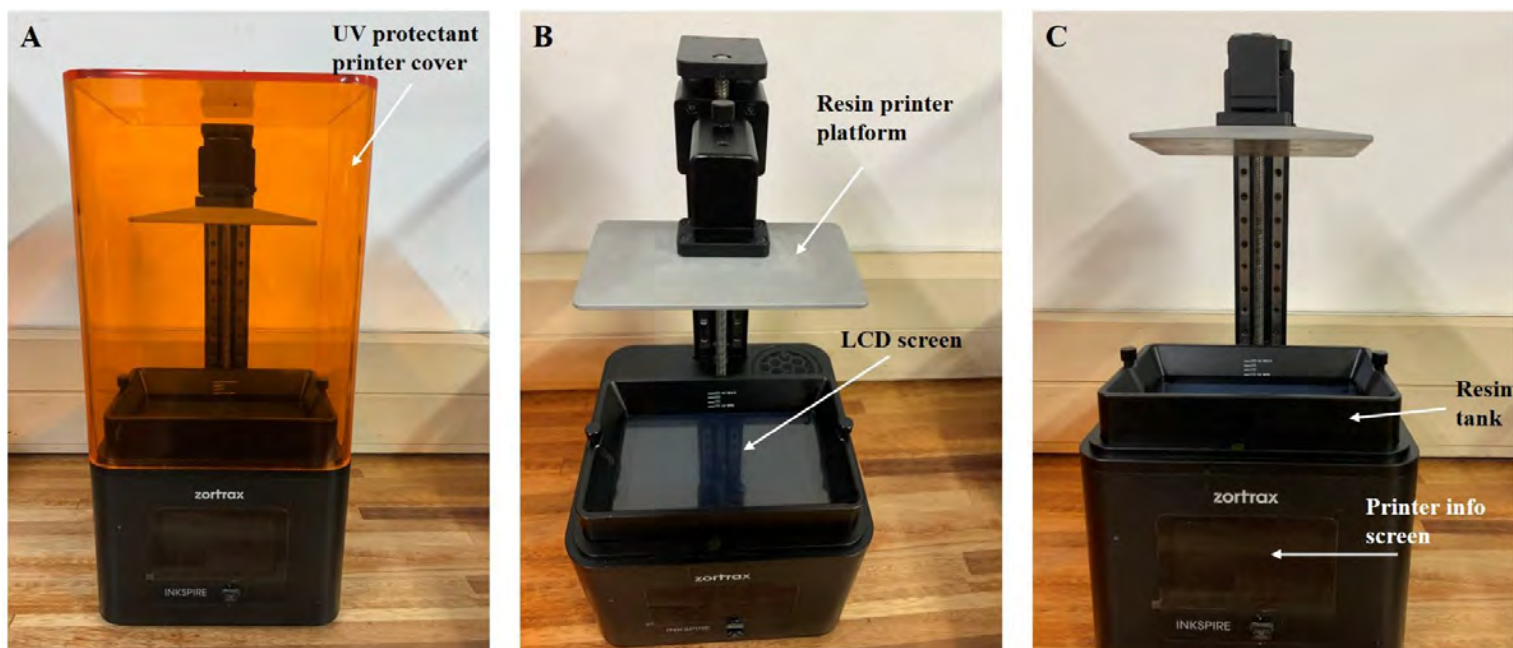


**Figure 30: Zortrax INKSPIRE Resin UV LCD Desktop 3D Printer.** A – Full view of the resin printer with protective UV cover. B – Top view of resin printer without UV protective cover showing the LCD screen and printing platform. C – Front view of resin printer showing the printer information screen and the resin tank.



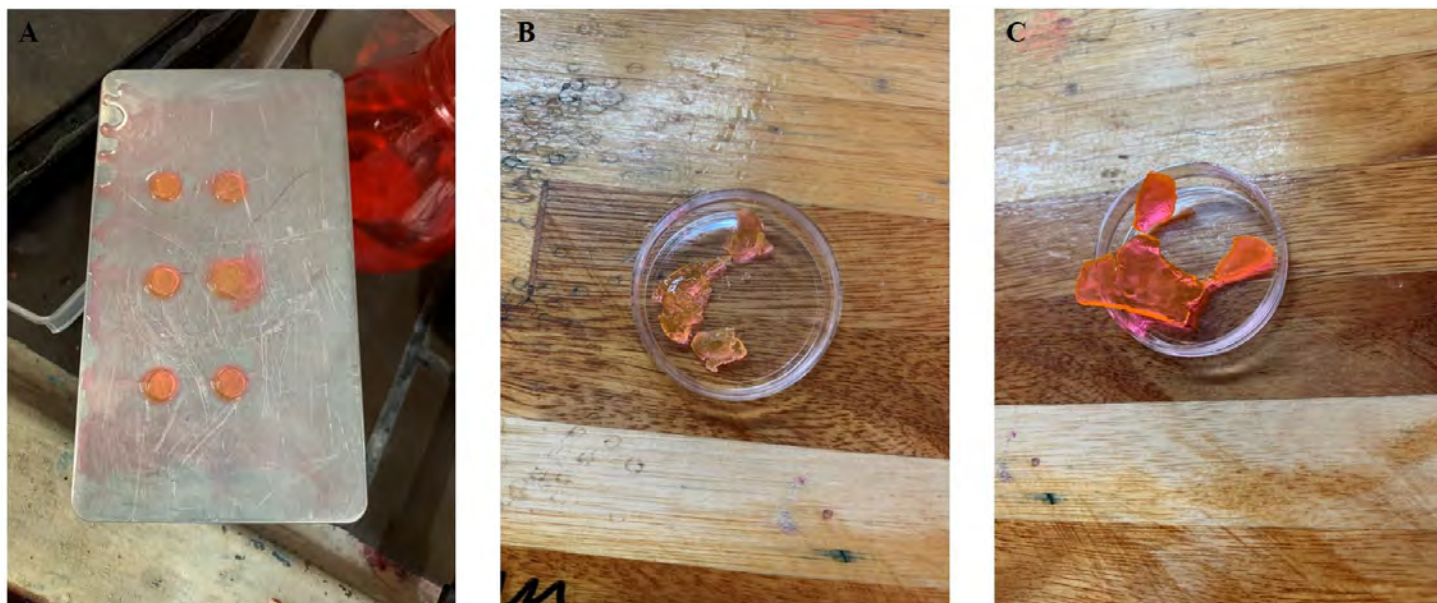


**Figure 31: PEGDA/HAMA 3D prints using the Zortrax resin printer.** A – 3D printed 10 % PEGDA/0.5 % HAMA disks attached to printing platform. B – PEGDA/HAMA printed disks after removal from printed platform. C – PEGDA/HAMA printed disks using scaffolds for supports.

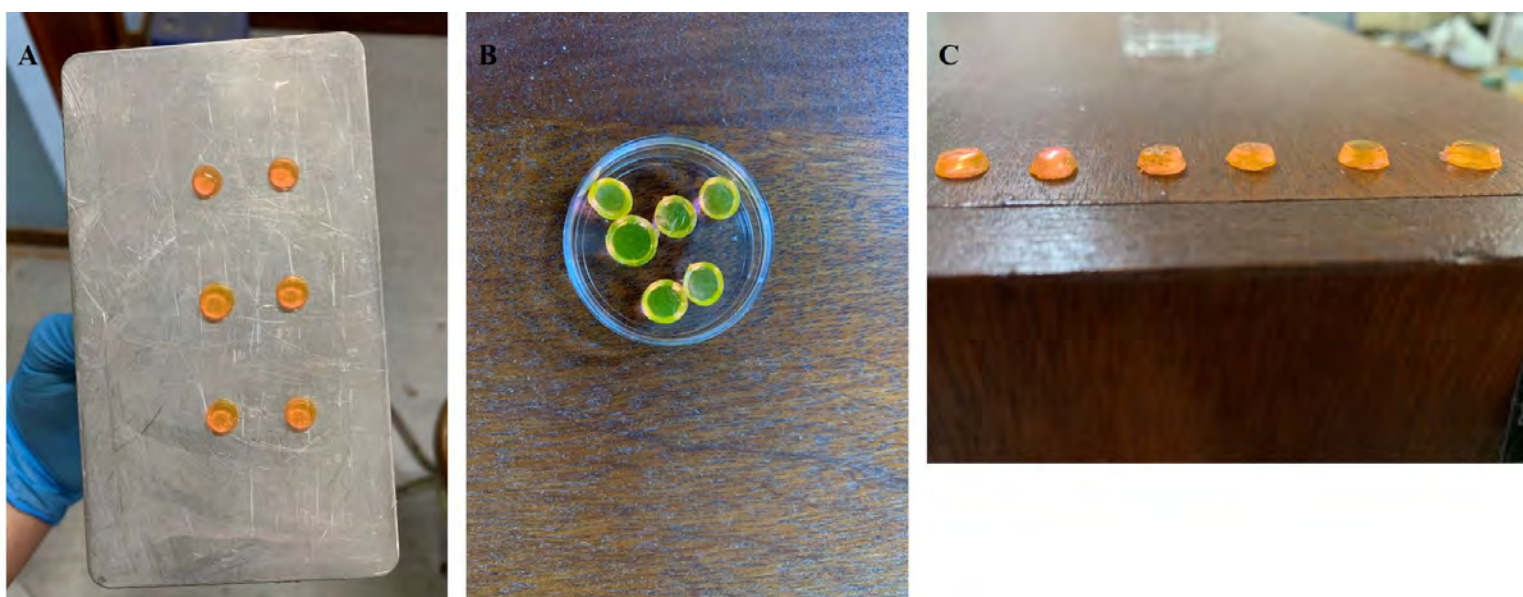


**Figure 32: GelMA/PEGDA 3D prints using Zortrax resin printer.** A – 5 % GelMA/5 % PEGDA 3D printed disks attached to resin printer platform. B and C – 3D printed GelMA/PEGDA disks once removed from resin printer platform.

Figures 31 and 32 show the proof of concept towards the 3D printing of the formulated hydrogels produced in this study. Only two selected hydrogel types were chosen based on the quick, efficient polymerisation times from the degradation, swelling and SEM assays. In addition to the polymerization time, the supply of GelMA and HAMA was limited to only one solution of 5 % GelMA/5 % PEGDA and 10 % PEGDA/0.5 % HAMA being made rather than use only one hybrid hydrogel for 3D printing consisting of 10 % GelMA/ 0.5 % HAMA.



Both prints without the use of support structures showed successful 3D printing whereas with the addition of supports for 10 % PEGDA/0.5 % HAMA lead to inaccurate printing and deformation of the designed construct, which can be seen in Figure 31C. Figure 31A shows the successful 3D print of PEGDA/HAMA however in the process of removing the prints from the printing platform, the disks broke and did not retain shape as seen in Figure 31B. The deformation of the disks could be due to overexposure of UV thereby over polymerizing the hydrogels making the disks too stiff and hard instead of being more gel-like causes them to break when removing them from the platform. Based on this, the UV exposure time was reduced by 2 minutes for the GelMA/PEGDA hybrid hydrogel 3D print and resulted in successful 3D prints on the design construct. The disks appeared to more gel-like than the PEGDA/HAMA printed constructs and thus were removed from the platform with greater ease and able to retain their printed shape as seen in Figure 32B and C. Prints with lower UV exposure time for the PEGDA/HAMA was performed with the use of supports, which resulted in the deformation of the disks seen in Figure 31C. The 3D print was more gel-like and was removed from the printing platform with greater ease. After the 2 prints of the PEGDA/HAMA hybrid hydrogel bioink, there was insufficient bioink to perform a third print using lower UV exposure times without supports to acquire successful gel-like printed disks as obtained in Figure 32. Based on the UV exposure times from the 3D prints, it can be concluded that the bioinks require less UV exposure time than required when performing the swelling, degradation, SEM and cell viability assays of the formulated hydrogels.

In conclusion the RTCA showed that Eosin-Y and TEA have cytotoxic effects on cell viability at concentrations of 0.01 mM and 0.5 % respectively. These values are slightly lower than than  $IC_{50}$  obtained in Table 7 can be used before a negative effect on cell viability is seen. Ascorbic acid and dexamethasone exhibited cytotoxic effects whereas TGF- $\beta$ 3 and L-Proline showed no cytotoxic effect on the HeLa cells. These results confer with findings observed from literature discussed above. Non-cancerous cells lines should be used for ascorbic acid to test the cytotoxic effects as ascorbic acid is directly linked to the treatment of cancerous cell lines and therefore does not give a true representation of the effects on normal mammalian cell lines. In addition to this, repeats of the cytotoxicity assay should be performed with non-cancer cell lines to test if the result differ considerably from the ones obtained in this study. The FTIR analysis of the formulated hydrogels showed partial characterization of the hydrogels however gaps in the spectrums when comparing to literature were observed. More repeats and collection of data from more batches of hydrogels for ATR-FTIR should be performed to increase the accuracy and strength of the results obtained, as well as the use of  $^1H$  NMR should be performed to better characterize the hydrogels (Salami *et al.*, 2020) and to give a better representation between the characterization and polymerization results observed in swelling, degradation and cell viability assays. Hydrogel bioinks PEGDA/HAMA and GelMA/PEGDA showed their printability through the printed constructs of the 3D resin printer using LCD UV screen however it is still a proof of concept and tuning and replicates still needs to be done to further confirm the hydrogel bioink

printability. In addition to this, characterization of the printed constructs needs to be done, as well as cell infiltration and viability. Three-dimensional resin printer using visible light should also be used for encapsulation of cells for tissue generation using 3D hydrogel scaffolds. This will allow for better understanding of the capability of using the formulated hydrogel bioinks as a steppingstone in 3D tissue engineering and regenerative medicine.

## Chapter 5: Cell adherence and viability on hydrogel scaffolds

### 5.1 Introduction

An essential characteristic of hydrogel scaffold design are the mechanical properties of the scaffold; specifically properties related to strength, stiffness, degradation, swelling, viscoelasticity, elasticity and surface (Beckett *et al.*, 2020; L. Wang *et al.*, 2020). In the *in vivo* environment cells are continuously exposed to the mechanical forces of the extracellular environment. The cells exhibit various mechanical signals based on the elasticity of a matrix. These mechanical signals are then transduced into various physiological responses. Several studies including Beckett *et al.*, 2020; L. Wang *et al.*, 2020, Tamura *et al.*, 2015 and Afewerki *et al.*, 2019, have shown evidence that the mechanical properties of hydrogel scaffolds influence the regulation of fundamental cellular programs such as migration, signalling pathways differentiation and proliferation. Some examples on the influences that the mechanical properties of biomaterials have on cell signalling pathways and behaviours are shown in Table 8.

**Table 8: Biomaterial mechanical property influence on cell and signalling pathways.** Table was adapted from (L. Wang *et al.*, 2020).

Mechanical Property	Influence on cell behaviour
Elasticity/ stiffness -Influencing	<ul style="list-style-type: none"> <li>• Differentiation induction of MSCs into various cell end points</li> <li>• Activation of <math>\beta</math>-catenin transduction and integrin pathway in ASCs</li> <li>• Influencing the phenotype and functionalization of terminal cell types</li> </ul>
Stress/strain	<ul style="list-style-type: none"> <li>• Inducing the nuclear translocation of myocardin related transcription factor in valve interstitial cells (VICs)</li> <li>• Activating the TGF<math>\beta</math> pathway and the MEK pathway in VICs</li> <li>• Affecting cell phenotypic change and functions</li> </ul>
Viscoelasticity/ stress relaxation	<ul style="list-style-type: none"> <li>• Influences cell spreading, differentiation and proliferation</li> <li>• <math>\beta</math>1 integrin, actin polymerization and actomyosin-based contractility in myoblasts</li> <li>• Can cause LINC complexes to be involved in the response in myoblasts</li> </ul>

As shown in Table 8, the effect of different mechanical properties of biomaterials plays a vital role in cell signalling and pathway and choice of the biomaterial and subsequent mechanical property will directly influence the effectiveness of tissue reconstruction of the defective tissue.

As part of the mechanical properties of hydrogels, surface area and porosity are important factors for nutrient transport and diffusion, cell migration and infiltration throughout the scaffold. If cells are seeded onto the scaffold, cellular adhesion to the scaffold is critical (Tamura *et al.*, 2015; Afewerki *et al.*, 2019). Polymer type, natural, synthetic or semi-synthetic determines the surface area and subsequent cell adhesion to the scaffold. One factor, which differs between the natural and synthetic is the binding sites present between the two polymers. Natural polymers such as gelatin, retain protein binding sites allowing the cell membrane proteins to interact and bind to the proteins of the scaffold surface. Synthetic polymers such as PEGDA lack protein binding sites for protein cell membranes to bind to the ligands present on the surface on the polymer. As a result modification to synthetic polymers such as RDG peptides need to be incorporated in the polymer to allow for effective cell adhesion (Lienert *et al.*, 2014; Tamura *et al.*, 2015; Beckett *et al.*, 2020). As the hydrogel scaffold acts the extracellular environment, the cell binding the proteins present in the hydrogel allows for increased cellular interaction between cells, the scaffold and nutrients present in the scaffold allowing the cells to carry out their biological functions (Tamura *et al.*, 2015). In short the biomaterial with matched mechanical properties to the defective tissue will improve the facilitation of the tissue reconstruction (L. Wang *et al.*, 2020).

Tissue engineering (TE) sets out to induce tissue-specific regeneration processes, allowing the immune system to overcome the consistent drawbacks of organ transplants, including organ donor shortages and organ rejection due to the immune system, which then requires immunosuppressive therapy. The principle of TE is the development of biological substitutes to maintain, restore and improve tissue function (Caddeo, Boffito and Sartori, 2017; Gensler *et al.*, 2020). In replicating tissues and organs for the maintenance, restoration and improvement of tissue function and even replacement, grafts need to be generated to help the transition of the generated tissue into the *in vivo* environment, reducing the risk of rejection. These grafts form part of scaffolds, 3D structures enabling cellular growth, proliferation and differentiation for the desired tissue. These scaffolds exhibit properties, including cell adhesion, biocompatibility, porosity, and can be of artificial or biological origin (Gensler *et al.*, 2020).

Tissue culture and engineering started and is still performed in a 2D manner for culturing cells for several different types of research areas ranging from cancer research, drug discovery and stem cell research (Ferreira, Gaspar and Mano, 2018). However, 2D monocultures for preclinical studies lack many requisite phenotypic characteristics important for their utility in predictive drug assays. In the *in vivo* environment, cells and tissues grow in a 3D setting, actively surrounding the extracellular matrix (ECM), allowing for the gene expression profile and providing stimuli that greatly influence cellular interactions, growth and differentiation (Edmondson *et al.*, 2014; Jensen and Teng, 2020). Three-dimensional models have gained much interest in the possibility of independently identifying and modulating cellular and molecular factors for disease progression and onset and tissue regeneration and formation in regenerative medicine. This 3D microenvironment and culture conditions plays a crucial factor in proper tissue development and growth (Gensler *et al.*, 2020). The choice of scaffold and

materials making up the scaffold composition is dependent on the target tissue and the type of cells that will be present to create the target tissue that has similar properties to that found in the *in vivo* environment, e.g. GelMA is towards chondrocytes, PEG and peptides used towards HMSCs and Fibrin used towards NT2 neurons (Billiet *et al.*, 2012; Gopinathan and Noh, 2018). Bioink types are tailored to specific cell types and have unique polymerization methods to create the 3D scaffold structure. Hyaluronic acid with gelatin methacrylate crosslinks via photopolymerization, agarose-based gels are polymerized via ionic cross-linking, collagen via pH-mediated cross-linking and Silk/PEG via thermal/chemical polymerization (Gopinathan and Noh, 2018).

Each type of polymerization method has its advantages and disadvantages, with specific reference to photoinitiation polymerization as it pertains to this study. The main drawback is the polymerization using UV light, which is detrimental to cell viability if cells are encapsulated during the photopolymerization. Although excess exposure harms cell viability, the use of UV for photopolymerization adds the advantage of effective sterilization if cells are added to the scaffold after polymerization. There are several different types of methods for cross-linking to avoid the harmful exposure of UV to cells however additional sterility methods are required to make the hydrogel scaffold suitable for tissue culture.

Long UV exposure will also affect the mammalian cell viability having a detrimental effect. Kotturi *et al.*, 2017; Noshadi *et al.*, 2017 and Xia *et al.*, 2017 demonstrate the effects of long UV exposure on cell viabilities within hydrogel scaffolds, with the majority of cell viabilities ranging within 60 % and sometimes higher. The approach with this cell viability assay was aimed at seed cells on top of the hydrogel to assess the hydrogel's biocompatibility with the HeLa cells, thereby evading UV exposure's detrimental effects. Seeding on top of the hydrogel disks also shows the cells' ability to infiltrate within the hydrogel disk and assess the subsequent cell viability.

**Aim for this chapter:**

- Determine the optimal hydrogel composition for mammalian cell viability and proliferation.

**Objectives for this chapter include:**

1. Perform sterility testing to determine if hydrogel scaffolds are suitable for cell culture.
2. Determine cell viability and proliferation of mammalian cells in hydrogel scaffolds using ReadyProbes™ Cell Viability Imaging Kit (Blue/Green).

## **5.2 Methods and Materials**

### **5.2.1 Materials**

Materials and solvents were acquired from Sigma-Aldrich and Thermo Fisher Scientific unless stated otherwise. Poly (ethylene) glycol diacrylate, gelatin-bovine skin, hyaluronic acid visible light photoinitiator Eosin Y, TEA and NVP, Vegitone infusion broth (Cat. No. 41960) and bacterial agar (Cat. No. A5306) were all sourced from Sigma-Aldrich. were all purchased from Sigma-Aldrich. Dulbecco's Phosphate Buffered Saline (DPBS) was  $\text{Ca}^{2+}/\text{Mg}^{2+}$ -free and all cell media and FBS from Gibco, which was sourced from Thermo Fisher Scientific. ReadyProbes™ Cell Viability Imaging Kit (Blue/Green) from Invitrogen™ via Thermo-Fisher Scientific (Cat. No. R37609).

### **5.2.2 Hydrogel preparation**

The GelMA, PEGDA, GelMA/PEGDA, GelMA/HAMA and PEGDA/HAMA hydrogels were prepared and cross-linked as previously discussed in Chapter 3 sections 3.2.2-3.2.6. Polymerization of the hydrogels was performed as described in section 3.2.2-3.2.6 using the same photoinitiator concentrations, mixing times and polymerization times under the UV light at wavelength 405 nm.

### **5.2.3 Hydrogel preparation for cell viability assay.**

Hydrogels were made up and cross-linked, as stated in 5.2.2. Once cross-linked, hydrogel disks ( $\varnothing = 8$  mm; height = 3 mm) were punched using a sterilized metal punch ( $\varnothing = 8$  mm). Hydrogels disks were transferred into mini petri dishes (NEST) and immersed in excess 70 % ethanol for 5 minutes in a Biosafety Class I hood. After 5 minutes of soaking in 70 % ethanol, the disks were washed twice with tissue culture grade DPBS  $\text{Ca}^{2+}/\text{Mg}^{2+}$ -free and placed in a 24-well plate, after which 1 ml of DMEM, 10 % FBS, 1 % Penicillin/Streptomycin was added to the wells with hydrogel disks present. The 24-well plate was then incubated at 37 °C, 5 %  $\text{CO}_2$  for 24-hours before seeding HeLa cells at cell densities of 5000 and 50 000 cells/ hydrogel disk.

### **5.2.4 Sterility testing of formulated hydrogels**

Vegitone agar plates (1 % w/v) were prepared by mixing Vegitone infusion broth at a ratio of 37 g/1000 ml ddH<sub>2</sub>O with bacterial agar at a ratio of 1 % w/v. The mixture was then autoclaved at 121 °C for 20 minutes. The agar plates were made up to test the sterility of pre-polymerized, non-sterilized and sterilized hydrogels. The hydrogel mixtures were made up as state in 5.2.2, after which the pre-polymerized mixture was spread plated (200  $\mu\text{l}$ ) onto the Vegitone agar plates. The hydrogels were polymerized, and disks of a diameter of 8 mm and 2 mm were punched using a sterile metal punch ( $\varnothing = 8$  mm) from the UV cross-linked gels. One set of hydrogel disks were plated onto the agar plates. The second set was washed with 70 % ethanol for 5 minutes, followed by two washes with tissue culture grade DPBS and plated onto the agar plates. The plates were incubated for 48-hours at 37 °C, after

which the colony-forming units (CFU) were assessed and counted. All plating was performed using standard microbiological aseptic technique, and the control consisted of tissue culture grade DPBS, which was used to make up hydrogel mixtures.

### 5.2.5 HeLa cell culturing and seeding onto hydrogels

HeLa cells were resuscitated from liquid nitrogen, grown in DMEM, 10 % FBS, 1 % Penicillin/Streptomycin, incubated at 37 °C, 5 % CO<sub>2</sub> for 4 days until 80 % confluent. Once the cells were confluent, they were lifted using trypsin, counted and seeded onto the hydrogel disks at cell densities of 5000 cell/hydrogel disk and 50 000 cells/hydrogels for the cell viability hydrogel assay.

### 5.2.6 Live/dead cell staining in GelMA, PEGDA, GelMA/PEGDA, GelMA/HAMA and PEGDA/HAMA hydrogels

Cell viability was carried out using ReadyProbes™ Cell Viability Imaging Kit (Blue/Green) from Invitrogen™. After 24-hours of incubation, the cell culture media was aspirated, and two drops/ml of each blue and green dye from the cell imaging kit was added as per manufacturer's instructions to fresh DMEM, 10 % FBS, 1 % Penicillin/Streptomycin. Once added and mixed with the media, 1 ml of media was added to each well and then viewed using the EVOS FL Auto 2 microscope. Images were taken using the DAPI (excitation/emission maxima: 360/460 nm), GFP (excitation/emission maxima: 504/523 nm) and Brightfield settings. Controls included hydrogels without cells seeded into the wells or on top of the hydrogels and positive controls with cells seeded in the plate's wells with no hydrogel present. Visualization and image capture were carried out using the EVOS FL Auto 2 microscope at 4 x magnification using DAPI (360/460 nm), GFP (504/523 nm) filter sets, and Brightfield microscopy. Cell viability was repeated in triplicates. Cell viability was quantified using Image J (1.52v, Java 1.80\_112 (64-bit)) software (Schneider, Rasband and Eliceiri, 2012) for all images captured for the hydrogels using the following equation:

$$\text{Cell Viability (\%)} = \frac{\text{Total live cells (Blue)}}{\text{Total Live(Blue) + Total dead (Green)}} \times 100$$

**Equation 3: Cell viability (%) formula modified from (Kartolo *et al.*, 2018).** Total live cells (blue) are divided by the total live (blue) & dead (dead) cells, multiplied by 100.

### **5.2.7 Numerical Data & Statistical Analysis**

All experiments were carried out in triplicate, and data represented as mean  $\pm$  standard deviation. The cell viability graphs were visualised using Microsoft Excel 365. All counting of cells from the DAPI/GFP images were performed using ImageJ (1.52v) software. All error bars are representative of standard deviation. Statistical analysis was done by TIBCO Statistica (version 13.5.0.17) software using a one-way ANOVA for single comparisons; Factorial ANOVA was performed to determine the statistical significance between cell viability days 1,3, and 7. A Tukey HSD post hoc test was performed for all comparisons.



## 5.3 Results and Discussion

### 5.3.1 Sterility testing of formulated hydrogels

Sterility testing of the pre-polymerized, non-sterile and sterilized hydrogels was performed using Vegitone nutrient agar over 48-hours. All hydrogel mixtures and disks were plated using aseptic technique. After 48-hours, the plates were assessed, and the CFU counted and recorded. The sterility results and CFU counts are shown below in Figure 33 and Table 9, respectively.

**Table 9: Contamination count from pre-polymerized, unsterilized and sterilized hydrogels plated on vegitone agar plates for 48-hours.**

Sample	Colony Forming Units (CFU)		
	Pre-polymerization	Unsterilized disks	Sterilized disks
10 % GelMA	TNTC	0	0
10 % PEGDA	0	0	0
5 % GelMA/ 5% PEGDA	0	0	0
10 % GelMA/0.5 % HAMA	0	0	0
10 % PEGDA/0.5 % HAMA	0	0	0
DPBS control	NA	0	0

\*Too Numerous To Count = TNTC

\*\*NA = nonapplicable

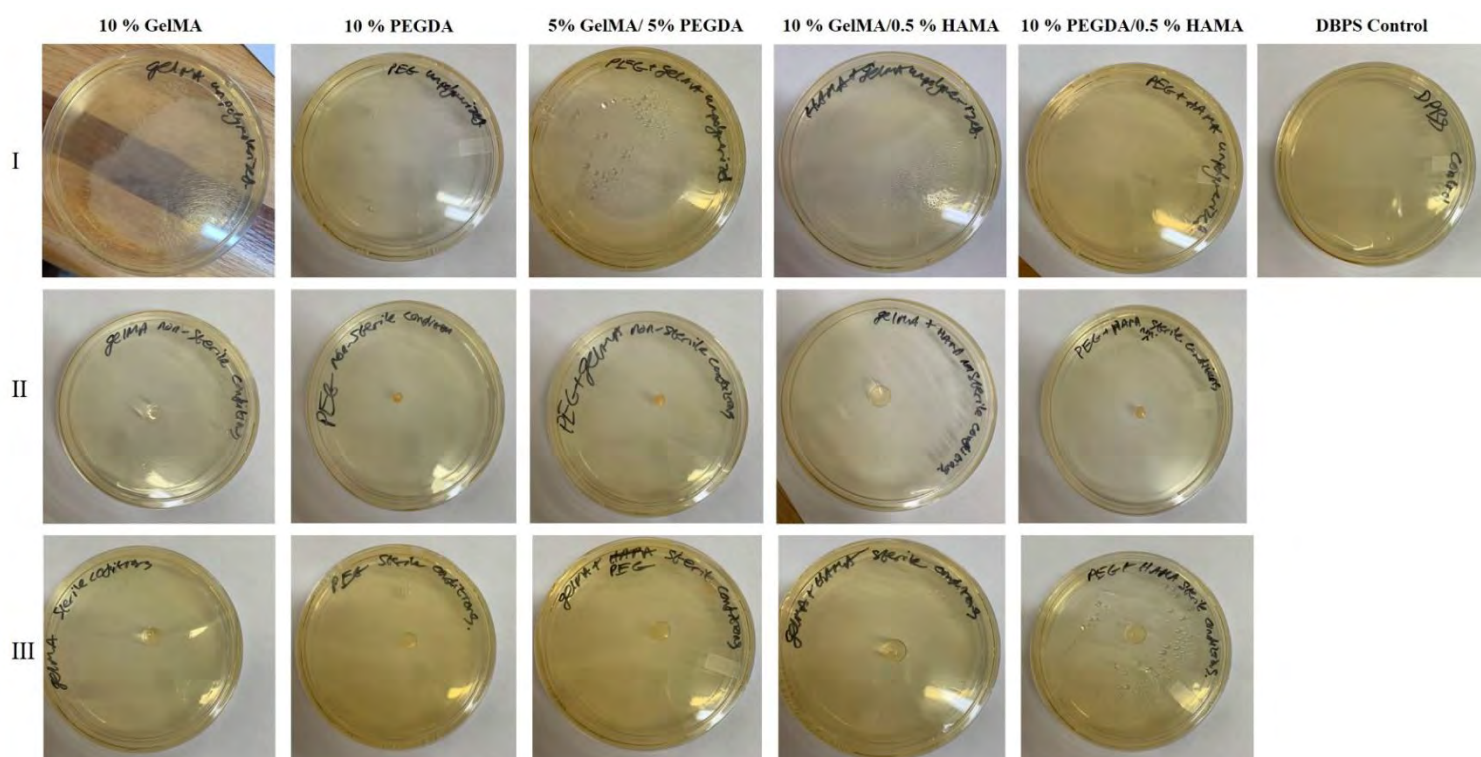


**Figure 33: Vegitone agar plates 48-hours after plating pre-polymerized (I), unsterilized (II) and sterilized (III) hydrogel disks. The control consisted of DBPS sterile for tissue culture (I). Images are representative of n=3.**

UV sterilization is a standard method of sterilization that is commonly used in the food industry; portable water and wastewater treatments offering several advantages such as no residue or by-products after sterilization, does not require heat for microbial inactivation, easy to use, and low cost (De Sá Silva *et al.*, 2003; Pullerits *et al.*, 2020). UV irradiation targets the nucleic acids, which absorb at 254 nm. It causes a mutagenic effect leading to cell division retardation as a result of the links formed between adjacent molecules of the pyrimidine dimers in the RNA and DNA, which then interferes with the transcription and replication of the microorganisms (De Sá Silva *et al.*, 2003; Pereira *et al.*, 2014). Different microorganisms have different UV susceptibility, where some only require short periods of UV exposure to cause cellular death, where others require more extended periods of UV exposure to cause cell death. In addition to this, some microorganisms can repair the UV damage by photoreactivation or dark repair because the UV exposure time is not long enough to do substantial damage to the DNA or RNA (Pullerits *et al.*, 2020). Using UV to polymerize the bioinks serves a dual purpose, cross-linking the bioinks to form 3D hydrogel scaffolds and sterilization of the bioinks for tissue culture. However, the UV exposure time must be efficient to sterilise the bioinks for tissue culture completely. However, this affects the degree of polymerization of the hydrogels, affecting porosity, stiffness and mechanical properties of the hydrogel scaffold. With this in mind, sterility testing should be performed to assay whether the time taken for the hydrogel scaffold to polymerize is efficient for scaffold sterilization or additional sterilization methods need to be taken such as ethanol sterilization.

The sterility testing shown in Figure 33 and Table 9 shows the CFU after 48-hours of incubation of the pre-polymerized hydrogel mixture, non-sterilized and sterilized polymerized hydrogel disks. The images in Figure 33 and CFU counted in Table 9, unpolymerized GelMA hydrogel mixture produced bacterial colonies that produced a lawn and were too numerous to count. The remainder of the unpolymerized hydrogel mixtures showed no bacterial colonies, and the non-sterilized, sterilized polymerized hydrogel disks and tissue culture grade DPBS control.

Figure 33 and Table 9 shows the sterilization effects used to prepare the hydrogel disks for tissue culture on the Vegitone agar plates (Figure 33) and subsequent counted colonies after 48-hours of incubation (Table 9). Three different hydrogel states were tested to determine the extent of sterility of each state of the hydrogels and whether the sterilization steps taken were adequate to use the hydrogels for tissue culture. A 48-hour incubation period was performed to test for any slow-growing contaminants that might not appear within 24 hours. The Vegitone agar was chosen to test for fastidious pathogenic cocci and other organisms associated with cell culture work and allied pathological investigation. Figure 33, row I, shows the pre-polymerized hydrogel mixture exposed to no UV light and plated sterilely under a flame. The 10 % GelMA hydrogel mixture was the only hydrogel to show contamination where the CFU was too numerous to count. The rest of the hydrogel mixtures showed no sign of contamination on the Vegitone agar plate after 48-hours of incubation. Both De Paula *et al.*, 2018 and Yue *et al.*, 2015 mention that GelMA exhibits as fast enzymatic degradation rate and poor mechanical properties

contributed to the lack of bactericidal properties of GelMA. In addition to this, Koser, Chinn and Saunders, 1938 reports that gelatin is a good source for bacterial growth and adhesiveness for bacterial films. These factors likely lead to the increase in susceptibility to contamination for the pre-polymerized GelMA hydrogel as seen in Figure 33 row I. Conversely based on literature from Wang *et al.*, 2019 and Romanò *et al.*, 2017, hyaluronic acid is routinely used in wound dressing as they demonstrate antimicrobial properties, as well as an antiadhesive barrier towards microbial agents. One of the interesting properties of hyaluronic acid is its ability to exert bactericidal effects due to its high viscosity (Cárdenas-Triviño *et al.*, 2017) and its ability to resist bacterial adhesion and prevention of biofilm production mainly due to its high hydrophilic nature (Cárdenas-Triviño *et al.*, 2017; Romanò *et al.*, 2017). Sautrot-Ba *et al.*, 2019 and Song, Rane and Christman, 2012 represent PEGDA as an antimicrobial agent and demonstrate its uses in wound healing dressing due its amphipathic and antifouling properties(Song, Rane and Christman, 2012; Sautrot-Ba *et al.*, 2019). Song, Rane and Christman, 2012 goes on to state that through the addition of lysine and arginine it can create antimicrobial peptides in the PEGDA polymer, which can facilitate binding and insertion into the bacterial membrane causing membrane disruption, depolarizing and inhibition of cell wall synthesis (Song, Rane and Christman, 2012). These properties of HA and PEGDA could explain the reasoning why no contamination was observed in the pre-polymerized hydrogels containing HA and PEGDA.

Row II shows the polymerized hydrogel disks exposed to UV light for the length of time it took to polymerize each hydrogel type. After 48-hours of incubation, no sign of contamination appeared on the plates after UV exposure to polymerize the hydrogels. These results show that the UV exposure to polymerize the hydrogels may have been sufficient to kill microorganisms present in the pre-polymerized 10 % GelMA polymer. Row III shows the sterility of the polymerized hydrogels disks exposed to UV, followed by various time lengths followed by washing 70 % ethanol and sterile DPBS  $\text{Ca}^{2+}/\text{Mg}^{2+}$ -free.

Based on the agar plates in row III, no contamination was seen on any of the plates showing that with UV light and 70 % ethanol, any contaminants present were killed and therefore would be suitable for tissue culture. The effect of sterility can further be seen in the negative controls of the live/dead cell staining of the hydrogels in Figures S8-S13 in the appendix section. Although no contamination was observed in row II, exposure to UV light without 70 % ethanol wash, the addition of 70 % ethanol to further sterilize the hydrogel disks reduces any chance of possible contamination that might occur even after UV exposure since the UV lamp used only produces UVA and UVB light. The addition of ethanol sterilization allows for those microorganisms that are able to survive when exposed to UVA and UVB light. Although UVA and UVB is able to kill the most common and non-pathological microorganism it is not effective against all. In order for UV sterilization to be completely effective, UVC light (200-280 nm) needs to be used and has shown to be an effective disinfectant (Mackenzie, 2020). UVA and UVB can be effective for sterilization of the most commonly encountered microorganisms however UVC is

the optimal UV light for effective sterilization against contaminants with however, if the length of UV light is not sufficient or a mutant contaminant species is present in the sample, the contaminant may be able to survive the UV exposure, thereby invalidating any results obtained from mammalian cell assays.

### **5.3.2 Cell viability analysis of hydrogel scaffolds**

Cell viability analysis was performed by seeding HeLa cells on polymerized hydrogel disks and evaluating the viability using standard DAPI (360/460 nm) - Live cells and GFP (504/523 nm) - dead cells filter sets. Cell viability assessment was performed 1, 3 and 7 days after cell seeding and a comparison between 5000 and 50 000 seeding densities on the cell viability was also performed. Results of the cell viability analysis are shown in Figures 34-41. Images of the negative controls can be found in the appendix section in Figures S8-S13.

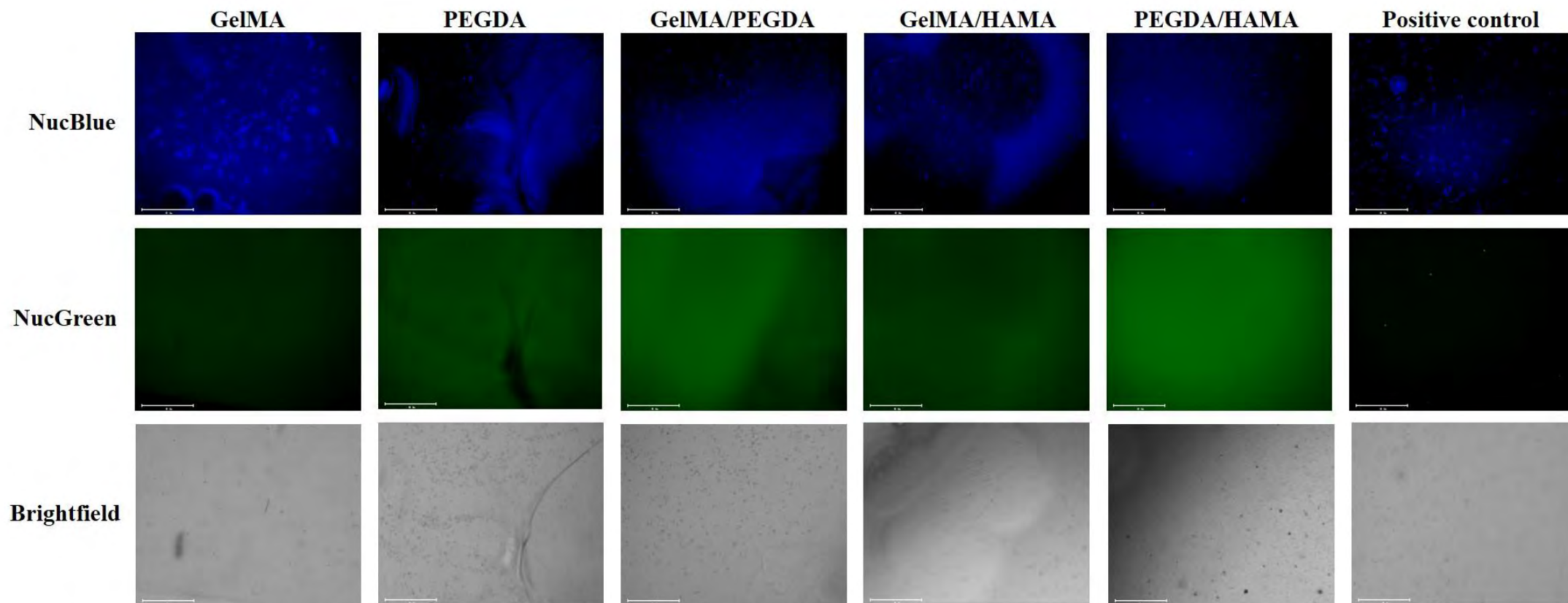


**Figure 34: Cell viability images from formulated hydrogels after 24-hours cell seeding at a cell density of 5000 cells/hydrogel disk.** Each image represents N = 9 and each batch experiment had n = 3. Scale bar on each image = 650  $\mu$ M.

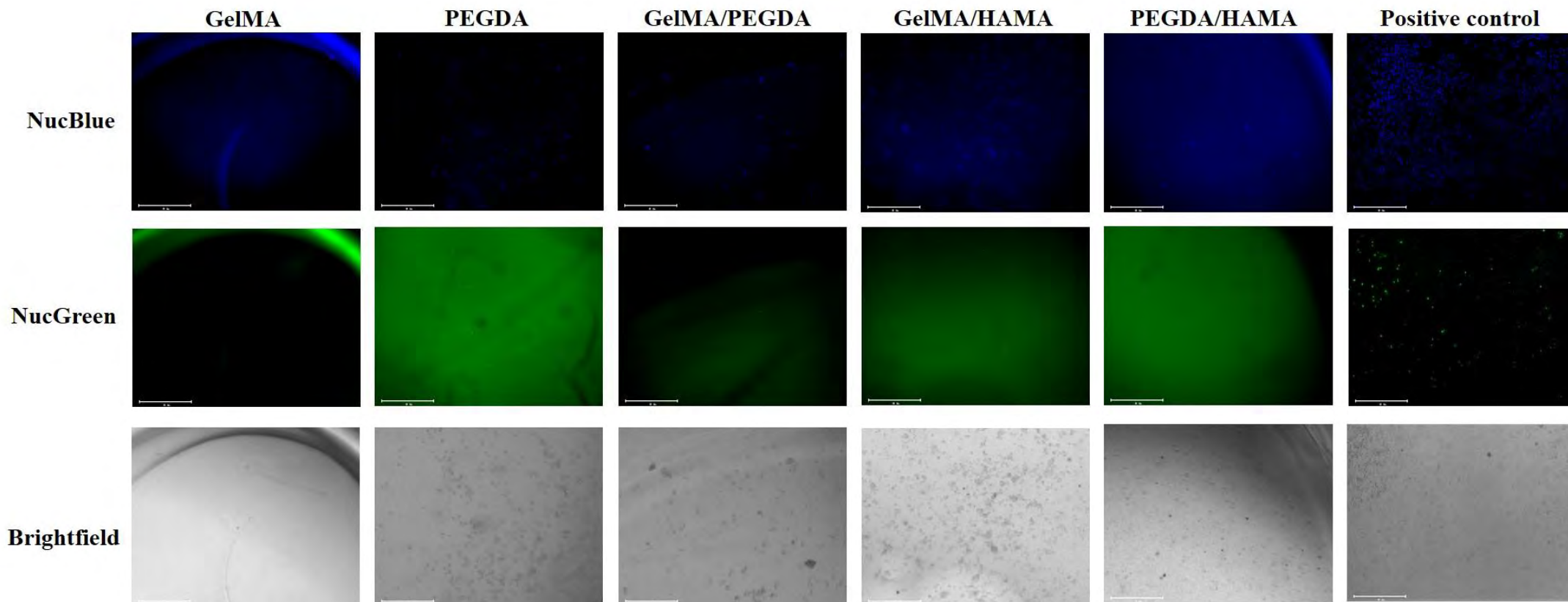


**Figure 35: Cell viability images from formulated hydrogels after 36-hours cell seeding at a cell density of 5000 cells/hydrogel disk.** Each image represents N = 9 and each batch experiment had n = 3. Scale bar on each image = 650  $\mu$ M.



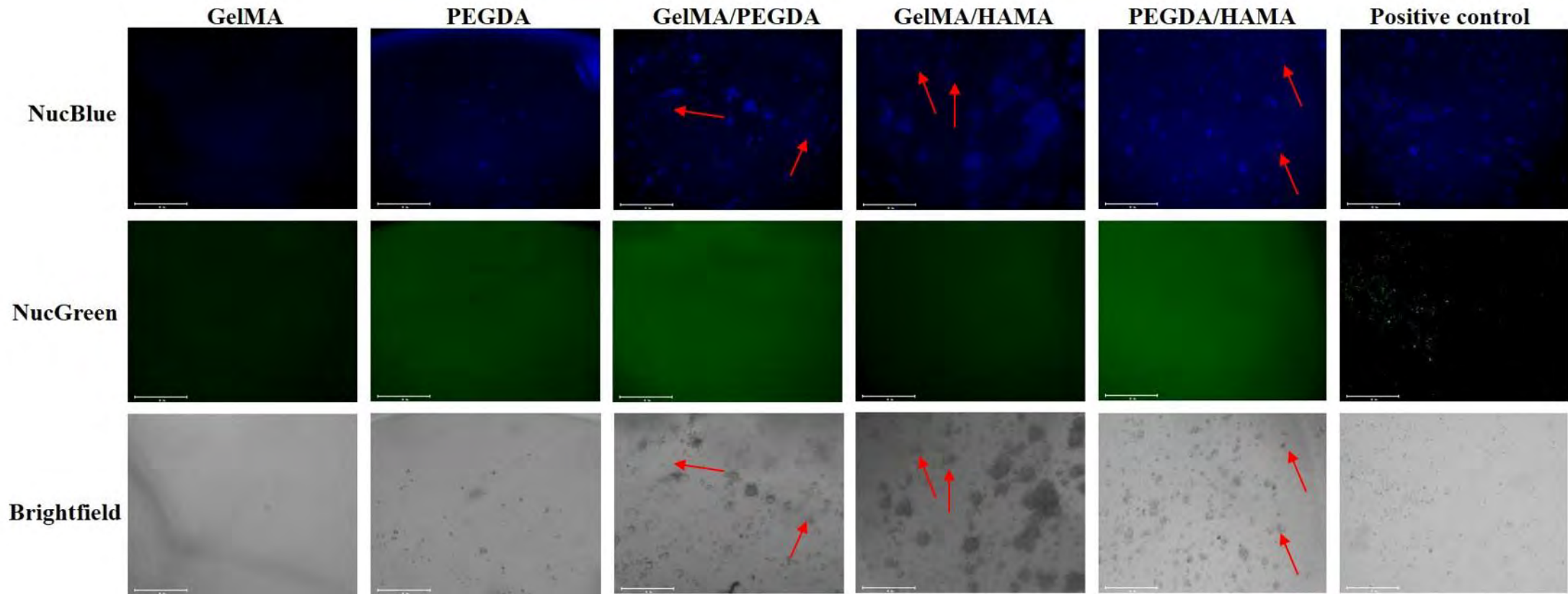


**Figure 36: Cell viability images from formulated hydrogels after seven days cell seeding at a cell density of 5000 cells/hydrogel disk. Each image represents N = 9 and each batch experiment had n = 3. Scale bar on each image = 650  $\mu$ M. Red arrows show the cell infiltration withing the hydrogel disk.**

Figure 34 shows the cell attachment, proliferation and infiltration of the hydrogels after 24-hours of incubation following cell seeding on top of the hydrogel disks. The NucBlue images shows the live cells using the DAPI filter present on the hydrogel scaffold disks. The GelMA disk showed the highest number of live cells followed by the GelMA/HAMA. The PEGDA/HAMA showed the lowest number of live cells present. Some absorption of the NucBlue reagent by the hydrogel is observed and is also slightly observed in the PEGDA negative controls in the appendix section. The NucGreen images show the dead cells present on the hydrogel disk surface using the GFP filter. Little to no cell death can be seen for most of the hydrogel disks with PEGDA/HAMA showing the most cell death when compared to the other hydrogel disks. Similar to the NucBlue reagent, high background absorption of the NucGreen reagent is shown in the hydrogel disks. Both the NucBlue and NucGreen background absorption can obscure live and dead cells present on the hydrogel disks and can cause inaccuracies of the cell viabilities of each hydrogel type. The PEGDA hydrogel seem to retain most of the NucGreen reagent giving the highest GFP background emission, which can also be seen in the negative controls found in the appendix section. The high background absorbance may be due to the phalloidins present within the fluorescent dyes and bind to the proteins within the hydrogels (Belin, Goins and Mullins, 2014). The brightfield images show the cells present on the hydrogel disk using the brightfield filter. The cells are represented as the dark grey spots while the hydrogel disk represent the light grey background. Difference between the GelMA NucBlue and brightfield images can be observed where more cells are represented in the NucBlue image than in the Brightfield. This could be the result of cell infiltration into the hydrogel thus displaying the live cells present in the hydrogel with little cells present on the surface of the hydrogel as seen the brightfield image. Similar differences between the NucBlue PEGDA and brightfield PEGDA images are also seen with more cells shown on the surface of the PEGDA in the brightfield image than the NucBlue and NucGreen images. This could be the result of the increased affinity for the PEGDA hydrogel to retain the NucBlue and NucGreen reagents causing higher DAPI and GFP background emission and thus causing live and dead cell obscurities. According to manufacturing's product information, NucGreen dead reagent stains only the nuclei of dead cells with comprised plasma membranes. In addition, no literature could be found explaining the uptake of the NucGreen reagent by the hydrogels and thus remains unknown. Further testing needs to be done to help explain the uptake of the reagent by the hydrogels.

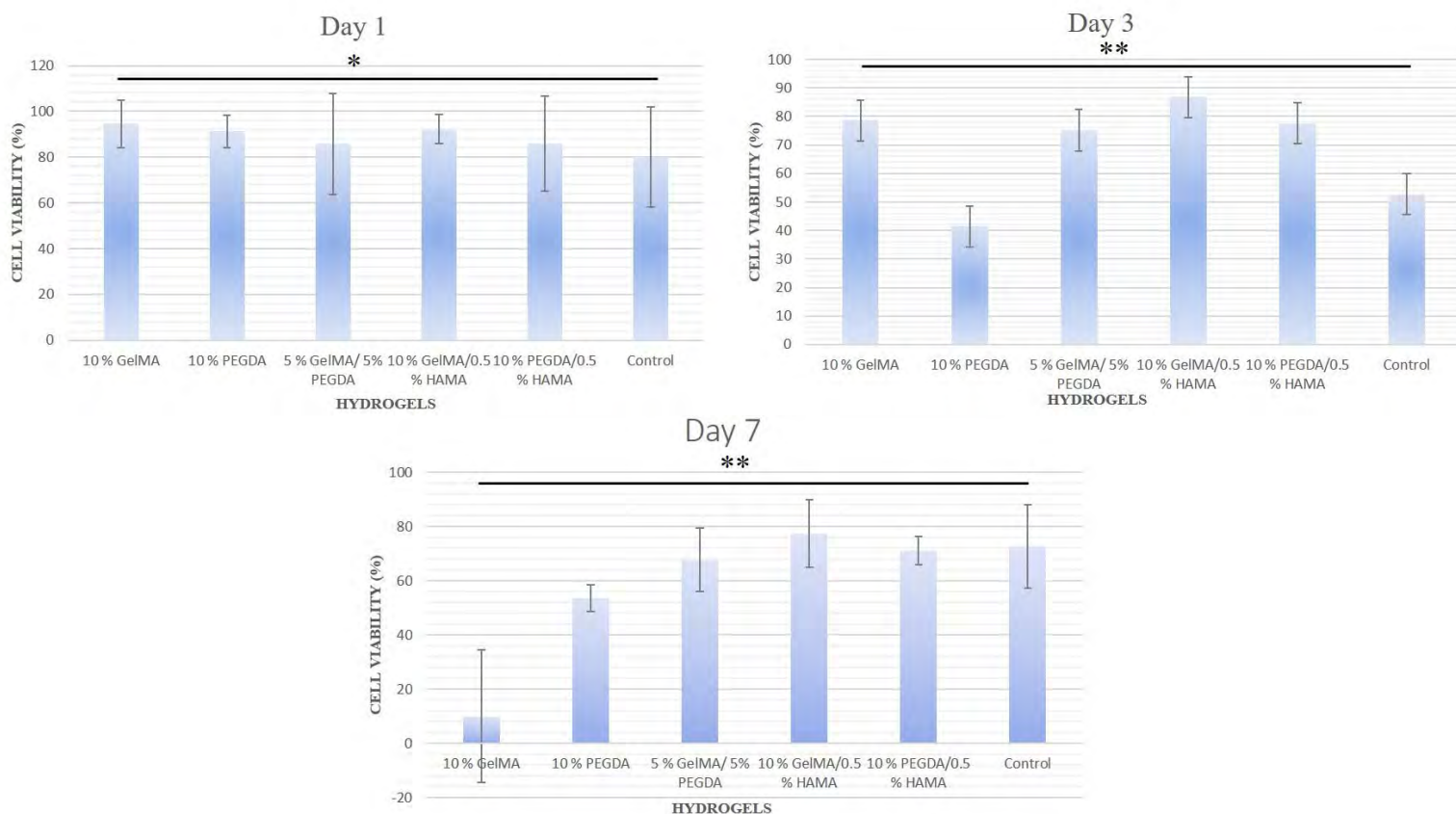
Figure 35 shows the cell attachment and proliferation of HeLa cells after 36-hours of incubation on the hydrogel disks. The hydrogel disks, 10 % GelMA/0.5 % HAMA followed by 10 % GelMA, showed the highest cell attachment and proliferation based on the live cells in the NucBlue images with only a few dead cells present in the NucGreen staining than all the other hydrogel disks. The 10 % PEGDA showing the lowest cell viability of all hydrogel disks as it displayed least amount of attached and proliferated cells in the NucBlue staining image and high amounts of dead cells in the NucGreen staining images. Similar to the hydrogel disk of PEGDA and PEGDA hybrid hydrogels in Figure 34,



the GFP background emission in the hydrogels is high creating obscure results for the number of dead cells present. Cell numbers present on the in the NucBlue images for GelMA hydrogel disk decreased from 24-hours to 36-hours, suggesting a decrease in the cellular attachment as the number of dead cells present in the NucGreen was not high enough to suggest mass cell death. The 5 % GelMA/5 % PEGDA hydrogel showed a similar trend in the cellular attachment; however, it still showed relatively high cell numbers present from the NucBlue staining with few dead cells observed in the NucGreen images. The same absorption of the NucGreen reagent by PEGDA and PEGDA associated hydrogels can be seen with the negative controls in the appendix section. All bright field images in Figure 35 show the same cell placement as the NucBlue and NucGreen staining. This indicates that little to no cell infiltration into the hydrogel disks occurred after 36-hours.

Figure 36 shows the cell viability of HeLa cells seven days after cell seeding. Based on the images, 10 % GelMA/0.5 % HAMA showed the greatest cell viability, producing the highest live cells present in the NucBlue image with few dead cells observed in the NucGreen images, followed by 10 % PEGDA/0.5 % HAMA and 5 % GelMA/5 % PEGDA. The PEGDA hydrogel disks showed an increase in cell viability from 36-hours as there was an increase in live cells present stained by NucBlue and lower dead cells stained by the NucGreen, whereas 10 % GelMA resulted in a mass decrease in cell viability from day 1 and 3 as the number of dead cells stained in the NucGreen images was higher than the previous 24-hour and 36-hour NucGreen staining results. The live cells present dramatically decreased compared to the 24 and 36-hour staining of NucBlue. The brightfield images mostly correlate with the NucBlue and NucGreen cell staining, however some cells in the NucBlue and Brightfield in the same focal plane are out of focus as shown with the dedicated red arrows in Figure 36. This suggests that some cell infiltration may have occurred based on the stained cells being out of the focal plane. Adjustment of the focal plane would bring them into focus as it would be focusing on the different sections within the hydrogel disk.

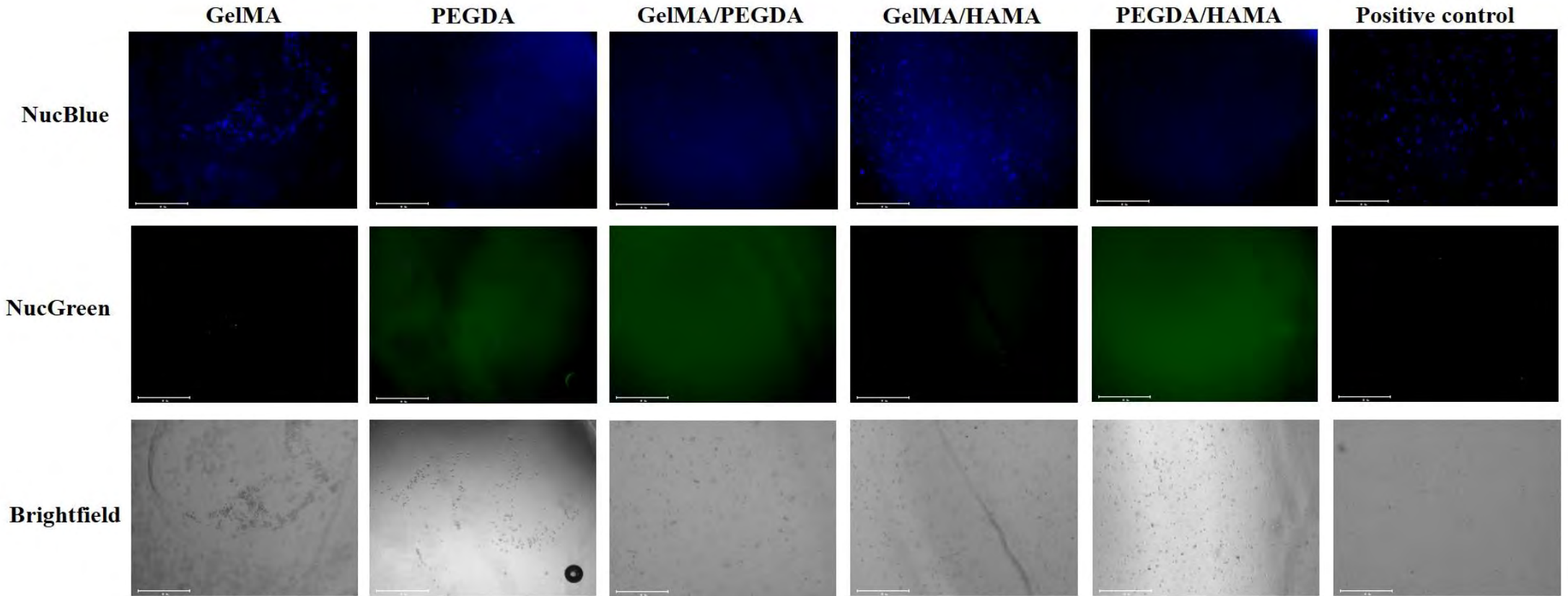
Cell viability was performed for the formulated polymerized hydrogels. On days 1,3, and 7, after cell seeding, NucBlue (live cells) and NucGreen (dead cells) staining was performed to determine the cell viability. Counting of the NucBlue and NucGreen fluorescent cells through DAPI (360/460 nm) and GFP (504/523 nm) filters was performed using ImageJ (1.52v) software where the threshold was adjusted respectively to take into account of cell aggregates and clumps present. The cell counts were then graphed using Microsoft Excel 365 for days 1,3 and 7 and are shown below in Figure 37 for 5000 cells/hydrogel disk.



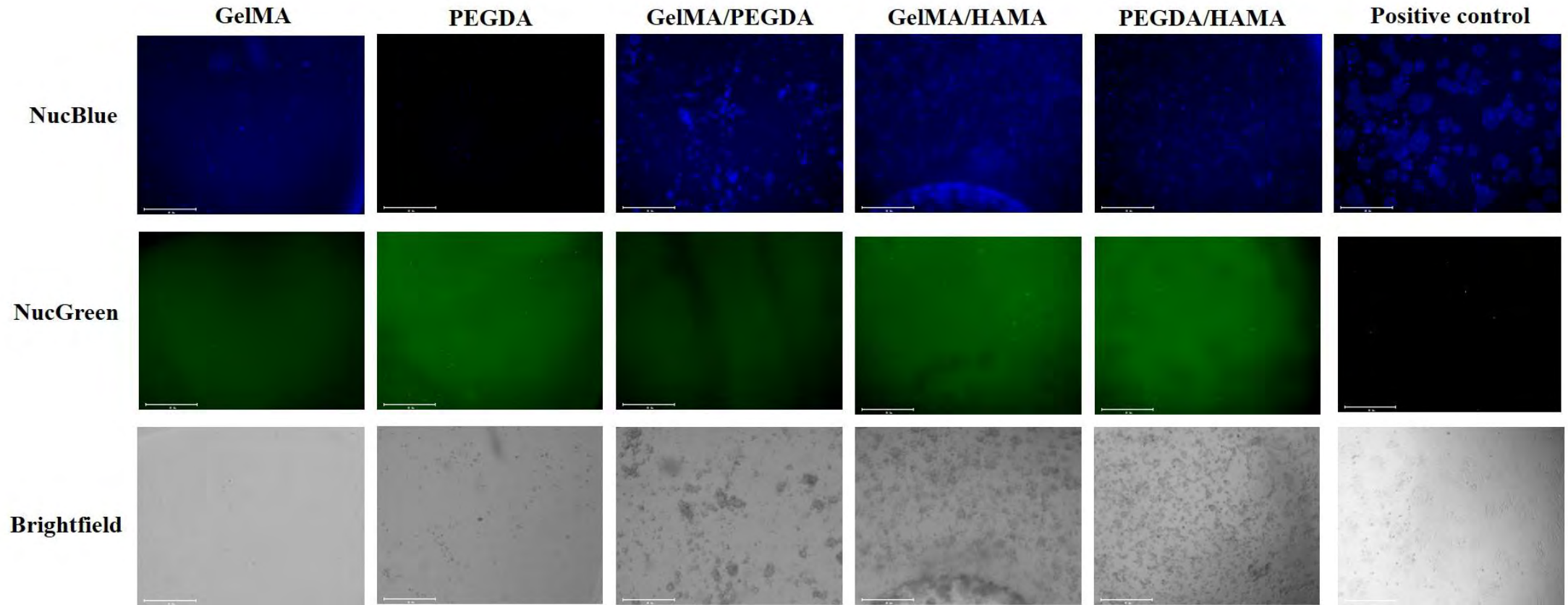
**Figure 37: Cell viability (%) of formulated hydrogels after 1,3 and 7 days with an initial 5000 cell seeding density using HeLa cells.** Graphs were generated from the live/dead cell count and using the cell viability (%) formula in equation 2. Cell counts were performed using Image J software (1.52v). Graphs were then generated using Microsoft Excel 365 software. Error bars represent standard deviation. Each bar graph represents live/dead cells counted from NucBlue/NucGreen images where N = 9 and each batch experiment had n = 3. The statistical significance resulted in \* $p > 0.05$  for day 1 and \*\* $p < 0.05$  for day 3 and 7.

Figure 37 shows a graphical representation of the cell viability observed in Figures 34-36. After one day of incubation on the hydrogel disks, the cell viability remained above 80 % for all hydrogel types with 10 % GelMA and 10 % GelMA/0.5 % HAMA resulting in the highest cell viability 94.6 % and 92.3 %, respectively. 10 % PEGDA and 10 % PEGDA/0.5 % HAMA resulted in cell viabilities of 91.28 % and 85.84 %, respectively and 5 % GelMA/5 % PEGDA having the lowest cell viability of 85.80 %. After three days, 10 % GelMA/0.5 % HAMA had the highest cell viability of 86.7 %, followed by 10 % GelMA with 78.6 %. A significant decrease in cell viability of 41.4 % in the 10 % PEGDA hydrogel from day 1 (91.3%) was observed on day 3. Hydrogel disks 5 % GelMA/5 % PEGDA and 10 % PEGDA/0.5 % HAMA produced cell viabilities of 75.16 % and 77.60 %, respectively. On day 7, 10 % GelMA/0.5 % HAMA remained to have the highest cell viability of 77.3 %, followed by 10 % PEGDA/0.5 % HAMA with 72.5 %. A significant decrease in cell viability for the 10 % GelMA of 10 % from 78.6 % on day three was observed. Hydrogel disks 10 % PEGDA and 5 % GelMA/5 % PEGDA produced cell viabilities of 53.64 % and 67.65 %, respectively. Day 1 cell viability produced a statistical

significance of  $p = 0.81958$  with a current effect of  $F(4,42) = 0.38142$ . Day 3 cell viability produced a statistical significance of  $p = 0.00426$  with a current effect of  $F(4,42) = 4.9917$ . Day 7 cell viability produced a statistical significance of  $p = 0.0000$  with a current effect of  $F(4,42) = 25.871$ . Figure 37 and the relevant statistics mentioned above show that there is no statistical difference between the hydrogel disks and the control on day 1. Day 3, 10 % PEGDA shows a statistical difference when compared to the control and the other formulated hydrogel disks. Day, 10 % GelMA shows a significant difference to the control and other hydrogel disks. Figure 37 and the statistics show that over a 7-day period, 10 % GelMA and 10 % PEGDA are not optimal hydrogels to support cell viability in comparison to the significant differences of the other hydrogels when compared to the hydrogel.



**Figure 38: Cell viability images from formulated hydrogels after 24-hours cell seeding at a cell density of 50 000 cells/hydrogel disk. Each image represents N = 9 and each batch experiment had n = 3. Scale bar on each image = 650  $\mu$ M.**



**Figure 39: Cell viability images from formulated hydrogels after 36-hours cell seeding at a cell density of 50 000 cells/hydrogel disk. Each image represents N = 9 and each batch experiment had n = 3. Scale bar on each image = 650  $\mu$ M.**

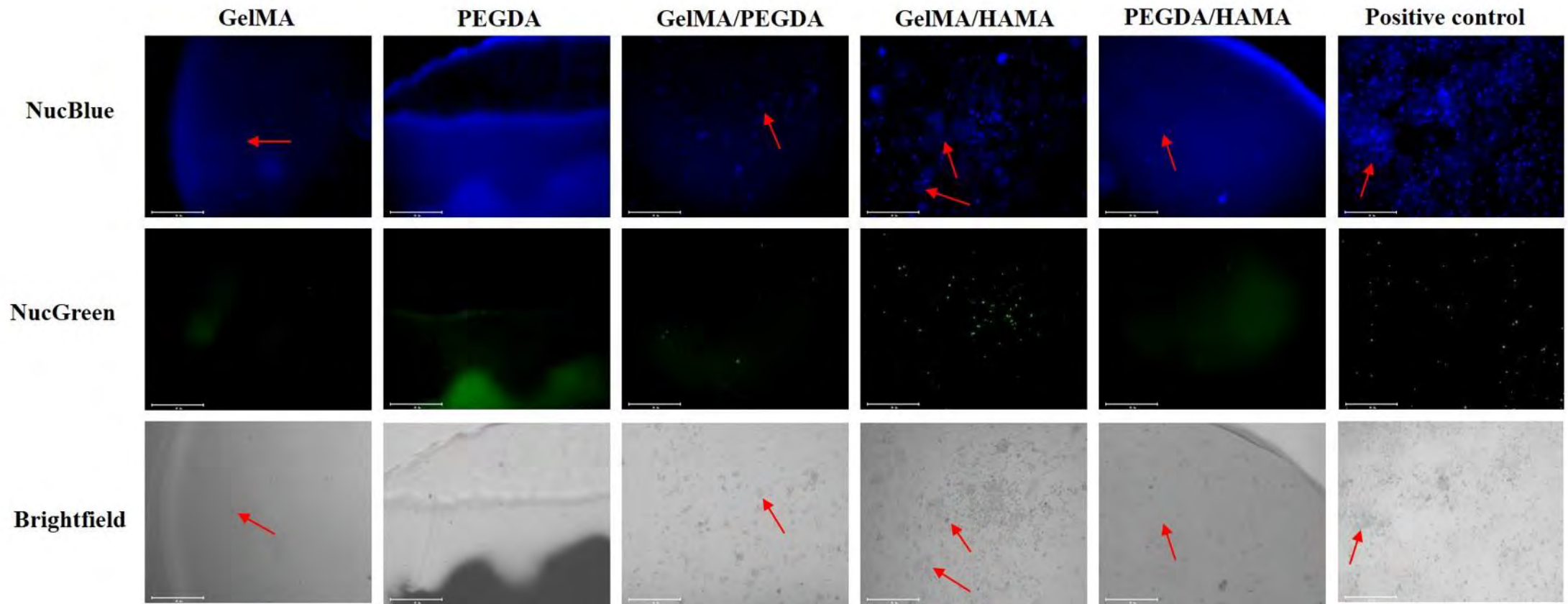


**Figure 40: Cell viability images from formulated hydrogels after seven days cell seeding at a cell density of 50 000 cells/hydrogel disk. Each image represents N = 9 and each batch experiment had n = 3. Scale bar on each image = 650  $\mu$ M.**

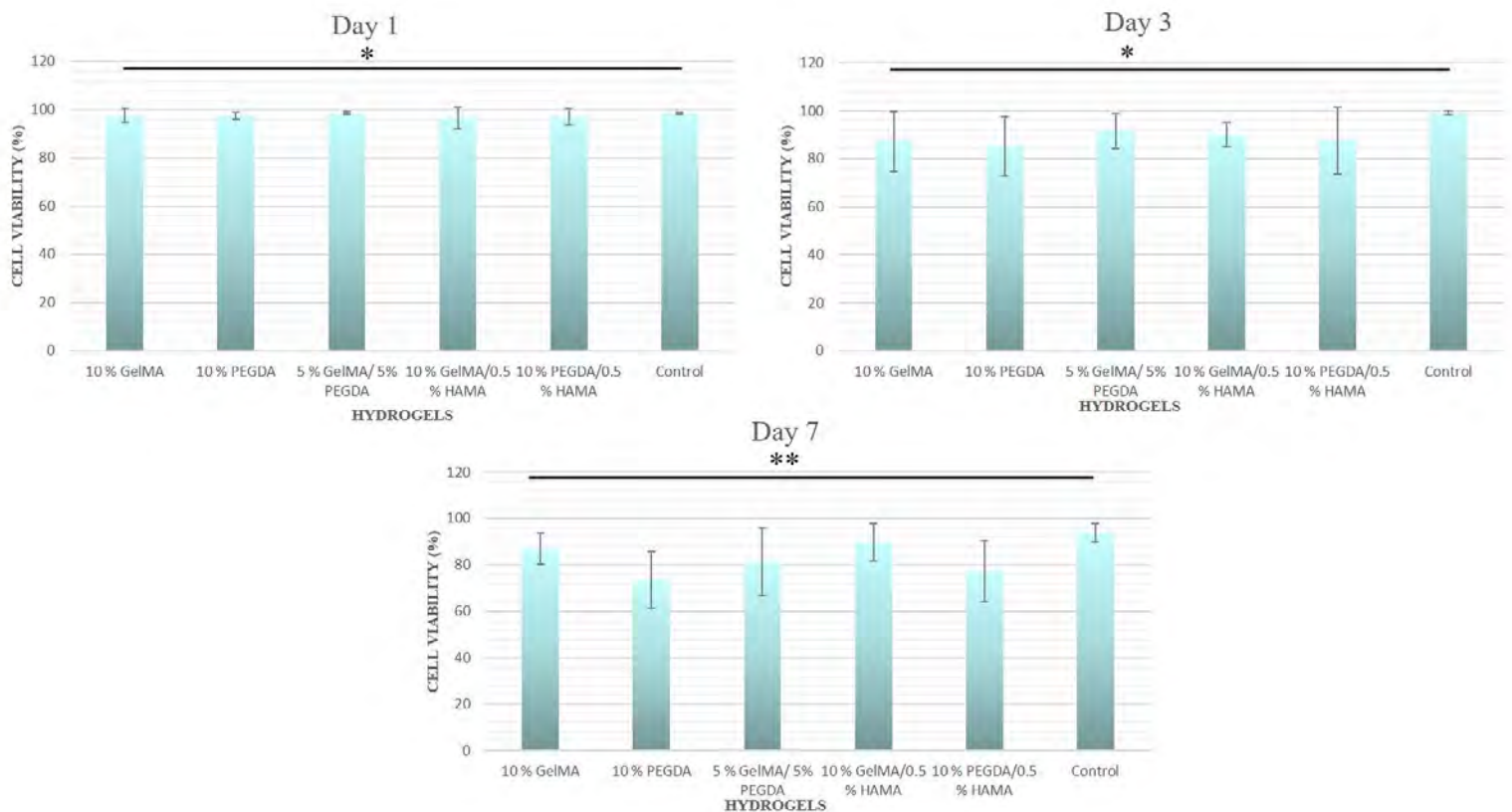
Figure 38 shows the cell attachment, proliferation and infiltration of the hydrogels after 24-hours of incubation following cell seeding of 50 000 HeLa cells on top of the hydrogel disks. The NucBlue images shows the live cells using the DAPI filter present on the hydrogel scaffold disks. The 5 % GelMA/5 % PEGDA hydrogel disk showed the highest cell attachment and proliferation shown through the number of NucBlue cell stained with little to no NucGreen cells seen, followed by the 10 % GelMA and 10 % PEGDA hydrogel disks. The 10 % GelMA/0.5 % HAMA showed the lowest cell attachment and proliferation after 24-hours of incubation with higher NucGreen cells present than the other hydrogel disks. Similar to the 5000 cell/disk images the cells in the brightfield images are represented by the dark grey spot where the hydrogel disk is shown be light grey.

Figure 39 shows the cell attachment and proliferation after 36-hours cell seeding, with the 5 % GelMA/5 % PEGDA showing the highest cell attachment and proliferation with high NucBlue cells present and low NucGreen cells stained followed by the 10 % GelMA/0.5 % HAMA hydrogel. The 10 % PEGDA hydrogel disk showed a decrease in cell attachment and proliferation from day one as there was an increase in NucGreen cell present and decrease of NucBlue cells with the 10 % GelMA and 10 % PEGDA/0.5 % HAMA hydrogel disks showing the same trend.

Figure 40 shows the cell viability seven days after cell seeding resulting in the 10 % GelMA/0.5 % HAMA hydrogel disk having the highest cell viability based off high NucBlue and low NucGreen cells visible compared to the other hydrogels, followed by the 10 % GelMA hydrogel disk. The 10 % PEGDA showed the lowest cell viability for all hydrogel types after seven days of incubation with increased NucGreen cells been stained and only few NucBlue stained cells present. Cell infiltration into the hydrogel disk was also observed as several NucBlue and NucGreen stained cells were out of focus in the same plane of view where others were in focus and is shown by the red arrows present on the images, suggesting the cells had imbedded themselves deeper within the hydrogel, thus demonstrating cell infiltration. The increase fluorescent absorbance with the NucGreen stain of the PEGDA and PEGDA associated hydrogels is apparent as seen in the Figures 38-40 above. The negative controls in the appendix section (Figures S8-S13) show the same fluorescent absorbance as seen in Figures 38-40. This fluorescent absorbance seems to be consistent through the PEGDA and PEGDA associated hydrogels as the same absorbance by the hydrogels was observed in the 5000 cells/disk images (Figures 34-36). The NucGreen fluorescent absorbance by the PEGDA and PEGDA associated hydrogels leads to obscurities of cell counting and subsequent cell attachment, proliferation and viability assessment of the hydrogels causing the validity of the results to come into question.



Cell viability was performed for the formulated polymerized hydrogels. After 24-hour, 36-hours and 7 days staining of NucBlue (live cells) and NucGreen (dead cells) was performed to determine the cell viability. Counting of the NucBlue and NucGreen fluorescent cells was performed using ImageJ (1.52v) software. The cell counts were then graphed using Microsoft Excel 365 for days 24-hours, 36-hours and 7 days and is shown below in Figure 41 for 50 000 cells/hydrogel disk.



**Figure 41: Cell viability (%) of formulated hydrogels after 1,3 and 7 days with an initial 50 000 cell seeding density using HeLa cells.** Graphs were generated from the live/dead cell count and using the cell viability (%) formula in equation 2. Cell counts were performed using Image J software (1.52v). Graphs were then generated using Microsoft Excel 365 software. Error bars represent standard deviation. Each bar graph represents live/dead cells counted from DAPI/GFP images where N = 9 and each batch experiment had n = 3. The statistical significance resulted in \*p > 0.05 for day 1 and 3 and \*\*p < 0.05 for day 7.

Figure 41 shows a graphical representation of the cell viability observed in Figures 38-40. After one day of incubation from seeding 50 000 cells/hydrogel disk of HeLa cells, cell viability for all hydrogels remained above 95 % with 5 % GelMA/5 % PEGDA having the highest cell viability of 98.66 %, followed by 10 % GelMA with 97.58 %, 10 % PEGDA with 97.41 %, 97.22 % for the 10 % PEGDA/0.5 % HAMA hydrogel disk and 10 % GelMA/0.5 % HAMA having the lowest cell viability of all the hydrogels with cell viability of 96.38 %. The positive control showed a 98.63 % cell viability. The statistical significance between the hydrogels for day one resulted in a p-value of p = 0.59449 with a current effect of F(4,42) = 0.70275.



After three days of incubation, 5 % GelMA/5 % PEGDA remained the highest cell viability with 91.57 %, 10 % GelMA/0.5 % HAMA with 90.02 %, 10 % PEGDA/0.5 % HAMA with 87.63 %, 10 % GelMA with 87.30 % and 10 % PEGDA with the lowest cell viability of 85.12 %. The control resulted in a 99.14 % cell viability. The statistical significance of cell viability between the hydrogel types resulted in a p-value of  $p = 0.76787$  with a current effect of  $F(4,42) = 0.45521$ .

Seven days after incubation resulted in 10 % GelMA/0.5 % HAMA having the highest cell viability of 89.64 %, followed by 10 % GelMA with 87.03 %, 5 % GelMA/5 % PEGDA with 81.47 %, 10 % PEGDA/0.5 % HAMA with 77.29 % and 10 % PEGDA having the lowest cell viability of 73.62 %. The positive control resulted in cell viability of 93.78 % after seven days of incubation in the 24-well plate. The statistical significance between the hydrogel disks after seven days of incubation resulted in a p-value of  $p = 0.03005$  with a current effect of  $F(4,42) = 2.9717$ . From day 1-3 no statistical differences were observed for the hydrogel disks when compared to the control as the p-value was not significant. On day 7, a statistical difference was observed for 10 % PEGDA when compared to the control and the other hydrogel disks. This shows that the 10 % PEGDA is less than optimal to support cell viability when compared to the control and other hydrogel disks for a 7-day period or longer.

**Table 10: Statistical analysis of the cell viability of the formulated hydrogels between 5000 cells/disk and 50 000 cells/disk after 1, 3 and 7 days of incubation.**

Days	P-Value	Current Effect F(4,84)
1	0.56002	0.75244
3	0.00532	4.1190
7	0.00000	14.477

After one day of incubation, there was no statistical difference in cell viability between any of the hydrogel types for 5000 cells/disk and 50 000 cells/disk datasets, respectively. In addition to this, no statistical significance was observed between the comparative cell viability assays of 5000 cells/disk and 50 000 cells/disk. This indicates, in addition to the live/dead cell images acquired, that all hydrogel types offer suitable forms for cellular attachment, with 10 % GelMA having the highest cell attachment with 5000 cells/disk and 5 % GelMA/5 % PEGDA having the highest with 50 000 cells/disk followed then by the 10 % GelMA. The discrepancy between 10 % GelMA having a higher cell attachment with 5000 cells/disk than with 50 000 cells/disks could result from inaccuracies when pipetting the cell solution onto the hydrogel disk. The hydrogel disk was smaller in diameter than the size of the well in the 24-well plate. In addition to this, media was added to each well 24-hour before cell seeding to increase the hydrogel porosity. The downside to this was the hydrogel took up the media's colour, making it challenging to pipette on top of the disk accurately. The consequence was that between the two cell seeding densities, the 50 000 cell/disks might have experienced more cell suspension overflow as a result of more volume of cell suspension required than with the 5000 cells/disk, causing a result in lower cell viability on day 1. The inaccuracies of pipetting and cell overflow is also the likely reason

the large standard deviations present within the bar graphs for day 1. Increasing the hydrogel disks' diameter to the wells' diameter would prevent cell overflow and show a better comparison of cell attachment, viability, and reduce the standard deviation and error as seen on day 1 in Figures 37. The use of a shaker to continuously shake the plate with the disks could evenly disperse the cells across the disk, as well as for any overflow of cells to move and allow them a chance to adhere to the disk. The use of a shaker may also improve the circulation of nutrients throughout the hydrogel disk, which would lead to increase cell survival.

After 3 and 7 days of incubation, a statistical significance was observed between the hydrogels seeded with 5000 cells/disk and 50 000 cells/disk with 50 000 cells/disk having a higher cell viability than 5 000 cells/disk. The differences in cell viabilities could be due to the lack of cellular niches and communications occurring with the 5000 cells/disk assay. Due to the large spatial areas between the cells, it may have caused a lack of cell-cell interaction, which is essential for cell survival and thus resulted in the increased cellular death as cells require communications and relay on each other for survival. Both Verma, Verma and Singh, 2020 and Wei and Huang, 2013 explain in great detail the importance of cell-cell interactions and the effects it has on cell functioning and survival. This observation can be seen in Figures 34-36, where there is a significant distance between each cell, whereas in Figures 38-40, the cells are significantly closer, forming cellular niches with each other and showing stable cell viability throughout the 7-days.

Studies performed by Kotturi *et al.*, 2017, Noshadi *et al.*, 2017 and Xia *et al.*, 2017 perform the hydrogels' cell viability after exposure to UV to encapsulate the cells within the hydrogel. The major downside to this is the UV exposure to a cell, as some bioinks require longer UV exposure times than others. The long UV exposure time results in a higher decrease in the cell viability of the hydrogel. Also, based on the polymerization times in chapter 3, the long UV exposure times to polymerize would have a significant adverse effect on cell viability. Since the photoinitiator used was a visible light based photoinitiator, cell encapsulation using visible light could have been performed in an aseptic environment. However in preliminary hydrogel polymerization tests performed, using visible light to polymerize the hydrogels at the non-cytotoxic concentrations discuss in chapter 4, the length of time to polymerize the hydrogels was lengthy. Polymerization times ranged based on the hydrogel type of nothing shorter than 45 minutes to one and half hours. This length of time would require the cells to be in an incubator environment (37 °C, 5 % CO<sub>2</sub>) or designed bioreactor to avoid cell death during the polymerization process. The choice of UV was faster, allowed for effective sterilization and for at least 95 % cell viability within the first 24-hours of seeding. Therefore, it was chosen to seed the cells on top of the hydrogel disks, assess the cell viability, and then observe if cell infiltration occurred. Throughout Figures 36 and 40, some cell infiltration was observed and can be seen pointed out with the red arrows present on the images. Cell infiltration into the hydrogel disk was observed as several NucBlue and NucGreen stained cells were out of focus in the same plane of view where others were in focus,

suggesting that some cells had imbedded themselves more profound within the hydrogel, thus demonstrating cell infiltration. For proper viewing and determination of cell infiltration and depth of cell infiltration, Z-stacked images can be performed giving 3D viewing of the hydrogel disks and positioning of the cells within the hydrogel disk. Part of chapter 3 shows the pore sizes of SEM measuring smaller than average cell size, indicating that the cells seeded on top of the disk would not infiltrate into the hydrogel disk. However, based on the results observed in the cell viability staining images, it shows that due to the 24-hour swelling before cell seeding, the pore sizes expanded, allowing for some cell infiltration into the cell. In addition to this, cells such as HeLa cells have shown to change their shape and size to squeeze through pores or channels that are smaller than the cell size and shape. Nath *et al.*, 2018 demonstrates the ability of HeLa cells of change shape and size, squeezing through constructed microcapillaries. Based on the fact that cells are able to change shape and size, given the small pores observed in the SEM images in chapter 3, it is possible that cells were able to infiltrate deeper within the hydrogel scaffolds.

The GelMA and GelMA hybrid hydrogels retained the highest cell viabilities compared to the PEGDA hydrogel and PEGDA hybrid hydrogels. The properties of GelMA such as excellent biocompatibility, strong cellular adhesion result from the aqueous environment and promotion of cell growth and proliferation (Pepeanova *et al.*, 2018; Liu *et al.*, 2020), support the findings observed in the cell viability staining for days 1 and 3. After seven days, however, the cell viability significantly fell with the 5000 cells/disk from 94 % to 10 %, which was unexpected due to the advantageous characteristics of GelMA. This could have been due to two reasons. Firstly, the low seeding cell densities causing a lack of cell-cell interactions, leading to cell death as mentioned above, or GelMA's poor mechanical property, which was observed during media changes and staining thought the 7-days. The GelMA hydrogel disk produced an ongoing problem where after an extended period, it became softer, gel-like and was sucked up by the pipette when changing media, whereas, with the other hydrogels, they retained a more rigid structure preventing from being aspirated. The aspiration of the hydrogel disk resulted in some of the disks to break up. This process may have led to an increase in cellular death. It was noted for the 50 000 cells/disk comparative assay where the cell viability of the GelMA was maintained at 87 % after 7-days. More care was taken when aspirating the media; however, the gel was aspirated in some instances. However, the gel kept its structure due to the care taken. The seeding density was also significantly increased to ensure cell-cell interactions. As a result, the changes in cell viability were minimal for the 10 % GelMA hydrogel and the rest of the hydrogel disks. Similar findings of cell viability for GelMA hydrogel done by Seo *et al.*, 2020 and Ramón-Azcón *et al.*, 2012 demonstrate the advantageous use for GelMA hydrogel cellular scaffolds show cell viabilities of 95 % for both studies.

A consistent trend in the decrease of cell viability of PEGDA hydrogels and PEGDA hybrid hydrogels despite the increase in cell density for cell-cell interactions was observed. Kotturi *et al.*, 2017 mentions that PEGDA scaffolds of more than 1 mm in height have shown a reduced cell viability due to

inadequate access to nutrients. The lack of porosity of PEGDA further amplifies the lack of nutrient delivery and thus increasing the cells that cannot survive within the PEGDA hydrogel scaffold. Khandaker *et al.*, 2016 reports the same observation made by Kotturi *et al.*, 2017 stating the PEGDA hydrogel scaffold of more than 1 mm in height leads to a significant reduction in cell viability. This is most likely the cause of the significant decrease observed by the PEGDA hydrogel and PEGDA hybrid hydrogels over the seven days. The hydrogel disks made in this study were made with a height of 2 mm, double the threshold height for PEGDA hydrogel scaffolds. Also, of the 2 mm height, the lack of porosity of PEGDA and the SEM images in the chapter explains why there was such a significant decrease in the PEGDA hydrogel's cell viability from day 1 to 7. A similar decrease in cell viability was observed Wang *et al.*, 2015, where the PEGDA hydrogel initially had an initial cell viability of 85 % and decreased down to 55 % after five days.

The use of hybrid hydrogels, using the primary polymer and incorporating small percentages of other polymers to increase the primary polymer's effectiveness, is becoming a more widely used type of hydrogel than the standard alone hydrogels such as GelMA PEGDA. The 10 % GelMA/0.5 % HAMA hybrid hydrogel showed the highest cell viability over seven days, with both seeding at 5000 cells/disk and 50 000 cells/disk achieving cell viabilities of 77 % and 89 %, respectively. GelMA has many advantageous properties for tissue culture, as mentioned above; however, the poor mechanical property and long gelation time observed in this study hinders the effectiveness of GelMA. Hyaluronic acid plays a crucial role in the proliferation, survival, growth and differentiation of cells (Yazdani *et al.*, 2019). It supports cellular structure and functioning (Zhai *et al.*, 2020), thus benefiting cell survival. Having the benefits of GelMA and HAMA thus increase the hydrogels ability to maintain cell viability within the scaffold, and its effects are seen in this study. Camci-Unal *et al.*, 2013 and Schuurman *et al.*, 2013 both performed a comparative assay between GelMA and GelMA/HAMA. Their results showed that the addition of HAMA significantly increases cell viability within the hydrogel scaffold when compared to standard polymer hydrogel GelMA. These results align with the results observed for the hybrid hydrogel 10 % GelMA/0.5 % HAMA. Schuurman *et al.*, 2013 also showed the trend that the hybrid hydrogel GelMA/HA had lower cell viability than the GelMA initially. After three days, the hybrid hydrogel had increased in cell viability 3 % and 10 % higher than the cell viability of the GelMA hydrogel. These results are also observed over the seven days compared to the GelMA hydrogel and the GelMA/HAMA hybrid hydrogel.

As mentioned above, with regards to the PEGDA hydrogel with reduced cell viability due to lack of nutrient exchange, the hybrid hydrogel 10 % PEGDA/0.5 % HAMA seems to maintain 71 % and 77 % 5000 cells/disk and 50 000 cells/disk, respectively. This hybrid hydrogel showed a significantly less reduction in cell viability (%) than the 10 % PEGDA hydrogel. Based on HA's properties, incorporating HAMA with the PEGDA greatly improved the efficiency of the PEGDA polymer as a cellular scaffold. The PEGDA/HAMA is a novel idea for a hybrid hydrogel, as such, literature is limited to the

combination of the two polymers. Yu *et al.*, 2014, however, did show cell viability results of PEG/HA, which showed excellent cell viability after seven days. Therefore, the addition of HAMA significantly improves the PEGDA hydrogel's capability to be used as a tissue scaffold. Similarly, the results showing the 5 % GelMA/5 % PEGDA showed a similar relationship to the PEGDA/HAMA, where the addition of GelMA generates a positive effect on the cell viability of the PEGDA hydrogel. There was still a decrease in cell viability, more so with 5000 cells/disk than the 50 000 cells/disk; however, in comparison to the PEGDA hydrogel, 5 % GelMA/5 % PEGDA retained cell viability of 81 % and 68 % for the 50 000 cells/disk and 5000 cells/disk where the PEGDA hydrogel had decreased 73 % and 53 % respectively after seven days, giving more than 10 % increase in cell viability. Wang *et al.*, 2015 and Y. Wang *et al.*, 2018 reported similar findings where the addition of GelMA to the PEGDA showed a significant increase in cell viability.

Although HeLa cells provide useful insight into cell viabilities and cellular attachment for hydrogel scaffolds, this study's scaffolds were not chosen and tailored specially for HeLa cells. These hydrogels are tailored towards articular cartilage and stem cells to differentiate into chondrocytes since gelatin and HA are the main constituents of articular cartilage. The use of stem cells or chondrocytes on the hydrogels would give a better representation of the cells' viability to be expected in an *in vivo* environment as all the polymers are targeted towards cellular growth, proliferation and differentiation of stem cells and articular cartilage.

In conclusion, all hydrogel formulations showed suitable cell attachment within the first 24-hours. Cell viability did start to decrease for all hydrogels after 24-hours, with PEGDA showing the most significant decrease in cell viability. Overall, the 10 % GelMA/0.5 % HAMA showed the best cell viability for HeLa cells; however, further testing will need to be done using stem cells. Repeats of this assay should be done using different cell viability staining reagents to avoid the high fluorescence background, which occurred with the hydrogels creating obscurities thereby hindering viewing and counting live and dead cells. These obscurities influence the validity and accuracy of the results and pose as a setback for this cell viability assay. Improvement to validity and accuracy of the cellular clusters can be made by using a higher magnification to properly identify what the clusters represent. Three-dimensional scanning of the hydrogels should be done to better show the cell infiltration within the hydrogel as questions of validity and accuracy of cellular infiltration can arise by just observing just different focal planes to conclude cell infiltrations. With regards to the comparison of cell density used for cell viability assays with hydrogel scaffolds, the seeding cell density does play a critical role in cell survival, and there was a significant increase in cell viability with the hydrogels seeded with 50 0000 cells/disk than those that were seeded with 5000 cells/disk. Cell seeding densities need to be high in order for effective cell-cell interactions to occur. Hydrogel disk diameters could be increased to the size of the wells to prevent over-flow to the cell suspension or the use of a shaker to evenly disperse the cells and allow for continuous circulation of the cells allowing the increase time to cell adherence.

## Chapter 6: Conclusions and Future Work

### 6.1 Conclusion

Additive manufacturing has shown great promise as a way forward for regenerative medicine and tissue engineering both for drug discovery and regeneration or replacement of tissues or organs. Organ and tissue transplants with specific reference to cartilage diseases such as rheumatoid arthritis and osteoarthritis are significant health challenges worldwide, particularly in South Africa, resulting in a great economic burden. Additive manufacturing and tissue engineering to reconstruct articular cartilage using three-dimensional scaffolds have gained much interest as a solution to diseases such as rheumatoid arthritis and osteoarthritis. However, much depends on the generation of the articular cartilage through first the choice of cells and secondly the scaffold choice, which acts as the extracellular environment that should mimic the *in vivo* one for successful reconstruction. The focus of optimizing and characterization of the scaffolds specific for cartilage tissue engineering is crucial as it allows for the establishment of adipose-mesenchymal stem cells towards chondrogenic differentiation.

Both Ad-MSCs showed chondrogenic differentiation ability with the A311019-02T cell line resulting in apparently more GAG and aggrecan secretion into the extracellular matrix than the A270620-01A cell line based on the Alcian Blue stain. However, the A270620-01A cell line resulted in higher collagen expression based on the Col10a1 and Col2a1 gene markers. Further validation and verification needs to be carried out as the number of replicates performed for the gene expression were insufficient. This gene expression could alter and differ from the 2D monolayer gene expression results obtained when the cells are placed into the 3D hydrogel scaffold. Based on literature readings and the importance of extracellular environments for cells, the extracellular environment of the hydrogel should have an impact on the differentiating and relative gene expression of the cells during the induction of chondrogenic differentiation and thus could show different gene expression results than the ones obtained in the 2D monolayer culture. Although the gene expression results correlate with the literature discussed in chapter 2, further optimization of the gene markers needs to be carried out, as well as with other important chondrogenic gene expression markers such as Aggrecan, Beta-Catenin, and Runx2 need to be quantified to correlate with the results obtained in the differentiation staining fully. Although both cell lines displayed chondrogenic differentiation ability, the stem cell isolation came from adipose tissue, a cell source not related to the target tissue, articular cartilage. Bone marrow stem cells are MSCs are used through numerous studies involving chondrogenic differentiation and cartilage stem cell-based studies. The thought being that by isolating stem cells closer to the target tissue, more capable and higher degree of differentiation may occur as these stem cells are present in a similar environment to that of the target tissue (Robey and Riminucci, 2019), carrying the epigenetic markers of their source whereas the adipose stem cells would carry the epigenetic markers for adipose tissue making them least

suitable for chondrogenic differentiation compared to the bone marrow stem cells (Robey and Riminucci, 2019; Kangari *et al.*, 2020).

Hydrogel characterisation resulted in the 10 % GelMA having the highest swelling ratio, followed by the 10 % PEGDA hydrogel. The PEGDA showed the greatest degradation ratio and was the least porous hydrogel. The 10 % GelMA/0.5 % HAMA hydrogel showed the least amount of degradation and comparable porosity with the 10 % GelMA hydrogel. Although these hydrogels showed promising swelling and degradation ratios, each assay's length of time is not equivalent to the length of time it would undergo in an animal model or human trial. Yan *et al.*, 2020, demonstrate and assess an injectable hyaluronic acid hydrogel as a hydrogel scaffold for porcine cartilage regeneration. The injected hydrogel was used in animal models, minipigs, and after 6-12 months the hydrogel scaffold resulted in superior and good histological healing, as well as better subchondral bone reconstruction after 6-12 months. Using an animal model over months-year period demonstrates the hydrogels' mechanical abilities and characterization over a long time. This thus sets up the hydrogel for human trials as a suitable scaffold for cartilage repair. This study shows the requirement for the developed hydrogels in this study to be characterized over long periods of time and is an essential requirement needed for future work for the hydrogels to progress to animal and human trials. The swelling and degradation assay was done over a 24-hour period and longer swelling assay and degradation ratios with more specific degradation enzymes, including hyaluronidase and collagenase, would give a much better representation of the hydrogel's effect could undergo in the *in vivo* setting. Based on the hydrogels' characterisation results, the 10 % GelMA/0.5 % hydrogel showed the most suitable mechanical and characterization properties of all hydrogel types and shows possible promise as a hydrogel to be used for further testing as a cellular scaffold for articular cartilage.

From the hydrogel and chondrogenic differentiation component characterisation and spectroscopic analysis, it can be concluded that the visible light photoinitiator and chondrogenic differentiation concentrations used to polymerize the hydrogels and differentiate ad-MSCs have no cytotoxic effect towards HeLa cells. They thus should have no cytotoxic effect on ad-MSC use for future work in the additive manufacturing of articular cartilage. The FTIR analysis of the formulated hydrogels showed partial characterization of the hydrogels with limited modification of the GelMA and HAMA shown in the analysis; however, the spectrums still show partial characterisation of each hydrogel type. Repeats and optimization of the FTIR and, as well as the using <sup>1</sup>H NMR analysis needs to be done as it provides higher sensitivity to better characterise the developed hydrogel chemical composition better.

The 10 % PEGDA/0.5 % HAMA and 5 % GelMA/5 % PEGDA hydrogels showed good 3D resin printing ability and resolution, matching closely with the designed CAD model in height and width. The 5 % GelMA/5 % GelMA showing the most promise between the two hydrogel bioinks printed as a 3D printing bioink to be used for further 3D resin printing. Further printing optimization needs to be

done with both hydrogel types and the 10 % GelMA/0.5 % HAMA, which could not be printed due to insufficient GelMA/HAMA material. The 5 % GelMA/5 % GelMA hydrogel bioink intricate printing ability with regards to controlled pore construction needs to be investigated, as well as 3D printing with cellular encapsulation would give better insight to capability and promise of the formulate hydrogel to be used as a possible scaffold for tissue engineering of articular cartilage.

The results from the cell viability assay in chapter 5 indicate that the 10 % GelMA/0.5 % HAMA hydrogel resulted in the highest cell viability using HeLa cells over a 7-day incubation period followed by the 5 % GelMA/5 % PEGDA having the second-highest cell viability. The difference in cell density seeding onto the hydrogel disks greatly influenced the cell viability results as it provided cells to be in a closer proximity than the 5000 cells/disk allowing to effective cell-cell interactions and communications to occur, essential for cell survival and proliferation and can therefore conclude that an increased cell density positively affects the cell viability of all the formulated hydrogel types.

In conclusion, the study was set out to develop five different hydrogel bioinks towards additive manufacturing of articular cartilage. This study shows that integrating two or more polymers, creating full-IPNs or semi-IPNs, improves the scaffolds mechanical and cellular properties, which positively affects the functionality as a cellular scaffold to be used towards additive manufacturing of articular cartilage.

## **6.2 Future Work**

Several shortcomings resulted in this study performed and several aspects that can be done to further the work done in this study, which could have great potential for the additive manufacturing of articular cartilage. As not all the chondrogenic gene expression markers could establish chondrogenic differentiation ultimately, Aggrecan, Beta-Catenin and Runx2 chondrogenic gene expression need to be done to verify the establishment of chondrogenic differentiation through RT-qPCR with A311019-02T and A270620-01A cell lines. In addition to this, replicates of Col2a1 and Col10a1 need to be done to verify the gene expression results obtained in this study and further optimise the RT-qPCR and relative annealing temperatures. The stem cells acquired originated from adipose tissue; a tissue source not related to articular cartilage. Using stem cells closely related to the target tissue may show a better degree of chondrogenic differentiation and expression compared to the adipose stem cells. A comparison between the two stem cell sources on their chondrogenic differentiation ability and expression would show which stem cell isolated source would be best suited towards additive manufacturing of articular cartilage. Further establishment of the mechanical properties of the formulated hydrogels in terms of the degradation rate with tuned degradation enzymes of those found in the respective *in vivo* environment to the relative hydrogels will show valuable insight to the effect degradation of each hydrogel type by similarly replicating the *in vivo* conditions. As these hydrogels were formulated as tissue scaffolds for articular cartilage, testing and evaluating the elastic modulus



and pressure absorbance would be more insight into each hydrogel scaffold's potential to be used in the *in vivo* of articular cartilage where significant pressure and force is exerted on the tissue. The elastic modulus will give insight into the hydrogels shock absorption, a crucial factor required in joints' cartilage tissue. The use of HeLa cells on the hydrogel scaffolds showed good insight for cell viability; however, the hydrogel scaffolds were tailored and designed for stem cell differentiation into chondrocytes to produce articular cartilage.

Cell viability using adipose-derived mesenchymal stem cells with the hydrogel scaffolds needs to be done to fully evaluate the scaffolds' ability to uphold cell survival and proliferation. In addition, the establishment of chondrogenic differentiation of the ad-MSCs in the hydrogel scaffolds needs to be performed evaluating the potential for articular cartilage formation. As a visible light photoinitiator was used to polymerize to the hydrogels, cellular encapsulation into the hydrogels using visible light should be done as the principle of additive manufacturing of articular cartilage is based on the use of 3D bioprinting of the bioinks and cells together. Following this, one can then design a light-based 3D bioprinter towards functional scaffolds for articular cartilage replacement or regeneration. Future work of these hydrogel scaffolds also involves *in vivo* studies using animal models such as a rat or guinea pig to assess the hydrogel scaffold's ability to repair and regenerate degenerated cartilage within the rat or guinea pig. This can be done by printing and encapsulating bone marrow stromal cells (BMSCs) within the hydrogel. The hydrogel would then be inserted into the joint of the defective cartilage surgically and cartilage repair and healing assessed after 6-12 months.

## Chapter 7: References

- Abbadessa, A. *et al.* (2016) 'A Synthetic Thermosensitive Hydrogel for Cartilage Bioprinting and Its Biofunctionalization with Polysaccharides', *Biomacromolecules*, 17(6), pp. 2137–2147. doi: 10.1021/acs.biomac.6b00366.
- Afewerki, S. *et al.* (2019) 'Gelatin-polysaccharide composite scaffolds for 3D cell culture and tissue engineering: Towards natural therapeutics', *Bioengineering & Translational Medicine*, 4(1), pp. 96–115. doi: 10.1002/btm2.10124.
- Aguirre-Soto, A. *et al.* (2019) 'On the role of: N-vinylpyrrolidone in the aqueous radical-initiated copolymerization with PEGDA mediated by eosin y in the presence of O<sub>2</sub>', *Polymer Chemistry*. Royal Society of Chemistry, 10(8), pp. 926–937. doi: 10.1039/c8py01459k.
- Aldana, A. A. *et al.* (2019) 'Fabrication of Gelatin Methacrylate (GelMA) Scaffolds with Nano- and Micro-Topographical and Morphological Features', *Nanomaterials*, 9(1), p. 120. doi: 10.3390/nano9010120.
- Aldridge, A. *et al.* (2013) 'Assay validation for the assessment of adipogenesis of multipotential stromal cells-a direct comparison of four different methods', *Cytotherapy*. Elsevier Inc, 15(1), pp. 89–101. doi: 10.1016/j.jcyt.2012.07.001.
- Alves, S. *et al.* (2017) 'Production and characterization of bacterial cellulose membranes with hyaluronic acid from chicken comb', *International Journal of Biological Macromolecules*. Elsevier B.V., 97, pp. 642–653. doi: 10.1016/j.ijbiomac.2017.01.077.
- An, J. *et al.* (2015) 'Design and 3D Printing of Scaffolds and Tissues', *Engineering*. THE AUTHORS, 1(2), pp. 261–268. doi: 10.15302/J-ENG-2015061.
- Ansari, S. *et al.* (2017) 'Alginate/hyaluronic acid hydrogel delivery system characteristics regulate the differentiation of periodontal ligament stem cells toward chondrogenic lineage', *Journal of Materials Science: Materials in Medicine*. Springer US, 28(10). doi: 10.1007/s10856-017-5974-8.
- Armiento, A. R. *et al.* (2018) 'Biomaterials for articular cartilage tissue engineering: Learning from biology', *Acta Biomaterialia*. Acta Materialia Inc., 65, pp. 1–20. doi: 10.1016/j.actbio.2017.11.021.
- Askari, F. *et al.* (2019) 'Reduction in protein absorption on ophthalmic lenses by PEGDA bulk modification of silicone acrylate - based formulation', *Progress in Biomaterials*. Springer Berlin Heidelberg, 8(3), pp. 169–183. doi: 10.1007/s40204-019-00119-x.

- Atala, A. and Murphy, S. V (2014) ‘3D bioprinting of tissues and organs’, *Nature Biotechnology*, 32(773), pp. 773–785. doi: org/10.1038/nbt.2958
- Badimon, L., Oñate, B. and Vilahur, G. (2015) ‘Adipose-derived mesenchymal stem cells and their reparative potential in ischemic heart disease’, *Revista Espanola de Cardiologia*, 68(7), pp. 599–611. doi: 10.1016/j.recesp.2015.02.025.
- Bahney, C. S. *et al.* (2011) ‘Visible light photoinitiation of mesenchymal stem cell-laden bioresponsive hydrogels’, *European Cells and Materials*, 22, pp. 43–55. doi: 10.22203/eCM.v022a04.
- Beckett, L. E. *et al.* (2020) ‘Enhancement of the Mechanical Properties of Hydrogels with Continuous Fibrous Reinforcement’, *ACS Biomaterials Science and Engineering*, 6(10), pp. 5453–5473. doi: 10.1021/acsbomaterials.0c00911.
- Belin, B. J., Goins, L. M. and Mullins, R. D. (2014) ‘Comparative analysis of tools for live cell imaging of actin network architecture’, *BioArchitecture*, 4(6), pp. 189–202. doi: 10.1080/19490992.2014.1047714.
- Bennour, S. and Louzri, F. (2014) ‘Study of Swelling Properties and Thermal Behavior of Poly(N,N-Dimethylacrylamide- co -Maleic Acid) Based Hydrogels ’, *Advances in Chemistry*, 2014, pp. 1–10. doi: 10.1155/2014/147398.
- Bertrand, J. and Held, A. (2017) ‘Role of Proteoglycans in Osteoarthritis’, in Grässel, S. and Aszódi, A. (eds) *Cartilage: Volume 2: Pathophysiology*. Springer International Publishing, pp. 63–80. doi: 10.1007/978-3-319-45803-8.
- Bhola, N. E. *et al.* (2013) ‘TGF- $\beta$  inhibition enhances chemotherapy action against triple-negative breast cancer’, *Journal of Clinical Investigation*, 123(3), pp. 1348–1358. doi: 10.1172/JCI65416.
- Bikram, M. *et al.* (2007) ‘Endochondral bone formation from hydrogel carriers loaded with BMP2-transduced cells’, *Annals of Biomedical Engineering*, 35(5), pp. 796–807. doi: 10.1007/s10439-007-9263-4.
- Billiet, T. *et al.* (2012) ‘A review of trends and limitations in hydrogel-rapid prototyping for tissue engineering’, *Biomaterials*. Elsevier Ltd, 33(26), pp. 6020–6041. doi: 10.1016/j.biomaterials.2012.04.050.
- Biological Industries (2015) *MSCgo™ Chondrogenic XF*. Available at: [https://www.bioind.com/worldwide/media/wysiwyg/chondrogenesis\\_protocol.pdf](https://www.bioind.com/worldwide/media/wysiwyg/chondrogenesis_protocol.pdf) (Accessed: 20 August 2020).
- BioRad (2006) *Real-Time PCR Applications Guide, Methods*. Available at: [https://www.bio-rad.com/webroot/web/pdf/lsr/literature/Bulletin\\_5279.pdf](https://www.bio-rad.com/webroot/web/pdf/lsr/literature/Bulletin_5279.pdf).

- Bishop, E. S. *et al.* (2017) '3-D bioprinting technologies in tissue engineering and regenerative medicine: Current and future trends', *Genes and Diseases*. Elsevier Ltd, 4(4), pp. 185–195. doi: 10.1016/j.gendis.2017.10.002.
- Bishop, P. N. (2010) 'Molecular composition of the vitreous and aging changes', *Encyclopedia of the Eye*, pp. 37–43. doi: 10.1016/B978-0-12-374203-2.00257-8.
- Browning, M. B. *et al.* (2014) 'Determination of the in vivo degradation mechanism of PEGDA hydrogels', *Journal of Biomedical Materials Research - Part A*, 102(12), pp. 4244–4251. doi: 10.1002/jbm.a.35096.
- Bunnell, B. A. *et al.* (2008) 'Adipose-derived stem cells: Isolation, expansion and differentiation', *Methods*, 45(2), pp. 115–120. doi: 10.1016/j.ymeth.2008.03.006.
- Burdick, J. A. and Prestwich, G. D. (2011) 'Hyaluronic acid hydrogels for biomedical applications', *Advanced Materials*, 23(12), pp. 41–56. doi: 10.1002/adma.201003963.
- Buxant, F. *et al.* (2015) 'Antiproliferative effect of dexamethasone in the MCF-7 breast cancer cell line', *Molecular Medicine Reports*, 12(3), pp. 4051–4054. doi: 10.3892/mmr.2015.3920.
- Caddeo, S., Boffito, M. and Sartori, S. (2017) 'Tissue engineering approaches in the design of healthy and pathological in vitro tissue models', *Frontiers in Bioengineering and Biotechnology*, 5(AUG), pp. 1–22. doi: 10.3389/fbioe.2017.00040.
- Camci-unal, G. *et al.* (2013) 'Synthesis and Characterization of Hybrid Hyaluronic Acid-Gelatin Hydrogels', *Biomacromolecules*, 14(4), pp. 1085–1092. doi: 10.1021/bm3019856.
- Camci-Unal, G. *et al.* (2013) 'Synthesis and characterization of hybrid hyaluronic acid-gelatin hydrogels', *Biomacromolecules*, 14(4), pp. 1085–1092. doi: 10.1021/bm3019856.
- Campbell, T. *et al.* (2012) 'Strategic Foresight Report', *Atlantic Council*, pp. 3–7.
- Cappelletti, P. *et al.* (2018) 'Proline oxidase controls proline, glutamate, and glutamine cellular concentrations in a U87 glioblastoma cell line', *PLoS ONE*, 13(4), pp. 1–20. doi: 10.1371/journal.pone.0196283.
- Cárdenas-Triviño, G. *et al.* (2017) 'Synthesis and Bactericidal Properties of Hyaluronic Acid Doped with Metal Nanoparticles', *Journal of Nanomaterials*, 2017. doi: 10.1155/2017/9573869.
- Carneiro, J. *et al.* (2016) 'Development and characterization of hyaluronic acid-lysine nanoparticles with potential as innovative dermal filling', *Brazilian Journal of Pharmaceutical Sciences*, 52, pp. 645–651.

- Chen, J. *et al.* (2021) ‘Modified hyaluronic acid hydrogels with chemical groups that facilitate adhesion to host tissues enhance cartilage regeneration’, *Bioactive Materials*. KeAi Communications Co., Ltd, 6(6), pp. 1689–1698. doi: 10.1016/j.bioactmat.2020.11.020.
- Chen, J. Y. *et al.* (2018) ‘Study of physical and degradation properties of 3D-printed biodegradable, photocurable copolymers, PGSA-co-PEGDA and PGSA-co-PCLDA’, *Polymers*, 10(11). doi: 10.3390/polym10111263.
- Chen, T. H. *et al.* (2007) ‘Sodium butyrate activates ERK to regulate differentiation of mesenchymal stem cells’, *Biochemical and Biophysical Research Communications*, 355(4), pp. 913–918. doi: 10.1016/j.bbrc.2007.02.057.
- Cho, J. S. *et al.* (2015) ‘Isolation and characterization of multipotent mesenchymal stem cells in nasal polyps’, *Experimental Biology and Medicine*, 240(2), pp. 185–193. doi: 10.1177/1535370214553898.
- Christensen, R. K. *et al.* (2020) ‘3D Printed Hydrogel Multiassay Platforms for Robust Generation of Engineered Contractile Tissues’, *Biomacromolecules*, 21(2), pp. 356–365. doi: 10.1021/acs.biomac.9b01274.
- Costantini, M. *et al.* (2016) ‘3D bioprinting of BM-MSCs-loaded ECM biomimetic hydrogels for in vitro neocartilage formation’, *Biofabrication*, 8(3). doi: 10.1088/1758-5090/8/3/035002.
- D’Aniello, C. *et al.* (2020) ‘Proline Metabolism in Tumor Growth and Metastatic Progression’, *Frontiers in Oncology*, 10(May), pp. 1–14. doi: 10.3389/fonc.2020.00776.
- Dahlin, R. L. *et al.* (2014) ‘TGF- $\beta$ 3-induced chondrogenesis in co-cultures of chondrocytes and mesenchymal stem cells on biodegradable scaffolds’, *Biomaterials*. Elsevier Ltd, 35(1), pp. 123–132. doi: 10.1016/j.biomaterials.2013.09.086.
- Dentistry, F. and Hospital, M. S. (1986) ‘Dexamethasone Induces Proliferation and Terminal Differentiation of Osteogenic Cells in Tissue Culture’, *The Anatomical Record*, 215(4), pp. 397–402.
- Derakhshanfar, S. *et al.* (2018) ‘3D bioprinting for biomedical devices and tissue engineering: A review of recent trends and advances’, *Bioactive Materials*. Elsevier, 3(2), pp. 144–156. doi: 10.1016/J.BIOACTMAT.2017.11.008.
- Dong, R. *et al.* (2018) ‘Repair and Attenuates Matrix Degradation by Activation of TGF- $\beta$  Signaling Pathway’, *Evidence-Based Complementary and Alternative Medicine*, 2018. doi: <https://doi.org/10.1155/2018/2734581>.
- Dzobo, K. *et al.* (2018) ‘Review Article Advances in Regenerative Medicine and Tissue Engineering: Innovation and Transformation of Medicine’, 2018.

- Edmondson, R. *et al.* (2014) ‘Three-Dimensional Cell Culture Systems and Their Applications in Drug Discovery and Cell-Based Biosensors’, *ASSAY and Drug Development Technologies*, 12(4), pp. 207–218. doi: 10.1089/adt.2014.573.
- Eom, J. *et al.* (2018) ‘Visualization and Quantification of Mesenchymal Cell Adipogenic Differentiation Potential with a Lineage Specific Marker’, *Journal of visualized experiments: JoVE*, (133), pp. 1–8. doi: 10.3791/57153.
- Eslami, M. *et al.* (2014) ‘Fiber-reinforced hydrogel scaffolds for heart valve tissue engineering’, *Journal of Biomaterials Applications*, 29(3), pp. 399–410. doi: 10.1177/0885328214530589.
- Eslaminejad, M. B., Karimi, N. and Shahhoseini, M. (2013) ‘Chondrogenic differentiation of human bone marrow-derived mesenchymal stem cells treated by GSK-3 inhibitors’, *Histochemistry and Cell Biology*, 140(6), pp. 623–633. doi: 10.1007/s00418-013-1121-x.
- Fairbanks, B. D. *et al.* (2009) ‘Photoinitiated polymerization of PEG-diacrylate with lithium phenyl-2,4,6-trimethylbenzoylphosphinate: polymerization rate and cytocompatibility’, *Biomaterials*. Elsevier Ltd, 30(35), pp. 6702–6707. doi: 10.1016/j.biomaterials.2009.08.055.
- Fanucci, S. (2017) *A comparison of RGD-modified Alginate, Methacrylated Gelatin/Alginate and native Alginate Hydrogels as scaffold material in the additive manufacturing of adipose tissue. Bachelor of Science (Honours)*. Faculty of Science, Rhodes University, Grahamstown.
- Fanucci, S., Barwick, M. W. and Prinsloo, E. (2019) ‘Bioprinting: Prospects, considerations and challenges for application in South African clinical environments’, *South African Medical Journal*, 109(8), pp. 34–39. doi: 10.7196/SAMJ.2019.v109i8b.13838.
- Ferreira, L. P., Gaspar, V. M. and Mano, J. F. (2018) ‘Design of spherically structured 3D in vitro tumor models -Advances and prospects’, *Acta Biomaterialia*. Acta Materialia Inc., 75, pp. 11–34. doi: 10.1016/j.actbio.2018.05.034.
- Findlay, D. M. and Atkins, G. J. (2014) ‘Osteoblast-chondrocyte interactions in osteoarthritis’, *Current Osteoporosis Reports*, 12(1), pp. 127–134. doi: 10.1007/s11914-014-0192-5.
- Francis, S. L. *et al.* (2018) ‘Adipose-derived mesenchymal stem cells in the use of cartilage tissue engineering: The need for a rapid isolation procedure’, *Stem Cells International*, 2018, pp. 13–16. doi: 10.1155/2018/8947548.
- Fujisawa, K. *et al.* (2018) ‘Evaluation of the effects of ascorbic acid on metabolism of human mesenchymal stem cells’, *Stem Cell Research & Therapy*. Stem Cell Research & Therapy, 9(93), pp. 1–12.

- Gauvin, R. *et al.* (2012) ‘Microfabrication of complex porous tissue engineering scaffolds using 3D projection stereolithography’, *Biomaterials*. Elsevier Ltd, 33(15), pp. 3824–3834. doi: 10.1016/j.biomaterials.2012.01.048.
- Gensler, M. *et al.* (2020) ‘3D printing of bioreactors in tissue engineering: A generalised approach’, *PLoS ONE*, 15(11 November), pp. 1–25. doi: 10.1371/journal.pone.0242615.
- Gojanovich, A. D. *et al.* (2018) ‘Human adipose-derived mesenchymal stem/stromal cells handling protocols. Lipid droplets and proteins double-staining’, *Frontiers in Cell and Developmental Biology*, 6(APR), pp. 1–16. doi: 10.3389/fcell.2018.00033.
- Goldstein, J. I. *et al.* (1992) *Scanning Electron Microscopy and X-Ray Microanalysis: A Text for Biologists, Material Scientists and Geologists*. 2nd edn, *Microscopy*. 2nd edn. Springer Science & Business Media. doi: 10.1007/978-1-4613-0491-3.
- Gopinathan, J. and Noh, I. (2018) ‘Recent trends in bioinks for 3D printing.’, *Biomaterials research*. BioMed Central, 22, p. 11. doi: 10.1186/s40824-018-0122-1.
- Groll, J. *et al.* (2019) ‘PERSPECTIVE • OPEN ACCESS A definition of bioinks and their distinction from biomaterial inks’, *Biofabrication*, 11(1), p. 013001. doi: 10.1088/1758-5090/aaec52.
- Gu, J. *et al.* (2014) ‘Identification and characterization of the novel Col10a1 regulatory mechanism during chondrocyte hypertrophic differentiation’, *Cell Death and Disease*, 5(10), pp. 1–11. doi: 10.1038/cddis.2014.444.
- Guertin, D. A. and Sabatini, D. M. (2006) ‘Cell Size Control’, *Encyclopedia of Life Sciences*. doi: 10.1038/npg.els.0003359.
- Gungor-Ozkerim, P. S. *et al.* (2018) ‘Bioinks for 3D bioprinting: an overview’, *Biomaterials Science*. Royal Society of Chemistry. doi: 10.1039/C7BM00765E.
- Guntoro, P. I. *et al.* (2019) ‘X-ray microcomputed tomography ( $\mu$ ct) for mineral characterization: A review of data analysis methods’, *Minerals*, 9(3), pp. 20–26. doi: 10.3390/min9030183.
- Guvendiren, M. *et al.* (2016) ‘Designing Biomaterials for 3D Printing’, *ACS Biomaterials Science and Engineering*, 2(10), pp. 1679–1693. doi: 10.1021/acsbomaterials.6b00121.
- Hamid, Z. A. A. and Lim, K. W. (2016) ‘Evaluation of UV-crosslinked Poly (ethylene glycol) Diacrylate / Poly (dimethylsiloxane) Dimethacrylate Hydrogel: Properties for Tissue Engineering Application’, *Procedia Chemistry*. Elsevier Ltd., 19, pp. 410–418. doi: 10.1016/j.proche.2016.03.032.
- Han, Yu *et al.* (2019) ‘Mesenchymal Stem Cells for Regenerative Medicine’, *Cells*, 8(8), p. 886. doi: 10.3390/cells8080886.

Hill, C. L., Sell, S. A. and Zustiak, S. P. (2017) 'Control of gelation, degradation and physical properties of polyethylene glycol hydrogels through the chemical and physical identity of the crosslinker', *Journal of Materials Chemistry B*, 5(14), pp. 2679–2691. doi: 10.1039/C6TB03050E.

Honiball, J. (2017) Development of A low-cost bioprinting system for the fabrication of cell-laden sodium alginate hydrogels: *A thesis submitted in fulfilment of the requirements for the degree of MASTER OF SCIENCE of By JOHN ROBERT HONIBALL February 2017*. Rhodes University.

Hosseini, S. *et al.* (2018) 'Regenerative medicine applications of mesenchymal stem cells', *Advances in Experimental Medicine and Biology*, 1089, pp. 115–141. doi: 10.1007/5584\_2018\_213.

Huang, T., Schor, S. L. and Hinck, A. P. (2014) 'Biological Activity Differences between TGF- $\beta$ 1 and TGF- $\beta$ 3 Correlate with Differences in the Rigidity and Arrangement of Their Component Monomers', *Biochemistry*, 53(36), pp. 5737–5749. doi: 10.1021/bi500647d.

Hu, C., Zhao, L. and Li, L. (2019) 'Current understanding of adipose-derived mesenchymal stem cell-based therapies in liver diseases', *Stem Cell Research and Therapy*. *Stem Cell Research & Therapy*, 10(1), pp. 1–13. doi: 10.1186/s13287-019-1310-1.

Hyaluronic acid.svg. (2020, October 26). Wikimedia Commons, the free media repository. Retrieved 18:21, March, 3, 2021 From:

[https://commons.wikimedia.org/w/index.php?title=File:Hyaluronic\\_acid.svg&oldid=501798731](https://commons.wikimedia.org/w/index.php?title=File:Hyaluronic_acid.svg&oldid=501798731).

Jakab, K. *et al.* (2010) 'Tissue engineering by self-assembly and bio-printing of living cells', *Biofabrication*, 2(2). doi: 10.1088/1758-5082/2/2/022001.

Javidnia, K. *et al.* (2013) 'Spectrochimica Acta Part A : Molecular and Biomolecular Spectroscopy Discrimination of edible oils and fats by combination of multivariate pattern recognition and FT-IR spectroscopy : A comparative study between different modeling methods', *SPECTROCHIMICA ACTA PART A: MOLECULAR AND BIOMOLECULAR SPECTROSCOPY*. Elsevier B.V., 104, pp. 175–181. doi: 10.1016/j.saa.2012.11.067.

Jensen, C. and Teng, Y. (2020) 'Is It Time to Start Transitioning From 2D to 3D Cell Culture?', *Frontiers in Molecular Biosciences*, 7(March), pp. 1–15. doi: 10.3389/fmolb.2020.00033.

Jones, D. G. (2009) 'Articular cartilage degeneration: etiologic association with obesity.', *The Ochsner journal*, 9(3), pp. 137–139.

Kaberova, Z. *et al.* (2020) 'Microscopic structure of swollen hydrogels by scanning electron and light microscopies: Artifacts and reality', *Polymers*, 12(3). doi: 10.3390/polym12030578.



- Kangari, P. *et al.* (2020) ‘Mesenchymal stem cells: amazing remedies for bone and cartilage defects’, *Stem Cell Research and Therapy*. *Stem Cell Research & Therapy*, 11(1), pp. 1–21. doi: 10.1186/s13287-020-02001-1.
- Kazarian, S. G. and Chan, K. L. A. (2006) ‘Applications of ATR-FTIR spectroscopic imaging to biomedical samples’, *Biochimica et Biophysica Acta (BBA) - Biomembranes*, 1758(7), pp. 858–867. doi: 10.1016/j.bbamem.2006.02.011.
- Khandaker, M. *et al.* (2016) ‘Biomechanical Performances of Networked Polyethylene Glycol Diacrylate: Effect of Photoinitiator Concentration, Temperature, and Incubation Time’, *International Journal of Biomaterials*, 2016. doi: 10.1155/2016/3208312.
- Kim, M. and Cha, C. (2018) ‘Modulation of functional pendant chains within poly(ethylene glycol) hydrogels for refined control of protein release’, *Scientific Reports*. Springer US, 8(1), pp. 1–12. doi: 10.1038/s41598-018-22249-1.
- Kizilel, S., Pérez-Luna, V. H. and Teymour, F. (2004) ‘Photopolymerization of poly(ethylene glycol) diacrylate on eosin-functionalized surfaces’, *Langmuir*, 20(20), pp. 8652–8658. doi: 10.1021/la0496744.
- Klenke, F. M. and Siebenrock, K. A. (2016) *Osteology in Orthopedics – Bone Repair, Bone Grafts and Bone Graft Substitutes, Reference Module in Biomedical Sciences*. Elsevier Inc. doi: 10.1016/b978-0-12-801238-3.99488-1.
- Klotz, B. J. *et al.* (2016) ‘Gelatin-Methacryloyl Hydrogels: Towards Biofabrication-Based Tissue Repair’, *Trends in Biotechnology*. Elsevier Ltd, 34(5), pp. 394–407. doi: 10.1016/j.tibtech.2016.01.002.
- Kong, L. *et al.* (2019) ‘Identification of two novel COL10A1 heterozygous mutations in two Chinese pedigrees with Schmid-type metaphyseal chondrodysplasia’, *BMC Medical Genetics*. BMC Medical Genetics, 20(1), pp. 1–9. doi: 10.1186/s12881-019-0937-1.
- Koser, S. A., Chinn, B. E. N. D. and Saunders, F. (1938) ‘Gelatin as a Source of Growth-Promoting Substances for Bacteria’, *Journal of Bacteriology*, 36(1), pp. 57–65. doi: 10.1128/JB.36.1.57-65.1938.
- Kotturi, H. *et al.* (2017) ‘Evaluation of Polyethylene Glycol Diacrylate-Polycaprolactone Scaffolds for Tissue Engineering Applications’, *Journal of Functional Biomaterials*, 8(3), p. 39. doi: 10.3390/jfb8030039.
- Kramer, A. H. *et al.* (2014) ‘Real-time monitoring of 3T3-L1 preadipocyte differentiation using a commercially available electric cell-substrate impedance sensor system’, *Biochemical and Biophysical Research Communications*. Elsevier Inc., 443(4), pp. 1245–1250. doi: 10.1016/j.bbrc.2013.12.123.
- Kraus, N. A. *et al.* (2016) ‘Quantitative assessment of adipocyte differentiation in cell culture’, *Adipocyte*. Taylor & Francis, 5(4), pp. 351–358. doi: 10.1080/21623945.2016.1240137.

- Krishnan, Y. and Grodzinsky, A. J. (2018) ‘Cartilage diseases’, *Matrix Biology*. Elsevier B.V., 71–72, pp. 51–69. doi: 10.1016/j.matbio.2018.05.005.
- Krueger, T. E. G. *et al.* (2018) ‘Concise Review: Mesenchymal Stem Cell-Based Drug Delivery: The Good, the Bad, the Ugly, and the Promise’, *Stem Cells Translational Medicine*, 7(9), pp. 651–663. doi: 10.1002/sctm.18-0024.
- Kumari, S. *et al.* (2018) ‘Reactive Oxygen Species: A Key Constituent in Cancer Survival’, *Biomarker Insights*, 13. doi: 10.1177/1177271918755391.
- Langer, R. and Vacanti, J. P. (1993) ‘Tissue engineering’, *Science*, 260(5110), pp. 920–926. doi: 10.1007/978-3-642-02824-3.
- Lee, S. H. *et al.* (2015) ‘Enhanced adipogenic differentiation of bovine bone marrow-derived mesenchymal stem cells’, *Journal of Applied Animal Research*. Taylor & Francis, 43(1), pp. 15–21. doi: 10.1080/09712119.2014.883320.
- Li, C., Mu, C. and Lin, W. (2016) ‘Novel hemocompatible nanocomposite hydrogels crosslinked with methacrylated gelatin’, *RSC Advances*. Royal Society of Chemistry, 6(49), pp. 43663–43671. doi: 10.1039/c6ra04609f.
- Li, H. *et al.* (2019) ‘The Application of Hyaluronic Acid-Based Hydrogels in Bone and Cartilage Tissue Engineering’, *Advances in Materials Science and Engineering*, 2019. doi: 10.1155/2019/3027303.
- Lienert, F. *et al.* (2014) ‘Synthetic biology in mammalian cells: Next generation research tools and therapeutics’, *Nature Reviews Molecular Cell Biology*. Nature Publishing Group, 15(2), pp. 95–107. doi: 10.1038/nrm3738.
- Lilly, J. L. *et al.* (2018) ‘Comparison of eosin and fluorescein conjugates for the photoinitiation of cell-compatible polymer coatings’, *PLoS ONE*, 13(1), pp. 13–15. doi: 10.1371/journal.pone.0190880.
- Liu, J. *et al.* (2019) ‘Amino Acid-Mediated Metabolism: A New Power to Influence Properties of Stem Cells’, *Stem Cells International*, 2019, p. 9. doi: 10.1155/2019/6919463.
- Liu, T. *et al.* (2020) ‘Applications of Gelatin Methacryloyl (GelMA) Hydrogels in Microfluidic Technique-Assisted Tissue Engineering’, *Molecules (Basel, Switzerland)*, 25(22). doi: 10.3390/molecules25225305.
- Liu, Y., Zhou, G. and Cao, Y. (2017) ‘Recent Progress in Cartilage Tissue Engineering—Our Experience and Future Directions’, *Engineering*. Elsevier LTD on behalf of Chinese Academy of Engineering and Higher Education Press Limited Company, 3(1), pp. 28–35. doi: 10.1016/J.ENG.2017.01.010.

- Mabuchi, K. *et al.* (1999) ‘Molecular weight independence of the effect of additive hyaluronic acid on the lubricating characteristics in synovial joints with experimental deterioration’, *Clinical Biomechanics*, 14(5), pp. 352–356. doi: 10.1016/S0268-0033(98)00084-9.
- Mackenzie, D. (2020) ‘Ultraviolet Light Fights New Virus’, *Engineering*. Chinese Academy of Engineering, 6(8), pp. 851–853. doi: 10.1016/j.eng.2020.06.009.
- Magalhães, J. *et al.* (2014) ‘Poly(2-ethyl-(2-pyrrolidone) methacrylate) and hyaluronic acid-based hydrogels for the engineering of a cartilage-like tissue using bovine articular chondrocytes’, *Journal of Bioactive and Compatible Polymers*, 29(6), pp. 545–559. doi: 10.1177/0883911514555609.
- Mahapatra, C., Jin, G. Z. and Kim, H. W. (2016) ‘Alginate-hyaluronic acid-collagen composite hydrogel favorable for the culture of chondrocytes and their phenotype maintenance’, *Tissue Engineering and Regenerative Medicine*, 13(5), pp. 538–546. doi: 10.1007/s13770-016-0059-1.
- Mamede, A. C. *et al.* (2012) ‘Cytotoxicity of Ascorbic Acid in a Human Colorectal Adenocarcinoma Cell Line (WiDr): In Vitro and In Vivo Studies Cytotoxicity of Ascorbic Acid in a Human Colorectal Adenocarcinoma Cell Line ( WiDr ): In Vitro and In Vivo’, *Nutrition and Cancer*, 64(7), pp. 37–41. doi: 10.1080/01635581.2012.713539.
- Markmee, R., Aungsuchawan, S. and Pothacharoen, P. (2019) ‘Heliyon Effect of ascorbic acid on differentiation of human amniotic fluid mesenchymal stem cells into cardiomyocyte-like cells’, *Heliyon*. Elsevier Ltd, 5(October 2018), p. e02018. doi: 10.1016/j.heliyon.2019.e02018.
- Matsumura, S. *et al.* (2008) ‘Stability and Utility of Pyridyl Disulfide Functionality in RAFT and Conventional Radical Polymerizations’, *Journal of Polymer Science: Part A: Polymer Chemistry*, 46(April), pp. 7207–7224. doi: 10.1002/pola.
- Mattern, J. *et al.* (2007) ‘Cell Cycle Arrest by Glucocorticoids May Protect Normal Tissue ND ES SC’, *Cancer Biology and Therapy*, 6(9), pp. 1341–1350. doi: 10.4161/cbt.6.9.4765.
- MedlinePlus (2020) *COL2A1 gene*, *National Library of Medicine*. doi: 10.32388/p1pmwq.
- Melucci, D. *et al.* (2019) ‘ATR-FTIR Spectroscopy, a New Non-Destructive Approach for the Quantitative Determination of Biogenic Silica in Marine Sediments’, *Molecules*, 24(21), p. 3927. doi: <https://doi.org/10.3390/molecules24213927>.
- Mero, A. and Campisi, M. (2014) ‘Hyaluronic acid bioconjugates for the delivery of bioactive molecules’, *Polymers*, 6(1), pp. 346–369. doi: 10.3390/polym6020346.
- Mironov, V., Kasyanov, V. and Markwald, R. R. (2011) ‘Organ printing: From bioprinter to organ biofabrication line’, *Current Opinion in Biotechnology*. Elsevier Ltd, 22(5), pp. 667–673. doi: 10.1016/j.copbio.2011.02.006.

- Moeinzadeh, S. and Jabbari, E. (2015) ‘Gelation characteristics, physico-mechanical properties and degradation kinetics of micellar hydrogels’, *European Polymer Journal*. Elsevier Ltd, 72, pp. 566–576. doi: 10.1016/j.eurpolymj.2015.04.028.
- Monteiro, N. *et al.* (2018) ‘Photopolymerization of cell-laden gelatin methacryloyl hydrogels using a dental curing light for regenerative dentistry’, *Dental Materials*, 34(3), pp. 389–399. doi: 10.1016/j.dental.2017.11.020.
- Mueller, M. B. *et al.* (2013) ‘Thyroid Hormone-Induced Hypertrophy in Mesenchymal Stem Cell Chondrogenesis Is Mediated by Bone Morphogenetic Protein-4’, *Tissue Engineering Part A*, 20(1–2), pp. 178–188. doi: 10.1089/ten.tea.2013.0023.
- Nath, B. *et al.* (2018) ‘Understanding flow dynamics, viability and metastatic potency of cervical cancer (HeLa) cells through constricted microchannel’, *Scientific Reports*, 8(1), pp. 1–10. doi: 10.1038/s41598-018-35646-3.
- Nava, M. M., Raimondi, M. T. and Pietrabissa, R. (2012) ‘Controlling self-renewal and differentiation of stem cells via mechanical cues’, *Journal of Biomedicine and Biotechnology*, 2012. doi: 10.1155/2012/797410.
- Ng, K. W. *et al.* (2008) ‘Amino acids supply in culture media is not a limiting factor in the matrix synthesis of engineered cartilage tissue’, *Amino Acids*, 35(2), pp. 433–438. doi: 10.1007/s00726-007-0583-3.
- Nguyen, A. K. *et al.* (2020) ‘The photoinitiator lithium phenyl (2,4,6-Trimethylbenzoyl) phosphinate with exposure to 405 nm light is cytotoxic to mammalian cells but not mutagenic in bacterial reverse mutation assays’, *Polymers*, 12(7), pp. 1–13. doi: 10.3390/polym12071489.
- Nguyen, Q. T. *et al.* (2012) ‘Cartilage-like mechanical properties of poly (ethylene glycol)-diacrylate hydrogels’, *Biomaterials*. Elsevier Ltd, 33(28), pp. 6682–6690. doi: 10.1016/j.biomaterials.2012.06.005.
- Noshadi, I. *et al.* (2017) ‘Engineering Biodegradable and Biocompatible Bio-ionic Liquid Conjugated Hydrogels with Tunable Conductivity and Mechanical Properties’, *Scientific Reports*. Springer US, 7(1), pp. 1–18. doi: 10.1038/s41598-017-04280-w.
- Nuzzi, R. *et al.* (2012) ‘Effect of In Vitro Exposure of Corticosteroid Drugs , Conventionally Used in AMD Treatment , on Mesenchymal Stem Cells’, *Stem Cells International*, 2012(vitamin C), p. 11. doi: 10.1155/2012/946090.
- O’Brien, F. J. (2011) ‘Biomaterials & scaffolds for tissue engineering’, *Materials Today*. Elsevier Ltd, 14(3), pp. 88–95. doi: 10.1016/S1369-7021(11)70058-X.

- Osmani, Q. *et al.* (2008) 'The use of FTIR and NMR spectroscopies to study prepolymerisation interactions in nitrogen heterocycles', *Analytical and Bioanalytical Chemistry*, (391), pp. 1229–1236. doi: 10.1007/s00216-008-1867-5.
- Pahoff, S. *et al.* (2019) 'Effect of gelatin source and photoinitiator type on chondrocyte redifferentiation in gelatin methacryloyl-based tissue-engineered cartilage constructs', *Journal of Materials Chemistry B*. Royal Society of Chemistry, 7(10), pp. 1761–1772. doi: 10.1039/c8tb02607f.
- Pan, J. *et al.* (2009) 'In situ measurement of transport between subchondral bone and articular cartilage', *Journal of Orthopaedic Research*, 27(10), pp. 1347–1352. doi: 10.1002/jor.20883.
- Paolini, A., Kollmannsberger, S. and Rank, E. (2019) 'Additive manufacturing in construction: A review on processes, applications, and digital planning methods', *Additive Manufacturing*. Elsevier, 30(September), p. 100894. doi: 10.1016/j.addma.2019.100894.
- Park, H. *et al.* (2009) 'Effect of swelling ratio of injectable hydrogel composites on chondrogenic differentiation of encapsulated rabbit marrow mesenchymal stem cells in vitro', *Biomacromolecules*, 10(3), pp. 541–546. doi: 10.1021/bm801197m.
- De Paula, M. M. M. *et al.* (2018) 'Understanding the impact of crosslinked PCL/ PEG/GelMA electrospun nanofibers on bactericidal activity', *PLoS ONE*, 13(12), pp. 1–19. doi: 10.1371/journal.pone.0209386.
- Pepelanova, I. *et al.* (2018) 'Gelatin-Methacryloyl (GelMA) Hydrogels with Defined Degree of Functionalization as a Versatile Toolkit for 3D Cell Culture and Extrusion Bioprinting', *Bioengineering*, 5(3), p. 55. doi: 10.3390/bioengineering5030055.
- Peran, M. *et al.* (2013) 'Activin/BMP2 chimeric ligands direct adipose-derived stem cells to chondrogenic differentiation', *Stem Cell Research*. Elsevier B.V., 10(3), pp. 464–476. doi: 10.1016/j.scr.2013.02.002.
- Pereira, R. F. and Bártolo, P. J. (2015) '3D Photo-Fabrication for Tissue Engineering and Drug Delivery', *Engineering*. THE AUTHORS, 1(1), pp. 090–112. doi: 10.15302/J-ENG-2015015.
- Pereira, R. V. *et al.* (2014) 'Evaluation of the effects of ultraviolet light on bacterial contaminants inoculated into whole milk and colostrum, and on colostrum immunoglobulin G', *Journal of Dairy Science*. Elsevier, 97(5), pp. 2866–2875. doi: 10.3168/jds.2013-7601.
- Pfeifer, C. G. *et al.* (2019) 'TGF- $\beta$  signalling is suppressed under pro-hypertrophic conditions in MSC chondrogenesis due to TGF- $\beta$  receptor downregulation', *International Journal of Stem Cells*, 12(1), pp. 139–150. doi: 10.15283/ijsc18088.
- Photoinitiators, T. I. (2001) 'Applications: Free Radical Initiators', *Spectroscopy*, 3(1), pp. 5–19. Available at: <http://www.pnas.org/content/108/23/E196.short>.

- Pittenger, M. F. *et al.* (2019) ‘Mesenchymal stem cell perspective: cell biology to clinical progress’, *npj Regenerative Medicine*. Springer US, 4(1). doi: 10.1038/s41536-019-0083-6.
- Popovic, N. and Wilson, E. (2010) ‘Cell Surface Receptors’, *Comprehensive Toxicology: Second Edition*, 2–14, pp. 81–91. doi: 10.1016/B978-0-08-046884-6.00206-2.
- Potten, C. S., Booth, D. and Haley, J. D. (1997) ‘Pretreatment with transforming growth factor beta-3 protects small intestinal stem cells against radiation damage in vivo’, *British Journal of Cancer*, 75(10), pp. 1454–1459. doi: 10.1038/bjc.1997.249.
- PromoCell GmbH (2015) *Chondrogenic Differentiation and Analysis of MSC*, PromoCell. doi: papers3://publication/uuid/5D093FF5-1A48-42D4-82F7-C9C40ED35A39.
- Pullerits, K. *et al.* (2020) ‘Impact of UV irradiation at full scale on bacterial communities in drinking water’, *npj Clean Water*. Springer US, 3(1), pp. 1–10. doi: 10.1038/s41545-020-0057-7.
- Ramón-Azcón, J. *et al.* (2012) ‘Gelatin methacrylate as a promising hydrogel for 3D microscale organization and proliferation of dielectrophoretically patterned cells’, *Lab on a Chip*, 12(16), pp. 2959–2969. doi: 10.1039/c2lc40213k.
- Rangiah, S., Govender, I. and Badat, Z. (2020) ‘A primary care approach to the management of arthritis’, *South African Family Practice*, 62(1), pp. 1–7. doi: 10.4102/safp.v62i1.5089.
- Rao, X. *et al.* (2013) ‘An improvement of the  $\Delta\Delta CT$  method for quantitative real-time polymerase chain reaction data analysis.’, *Biostatistics, bioinformatics and biomathematics*, 3(3), pp. 71–85. doi: 10.1089/cmb.2012.0279.
- Ravi, M. *et al.* (2015) ‘3D cell culture systems: Advantages and applications’, *Journal of Cellular Physiology*, 230(1), pp. 16–26. doi: 10.1002/jcp.24683.
- Regeneration, C. *et al.* (2021) *Cartilage Regeneration Market Size Worth \$ 6.7 Billion By 2025*. Available at: <https://www.grandviewresearch.com/press-release/global-cartilage-repair-regeneration-market>.
- Rennie, M. Y. *et al.* (2014) *Scanning Electron Microscopy and Micro-Computed Tomography Imaging of the Utero- and Fetoplacental Circulations, The Guide to Investigation of Mouse Pregnancy*. Elsevier. doi: 10.1016/b978-0-12-394445-0.00055-2.
- Riley, S. L. *et al.* (2001) ‘Formulation of PEG-based hydrogels affects tissue-engineered cartilage construct characteristics’, 2, pp. 983–990.
- Rimann, M. and Graf-Hausner, U. (2012) ‘Synthetic 3D multicellular systems for drug development’, *Current Opinion in Biotechnology*. Elsevier Ltd, 23(5), pp. 803–809. doi: 10.1016/j.copbio.2012.01.011.

- Roberts, B. M. *et al.* (2015) 'High concentrations of L-ascorbic acid ( Vitamin C ) induces apoptosis in a human cervical cancer cell line ( HeLa ) through the intrinsic and extrinsic pathways High concentrations of L-ascorbic acid ( Vitamin C ) induces apoptosis in a human cervical ca', *BIOS*, 86(3), pp. 134–143. doi: doi: 10.1893/BIOS-D-14-00019.1.
- Robey, P. G. and Riminucci, M. (2019) *Skeletal stem cells: Tissue-specific stem/progenitor cells of cartilage, bone, stroma, and marrow adipocytes*, *Principles of Bone Biology*. Elsevier Inc. doi: 10.1016/B978-0-12-814841-9.00002-6.
- Robin Poole, A. *et al.* (2004) 'The assessment of cartilage degradation in vivo: Development of an immunoassay for the measurement in body fluids of type II collagen cleaved by collagenases', *Journal of Immunological Methods*, 294(1–2), pp. 145–153. doi: 10.1016/j.jim.2004.09.005.
- Romanò, C. L. *et al.* (2017) 'Hyaluronic Acid and Its Composites as a Local Antimicrobial/Anti-adhesive Barrier', *Journal of Bone and Joint Infection*, 2(1), pp. 63–72. doi: 10.7150/jbji.17705.
- Romeo, M. *et al.* (2004) 'Infrared Microspectroscopy of Individual Human Cervical Cancer (HeLa) Cells', *Biopolymers*, 74(1–2), pp. 168–171. doi: 10.1002/bip.20065.
- De Sá Silva, C. A. *et al.* (2003) 'Evaluation of ultraviolet radiation to control microorganisms adhering to low-density polyethylene films', *Brazilian Journal of Microbiology*, 34(2), pp. 175–178. doi: 10.1590/s1517-83822003000200017.
- Salami, A. *et al.* (2020) 'Cost-effective FTIR and <sup>1</sup>H NMR spectrometry used to screen valuable molecules extracted from selected West African trees by a sustainable biochar process', *Scientific African*. Elsevier B.V., 8, pp. 1–13. doi: 10.1016/j.sciaf.2020.e00315.
- Sánchez-Téllez, D. A., Téllez-Jurado, L. and Rodríguez-Lorenzo, L. M. (2017) 'Hydrogels for cartilage regeneration, from polysaccharides to hybrids', *Polymers*, 9(12), pp. 1–32. doi: 10.3390/polym9120671.
- Sautrot-Ba, P. *et al.* (2019) 'Photoinduced chitosan-PEG hydrogels with long-term antibacterial properties', *Journal of Materials Chemistry B*. Royal Society of Chemistry, 7(42), pp. 6526–6538. doi: 10.1039/c9tb01170f.
- Schneider, C. A., Rasband, W. S. and Eliceiri, K. W. (2012) 'NIH Image to ImageJ: 25 years of image analysis', *Nature Methods*. Nature Publishing Group, 9(7), pp. 671–675. doi: 10.1038/nmeth.2089.
- Schuurman, W. *et al.* (2013) 'Gelatin-methacrylamide hydrogels as potential biomaterials for fabrication of tissue-engineered cartilage constructs', *Macromolecular Bioscience*, 13(5), pp. 551–561. doi: 10.1002/mabi.201200471.

- Schwalm, R. (2001) 'Photoinitiators and Photopolymerization', *Encyclopedia of Materials: Science and Technology (Second Edition)*, pp. 6946–6951. doi: <https://doi.org/10.1016/B0-08-043152-6/01230-4>.
- Seale, N. *et al.* (2018) 'Macroporous Dual-compartment Hydrogels for Minimally Invasive Transplantation of Primary Human Hepatocytes', *Transplantation*, 102(9), pp. e373–e381. doi: 10.1097/TP.0000000000002330.
- Seo, J. W. *et al.* (2020) 'Cell-laden gelatin methacryloyl bioink for the fabrication of z-stacked hydrogel scaffolds for tissue engineering', *Polymers*, 12(12), pp. 1–15. doi: 10.3390/polym12123027.
- Seol, Y. J. *et al.* (2014) 'Bioprinting technology and its applications', *European Journal of Cardiothoracic Surgery*, 46(3), pp. 342–348. doi: 10.1093/ejcts/ezu148.
- Seystahl, K. *et al.* (2017) 'Biological role and therapeutic targeting of TGF- $\beta$ 3 in glioblastoma', *Molecular Cancer Therapeutics*, 16(6), pp. 1177–1186. doi: 10.1158/1535-7163.MCT-16-0465.
- Shih, H. and Lin, C. C. (2013) 'Visible-light-mediated thiol-ene hydrogelation using eosin-Y as the only photoinitiator', *Macromolecular Rapid Communications*, 34(3), pp. 269–273. doi: 10.1002/marc.201200605.
- Shirahama, H. *et al.* (2016) 'Precise tuning of facile one-pot gelatin methacryloyl (GelMA) synthesis', *Scientific Reports*. Nature Publishing Group, 6(July), pp. 1–11. doi: 10.1038/srep31036.
- Shrimali, P. *et al.* (2018) 'Efficient in situ gene delivery via PEG diacrylate matrices', *Biomaterials Science*, 6, pp. 3241–3250. doi: 10.1039/C8BM00916C.
- Sinha, S. K. (2020) *Additive manufacturing (AM) of medical devices and scaffolds for tissue engineering based on 3D and 4D printing, 3D and 4D Printing of Polymer Nanocomposite Materials: Processes, Applications, and Challenges*. Elsevier Inc. doi: 10.1016/B978-0-12-816805-9.00005-3.
- Song, A., Rane, A. A. and Christman, K. L. (2012) 'Antibacterial and cell-adhesive polypeptide and poly(ethylene glycol) hydrogel as a potential scaffold for wound healing', *Acta Biomaterialia*. Acta Materialia Inc., 8(1), pp. 41–50. doi: 10.1016/j.actbio.2011.10.004.
- Sophia Fox, A. J., Bedi, A. and Rodeo, S. A. (2009) 'The basic science of articular cartilage: Structure, composition, and function', *Sports Health*, 1(6), pp. 461–468. doi: 10.1177/1941738109350438.
- Spicer, C. D. (2020) 'Hydrogel scaffolds for tissue engineering: The importance of polymer choice', *Polymer Chemistry*. Royal Society of Chemistry, 11(2), pp. 184–219. doi: 10.1039/c9py01021a.
- Subramani, R. *et al.* (2020) 'The Influence of Swelling on Elastic Properties of Polyacrylamide Hydrogels', *Frontiers in Materials*, 7(July), pp. 1–13. doi: 10.3389/fmats.2020.00212.



- Sun, D. (2010) *Infrared Spectroscopy for Food Quality Analysis and Control*. doi: 10.1016/j.tifs.2009.08.004.
- Sun, M. *et al.* (2018) ‘Synthesis and properties of gelatin methacryloyl (GelMA) hydrogels and their recent applications in load-bearing tissue’, *Polymers*, 10(11). doi: 10.3390/POLYM10111290.
- Tamay, D. G. *et al.* (2019) ‘3D and 4D printing of polymers for tissue engineering applications’, *Frontiers in Bioengineering and Biotechnology*, 7(JUL). doi: 10.3389/fbioe.2019.00164.
- Tamura, M. *et al.* (2015) ‘Click-crosslinkable and photodegradable gelatin hydrogels for cytocompatible optical cell manipulation in natural environment’, *Scientific Reports*. Nature Publishing Group, 5(June), pp. 1–12. doi: 10.1038/srep15060.
- Tanthaisong, P. *et al.* (2017) ‘Enhanced chondrogenic differentiation of human umbilical cord wharton’s jelly derived mesenchymal stem cells by GSK-3 Inhibitors’, *PLoS ONE*, 12(1), pp. 1–15. doi: 10.1371/journal.pone.0168059.
- Uetaki, M. *et al.* (2015) ‘Metabolomic alterations in human cancer cells by vitamin C-induced oxidative stress’, *Nature Publishing Group*. Nature Publishing Group, 5, pp. 1–9. doi: 10.1038/srep13896.
- Ullah, I., Subbarao, R. B. and Rho, G. J. (2015) ‘Human mesenchymal stem cells - current trends and future prospective’, *Bioscience Reports*, 35(2), pp. 1–18. doi: 10.1042/BSR20150025.
- Verma, A., Verma, M. and Singh, A. (2020) *Animal tissue culture principles and applications*, *Animal Biotechnology*. INC. doi: 10.1016/b978-0-12-811710-1.00012-4.
- Voga, M. *et al.* (2019) ‘Silk fibroin induces chondrogenic differentiation of canine adipose–derived multipotent mesenchymal stromal cells/mesenchymal stem cells’, *Journal of Tissue Engineering*, 10. doi: 10.1177/2041731419835056.
- Wahdan-Alaswad, R. *et al.* (2016) ‘Metformin attenuates transforming growth factor beta (TGF- $\beta$ ) mediated oncogenesis in mesenchymal stem-like/claudin-low triple negative breast cancer’, *Cell Cycle*. Taylor & Francis, 15(8), pp. 1046–1059. doi: 10.1080/15384101.2016.1152432.
- Walimbe, T. and Panitch, A. (2020) ‘Proteoglycans in biomedicine: Resurgence of an underexploited class of ECM molecules’, *Frontiers in Pharmacology*, 10(January), pp. 1–13. doi: 10.3389/fphar.2019.01661.
- Walsh, S. *et al.* (2001) ‘High concentrations of dexamethasone suppress the proliferation but not the differentiation or further maturation of human osteoblast precursors in vitro: Relevance to glucocorticoid-induced osteoporosis’, *Rheumatology*, 40(1), pp. 74–83. doi: 10.1093/rheumatology/40.1.74.

- Wang, H. *et al.* (2012) 'Dexamethasone has variable effects on mesenchymal stromal cells', *Cytotherapy*, 14(4), pp. 423–430. doi: 10.3109/14653249.2011.652735.
- Wang, Lu *et al.* (2020) *Influence of the mechanical properties of biomaterials on degradability, cell behaviors and signaling pathways: Current progress and challenges*, *Biomaterials Science*. doi: 10.1039/d0bm00269k.
- Wang, L. J. *et al.* (2016) 'Dexamethasone suppresses the growth of human non-small cell lung cancer via inducing estrogen sulfotransferase and inactivating estrogen', *Acta Pharmacologica Sinica*. Nature Publishing Group, 37(6), pp. 845–856. doi: 10.1038/aps.2016.39.
- Wang, M. *et al.* (2017) 'Advances and Prospects in Stem Cells for Cartilage Regeneration', *Stem Cells International*, 2017. doi: <https://doi.org/10.1155/2017/4130607>.
- Wang, W., Rigueur, D. and Lyons, K. M. (2014) 'TGF $\beta$  signaling in cartilage development and maintenance', *Birth Defects Research Part C - Embryo Today: Reviews*, 102(1), pp. 37–51. doi: 10.1002/bdrc.21058.
- Wang, X. *et al.* (2019) 'Preparation of Antimicrobial Hyaluronic Acid/Quaternized Chitosan Hydrogels for the Promotion of Seawater-Immersion Wound Healing', *Frontiers in Bioengineering and Biotechnology*, 7(December), pp. 1–20. doi: 10.3389/fbioe.2019.00360.
- Wang, Y. *et al.* (2018) 'Development of a photo-crosslinking, biodegradable GelMA/PEGDA hydrogel for guided bone regeneration materials', *Materials*, 11(8), pp. 6–8. doi: 10.3390/ma11081345.
- Wang, Yihu *et al.* (2020) 'A GelMA-PEGDA-nHA composite hydrogel for bone tissue engineering', *Materials*, 13(17), pp. 1–12. doi: 10.3390/MA13173735.
- Wang, Yuxuan *et al.* (2020) 'Overview of 3D additive manufacturing (AM) and corresponding AM composites', *Composites Part A: Applied Science and Manufacturing*. Elsevier, 139(January), p. 106114. doi: 10.1016/j.compositesa.2020.106114.
- Wang, Z. *et al.* (2015) 'A simple and high-resolution stereolithography-based 3D bioprinting system using visible light crosslinkable bioinks', *Biofabrication*. IOP Publishing, 7(4), p. 45009. doi: 10.1088/1758-5090/7/4/045009.
- Wang, Z. *et al.* (2018) 'Visible Light Photoinitiation of Cell-Adhesive Gelatin Methacryloyl Hydrogels for Stereolithography 3D Bioprinting', *ACS Applied Materials and Interfaces*. American Chemical Society, 10(32), pp. 26859–26869. doi: 10.1021/acsami.8b06607.
- Wei, Q. and Huang, H. (2013) *Insights into the role of cell-cell junctions in physiology and disease*. 1st edn, *International Review of Cell and Molecular Biology*. 1st edn. Elsevier Inc. doi: 10.1016/B978-0-12-407694-5.00005-5.

- Wu, F., Pang, Y. and Liu, J. (2020) ‘Swelling-strengthening hydrogels by embedding with deformable nanobarriers’, *Nature Communications*. Springer US, 11(1), pp. 1–10. doi: 10.1038/s41467-020-18308-9.
- Wu, G. *et al.* (2011) ‘Proline and hydroxyproline metabolism: Implications for animal and human nutrition’, *Amino Acids*, 40(4), pp. 1053–1063. doi: 10.1007/s00726-010-0715-z.
- Wu, Z. *et al.* (2016) ‘Bioprinting three-dimensional cell-laden tissue constructs with controllable degradation’, *Scientific Reports*. Nature Publishing Group, 6(April), pp. 1–10. doi: 10.1038/srep24474.
- Xia, B. *et al.* (2017) ‘Cytocompatible cell encapsulation via hydrogel photopolymerization in microfluidic emulsion droplets’, *Biomicrofluidics*, 11(4). doi: 10.1063/1.4993122.
- Xiao, Y. *et al.* (2010) ‘Dexamethasone treatment during the expansion phase maintains stemness of bone marrow mesenchymal stem cells’, *Journal of Tissue Engineering and Regenerative Medicine*, 4(5), pp. 374–386. doi: 10.1002/term.
- Yan, Wenqiang *et al.* (2020) ‘An Injectable Hydrogel Scaffold With Kartogenin-Encapsulated Nanoparticles for Porcine Cartilage Regeneration: A 12-Month Follow-up Study’, *American Journal of Sports Medicine*, 48(13), pp. 3233–3244. doi: 10.1177/0363546520957346.
- Yao, R. *et al.* (2013) ‘A biomimetic physiological model for human adipose tissue by adipocytes and endothelial cell cocultures with spatially controlled distribution’, *Biomedical Materials*, 8, p. 045005. doi: 10.1088/1748-6041/8/4/045005.
- Yazdani, M. *et al.* (2019) ‘A hyaluronan hydrogel scaffold for culture of human oral mucosal epithelial cells in limbal stem-cell therapy’, *Bioengineering*, 6(4). doi: 10.3390/bioengineering6040097.
- Ye, J. *et al.* (2012) ‘Primer-BLAST: A tool to design target-specific primers for polymerase chain reaction’, *BMC Bioinformatics*, 13(134). doi: 10.1186/1471-2105-13-134.
- Yousefi, F., Kandel, S. and Pleshko, N. (2018) ‘Infrared Spectroscopic Quantification of Methacrylation of Hyaluronic Acid: A Scaffold for Tissue Engineering Applications’, *Applied Spectroscopy*, 72(10), pp. 1455–1466. doi: 10.1177/0003702818785353.
- Yu, F. *et al.* (2014) ‘An injectable hyaluronic acid/PEG hydrogel for cartilage tissue engineering formed by integrating enzymatic crosslinking and Diels–Alder “click chemistry”, *Polymer Chemistry*, 5(3), pp. 1082–1090. doi: <https://doi.org/10.1039/C3PY00869J>.
- Yue, K. *et al.* (2015) ‘Synthesis, properties, and biomedical applications of gelatin methacryloyl (GelMA) hydrogels’, *Biomaterials*, 73, pp. 254–271. doi: 10.1016/j.biomaterials.2015.08.045.
- Zhai, P. *et al.* (2020) ‘The application of hyaluronic acid in bone regeneration’, *International Journal of Biological Macromolecules*. The Authors, 151, pp. 1224–1239. doi: 10.1016/j.ijbiomac.2019.10.169.

- Zhang, J. and Xiao, P. (2018) '3D printing of photopolymers', *Polymer Chemistry*. Royal Society of Chemistry, 9(13), pp. 1530–1540. doi: 10.1039/c8py00157j.
- Zhang, L. *et al.* (2010) 'Chondrogenic differentiation of human mesenchymal stem cells: A comparison between micromass and pellet culture systems', *Biotechnology Letters*, 32(9), pp. 1339–1346. doi: 10.1007/s10529-010-0293-x.
- Zhang, Y. S. *et al.* (2017) '3D Bioprinting for Tissue and Organ Fabrication', *Annals of Biomedical Engineering*, 45(1), pp. 148–163. doi: 10.1007/s10439-016-1612-8.
- Zhang, Z. *et al.* (2011) 'Selective suppression of cervical cancer HeLa cells by 2- O -  $\beta$  - D - glucopyranosyl- L -ascorbic acid isolated from the fruit of *Lycium barbarum* L .', *Cell Biology and Toxicology*, 27, pp. 107–121. doi: 10.1007/s10565-010-9174-2.
- Zhao, X. *et al.* (2016) 'Photocrosslinkable Gelatin Hydrogel for Epidermal Tissue Engineering', *Advanced Healthcare Materials*, 5(1), pp. 108–118. doi: 10.1002/adhm.201500005.
- Zhou, X. *et al.* (2016) '3D Bioprinting a Cell-Laden Bone Matrix for Breast Cancer Metastasis Study', *Applied Materials and Interfaces*, 8, pp. 30017–30026. doi: 10.1021/acsami.6b10673.
- Zhu, J. and Marchant, R. E. (2011) 'Design properties of hydrogel tissue-engineering scaffolds', *Expert Review of Medical Devices*, 8(5), pp. 607–626. doi: 10.1586/erd.11.27.
- Zhu, M. *et al.* (2019) 'Gelatin methacryloyl and its hydrogels with an exceptional degree of controllability and batch-to-batch consistency', *Scientific Reports*, 9(1), pp. 1–13. doi: 10.1038/s41598-019-42186-x.
- Zoratto, N. and Matricardi, P. (2018) *Semi-IPNs and IPN-based hydrogels*, *Polymeric Gels*. Elsevier Ltd. doi: 10.1016/b978-0-08-102179-8.00004-1.
- Zubillaga, V. *et al.* (2020) 'Adipose-derived mesenchymal stem cell chondrospheroids cultured in hypoxia and a 3D porous chitosan/chitin nanocrystal scaffold as a platform for cartilage tissue engineering', *International Journal of Molecular Sciences*, 21(3), pp. 1–17. doi: 10.3390/ijms21031004.
- Zuliani, C. C. *et al.* (2018) 'Micromass cultures are effective for differentiation of human amniotic fluid stem cells into chondrocytes.', *Clinics (Sao Paulo, Brazil)*, 73(7), p. e268. doi: 10.6061/clinics/2018/e268.
- Zustiak, S. P. and Leach, J. B. (2010) 'Hydrolytically Degradable Poly (Ethylene Glycol) Hydrogel Scaffolds with Tunable Degradation and Mechanical Properties', *Biomacromolecules*, 11, pp. 1348–1357. doi: 10.1021/bm100137q.

## Appendix

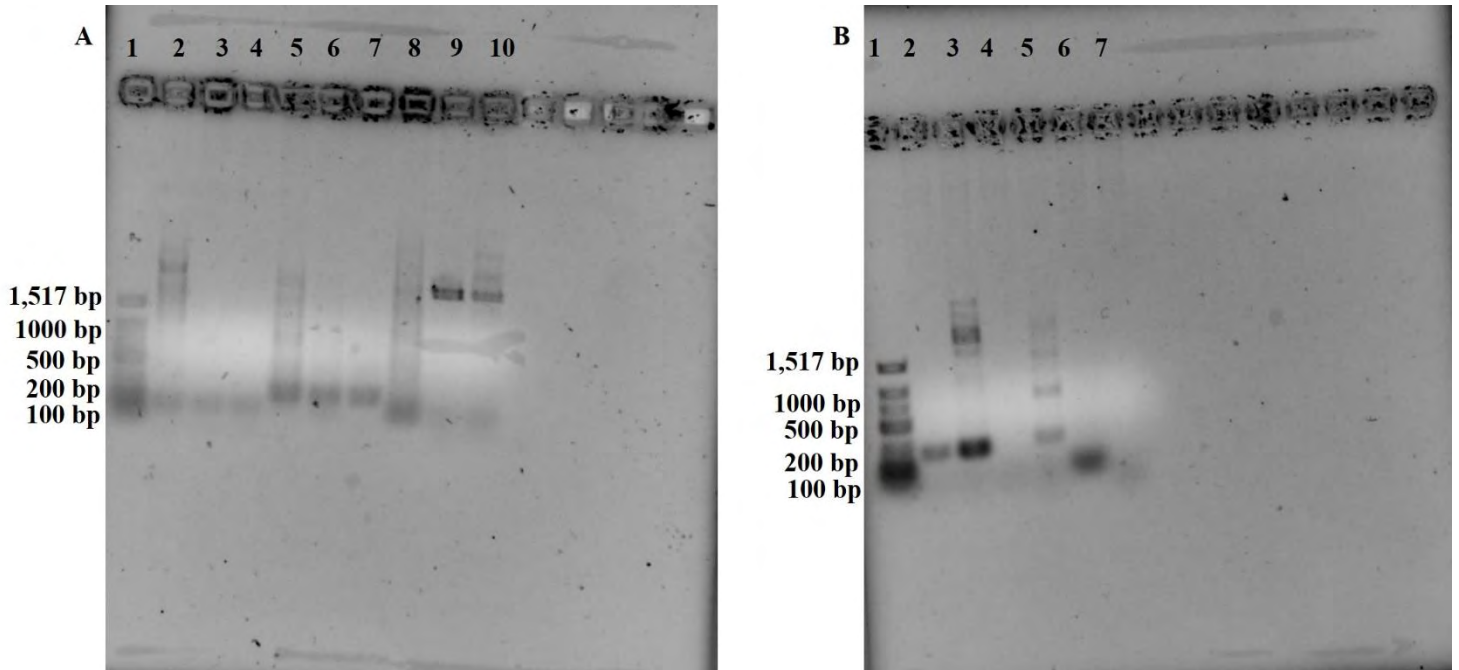


**Figure S 1: Primer optimization of gene markers Col2a1 (2-4), Runx2 (Lane 5-7) and Aggrecan (Lane 8-10) (A) and Col10a1 (Lanes 2-4) and Beta-Catenin (Lanes 5-7) (B).** Each lane shows the various annealing temperatures ( $T_a$ ) used during optimization of the gene expression markers. For gel A: Lane 1 – 100 bp DNA ladder; Lane 2 –  $T_a = 55^\circ\text{C}$ ; Lane 3 –  $T_a = 57^\circ\text{C}$ ; Lane 4 –  $T_a = 62^\circ\text{C}$ ; Lane 5 –  $T_a = 55^\circ\text{C}$ ; Lane 6 –  $T_a = 57^\circ\text{C}$ ; Lane 7 –  $T_a = 62^\circ\text{C}$ ; Lane 8 –  $T_a = 55^\circ\text{C}$ ; Lane 9 –  $T_a = 57^\circ\text{C}$ ; Lane 10 –  $T_a = 62^\circ\text{C}$ . For gel B: Lane 1 – 100 bp DNA ladder; Lane 2 –  $T_a = 53^\circ\text{C}$ ; Lane 3 –  $T_a = 58^\circ\text{C}$ ; Lane 4 –  $T_a = 62^\circ\text{C}$ ; Lane 5 –  $T_a = 53^\circ\text{C}$ ; Lane 6 –  $T_a = 58^\circ\text{C}$ ; Lane 7 –  $T_a = 62^\circ\text{C}$ . A 1.5 % (w/v) TAE agarose gel was used to run PCR products at 60 V, 30 mA for 1 hour. Gels were stained with 0.5  $\mu\text{g/ml}$  ethidium bromide post run. Each gel image is representative of  $n = 1$  as other PCR runs were unsuccessful in producing bands for the above gene expression markers.

In Figure 11, gel A, Col2a1 and Runx2 produced the most intense bands at an annealing temperature of  $55^\circ\text{C}$ , Aggrecan produced the most intense bands  $57$  and  $62^\circ\text{C}$  however show the incorrect product size for aggrecan therefor the band produced at  $55^\circ\text{C}$  is the correct size for aggrecan and can conclude its annealing temperature is at  $55^\circ\text{C}$ . In Figure 11, gel B, both Col10a1 and Beta-catenin produced bands at  $58^\circ\text{C}$  corresponding to the correct product sizes.

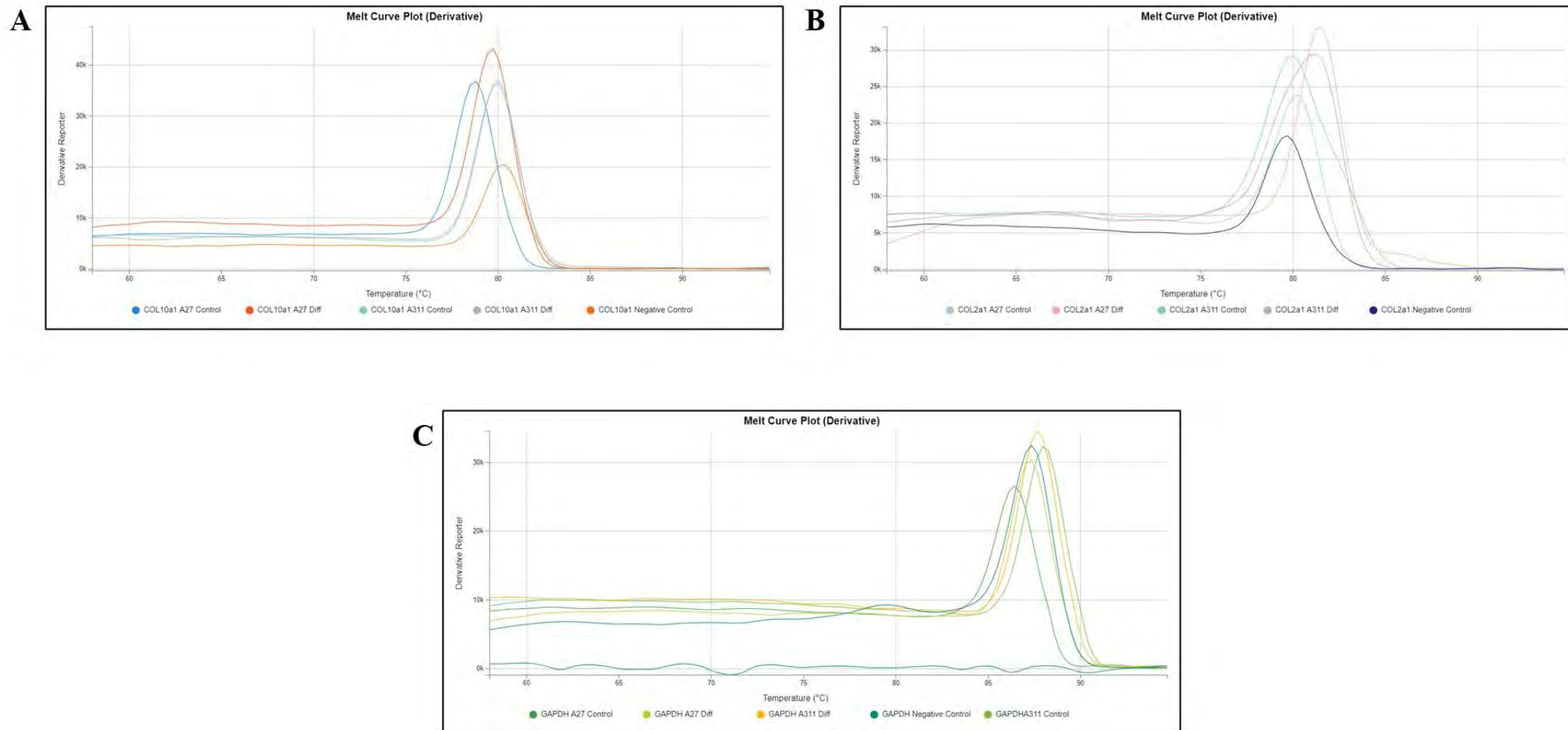


**Figure S 2: Melt Curve plots of the Gene Expression Levels of chondrogenic differentiation marker genes for collagen (A) Col10a1, (B) Col2a1 and the housekeeping gene GAPDH (C).** Melt curve graphs were generated using the Thermo Fisher Connect™, Design and Analysis New qPCR application. Each line plot for the gene markers Col10a1, GAPDH and Col2a1 is representative of N=2 where (A) and (B) are representative of n=2 and n = 1 respectively.

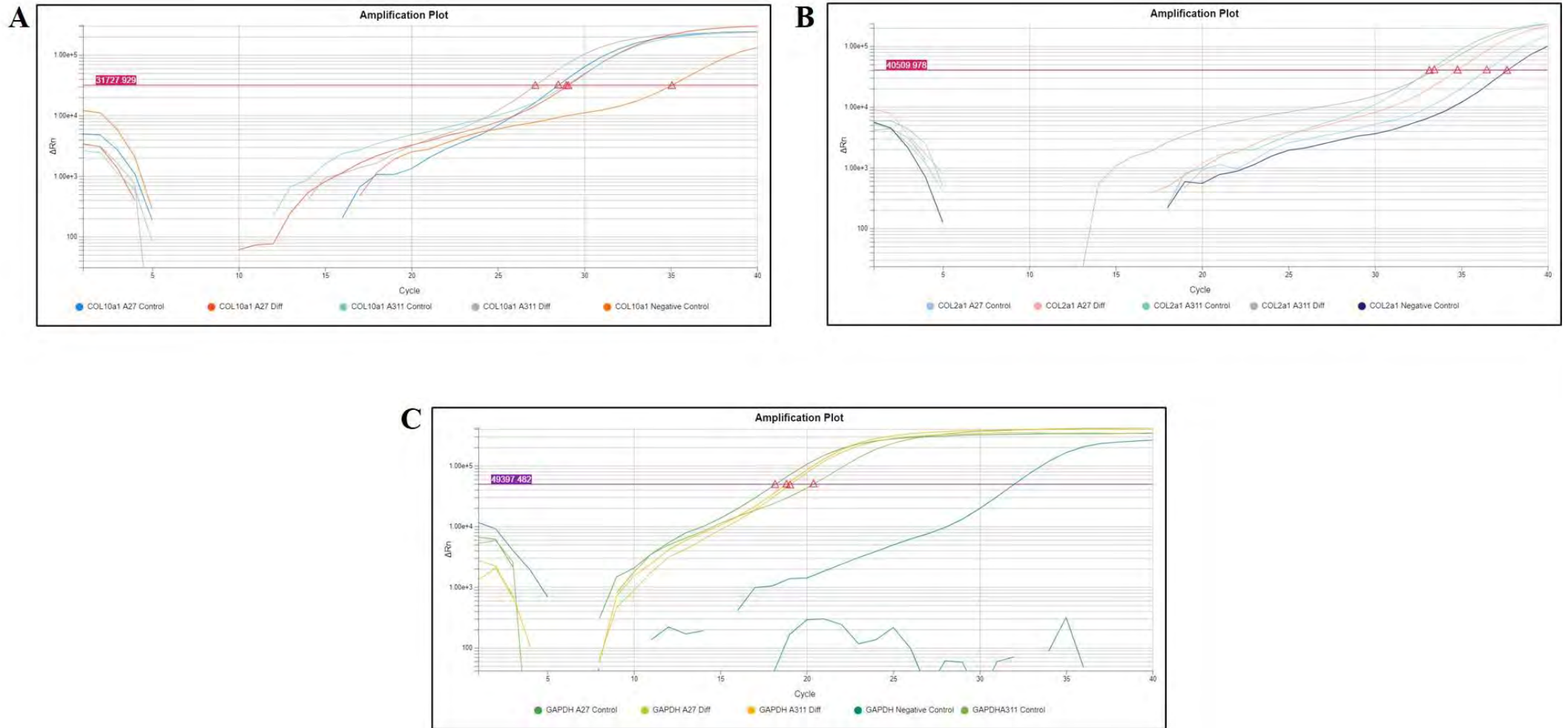


**Figure S 3: Amplification plots of the Gene Expression Levels of chondrogenic differentiation marker genes for collagen (A) Col10a1, (B) Col2a1 and the housekeeping gene GAPDH (C).** Melt curve graphs were generated using the Thermo Fisher Connect™, Design and Analysis New qPCR application. Each line plot for the gene markers Col10a1, GAPDH and Col2a1 is representative of N=2 where (A) and (B) are representative of n=2 and n = 1 respectively.

$R_n$  is the fluorescence of the reporter dye divided by the fluorescence of a passive reference dye; i.e.,  $R_n$  is the reporter signal normalized to the fluorescence signal of SYBR Green dye.  $\Delta R_n$  is  $R_n$  minus the baseline;  $\Delta R_n$  is plotted against PCR cycle number.

Figure 36 shows the melt curve plot (derivatives) produced from the gene expression markers Col10a1, Col2a1 and GAPDH (housekeeping gene) after the RT-qPCR assay. Cell line A270620-01A, which was exposed to chondrogenic differentiation media (diff) continuously showed the highest melt curve peaks for all gene expression markers ranging between 30-45K followed by the A311019-02T diff cell line. The control group of A311019-02T showed similar peaks to the A311019-02T diff group and the A270620-01A control group showed lower peaks between 20-35K. For the gene expression markers Col10a1 and Col2a1 the negative control displayed small peaks between 17-20K, which could be the result of primer dimerization. The negative control for GAPDH showed no peaks present. Gene marker Col10a1 resulted in the melt curve points to average at 78-81°C, Col2a1 resulted in the melt curve point to average at 79-83 °C and GAPDH to average at 87-88 °C.

Figure 37 shows the amplification plots of the RT-qPCR run for the gene expression markers Col10a1, Col2a1 and GAPDH (housekeeping gene). Amplification threshold for Col10a1 resulted at 31727.929 between cycles 27-29 for the differentiation and control samples. The negative control reached the threshold after 36 cycles. The amplification threshold for Col2a1 resulted at 40509.978 between cycles 33-35. The negative control reached the cycle threshold at cycle 37. Amplification threshold for GAPDH resulted at 49397.482 between 17-18 cycles. The negative control reached the cycle threshold after 32 cycles.



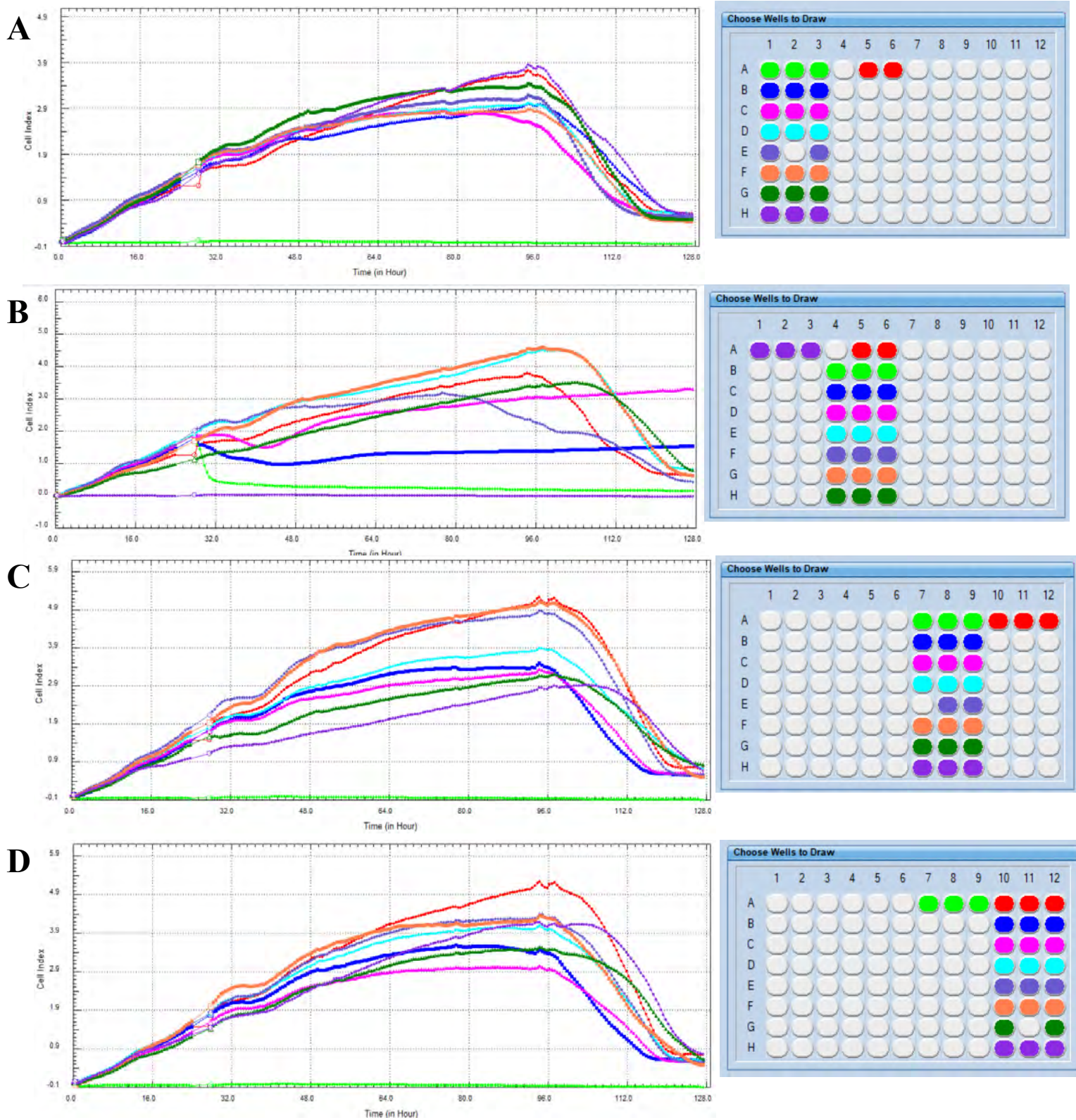


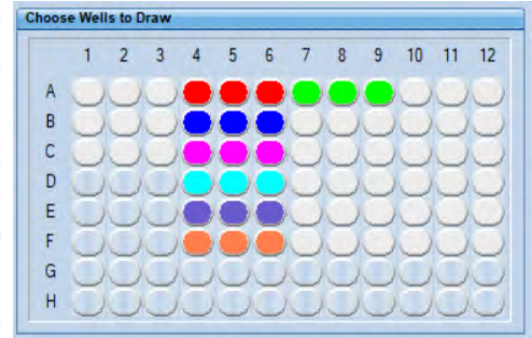
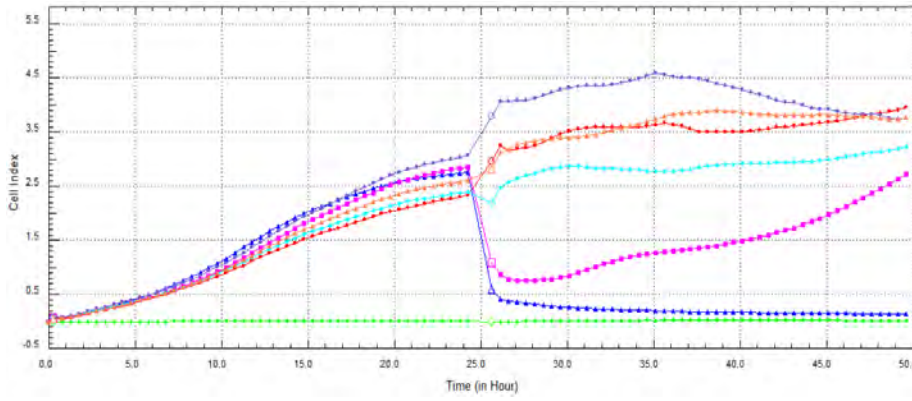
**Figure S 4: RTCA cell index graphs of Ascorbic Acid(A), Dexamethasone (B), TGF-β3 (C), L-Proline (D).** Cell index graph is shown on the left with the well key shown on the right. Specific wells were emitted due to well electrode error.

	1	2	3	4	5	6	7	8	9	10	11	12
A	Media	Media	Media	Control	Control	Control	Media	Media	Media	Control	Control	Control
B	Hela 6000 corbicAcid 500.00ug/ml	Hela 6000 corbicAcid 500.00ug/ml	Hela 6000 corbicAcid 500.00ug/ml	Hela 6000 xanthasone 1.00e+003	Hela 6000 xanthasone 1.00e+003	Hela 6000 xanthasone 1.00e+003	Hela 6000 TGF-B3 (100.00ng/ml)	Hela 6000 TGF-B3 (100.00ng/ml)	Hela 6000 TGF-B3 (100.00ng/ml)	Hela 6000 L-Proline 400.00ug/ml	Hela 6000 L-Proline 400.00ug/ml	Hela 6000 L-Proline 400.00ug/ml
C	Hela 6000 corbicAcid 350.00ug/ml	Hela 6000 corbicAcid 350.00ug/ml	Hela 6000 corbicAcid 350.00ug/ml	Hela 6000 xanthasone 600.00ml	Hela 6000 xanthasone 600.00ml	Hela 6000 xanthasone 600.00ml	Hela 6000 TGF-B3 (60.00ng/ml)	Hela 6000 TGF-B3 (60.00ng/ml)	Hela 6000 TGF-B3 (60.00ng/ml)	Hela 6000 L-Proline 250.00ug/ml	Hela 6000 L-Proline 250.00ug/ml	Hela 6000 L-Proline 250.00ug/ml
D	Hela 6000 corbicAcid 150.00ug/ml	Hela 6000 corbicAcid 150.00ug/ml	Hela 6000 corbicAcid 150.00ug/ml	Hela 6000 xanthasone 300.00ml	Hela 6000 xanthasone 300.00ml	Hela 6000 xanthasone 300.00ml	Hela 6000 TGF-B3 (30.00ng/ml)	Hela 6000 TGF-B3 (30.00ng/ml)	Hela 6000 TGF-B3 (30.00ng/ml)	Hela 6000 L-Proline 120.00ug/ml	Hela 6000 L-Proline 120.00ug/ml	Hela 6000 L-Proline 120.00ug/ml
E	Hela 6000 corbicAcid 50.00ug/ml	Hela 6000 corbicAcid 50.00ug/ml	Hela 6000 corbicAcid 50.00ug/ml	Hela 6000 xanthasone 100.00ml	Hela 6000 xanthasone 100.00ml	Hela 6000 xanthasone 100.00ml	Hela 6000 TGF-B3 (10.00ng/ml)	Hela 6000 TGF-B3 (10.00ng/ml)	Hela 6000 TGF-B3 (10.00ng/ml)	Hela 6000 L-Proline 40.00ug/ml	Hela 6000 L-Proline 40.00ug/ml	Hela 6000 L-Proline 40.00ug/ml
F	Hela 6000 corbicAcid 35.00ug/ml	Hela 6000 corbicAcid 35.00ug/ml	Hela 6000 corbicAcid 35.00ug/ml	Hela 6000 xanthasone 60.00ml	Hela 6000 xanthasone 60.00ml	Hela 6000 xanthasone 60.00ml	Hela 6000 TGF-B3 (6.00ng/ml)	Hela 6000 TGF-B3 (6.00ng/ml)	Hela 6000 TGF-B3 (6.00ng/ml)	Hela 6000 L-Proline 25.00ug/ml	Hela 6000 L-Proline 25.00ug/ml	Hela 6000 L-Proline 25.00ug/ml
G	Hela 6000 corbicAcid 15.00ug/ml	Hela 6000 corbicAcid 15.00ug/ml	Hela 6000 corbicAcid 15.00ug/ml	Hela 6000 xanthasone 30.00ml	Hela 6000 xanthasone 30.00ml	Hela 6000 xanthasone 30.00ml	Hela 6000 TGF-B3 (3.00ng/ml)	Hela 6000 TGF-B3 (3.00ng/ml)	Hela 6000 TGF-B3 (3.00ng/ml)	Hela 6000 L-Proline 12.00ug/ml	Hela 6000 L-Proline 12.00ug/ml	Hela 6000 L-Proline 12.00ug/ml
H	Hela 6000 corbicAcid 5.00ug/ml	Hela 6000 corbicAcid 5.00ug/ml	Hela 6000 corbicAcid 5.00ug/ml	Hela 6000 xanthasone 10.00ml	Hela 6000 xanthasone 10.00ml	Hela 6000 xanthasone 10.00ml	Hela 6000 TGF-B3 (1.00ng/ml)	Hela 6000 TGF-B3 (1.00ng/ml)	Hela 6000 TGF-B3 (1.00ng/ml)	Hela 6000 L-Proline 4.00ug/ml	Hela 6000 L-Proline 4.00ug/ml	Hela 6000 L-Proline 4.00ug/ml

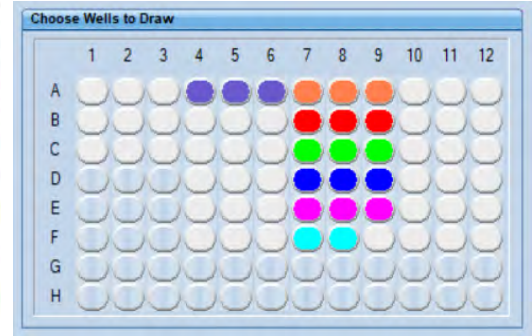
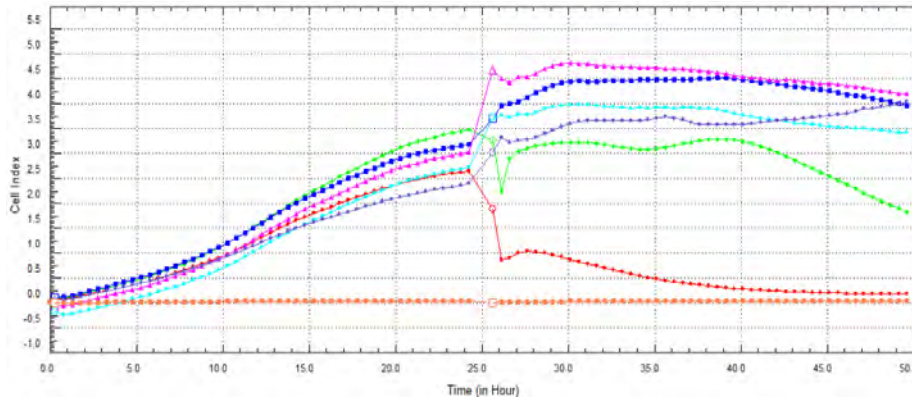
**Figure S 5: RTCA well plate layout of the chondrogenic differentiation components and ranging concentrations.**



**A**



**B**



**C**

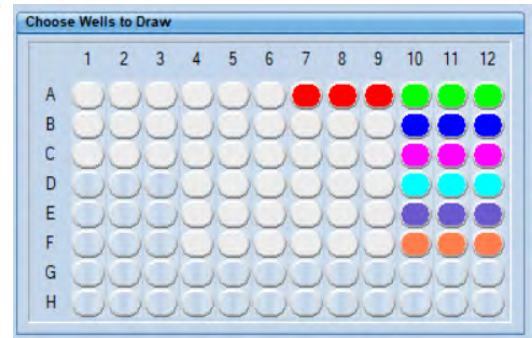
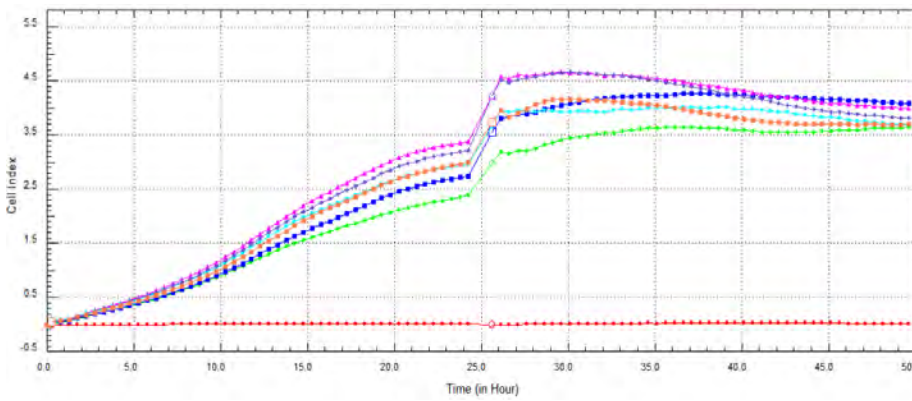


**Figure S 6: RTCA cell index graphs of Eosin Y (A), TEA (B) and NVP (C). Cell index graph is shown on the left with the well key shown on the right. Specific wells were emitted due to well electrode error.**

	1	2	3	4	5	6	7	8	9	10	11	12
A				Hela 6000	Hela 6000	Hela 6000	media	media	media	Hela 6000	Hela 6000	Hela 6000
B				Hela 6000 EosinY 100.00uM	Hela 6000 EosinY 100.00uM	Hela 6000 EosinY 100.00uM	Hela 6000 TEA 1.00%	Hela 6000 TEA 1.00%	Hela 6000 TEA 1.00%	Hela 6000 NVP 370.00nM	Hela 6000 NVP 370.00nM	Hela 6000 NVP 370.00nM
C				Hela 6000 EosinY 50.00uM	Hela 6000 EosinY 50.00uM	Hela 6000 EosinY 50.00uM	Hela 6000 TEA 0.50%	Hela 6000 TEA 0.50%	Hela 6000 TEA 0.50%	Hela 6000 NVP 150.00nM	Hela 6000 NVP 150.00nM	Hela 6000 NVP 150.00nM
D				Hela 6000 EosinY 10.00uM	Hela 6000 EosinY 10.00uM	Hela 6000 EosinY 10.00uM	Hela 6000 TEA 1.00e+003%	Hela 6000 TEA 1.00e+003%	Hela 6000 TEA 1.00e+003%	Hela 6000 NVP 37.00nM	Hela 6000 NVP 37.00nM	Hela 6000 NVP 37.00nM
E				Hela 6000 EosinY 5.00uM	Hela 6000 EosinY 5.00uM	Hela 6000 EosinY 5.00uM	Hela 6000 TEA 500.00%	Hela 6000 TEA 500.00%	Hela 6000 TEA 500.00%	Hela 6000 NVP 15.00nM	Hela 6000 NVP 15.00nM	Hela 6000 NVP 15.00nM
F				Hela 6000 EosinY 1.00uM	Hela 6000 EosinY 1.00uM	Hela 6000 EosinY 1.00uM	Hela 6000 TEA 100.00%	Hela 6000 TEA 100.00%	Hela 6000 TEA 100.00%	Hela 6000 NVP 3.70nM	Hela 6000 NVP 3.70nM	Hela 6000 NVP 3.70nM

**Figure S 7: RTCA well plate layout of the visible light photoinitiator components and ranging concentrations.**

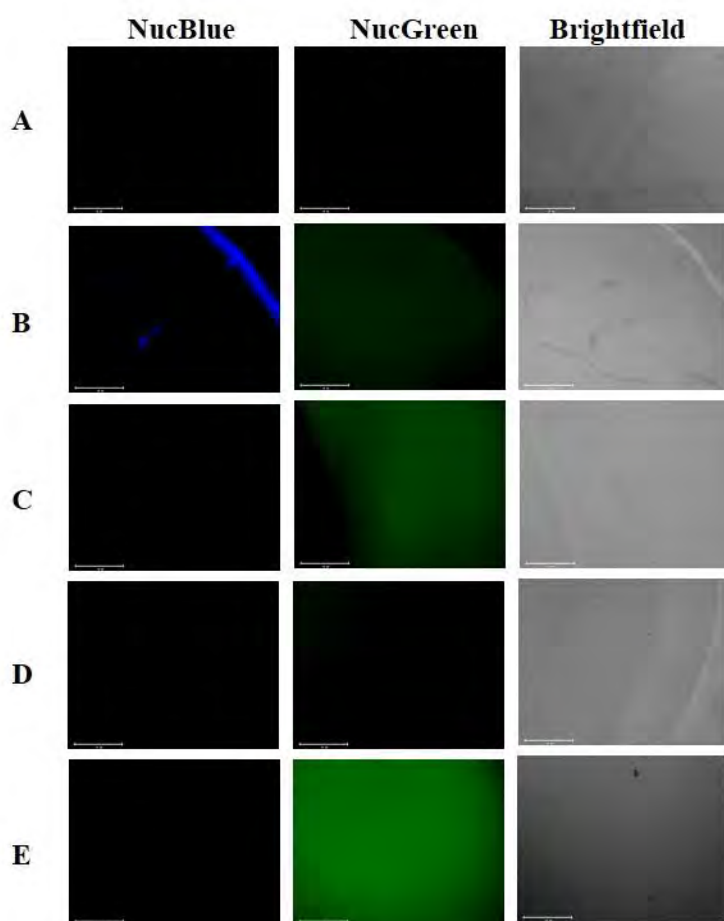


**Figure S 8: Cell viability images of negative controls from formulated hydrogels after 24-hours cell seeding at a cell density of 5000 cells/hydrogel disk.** A – 10 % GelMA, B – 10 % PEGDA, C – 5 % GelMA/ 5 % PEGDA, D – 10 % GelMA/0.5 % HAMA and E – 10 % PEGDA/0.5 % HAMA. Each image represents N = 3 and each batch experiment had n = 3. Scale bar on each image = 650  $\mu$ M.

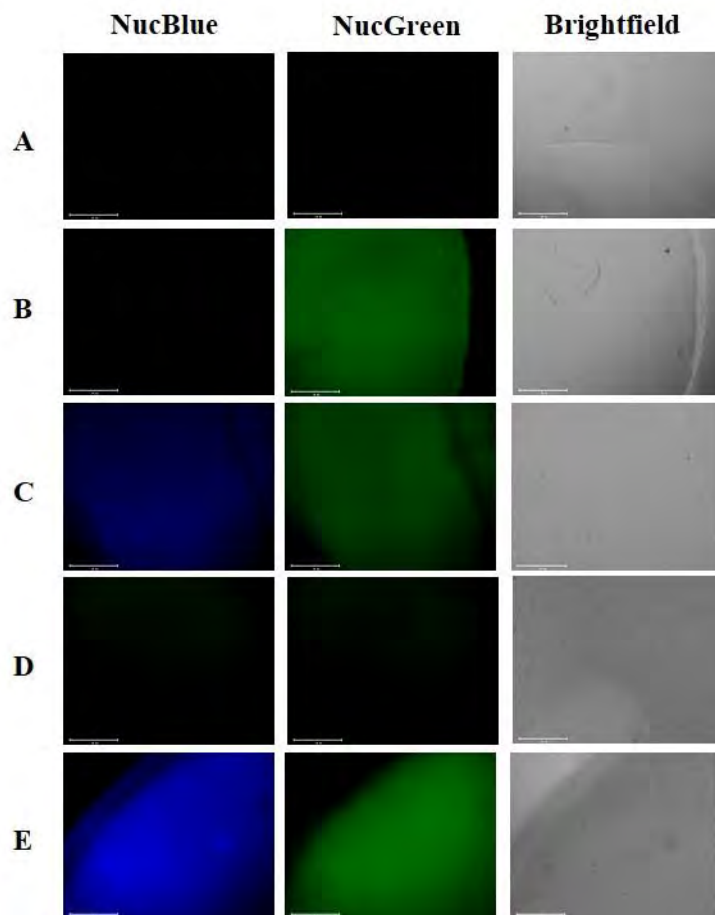


**Figure S 9: Cell viability images of negative controls from formulated hydrogels after 36-hours cell seeding at a cell density of 5000 cells/hydrogel disk. A – 10 % GelMA, B – 10 % PEGDA, C – 5 % GelMA/ 5 % PEGDA, D – 10 % GelMA/0.5 % HAMA and E – 10 % PEGDA/0.5 % HAMA. Each image represents N = 3 and each batch experiment had n = 3. Scale bar on each image = 650  $\mu$ M.**

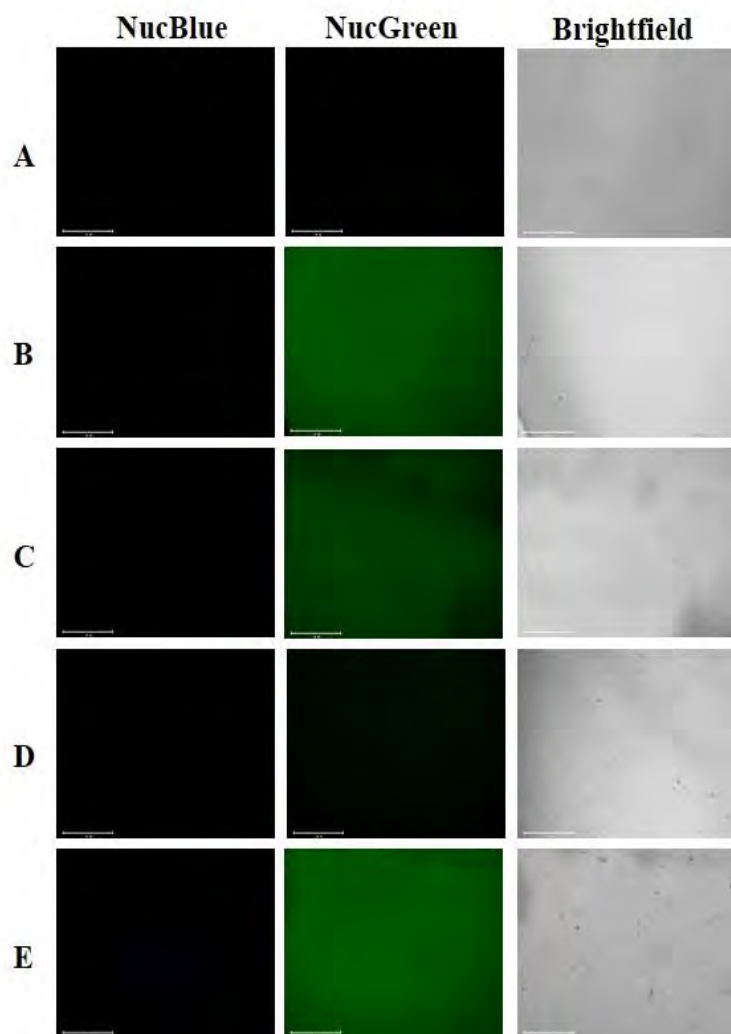


**Figure S 10: Cell viability images of negative controls from formulated hydrogels after 7 days cell seeding at a cell density of 5000 cells/hydrogel disk. A – 10 % GelMA, B – 10 % PEGDA, C – 5 % GelMA/ 5 % PEGDA, D – 10 % GelMA/0.5 % HAMA and E – 10 % PEGDA/0.5 % HAMA. Each image represents N = 3 and each batch experiment had n = 3. Scale bar on each image = 650  $\mu$ M.**

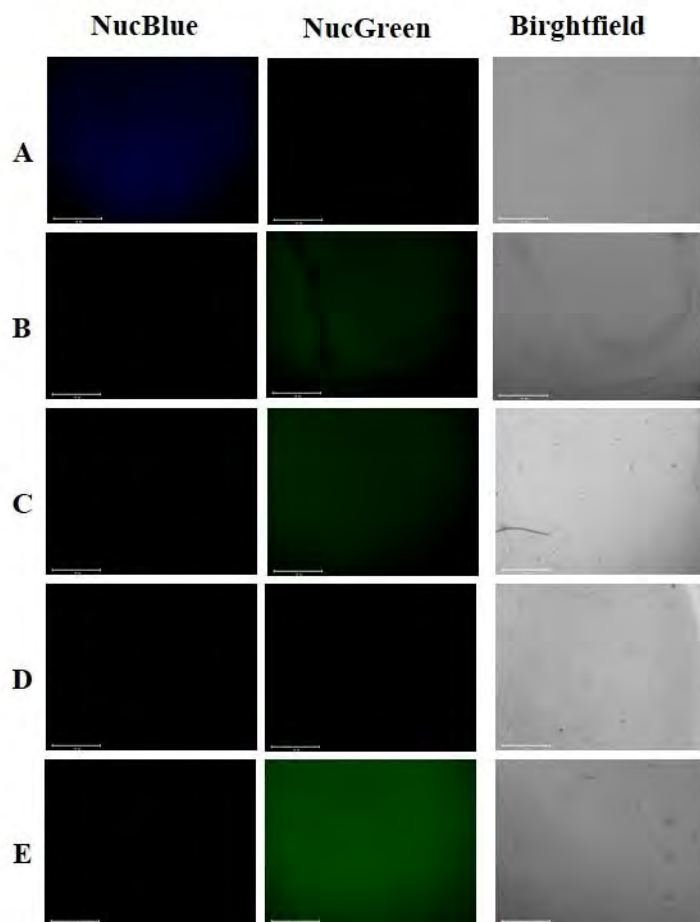


**Figure S 11: Cell viability images of negative controls from formulated hydrogels after 24-hours cell seeding at a cell density of 50 000 cells/hydrogel disk. A – 10 % GelMA, B – 10 % PEGDA, C – 5 % GelMA/ 5 % PEGDA, D – 10 % GelMA/0.5 % HAMA and E – 10 % PEGDA/0.5 % HAMA. Each image represents N = 3 and each batch experiment had n = 3. Scale bar on each image = 650  $\mu$ M.**

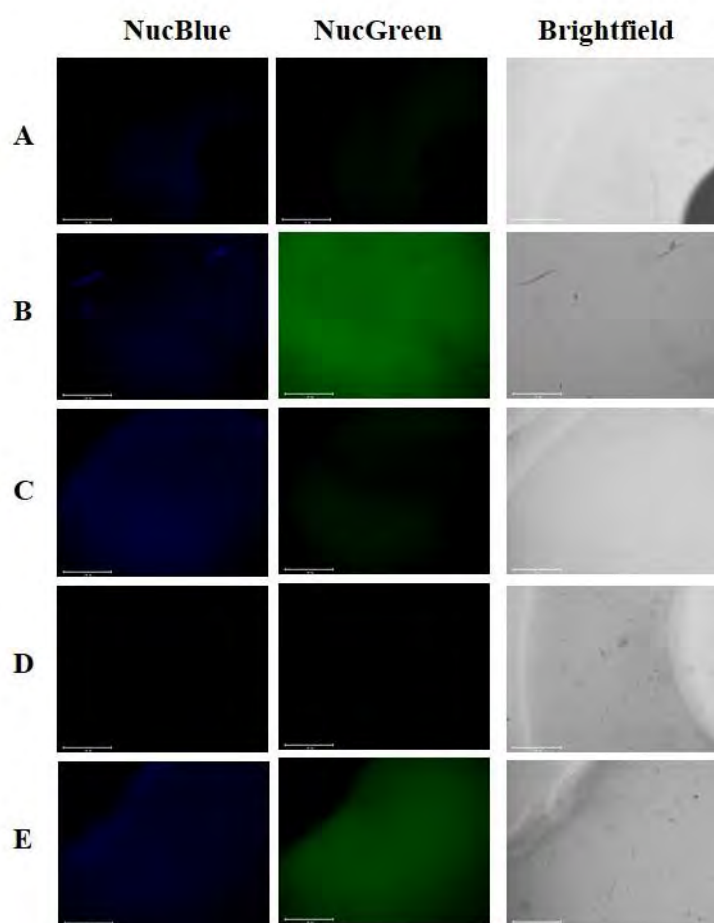


**Figure S 12: Cell viability images of negative controls from formulated hydrogels after 36-hours cell seeding at a cell density of 50 000 cells/hydrogel disk. A – 10 % GelMA, B – 10 % PEGDA, C – 5 % GelMA/ 5 % PEGDA, D – 10 % GelMA/0.5 % HAMA and E – 10 % PEGDA/0.5 % HAMA. Each image represents N = 3 and each batch experiment had n = 3. Scale bar on each image = 650  $\mu$ M.**



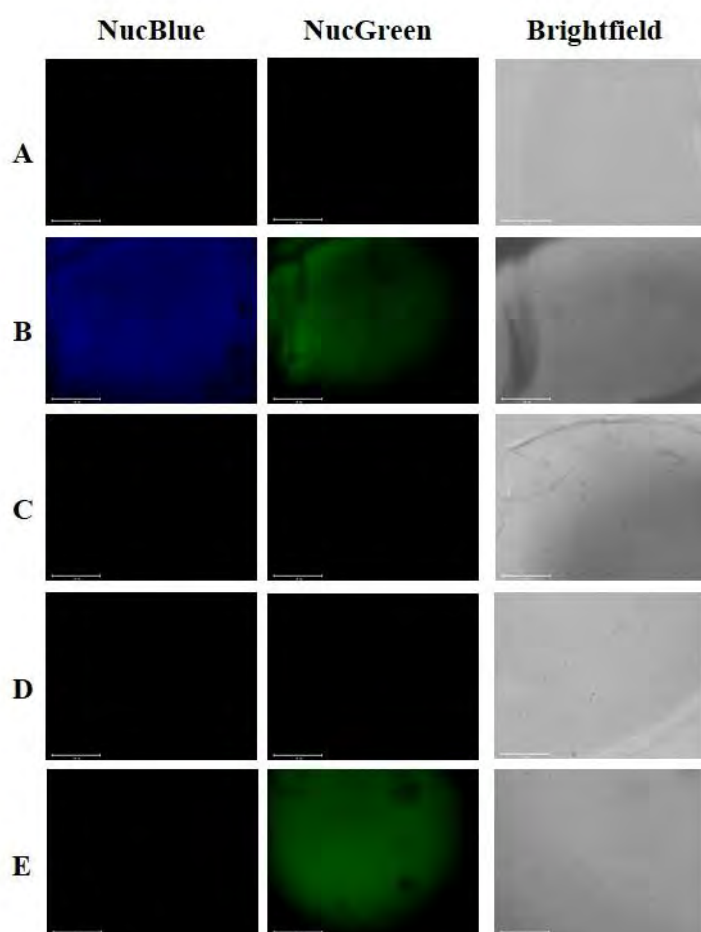


**Figure S 13: Cell viability images of negative controls from formulated hydrogels after 7 days cell seeding at a cell density of 50 000 cells/hydrogel disk. A – 10 % GelMA, B – 10 % PEGDA, C – 5 % GelMA/ 5 % PEGDA, D – 10 % GelMA/0.5 % HAMA and E – 10 % PEGDA/0.5 % HAMA. Each image represents N = 3 and each batch experiment had n = 3. Scale bar on each image = 650  $\mu$ M.**